Gold Nanorods: Seedless Synthesis with High Yield, One-Step Surface Functionalization, and Applications

A thesis submitted for the degree of

Doctor of Philosophy

By

Kang Liu

Department of Chemical Engineering

Monash University

Australia

September 2017

Copyright notice

Abstract

Since discovered by electrochemical synthesis in the 1990s, gold nanorods (AuNRs) have received tremendous attentions due to their unique tunable optical properties, i.e., longitudinal surface plasmon resonance (LSPR). The intense LSPR can significantly enhance the light scattering, which makes AuNRs promising for the biomedical imaging and surface-enhanced Raman spectroscopy (SERS). In addition, the LSPR can boost the light absorption and effectively convert the absorbed light to heat, which makes AuNRs well-suited for photo-thermal therapy by destructing cell and tissue. Despite of the above appealing applications, great challenges still exist in the nanorods synthesis and surface modification, which seriously hinder their applications. The main objective of the work presented in this thesis was to overcome these challenges and make the synthesis and surface modification of nanorods much easier towards their applications.

1. Nanorods synthesis. The conventional seed-mediated synthesis is not only limited by the operational complexity and the over-sensitivity towards subtle changes in the experimental parameters, but also suffers from low yield (only ~15% of the Au precursor is reduced to metallic Au), which seriously impede their practical applications. We designed a facile seedless synthetic method to overcome the above challenges via synergistic template modification and growth kinetics regulation.

2. Nanorods surface modification. The as-synthesized AuNRs are encapsulated by bilayer cetyltrimethylammonium bromide (CTAB). The CTAB tightly adsorbs on the gold surface to form a dense surface-confined cationic bilayer with the trimethylammonium head facing the external environment. Before most applications, the CTAB bilayers must first be replaced with the proper organic or inorganic material to grant stability and functionality. But the surface modification of AuNRs can be quite challenging due to the strong interaction between CTAB and gold surface. To address the above issue, we developed a novel, facile, one-step surface functionalization method that involves the use of Tween 20 to stabilize AuNRs, bis(p-sulfonatophenyl)phenylphosphine (BSPP) to activate the AuNR surface for the subsequent thiolated-ligands conjugation, and NaCl to etch silver from the AuNRs. This method allows for the complete removal of the surface-bound CTAB and produces

stable functionalized AuNRs. The surface modification method developed can be easily extended to negatively charged surface ligands, for example, thiol-PEG-carboxyl, and other nanoparticle (NP) systems with different compositions and shapes.

3. After the challenges in synthesis and surface modification were overcome, AuNRs were investigated in photocatalytic applications. AuNRs and TiO_2 were conjugated for efficient hydrogen production, mainly because AuNRs possess widely tunable SPR band from visible to near-infrared (NIR) range with a large cross-~~-~~section. The fabrication of AuNRs and TiO_2 nanostructures aiming at utilizing UV-Vis-NIR light, however, is still challenging. This is mainly due to the fact that ~~As calcination at h~~high calcination temperatures (above 450 °C), which is usually required to obtain a UV-active TiO_2 in the anatase phase, is detrimental for anisotropic AuNRs. We reported the facile synthesis of AuNRs@crystalized TiO_2 core-shell nanostructures by uniformly coating TiO_2 on AuNRs through elaborate-controlled hydrolysis of titania precursor and subsequent hydrothermal treatment (~75 °C). The crystalized TiO_2 shell as an effective physical barrier together with relatively low-~~-~~temperature treatment is~~are~~ important in preserving the intactness of the gold core. The as-synthesized AuNRs@TiO_2 core-shell nanoparticles (NPs) show significantly enhanced H_2 generation ability under UV-Vis-NIR light irradiation.

Declaration

This thesis contains no material which has been accepted for the award of any other degree or diploma at any university or equivalent institution and that, to the best of my knowledge and belief, this thesis contains no material previously published or written by another person, except where due reference is made in the text of the thesis.

Signature: 

Print Name: Kang Liu

Date: …….

List of Publications

1. **Kang Liu,** Yuanhui Zheng, Xun Lu, Thibaut Thai, Nanju Alice Lee, Udo Bach, and J. Justin Gooding. Biocompatible Gold Nanorods: One-Step Surface Functionalization, Highly Colloidal Stability, and Low Cytotoxicity. *Langmuir*, **2015**, *31* (17), pp 4973–4980.

2. **Kang Liu,** Yanru Bu, Dr. Yuanhui Zheng, Prof. Xuchuan Jiang, Prof. Aibing Yu, Prof. Huanting Wang. Seedless Synthesis of Monodispersed Gold Nanorods with Remarkably High Yield: Synergistic Effect of Template Modification and Growth Kinetics Regulation. *Chem. Eur. J.* **2017**, 23, 1-10.

3. Yanru Bu, **Kang Liu,** Yaoxin Hu, Yusuf V. Kaneti, Arnaud Brioude, Xuchuan Jiang, Huanting Wang and Aibing Yu. Bilayer Composites Consisting of Gold Nanorods and Titanium Dioxide as Highly Sensitive and Self-cleaning SERS Substrates. *Microchimica Acta. **2017**, 184(8), 2805-2813. DOI 10.1007/s00604-017-2301-5*

4. **Kang Liu,** Yanru Bu, Yan Liang, Zhouyou Wang, Xiwang Zhang, Aibing Yu, Xuchuan Jiang and Huanting Wang. (Gold Nanorods)@(Anatase TiO_2) Core-Shell Nanostructures for Efficient Hydrogen Generation under Wide-Range UV-Vis-NIR Light. (Manuscript drafted)

5. **Kang Liu,** Yanru Bu, Yuanhui Zheng, Huanting Wang and Aibing Yu. Surface-Enhanced Raman Spectroscopy (SERS): Recent Advances and Molecular Trapping Technique. (Manuscript drafted)

6. Yanru Bu, **Kang Liu,** Xuchuan Jiang*, Aibing Yu, Systematically Design and Optimizing the Preparation of Nano-porous SiO_2-TiO_2 Self-Cleaning Films. (Manuscript drafted)

7. Yanru Bu, **Kang Liu**, Xuchuan Jiang*, Aibing Yu, Optional Electro-Deposition of Au Nano-Flowers Inside or Outside Pores as SERS Substrates Using Porous Titanium Dioxide Films as Templates. (Manuscript drafted)

Oral and Poster Presentations

1. **Kang Liu**, Yuanhui Zheng, Alice Lee, J. Justin. Gooding. Biocompatible gold nanorods: Surface modification and Cytotoxicity Investigation. Symposium on Food Innovation – Present & Future, Nov, 27-28, 2014, UNSW, Kensington campus, Australia (Oral Presentation).

2. **Kang Liu**, Yuanhui Zheng, J. Justin. Gooding, Huanting Wang. Biocompatible gold nanorods: Synthesis and Surface Mmodification. 5th Chemical Engineering Postgraduate Association Conference, Oct, 28, 2015, Monash University, Clayton, Australia (Poster Presentation).

3. **Kang Liu**, Yanru Bu, Yuanhui Zheng, Xuchuan Jiang, Aibing Yu, and Huanting Wang. Monodisperse Gold Nanorods: Seedless Synthesis and High Yield of Gold Conversion. (European Materials Research Society) E-MRS 2017 Spring Meeting, May, 22-26, 2017, Strasbourg, France (Oral Presentation).

Acknowledgements

I would like to thank the people for their support and contribution towards my successful accomplishment of my Ph.D. First of all, I would like to express my gratitude to my supervisors, Prof. Huanting Wang and Prof. Aibing Yu, who gave me this precious opportunity to study in Monash University and all the help and guidance. I would like to thank Dr. Ruiping Zou and Lilyanne Price for their help during the transfer from University of New South Wales (UNSW).

I also want to thank the supervisors while I was in UNSW, Prof. John Justin Gooding, and Dr. Alice Lee, for their guidance with knowledge and encouragement. Special thanks to Dr. Yuanhui Zheng, I would not be able to successfully accomplish this Ph.D.~~D~~ without his help. His profound knowledge, prudent attitude and extensive experience have set a positive example of~~n~~ what a real scientist is and shown me how to perform scientific research. During the early stage of struggle, his elaborate supervision and mental consolation are~~is~~ always there to keep me motivated and away from discouragement.

I would like to thank all the members in Huanting group, Laboratory for Simulation and Modeling of Particulate Systems (SIMPAS) group, Xiwang group (Prof. Xiwang Zhang), Gooding group and Alice group. Es~~S~~pecially, I want to thank Yaoxin Hu for electron microscope measurements, and Yan Liang for electron microscope and x-ray diffraction (XRD) measurements. I would like to thank Dr. Xiya Fang from Monash Centre for Electron Microscopy (MCEM) for her help on the scanning electron microscope (SEM) characterization~~,~~ and thank Marius M. J. Marius of HRL Technology Group Pty Ltd. for assistance in the characterization using inductively coupled plasma atomic emission spectroscopy (ICP-OES). Also, thanks to Mr. Finlay Shanks and Yanru Bu for providing technical assistance with surface--enhanced Raman scattering (SERS) experiments~~,~~ and Prof. Xiwang Zhang and Emily Wang for the provision of training and access to gas chromatography (GC).

I would like to thank UNSW and Australian Research Council (ARC) training center~~re~~ for providing me scholarship while I was in UNSW, and Monash University and

SIMPAS for the provision of Monash Departmental Scholarship (MDS). OAnother thanks tofor the kind staffs in Department of Chemical Engineering, especially Lilyanne Price, Kim Phu, Jill Crisfield, and Rebecca Bulmer. Their help makes my Ph.D.D life in Chemical Engineering much more convenient and makes me proud being a student atin Monash University.

I am deeply grateful to Yanru Bu, my wife, and best lab partner, for her love, understanding, and moral support. Thank you for never losing faith in me especially in the difficult moments.

Finally, I would like to thank my sister and parents. They are my greatest supporter and always had my back no matter what.

Contents

List of Abbreviations

AA Ascorbic Acid

APTES (3-Aminopropyl)triethoxysilane

AuNPs Gold Nanoparticles

AuNRs Gold Nanorods

AuNSs Gold Nanospheres

BDAC Benzyldimethylhexadecylammonium Chloride

BSPP Bis(p-sulfonateophenyl)phenylphosphine Dihydrate Dipotassium Salt

CB Conduction Band

CMC Critical Micelle Concentration

CTAB Cetyltrimethylammonium Bromide

CTAC Alkyltrimethylammonium Chloride

CDs Carbon Dots

DTT Dodecanethiolacetone

DMEM Dulbecco's modified Eagle's Medium

DMSO Dimethyl Sulfoxide

EBL Electron Beam Lithography

EDX Energy-Dispersive X-ray

EXAFS Extended X-ray Absorption Fine Structure

FID Flame Ionization Detector

FTO Fluorine-doped Tin Oxide

GC Gas Chromatograph

HQ Hydroquinone

ICP-OES Inductively Coupled Plasma Optical Emission Spectrometer

LBL	Layer-by-Layer
LSPR	Localized Surface Plasmon Resonance
MA	Maleic Acid
MTAB	(16-mercaptohexadecyl) trimethylammonium Bromide
MUA	Mercaptoundecanoic Acid
MUDA	11-Mercaptoundecanoic Acids
NAOL	Sodium Oleate
NIR	Near-Infrared
NPs	Nanoparticles
OTAB	Octadecyltrimethylammonium Bromide
PAA	Polyacrylic Acid
PEG	Polyethylene Glycol
PL	Photoluminescence
PSS	Poly(Sodium-4-Styrenesulfonate)
PTT	Plasmon-Assisted Photothermal Therapy
SEM	Scanning Electron Microscopy
SERS	Surface--Enhanced Raman Scattering
STEM	Scanning Transmission Electron Microscopy
TEM	Transmission Electron Microscopy
TOAB	Tetradodecylammonium Bromide
TSPR	Transverse Surface Plasmon Resonance
Tween 20	Polyoxyethylene (20) sorbitan monlaurate
UPD	Underpotential Deposition
VB	Valence Band
XPS	X-ray Photoelectron Spectroscopy

List of Figures

List of Tables

Chapter 1 Introduction

Gold has been regarded as one of the most precious matters in the world ever since its first extraction in the 5th century BC. By nature, it is highly inert and as such, gold in its bulk form has been widely used in jewellery, coinage, and electronics. It becomes more 'precious' when it is divided into fragments of sizes reaching down to ~100 nm nanogold. The word "*nano*", derived from the Greek *nanos*, meaning dwarf, is used to describe any material or property with dimensions on the nanometer scale (1~100 nm). The nanoscale confinement of electrons on the surface of gold nanoparticles (AuNPs) grants them shape- and size-dependent properties not seen in their bulk-scale.[1-2] Though AuNPs represent one of the most remarkable areas of modern nanoscience and nanotechnology, gold nanospheres (AuNSs) have been known for thousands of years. Most famous examples are the beautiful Lycurgus Cup (5th to 4th century B.C.)[3] and wet chemical synthesis of gold colloids, initiated by Michael Faraday (1857).[4] Initially, spherical or quasi-spherical AuNPs received the most attention due to the ease of synthesis of such structures. Indeed, this is perhaps unsurprising given that the spherical shape is often the most thermodynamically and kinetically favourable morphology. The free mobile electrons are spatially confined in a quantum box (the particle) and show the collective oscillation frequency of the localized surface plasmon resonance (LSPR).[5-6] This unique capability enables extremely large electric field enhancements around the NPs, giving rise to a variety of light–matter interactions with new mechanisms, such as plasmon-enhanced spectroscopies,[7] high-harmonic generation,[8] optical nanoantenna effect,[9] plasmon-induced vacuum Rabi splitting,[10-11] photothermal conversion,[12] and plasmon-assisted photochemical reactions.[13-14] Driven by the utilization of these fascinating optical properties, LSPRs have become a flourishing new field of science as well as technology.

One remarkable feature of AuNPs is that their LSPR properties can be tailored by synthetically tuning their sizes and shapes. Due to the limited LSPR tunability of AuNSs (non-hollow), the investigations of anisotropic AuNPs have increased during the last decade, most often relying on the development of seed-mediated synthetic methods. In particular, compared to AuNSs (non-hollow), the main attractive feature of most

anisotropic and hollow AuNPs is probably the appearance of a plasmon band in the near-infrared (NIR) region, where absorption by tissues is low. Therefore, the "water window" between 800 nm and 1300 nm can be used for medicinal diagnostics and photothermal therapy.[15-17] Other noteworthy properties of anisotropic AuNPs are the enhancement of the SERS effect[18] and the catalytic properties of small AuNPs (<5 nm) on textured surfaces.[2, 19-20]

Among various anisotropic AuNPs, much attention has been paid to those with rod-like shapes, namely, Au nanorods (AuNRs). Compared to other anisotropic AuNPs, AuNRs offer significant advantages in greatly broadening the tunability of their LSPRs. Due to the anisotropic morphology of AuNRs, they display two separate LSPR bands corresponding to their width and length known as the transverse LSPR and longitudinal LSPR.[21] The transverse LSPR is located at just above 500 nm while the longitudinal LSPR can be synthetically tuned across a broad spectral range, covering the visible (600 nm) and near-infrared regions (NIR, 1100+ nm) by tailoring their aspect ratios, that is, the ratio between the length and diameter.[21-22] These unique properties make AuNRs particularly well-suited for biomedical applications and allow for huge electromagnetic field enhancements (mainly located in the regions around the two ends of the nanorods) under resonant excitation.[21] Furthermore, AuNRs can be self-assembled into a number of superstructures in different geometries, which results in even richer plasmonic properties due to the anisotropic nature of AuNRs.

AuNRs were first synthesized in the mid-1990s through an approach based on electrochemical reduction into rod-shaped templates.[23-25] Modern concepts of seed-mediated bottom-up synthesis of AuNRs, initially proposed by Murphy group and subsequently modified by El-Sayed group,[26-28] is strictly dependent upon the use of cetyltrimethylammonium bromide (CTAB) as the capping agent, which despite the significant progress in the synthetic protocols has remained the almost indispensable surfactant used in the synthesis of this type of nanoparticle.[29-30] CTAB forms a chemisorbed bilayer (~3.2 nm)[31] tightly adsorbed on the surface of the AuNRs with the cationic CTA+ head groups pointing toward the external environment, thus rendering them stability and dispersity in water.

For nearly all applications, the ability to properly functionalize the nanorod surface can determine the success or failure of the project. In general, the functionalization of AuNRs can be significantly more challenging than the functionalization of AuNSs, even through the well-known gold-thiol chemistry, due to the unique surfactant capping of as-synthesized nanorods. While spherical particles may be directly thiol-coated during the synthesis or coated only with a weakly-bound anion, AuNRs are usually synthesized in the presence CTAB, which binds more strongly to the nanorod surface. This positively-charged CTAB bilayer tightly adsorbed on AuNRs and significantly limits their applications mainly in four aspects: 1). The structure of CTAB bilayer appears unstable at high ionic strengths which is common for high salt buffer solutions in the biological application; 2). The presence of CTAB and silver on the AuNRs surface poses a threat to many biological systems, as CTAB and silver ions are known to be highly cytotoxic; 3). The absence of functional moieties in CTAB bilayers indicates that they must be replaced with the proper organic or inorganic material to grant stability and functionality, however, the strong interaction between CTAB and gold blocks functional linkers from approaching the AuNRs surface to functionalize them; 4). Spontaneous reaction of alkanethiol molecules with gold under ambient temperature only occurs at the tips of AuNRs to produce partially-functionalized AuNRs. In these AuNRs, the remaining CTAB, which is positively charged attracts negatively-charged linker molecules, can cause severe nonspecific binding aggregation problems.

Many of the applications of AuNRs, whether in plasmonic or biological imaging, are closely dependent upon our ability to tailor their surface functionalization and tune their properties. However, the lack of effective functionalization methods will most likely negatively impact our ability to employ AuNRs in technological applications of high complexity, unless we are able to design the surface chemical properties of AuNRs and fully understand AuNRs interface before and after modification. In this thesis, we aim to develop a facile, highly reproducible seedless synthesis technique to produce monodisperse AuNRs in large-scale, then, another major goal is to design a simple, versatile, robust functionalization procedure to produce functionalized and biocompatible (i.e., CTAB free) AuNRs. Finally, the application of AuNRs wasere investigated in the field of photocatalysis.

1.1 Localized Surface Plasmon Resonance (LSPR)

1.1.1 Introduction to LSPR of AuNRs

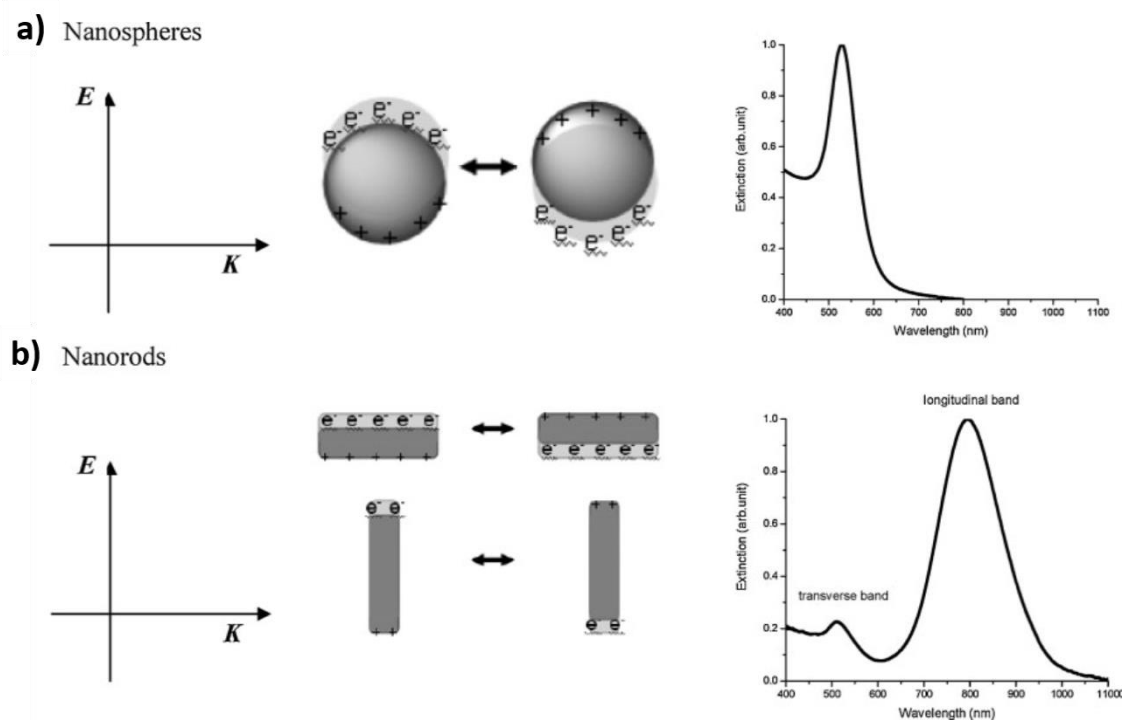

Figure 1. 1. Surface plasmon oscillations and corresponding absorption bands of AuNSs and AuNRs. Reproduced with permission from [22]. Copyright (2009) WILEY.

Metal NPs with the size comparable to, or smaller than the electron mean free path have particular optical properties which are significantly different from those observed in the bulk metal. In the presence of an oscillating electromagnetic field of light, the conduction band electrons of a metal NP undergo a collective coherent oscillation in resonance with the frequency of light, called localized surface plasmon resonance (LSPR).[22, 32-33] The electric field of the incident light interacts with the free electrons in the NPs, leading to a charge separation between the free electrons and the ionic metal core and in turn the Coulomb force makes the electrons oscillate back and forth on the particle surface, which results in the collective oscillation of electrons or, in another words, the excitation of LSPR. Figure 1. 1a illustrates the UV-Vis absorption of a spherical AuNSs, where only one absorption band can be observed. In case of AuNRs,

two absorption bands present in its absorbance spectrum, i.e., the longitudinal LSPR and the transverse LSPR, corresponding to electrons oscillate along the long and the short axes, respectively. (Figure 1. 1b). The relative weak transverse LSPR locates in the visible region at the wavelength (~520 nm) similar to that of AuNSs, while longitudinal LSPR is a much stronger absorption band in the longer wavelength region. The transverse band is insensitive to the size of the nanorods and the surrounding refractive index, whereas the longitudinal band shows a gradual red-shift from the visible to NIR region as the aspect ratio (length/width) increases (Figure 1. 2). This optical behaviour can be well-understood using Gans theory which was proposed for the explanation of optical properties of ellipsoid particles based on a dipole approximation.[34] In aqueous solution, the absorption maximum (λ_{max}) is linearly proportional to the aspect ratio (R) by the following relationship:[35-37]

$$\lambda_{max} = 95R + 420 \qquad \text{(Equation 1. 1)}$$

This provides a facile method to efficiently tune the optical properties of AuNRs by simply adjusting the aspect ratio, which is quite different from spheres for which the SPR has limited tunability. AuNSs (non-hollow) generally show a size-relative absorption peak from 500 to 550 nm as the size increases from 1 nm to 100 nm.[38-40] In contrast, the absorption band of AuNRs can be easily tuned into NIR region, where tissue absorption is minimal, is very useful for potential *in vivo* applications in nanomedicine and photocatalysis.

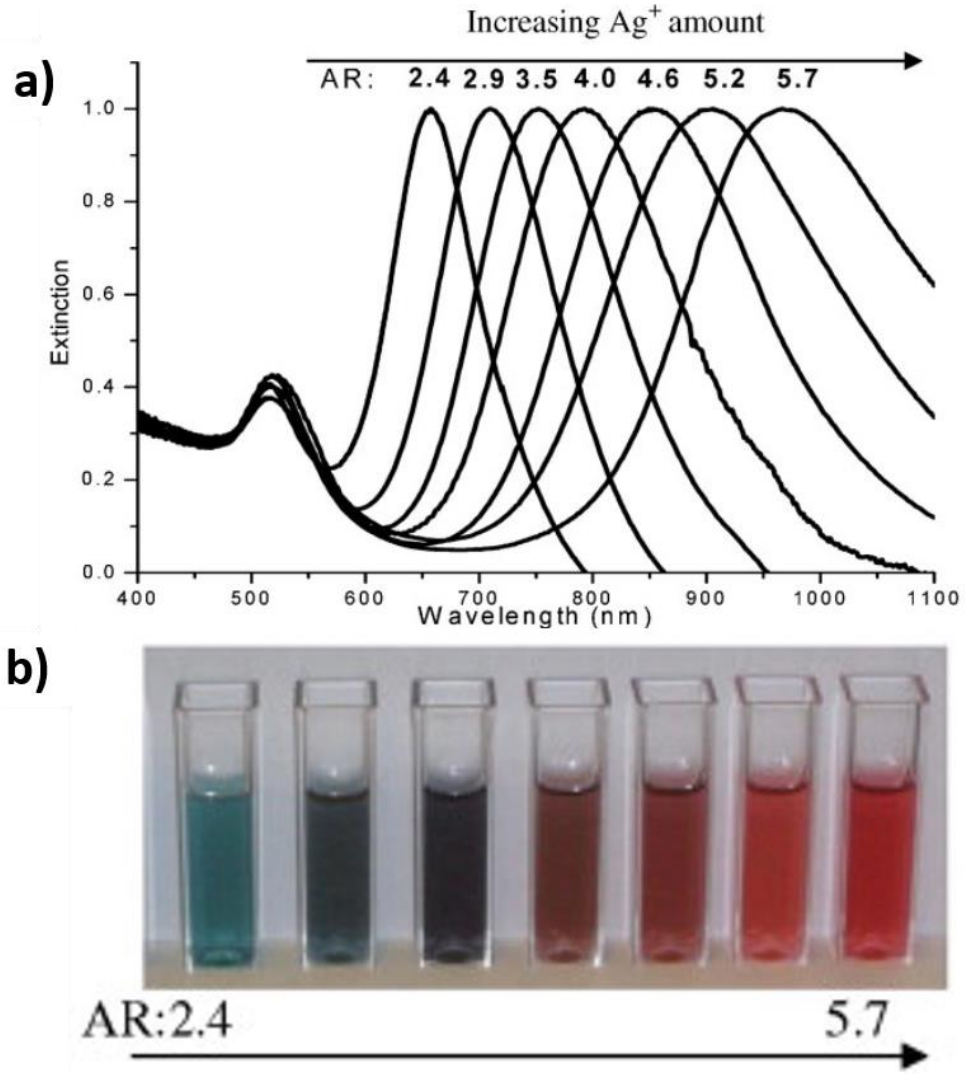

Figure 1. 2. The absorption band and optical image of AuNRs as a function of aspect ratio. a) Reproduced with permission from [22]. Copyright (2009) WILEY. b) Reproduced with permission from [41]. Copyright (2009) Elsevier.

Noble (plasmonic) metal NPs are able to effectively focus resonantly coupled light through LSPR. Accordingly, all radiative properties, such as light absorption, fluorescence, Rayleigh scattering (Mie), and Raman scattering are enhanced by orders of magnitude.[22] This can be seen from the quantitative description of the cross-sections of absorption (C_{abs}), scattering (C_{sca}), and total extinction (C_{ext}), derived from Gans theory:[22, 35, 42-43]

$$C_{abs} = \frac{2\pi}{3\lambda}\varepsilon_m^{3/2} V \sum_i \frac{\varepsilon_2/(n^{(i)})^2}{(\varepsilon_1+[(1-n^{(i)})/n^{(i)}]\varepsilon_m)^2+\varepsilon_2^2} \quad \text{(Equation 1. 2)}$$

$$C_{sca} = \frac{8\pi^3}{9\lambda^4}\varepsilon_m^2 V^2 \sum_i \frac{(\varepsilon_1-\varepsilon_m)^2+\varepsilon_2^2/(n^{(i)})^2}{(\varepsilon_1+[(1-n^{(i)})/n^{(i)}]\varepsilon_m)^2+\varepsilon_2^2} \quad \text{(Equation 1. 3)}$$

$$C_{ext} = C_{abs} + C_{sca} \quad \text{(Equation 1. 4)}$$

where λ is the wavelength of light, V the unit volume of the nanoparticle, ε_m the dielectric constant of the surrounding medium, ε the dielectric constant of the metal given by $\varepsilon = \varepsilon_1 + i\varepsilon_2$(in which, ε_1 and ε_2 are the real and imaginary components of the dielectric constant), and $n^{(i)}$ the depolarization factor, defined by:

$$n^{(a)} = \frac{2}{R^2-1}\left(\frac{R}{2\sqrt{R^2-1}} ln \frac{R+\sqrt{R^2-1}}{R-\sqrt{R^2-1}} - 1\right) \quad \text{(Equation 1. 5)}$$

$$n^{(b)} = n^{(c)} = (1 - n^{(a)})/2 \quad \text{(Equation 1. 6)}$$

where a, b, and c are the three axes of the nanoparticle, a > b = c, and the aspect ratio, R, is equivalent to a/b. In case of spheres, $n^i = 1/3$. The SPR occurs at $\varepsilon_1 = -(1 - n^{(i)}) \times \varepsilon_m/n^{(i)}$, where $i = a$ for the longitudinal resonance and $i = b, c$ for the transverse resonance. At such resonance wavelengths, the absorption, scattering, and total extinction are all strongly enhanced, which is the basis for their application in biological and biomedical imaging and therapeutics.[22]

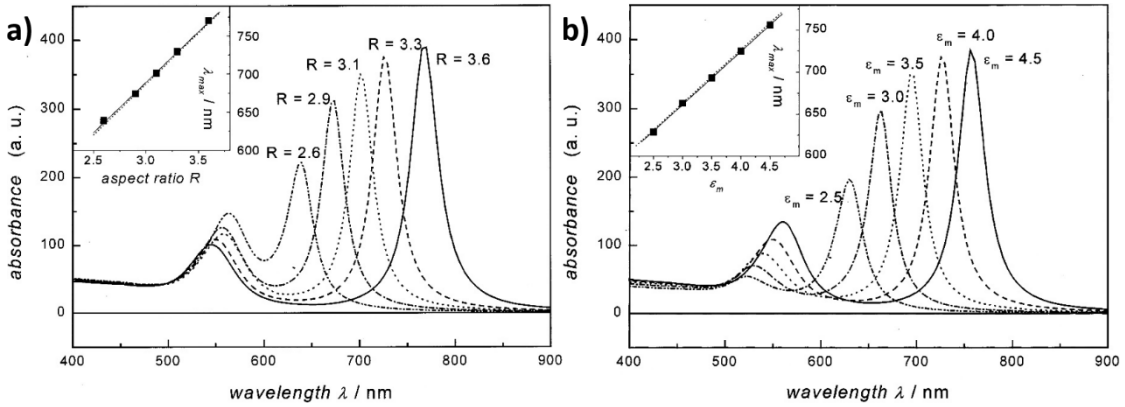

Figure 1. 3. (a) Simulated LSPR absorption spectra of AuNRs with various aspect ratios in the medium with a constant dielectric constant (inset: peak wavelength of longitudinal LSPR increases linearly with aspect ratio of AuNRs). (b) Simulated LSPR absorption spectra of AuNRs with a constant aspect ratio in the medium with varying dielectric constant (inset: peak wavelength of longitudinal LSPR increases linearly with dielectric constant of the surrounding medium). a, b) Reproduced with permission from [35]. Copyright (1999) American Chemical Society.

The optical properties of AuNRs strongly depends on the wavelength of the incident light, aspect ratio and size of the particles. El-Sayed and co-workers reported the simulation of the absorption spectra of AuNRs as a function of their aspect ratio, based on Gans theory (Figure 1. 3a).[35] Figure 1. 3a shows that the transverse LSPR has a small blue-shift while the longitudinal LSPR has a huge red-shift with increasing aspect ratio of the AuNRs. Further, a linear relationship was also observed between the peak wavelength of the longitudinal LSPR and the aspect ratio of the AuNRs, which is in good agreement with the experimental data.[35]

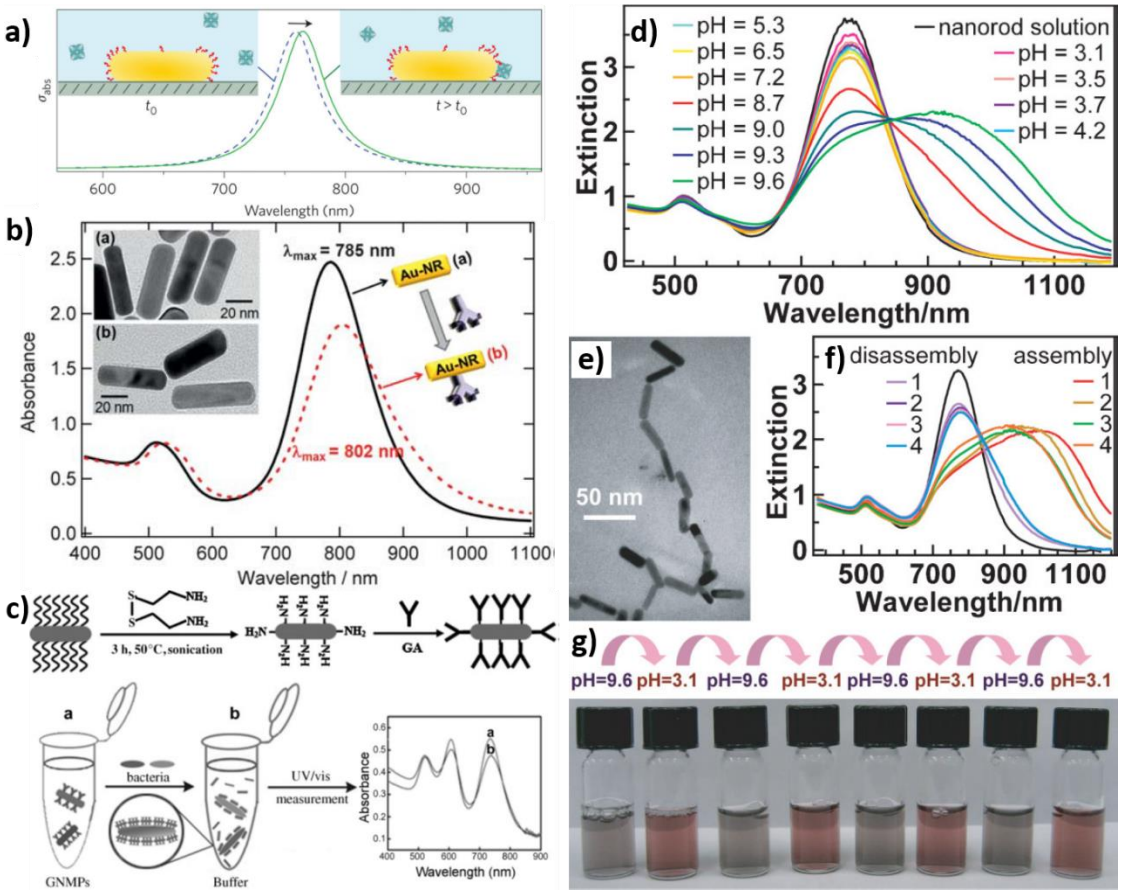

Figure 1. 4. a) Schematic illustration of optical sensing using LSPR of AuNRs. b) UV-vis spectra change of AuNRs upon anti-IgE coating. c) Schematic representation of the use of pathogen-antibody-conjugated AuNRs in simultaneous detection of two species of pathogens. d-g) UV-vis spectra change of AuNRs upon reversible pH changing. a) Reproduced with permission from [44]. Copyright (2012) Nature Publishing Group. b) Reproduced with permission from [45]. Copyright (2010) Royal Society of Chemistry. c) Reproduced with permission from [46]. Copyright (2008) WILEY. d-g) Reproduced with permission from [47]. Copyright (2008) WILEY.

They also simulated the absorption spectra of the AuNRs with a constant aspect ratio, in a medium with varying dielectric constant (Figure 1. 3b). Figure 1. 3b shows that both the transverse LSPR and longitudinal LSPR red-shift as the dielectric constant of the surrounding medium increases, however, the longitudinal LSPR shifts more prominent than that for the transverse LSPR, indicating that the longitudinal LSPR is more sensitive to the change of dielectric constant of the surrounding medium. The

sensitivity, defined as a shift in the longitudinal LSPR wavelength ($\Delta\lambda$) relative to the refractive index change of the surrounding medium, may be described by the following relationship:[32, 48-49]

$$\Delta\lambda = m\Delta n\left[1 - exp\left(\frac{-2d}{l_d}\right)\right] \qquad \text{(Equation 1. 7)}$$

where $\Delta\lambda$ is the change in refractive index (RIU), m is the bulk refractive index response of the NPs (measured in nm per refractive index unit, nm/RIU), d is the effective thickness of the adsorbed layer (nm) and l_d is the characteristic electromagnetic field decay length (nm). Equation 1.7 forms a basis for LSPR-shift based biosensors, where the wavelength-shift is used to monitor the refractive index change in the vicinity of the nanorods (Figure 1. 4).[44-47] Additionally, experimental comparison of the sensitivity of NPs of various shapes found that AuNRs show much higher sensitivity than similarly sized nanospheres, thus making AuNRs excellent colorimetric probes.[50]

1.1.2 SERS Properties of AuNRs

In the presence of incident light, the resonant photons excite LSPR, which give rise to strong surface electromagnetic fields that propagate around the particle and decay exponentially over a distance comparable to the particle size.[51] In addition, the LSPR can effectively confine the resonant photons within small nanoparticle size, leading to a huge decrease in wavelength and a great increase in the amplitude of the photon wave accordingly. Since the electromagnetic field is proportional to the square of the amplitude of the light wave, this will greatly boost the electromagnetic field intensity.[22] The SERS effect mainly originates from this dramatic amplification of electromagnetic fields and the SERS intensity is proportional to the fourth power of the electromagnetic field intensity.[52] Another contribution to SERS is the chemical enhancement that enhances the Raman-scattering cross-section of the analyte ~~through~~ by increasing its electronic polarizability via ~~by~~ charge transfer between the analyte and the metal surface.[53]

High curvature NPs with sharp edges and tips are beneficial for additional SERS enhancement due to the optical antenna effect.[54-55] Schatz and co-workers have compared the field enhancement for various NPs using DDA calculations.[56] The results showed that prisms, rods, and spheroids with similar size dimension show similar enhancement with $|E|^2/|E_0|^2$ on the scale of $>10^3$, which is significantly higher than spheres ($\sim 10^2$) and E_0 is the electrical field of incident light. The nanorod shows much stronger electromagnetic fields at the end of the long axis and weakest fields at the centre of the rods. The field enhancement at their resonance wavelength increases with increasing aspect ratio for the same total particle volume.

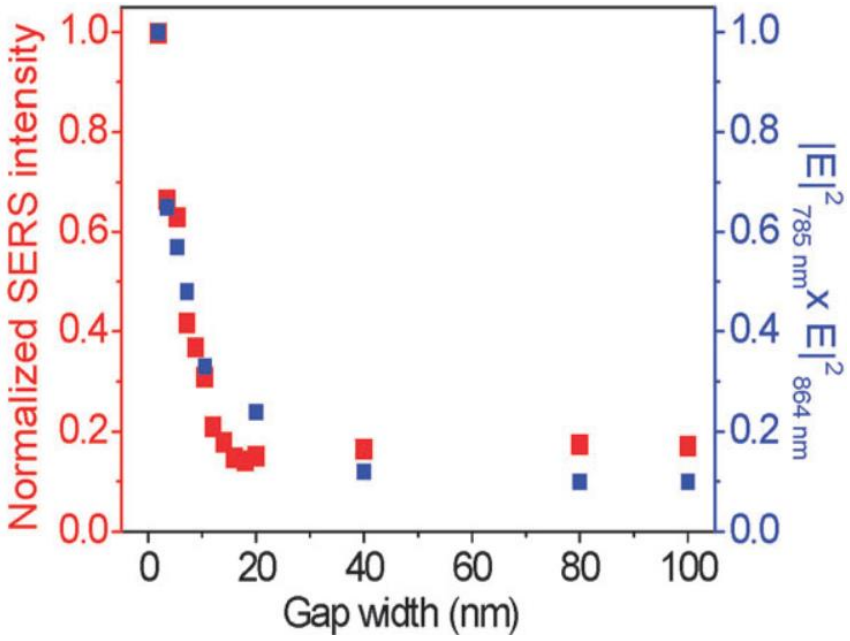

Figure 1. 5. Gap-width dependence of the SERS intensity normalized by extinction values at the incident laser wavelength and Raman scattering wavelength (shown in red), and the gap-width dependence of the averaged enhancement factor by multiplying FDTD intensity maps monitored at the incident laser wavelength by the map monitored at the Raman scattering wavelength. Reproduced with permission from [57]. Copyright (2011) Royal Society of Chemistry.

The electromagnetic field coupling happens when plasmonic NPs are brought in close proximity to one another, thus, the SERS in the small gap between the NPs is enormously amplified. Misawa and co-workers investigated the relationship between

the SERS intensity and gap-width using dimer type Au nanoblocks (Figure 1. 5).[57] To rule out the difference in the plasmonic coupling efficiency at each wavelength of incident light and Raman scattering light, the SERS intensity was normalized using the extinction value at each wavelength.[58] The red plots in Figure 1. 5 show the gap-width dependence of the normalized SERS intensity, which is obtained by dividing the SERS intensity by each extinction value. And the SERS intensity continuously increased with decreasing gap width.

1.1.3 Photoluminescence (PL) Properties of AuNRs

The rapid non-radiative electron–hole recombination processes in bulk metal (Au, Ag, and Cu) produces extremely weak fluorescence (PL) (quantum yield of ~10^{-10}).[59] This is expected for metals, where the non-radiative decay processes are very fast. The PL efficiency in AuNSs is 10^5–10^7 times higher than in bulk Au, and in AuNRs it is ~10^2 times higher than in AuNSs.[60-61] Like bulk metal, the PL response in AuNRs involves a three-step process:[59, 62-64] 1) the generation of electron-hole pairs by excitation of *d* band electrons to the *sp* band; 2) electrons lose energy to the phonon lattice through electron-hole scattering processes, which relax to lower energy levels above the Fermi level; and 3) excited electrons in the *sp* band recombine with holes in the *d* band, resulting in photon emissions.[22] The effect's strong dependence on the nanorod's length, combined with the fact that similar enhancements are not observed for nanospheres, suggested that the strong electromagnetic fields of the longitudinal LSPR are the origin of the fluorescence enhancement. This is also supported by Okamoto group's work, in which locally exciting regions along the length of the nanorod and simultaneously monitoring the PL from the entire rod was carried out to determine the portions of the rod that yielded the strongest PL response.[65] Also, the spatial distribution obtained mapped out the plasmon mode. Therefore, where the plasmon shows the strongest internal electromagnetic field, it also shows the strongest PL. However, there is experimental and theoretical evidence that the PL yield decreases while increasing the electromagnetic field at the junction between two NPs, indicating that the hypothesis of a plasmonically enhanced luminescence requires further investigation.[66]

1.1.4 Photo-Induced Hot-Carrier Effects

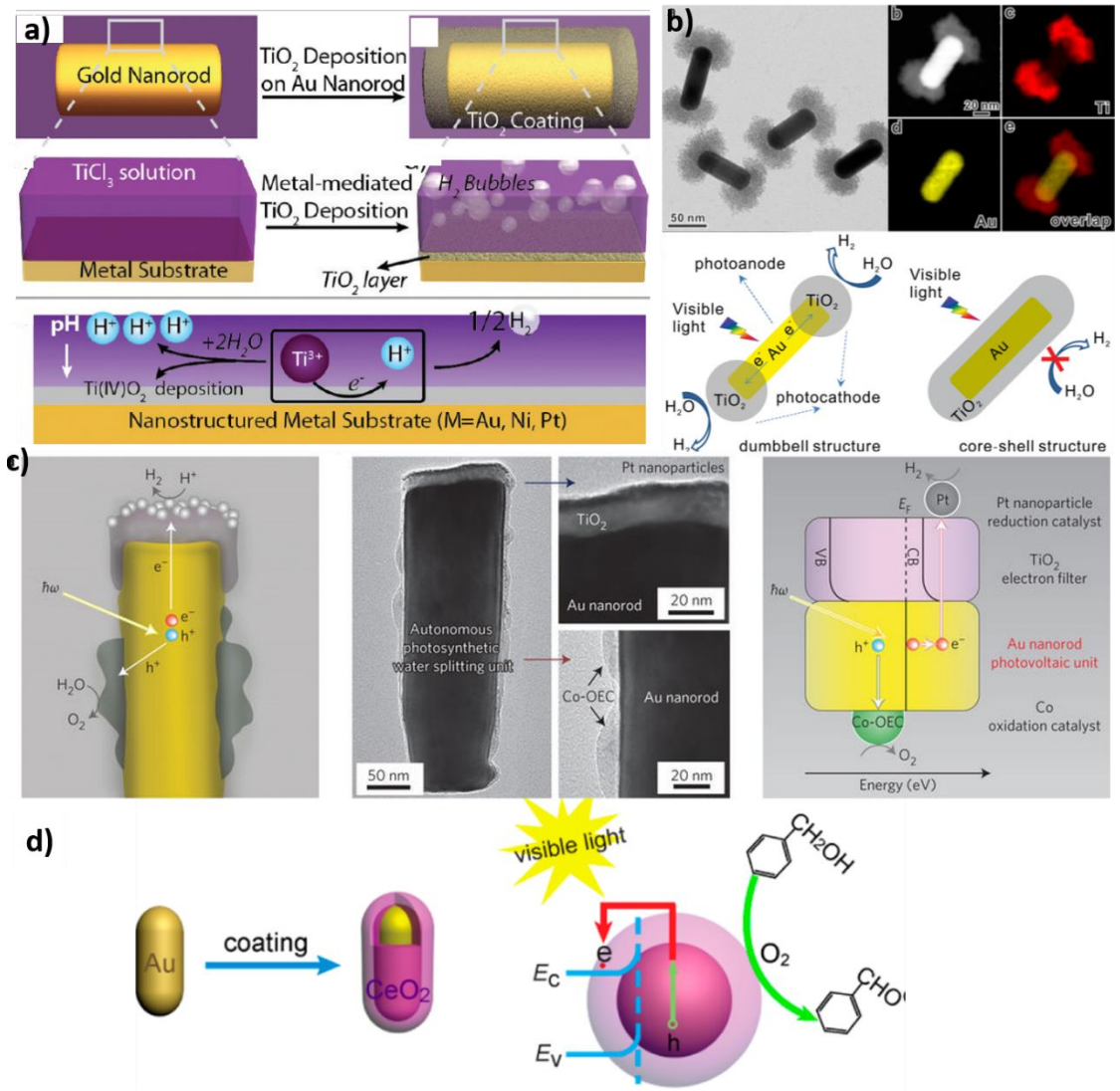

Figure 1. 6. a) The synthesis of AuNRs and TiO_2 core-shell structures for H_2 production. b) The synthesis of AuNRs and TiO_2 dumbbell nanostructure for H_2 production using visible light. c) Structure and mechanism of operation of the AuNRs based autonomous plasmonic solar water splitter. d) The synthesis of AuNRs and ceria core-shell nanostructures for visible light-induced photocatalytic reactions. a) Reproduced with permission from [67]. Copyright (2012) American Chemical Society. b) Reproduced with permission from [68]. Copyright (2016) American Chemical Society. c) Reproduced with permission from [69]. Copyright (2013) Nature Publishing Group. d) Reproduced with permission from [70]. Copyright (2014) American Chemical Society

The relaxation of LSPR yields to the alteration of the equilibrium electron Fermi distribution in the metal and the formation of 'hot electrons', namely, electrons with higher energies than the thermal excitation at room temperature.[71-73] The excitation of electrons in a solid will always lead to the generation of holes, suggesting that the presence of hot electrons will bring about 'hot holes' with lower energies than at room temperature.[72, 74-75] Hot electrons can transfer into unoccupied levels of acceptor molecules or materials in contact with the AuNP surface due to their excess kinetic energy.[76] Similarly, electron transfer from occupied adsorbate orbitals to hot holes (i.e. transiently unoccupied states below Fermi energy in the metal) has also been demonstrated.[72] This hot-carrier transfer is suppressed by their rapid relaxation and conversion into heat, and the difficulty of matching their energy with the donors/acceptor levels. It has been reported that this process is only possible for acceptor or donor electronic levels with energy close to the metal Fermi level.[72, 77] Despite these challenges, hot carriers have been widely explored for multiple applications such as in light-harvesting, photodetection, doping, and photochemical reactions.[72] In terms of AuNRs, their composition with semiconductors (e.g. TiO_2 and ceria) have been extensively applied in photocatalysis due to their wide-range light harvesting ability and intense electromagnetic field (Figure 1. 6).[67-70, 78-80]

1.1.5 Photothermal Effect of AuNRs

The absorbed light is converted into heat by the plasmonic NPs via a series of photophysical processes, which can lead to temperature rises in the surrounding environment.[60, 81-84] Basically, these photophysical processes start with a fast loss of the phase of the coherently excited electrons on the few femtosecond timescales. This is followed by energy loss to the phonon bath, and the electrons and holes cascade down the energy scale by electron-phonon processes on the order of 0.5–1 ps.[22] The lattice cools off by passing its heat to the surrounding medium via phonon-phonon relaxation within ~100 ps, leading to the complete cooling of the whole NP. Consequently, the surrounding medium can be heated, melted, vaporized, or deteriorated depending on the temperature reached by the NPs. In all cases, a stress wave due to the medium thermal expansion propagates in the surroundings of the heated NPs.

The conversion of light into heat is extremely efficient in AuNPs due to the combination of the following features:[71, 85-87] 1) efficient plasmon absorption in the visible and NIR regions; 2) excellent photostability compared to organic dyes; 3) low luminescence yield; 4) rapid relaxation of the LSPR. The ability to convert~~of converting~~ light into heat through the excitation of plasmonic resonances has made AuNPs excellent candidates for photothermal therapy.[15-17] AuNRs offer additional merits as photothermal conversion agents. Firstly, their longitudinal LSPR can be synthetically tuned into the NIR region where tissues show minimum light absorption. Secondly, compared with other light-absorption species, such as organic dye molecules, semiconductor nanocrystals, and AuNSs, AuNRs exhibit much stronger light absorption at their plasmon resonances.[38] Therefore, in recent years, studies of the photothermal conversion properties of AuNRs and their related applications have gained much interest.

The photothermal conversion efficiency of plasmonic NPs, governed by the competition between the radiative and non-radiative decays of the LSPR, is the most critical factor for photothermal conversion-based applications.[21] The photothermal conversion efficiency is straightforwardly dependent on the geometries and plasmonic properties of NPs. Both experimental measurements and theoretical simulations have shown that the photothermal conversion efficiency decreases as the particle volume of AuNPs increases.[88] Its origin is ascribed to the reduced radiative decay of the plasmon resonance in smaller NPs, therefore, the absorbed light energy is mainly converted into heat. In case of AuNRs, the photothermal conversion will be highest when longitudinal LSPR of AuNRs is very close to the incident laser wavelength.[88] Under this condition, the incident laser can efficiently excite the plasmon resonance of the nanorods, through which its energy can be effectively converted into heat.

In 2010, Quidant *et al.* utilized a novel thermal microscopy technique to image the heat distribution around a single AuNR by recording molecular fluorescence polarization anisotropy.[89] The found that the temperature distribution around the nanorod is found to be fairly uniform and the thermal ‘hotspots’ usually do not coincide with the optical ‘hotspots’ of the plasmon mode. However, the spatial resolution of the thermal imaging

(~300 nm) might be not high enough for the quantitative analysis of the plasmonic photothermal heating and induced thermal diffusion at the nanoscale.

1.1.5.1 Photothermal Therapy

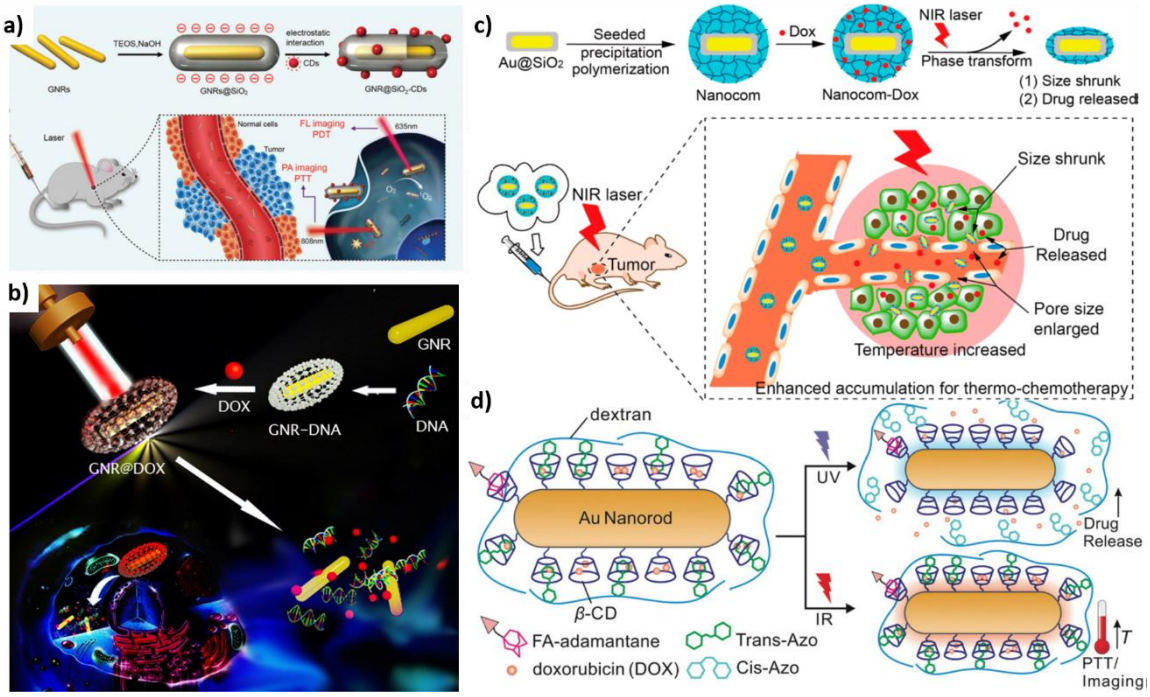

Figure 1. 7. a) Schematic illustration of AuNR@SiO_2-CDs as both photoacoustic (PA) imaging and PTT agents. b) Scheme illustrating of thermal-induced drug (DOX) delivery and photothermal ablation cancer therapy. c) Schematic illustration of NIR laser–induced targeted thermo-chemotherapy using the thermos-sensitive polymer coated AuNRs. d) (A) Schematic representation of the multifunctional AuNR complex for UV-triggered drug delivery and IR-induced PTT and cell imaging. a) Reproduced with permission from [90]. Copyright (2016) Royal Society of Chemistry. b) Reproduced with permission from [91]. Copyright (2014) Elsevier. c) Reproduced with permission from [92]. Copyright (2014) American Chemical Society. d) Reproduced with permission from [93]. Copyright (2015) Royal Society of Chemistry.

Plasmon-assisted photothermal therapy (PTT) is a non-invasive treatment where NPs act as an efficient photothermal transducer, moderately increasing the temperature at targeted sites, and hence inducing the denaturation of proteins and disorganization of

cellular components that lead to cell death.[21, 94-95] PTT requires that strong photoabsorbers are located selectively in~~at~~ the targeted region, which can be achieved by surface modification of AuNPs with specific ligands, to reduce nonspecific injury to adjacent healthy tissue.[96] The first example of using AuNRs for photothermal cancer therapy was presented by El-Sayed *et al*. in 2006, where anti-EGFR-functionalized AuNRs were selectively bound to human oral cancer cells.[97] Under the NIR laser irradiation, the cancer cells are killed through the photothermal heating of the AuNRs. Following their pioneering study, many efforts have been made towards using Au nanorods in cancer cell treatments. Bhatia and co-workers demonstrated an excellent example of *in vivo* PTT, where a single intravenous injection of polyethylene glycol (PEG)-capped AuNRs in human xenograft tumo~~u~~rs in mice completely eradicated the~~the~~ tumo~~u~~r without regrowth for over 50 d.[98] Recently, Wang *et al.* reported AuNRs@silica-carbon dots (CDs) hybrid nanostructures by coating AuNRs with SiO_2 and CDs molecules (Figure 1. 7a).[90] The obtained hybrid nanostructures allow for simultaneous *in vivo* fluorescence imaging and photothermal therapy of tumo~~u~~rs in mice.

1.1.5.2 Photothermal-Induced Drug/Gene Delivery

Precise control of drug/gene delivery and release in live cells or organic tissues is in high demand for biomedical therapeutics as well as for studying the evolution pathways in biological systems.[21] Nano-platforms enabling loading and releasing of drugs/genes under remote triggers are foremost for this technique. The diffusion coefficient D of any molecular compound in a fluid medium is described by the Einstein–Smoluchowski law:[99]

$$D = f_{\mathrm{geom}} \frac{k_{\mathrm{B}} T}{\eta_{\mathrm{m}}} \approx T e^{-a/T} \qquad \text{(Equation 1. 8)}$$

where k_{B} is the Boltzmann constant, f_{geom} is a geometrical factor depending on molecule shape, and η_{m} is the medium viscosity, that scales approximately as $e^{-a/T}$ with T. Therefore, the local increase of T is a way to activate the diffusion of molecules near the NP surface.[71, 100] For realizing controlled drug/gene delivery, AuNRs are

usually functionalized or capped with specific drugs/genes, which can be released at increased *T* under the illumination of laser light in resonance with their longitudinal LSPR. The near unity photothermal conversion efficiency of AuNRs allows drug/gene release to be activated with minimum optical exposures, therefore resulting in negligible damage to cells or tissues.[21]

An alternative drug/gene release strategy is to incorporate AuNRs into composite materials loaded with drug/gene, where AuNRs act as the light absorber and the composites are drug carriers. Under laser illumination, the photothermal conversion of the nanorods heats up the surrounding composites, leading to their structural changes and thereafter the release of the embedded drugs/genes.[21] Figure 1. 7b shows the fabrication of DNA-wrapped AuNRs with chemotherapeutic drugs (doxorubicin (DOX)) loading, and cellular mechanism for combinational drug-delivery and photothermal ablation cancer therapy.[91] DOX was loaded within DNA-modified AuNRs matrix via intercahelating. Upon NIR laser irradiation, DOX was released from the AuNRs due to thermal-triggered DNA melting/dehybridization or lysosomal hydrolases-caused DNA degradation. The tumour growth inhibition property was achieved by a synergistic effect between DOX-induced apoptosis and laser irradiation-caused necrosis of primary tumours cells. Similarly, Chen *et al.* used thermos-responsive polymer, poly(*N*-isopropylacrylamide-*co*-acrylic acid), to fabricate polymer-AuNR-DOX composites, which can effectively release the loaded DOX at thermo-induced size shrunk upon NIR light irradiation (Figure 1. 7c).[92] Recently, Gu *et al.* reported multifunctional AuNRs complex for anticancer treatment (Figure 1. 7d).[93] The AuNR was functionalized with *β*-cyclodextrin for encapsulation of doxorubicin, with folic acid for selective targeting, and with a photo-responsive dextran-azo compound for intracellular controlled drug release. The drug release was triggered upon UV irradiation, in which dextran-azo compound serves as a capping/uncapping agent due to the *trans*-–*cis* isomerization of the azo moiety upon UV irradiation.

1.1.5.3 Photothermal-Reshaping and Thermal-Stability of AuNRs

The lattice heating by the electrons and cooling by the surrounding medium is a competitive process. If the heating rate is much faster than the cooling rate, heat can be

accumulated within the lattice causing a temperature rise of the nanoparticle in a short time. This temperature increase could be sufficient enough to lead to particle structural changes if the structural change, such as shape transformation and particle fragmentation, takes the time on the scale between the lattice heating and cooling timescales.[22]

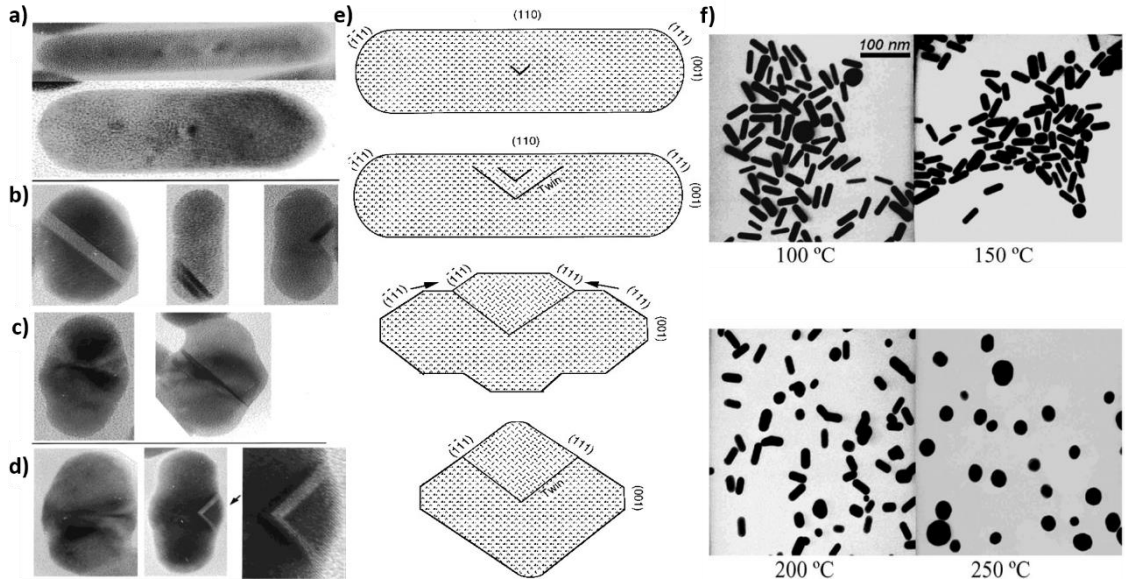

Figure 1. 8. a, b) HRTEM image of AuNRs after exposure to femtosecond laser pulses with a fluence of 1 mJ cm^{-2} (0.5 μJ per pulse). a) shows two examples of nanorods with point defects, while b) shows three twinned particles. c, d) HRTEM image of AuNRs after exposure to nanosecond laser pulses with a fluence of 250 mJ cm^{-2} (20 μJ per pulse). c) shows nanorods with stacking faults and d) twinned particles. e) A schematic process for the structural transformation from nanorod to nanodot. f) TEM images of the final state of the nanorods after heating at different temperatures for 20 h. a-e) Reproduced with permission from [101]. Copyright (2000) American Chemical Society. f) Reproduced with permission from [102]. Copyright (2005) Royal Society of Chemistry.

El-Sayed group observed that the femtosecond irradiation melts the nanorods to near spherical particles of comparable volumes at moderate energies, while the nanosecond pulses (or femtosecond irradiation at high energies) fragment them to smaller near-spherical particles (Figure 1. 8a-d).[103-104] Using pump-probe fs transient absorption

spectroscopy, they measured the bleaching rate of the longitudinal LSPR as the nanorods melted into spheres and found that it took about 35 ps for a nanorod reshaped into a sphere.[105] Using high-resolution TEM, they found that while the as-prepared nanorods are defect-free, laser-irradiation generates point and line defects inside the nanorods, driving the nanorods to convert their {110} facets into the more stable {100} and {111} facets and hence minimize their surface energy (Figure 1. 8e).[101, 106] These observations suggest that photothermal melting begins with the creation of defects inside the nanorods followed by surface reconstruction and diffusion, in contrast with the thermal melting of the rods or the bulk material, where the melting starts at the surface (Figure 1. 8f).[101]

Different from laser-induced reshaping, Mohamed *et al*. investigated the reshaping of AuNRs with micelles by dissolving the micelles with heat.[107] They suggested that the observed relative instability of the longer nanorods in the micellar solutions is attributed to the relative instability of their capping micelles. They also found that most stable rod-shaped micelle is found to have an aspect ratio of 2.0 and dissolution temperature of these micelles is found to be ~155 °C. Niidome group compared the thermal-stability of AuNRs with different surface passivating layers, including poly(styrene sulfonate), poly(vinylpyrrolidone), poly(ethylene glycol), phosphatidylcholine, and CTAB.[108] They found that CTAB layers were~~as~~ a better thermal insulator that helped to enhance the photothermal reshaping of the AuNRs. Besides, the removal of the excessive CTAB via centrifugation allows for rapid heat diffusion, thus, suppressing the photothermal reshaping of the AuNRs. Yang *et al*. attributed the thermal-induced reshaping to an Ostwald ripening process.[109] They found that a lower CTAB concentration contributed to a higher stability of AuNRs, as the low concentration of Br^- in the solution that reduces the formation of the soluble gold species and then slows down the Ostwald ripening process.

The thermal-stability of AuNRs has to be addressed when considering any potential applications. The thermodynamic tendency of lowering surface energy makes the anisotropic nanostructures potentially unstable.[101, 106, 109] AuNRs are likely to undergo morphological and structural transitions into the most thermodynamic stable spherical

shape if sufficient energy is provided, thus losing their peculiar properties.[106] As the shape deformation was attributed to Ostwald ripening, this process can be significantly suppressed by reducing the concentration of CTAB or providing a stiffer coating.[109]

1.2 Capping Agents of AuNRs: CTAB and Silver

In the wet-chemical synthesis of AuNRs, chemical reagents that influence the AuNRs growth have been utilized in aiding the anisotropic crystal growth. These chemicals include~~s~~ CTAB, silver nitrate, benzyldimethylhexadecylammonium chloride (BDAC), halides, dioctyl sulfosuccinate (Aerosol-T), Pluronic F-127, alkyltrimethylammonium chloride (CTAC) and sodium oleate, and salicylic acid derivatives.[26-28, 30, 110-113] Although several articles have been reported to synthesize AuNRs in the absence of CTAB,[29-30, 113] they hardly yield the reproducibility and sample monodispersity that are typically achievable when employing it.

For AuNRs synthesized in the presence of a CTAB surfactant, the surface of these as-synthesized AuNRs is covered by a bilayer of positively charged CTAB molecules. The CTAB surfactant is important in terms of working as a "structure-directing agent" to control the particle dimensions and acting as a stabilizer to protect the as-synthesized AuNRs against aggregation. The role of silver lies in controlling the aspect ratio of AuNRs and improving the morphological monodispersity and rod-shape yield.

1.2.1 The Micellar Behaviour of CTAB

It is first necessary to understand the general structure and properties of the CTAB coating on the surface of rods. The CTAB molecules form a partially-interdigitated bilayer on the surface of AuNRs, similar to the structure of a vesicle or cell membrane (Figure 1. 9b).[114] Gómez-Graña and co-workers carried out small angle X~~x~~-ray (SAXS) and neutron (SANS) scattering to investigate the structure of the CTAB bilayer, they were able to determine a bilayer thickness of 3.2 nm, which is less than a fully extended bilayer thickness of 4 nm and thus leads to the likelihood of partial-interdigitation between the two CTAB layers.[31] The positively-charged quaternary ammonium head group binds tightly to the Au surface through electrostatic interaction,

leading to the formation of the inner layer, while the hydrophobic tails of the external layer interact with those of the inner layer with the ammonium groups expose to the external bulk solution.[114] This bilayer assembly is energetically favoured as it guarantees hydrophobic interactions between the surfactant tails in the bilayer core and hydrophilic interactions of the charged head group with the aqueous media at the nanoparticle-solvent interface. Thermogravimetric analysis results illustrated that the CTAB bilayer shows different desorption properties corresponding to a weak binding outer layer and a stronger binding inner layer.[114] Accordingly, the bilayer can be easily disrupted when the CTAB concentration is lower than its critical micelle concentration (CMC) or when organic solvents, salts, or some other external stimuli are applied to the AuNRs solution, making AuNRs of limited usefulness for many applications.[115-116].

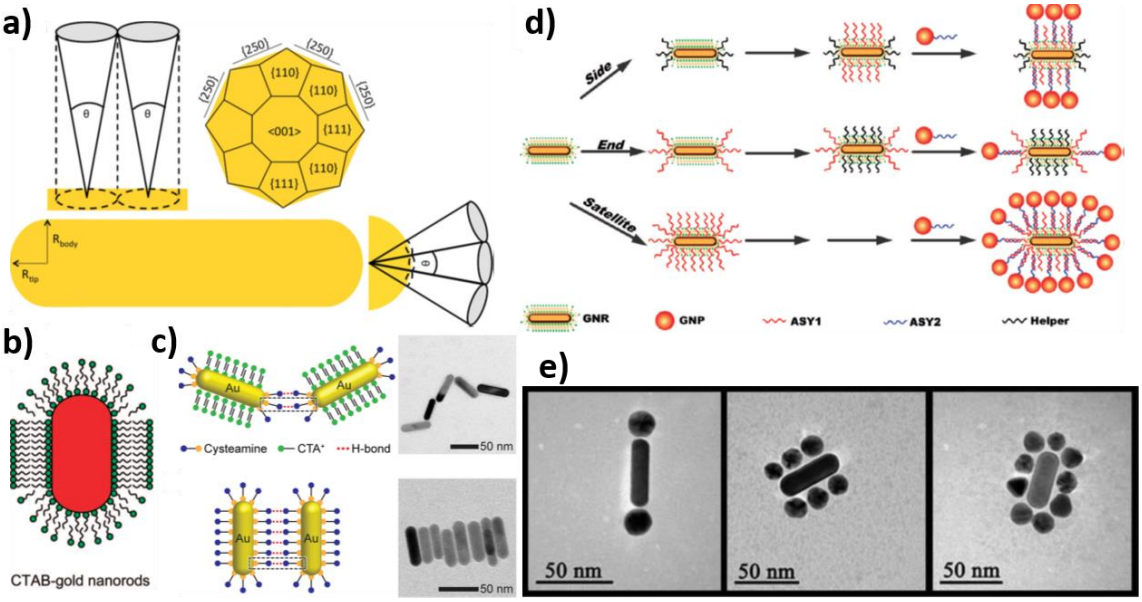

Figure 1. 9. a) The influence of nanorod surface curvature on CTAB packing density. Figure a) also highlights the variation in curvature between the NR tip and body, where the radius of curvature of the body and tip is represented by R_{body} and R_{tip}, respectively. b) Cartoon showing the possible distribution of CTAB on AuNRs with highly curved nanorod ends. c) End-to-End and Side-to-Side assembly modes of AuNRs achieved by selective modification. d, e) Synthetic method for regiospecific NPs assemblies. a) Reproduced with permission from [94]. Copyright (2014) WILEY. b) Reproduced with permission from [117]. Copyright (2009) American Chemical Society. c) Reproduced

with permission from [118]. Copyright (2017) American Chemical Society. d, e) Reproduced with permission from [119]. Copyright (2012) American Chemical Society.

The CTAB bilayer molecules are unevenly distributed on the surface of AuNRs due to the variation of surface curvature between the longitudinal and the transverse surfaces, as well as the tips (which can be either truncated or sphero-cylindrical depending on the synthetic procedure) (Figure 1. 9a, b).[120] Additionally, the inhomogeneity in the packing density of the adsorbed CTAB bilayer, where the highly curved tip exhibits a lower density of CTAB than the longitudinal facets, making the functionalization of the tips energetically more favourable than that of the sides (Figure 1. 9b).[121] The selective functionalization can be taken advantage of to assemble the AuNRs either tip-to-tip or side-by-side, and has been widely exploited in the device community (Figure 1. 9c-e).[119, 122-131]

1.2.2 The Role of CTAB and Silver in Anisotropic Growth of AuNRs

1.2.2.1 Template Mechanism

The growth mechanism of AuNRs synthesized in CTAB-micellar solutions has received a large amount of attention. It has become quite evident that the presence of CTAB and silver is essential for rod formation, but some disagreement exists as to the exact mechanism of their action. The widely used surfactants CTAB might act as "soft-templates" to direct the longitudinal growth of AuNRs.[27] Missel *et al*. proposed a thermodynamic model that predicts the sphere-to-rod micellar transitions, which are of fundamental importance for the successful synthesis of AuNRs (Equation 1.9).[132-137]

$$\log k = \alpha n_c^2 \left[\frac{\Delta F_{el}}{RT} + \gamma_{HI} \frac{(A_s - A_c)}{RT} \right] \qquad \text{(Equation 1. 9)}$$

where k is the thermodynamic parameter that contains both electrostatic and hydrophobic contributions, which reflects the micellar morphology evolution from spherical to rod-like. The coefficient αn_c^2, where α is a constant and n_c is the carbon chain length, is derived from Israelachvili's calculation of the critical aggregation

number (N_C) for a spherical micelle, which is defined as follows: $N_C = 4\pi R^3/3v = 4\pi R^2/a_o \approx \alpha n_c^2$, where R is the fully extended amphiphilic carbon chain length, v is the volume of the micellar core, and a_o is the surface area of the surfactant head group at the liquid micelle interface.[132-133, 137] According to this analysis, spherical micelles are only favoured when the geometric parameter $G = v/a_o R \leq 1/3$.[137] In conclusion, the micellar growth from spherical to elongated depends on the molecular structure and chemistry of the surfactant, by the ionic strength of the solution, and by the surfactant counterion's ability to screen micellar surface charge density.[94]

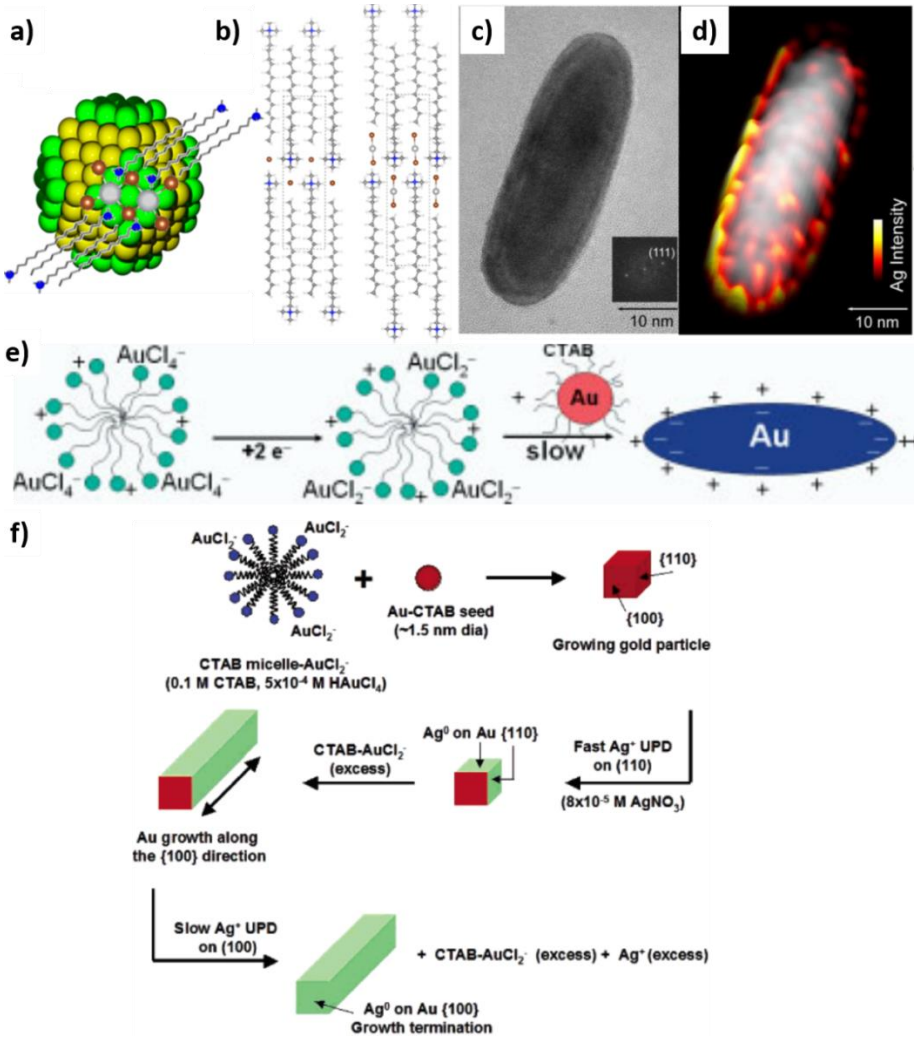

Figure 1. 10. a) The adsorption of CTAB-AgBr complex on {100} planes of seed. Note that due to the competition between electrostatic and chain interactions it is impossible

to cover all six {100} facets and thus a cylindrical configuration is templated during growth. Yellow planes are {111} and green ones are {100} facets. b) Crystal lattices of (left) CTAB and (right) CTAB-AgBr. (Br, brown; Ag, large light gray spheres; C, gray; H, white; N, blue). c-d) HRTEM images and correlated STEM-EDS maps of AuNR. e) The eElectric-field-directed mechanism in the absence of silver ions. f) The mMechanism for AuNR growth from CTAB-protected gold seed particles in the presence of silver ions. a, b) Reproduced with permission from [138]. Copyright (2014) American Chemical Society. c, d) Reproduced with permission from [139]. Copyright (2014) American Chemical Society. e) Reproduced with permission from [140]. Copyright (2004) WILEY. f) Reproduced with permission from [141]. Copyright (2006) American Chemical Society.

Many groups have explored the factors that influence the packing density and micellar morphology of CTAB templates. El-Sayed reported that the use of a bulkier co-surfactant, BDAC, along with CTAB produced AuNRs with higher aspect ratio, but also led to a significant low yield of rod-shape NPs.[28] High CTAB concentration (~100 mM) above the second CMC (about 20 mM) is indispensable for high yield AuNRs synthesis.[142-143] Recent progress has been made by Murray group that the addition of aromatic additives can reduce the CTAB concentration by 50% while still maintaining excellent monodispersity of rods.[144] NMR results demonstrated that salicylate ions are able to insert into the CTAB micelles and promotes their spherical to rod-like transition. The counterion's contributions toon the solution-phase micellar growth of CTAB also show significant effects on the morphology of CTAB micelles.[145-147] The influence of the counterion on CTA^+ micellar adsorption and growth showed that bromide exhibits a higher binding affinity to the CTA^+ micellar surface compared with chloride, and CTA^+-Br^- aggregates adsorb as worm-like micelles with an observed proclivity to coalesce into a laterally homogeneous structure, presumably a bilayer, while the morphology of the adsorbed CTA^+-Cl^- aggregates appear as circular projections.[145-147]

1.2.2.2 Selective Binding Mechanism

Differential binding of various species to a particular set of growing facets might also affect the deposition rate of gold onto those facets, thereby controlling the final shape of

the nanocrystal. It is clear that bromide, silver, and the CTA^+ cation have a huge impact on the anisotropic growth, though the exact surface-binding species are still under debate. El-Sayed and co-workers attributed the enhanced growth of {111} tip facets to the stronger binding affinity of CTAB to the {110} side facets, which have a higher surface energy due to larger interatomic distances.[28, 148] In this regard, the Ag^+ forms ion pairs [AgBr] decrease the charge density of bromide ions and thus decrease the repulsion of neighbouring CTAB headgroups. This repulsion promotes CTAB elongation and AuNR formation.[28] It was alternative argues that [AgBr] could precipitate onto the gold-CTAB interface to both stabilize the rods and guide the anisotropic growth by inhibiting growth from a specific facet.[110, 149] Later reports indicates that the CTA^+AgBr^{2-} complex is potentially the active surfactant, which is expected to alter both micellization and specific adsorption.[138, 150] López *et al.* utilized density functional theory simulations to provide an atomistic description of the role of different compounds in the synthesis of AuNRs.[138] Their work indicates that anisotropic growth is caused by the formation of CTAB-AgBr complex that preferentially adsorbs on {100} facets of the seeds, blocking them from further growth (Figure 1. 10a-b). In addition, they found that Br^- ions are important in the synthesis. All halides (Cl^-, Br^-, I^-) prefer to adsorb and block the defective positions of the seeds, however, the specific adsorption of Br^- species is strong enough for the anisotropic growth but weak enough for the growth process. In contrary, the adsorption of Cl^- is too labile to block surface growth due to rapid adsorption/desorption processes, while I^- is too strongly bound to the surface, thus blocking the growth process.[138]

Detailed Extended X-ray Absorption Fine Structure (EXAFS) measurements of AuNRs were performed to determine the chemical and coordination state of silver and demonstrated that Ag(0) is present in metallic rather than ionic form in the final product.[151-152] The presence of Ag(0) coating supports a different growth mechanism driven by underpotential deposition (UPD) of silver onto growing nanorods. UPD is the deposition of a metal layer onto another metal surface (Au) below the Nernst reduction potential (up to 0.5 to 0.9 V) of the metal ions ($AgNO_3$/Ag), as a result of strong bonding interactions between the two metals in the adsorbed layer.[153-154] According to this hypothesis, $AgNO_3$ immediately forms AgBr in the presence of CTAB in the

growth solution and cannot be reduced by ascorbic acid at acidic pH values, (typically pH = 3) because the ascorbic acid reductant is too weak.[155] Liu and Guyot-Sionnest proposed that the deposition of silver on the AuNR surface can happen at a lower potential (UPD) and that silver reduction is more likely to occur on the longitudinal {110} facets, thus blocking these facets for anisotropic growth.[156] However, Wright *et al*. used HRTEM paired with corresponding scanning transmission electron microscopy (STEM)-EDS map to image the position of silver on AuNRs (Figure 1. 10c-d).[139] The silver signal follows the surface of the AuNR, indicating that the detected silver is on the surface rather than doped into the particle. Furthermore, the results of mapping 38 individual AuNRs suggest that the location of silver atoms does not correspond to~~with~~ any one particular facet. The analysis also indicates that the silver atoms distribute homogeneously over the AuNR surface, seeming to give support to those growth mechanisms, like the proposed "soft template" mechanism, that does not rely on the face-specific deposition of Ag species.

1.2.2.3 Electric-Field-Directed Mechanism

The other theory is the electric-field-directed growth mechanism proposed by Mulvaney group (Figure 1. 10e).[140] In this mechanism, $AuCl_4^-$ is bound to CTAB micelles and reduced to $AuCl_2$–CTAB micelles. This complex binds to the CTAB-capped seed particles through collisions which are controlled by the electric double layer between the positively-charged seed and negatively-charged $AuCl_2^-$ on the CTAB micelles. A higher electric field exists at the tips of AuNRs, leading to a faster collision at the tips than the sides of the seeds and thus facilitate the rod-shape growth. In 2006, Orendorff and Murphy proposed a mechanism to clearly elucidates the growth process, by combining the UPD, electric-driving-directed, and surfactant preferential binding theories (Figure 1. 10f).[141] In this theory, $AuCl_2^-$ on the CTAB micelles diffuses to CTAB-capped seeds by electric field interactions, and the sphere symmetry growth is broken by CTAB preferential binding onto the {110} facet. Silver ions selectively deposit onto the {110} side facet faster than they do onto the {100} end facet, resulting in the anisotropic growth along the <110> direction. Complete deposition of silver ions onto {100} end facet stops the particle growth, which limits the AuNRs shorter than 100

nm (sliver-assisted methods). This mechanism is well-supported by the fact that silver-assisted nanorods are shorter than those synthesized without silver ions.[27] An increase in silver ions over a threshold concentration could not further increase the aspect ratio due to the blocking of the end facet of the nanorods by silver metal deposition.[22, 28]

1.2.3 The Crystal Structure of AuNRs

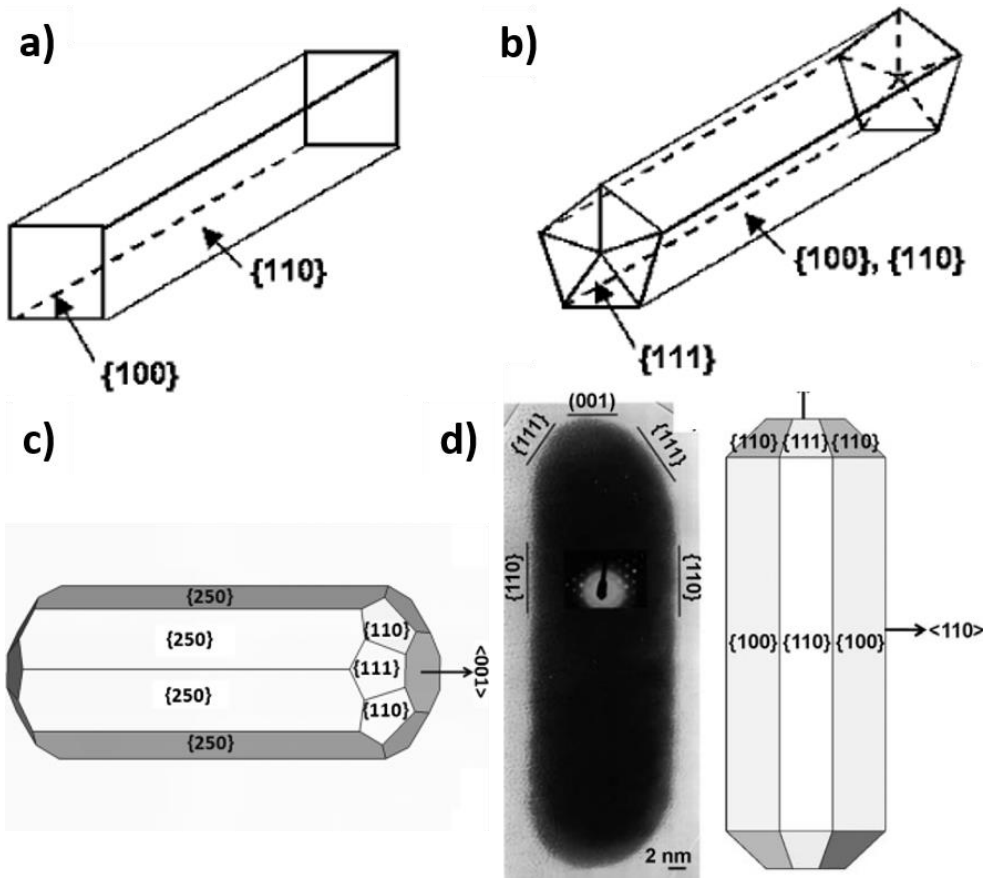

Figure 1. 11. Crystal structure of AuNRs synthesized by a, c) seed-mediated growth method using CTAB-capped seed in the presence of silver ions, b) seed-mediated growth method using citrate-capped seed in the absence of silver ions, and d) electrochemical reduction method using CTAB and tetradecylammonium bromide as surfactant. a, b) Reproduced with permission from [141]. Copyright (2006) American Chemical Society. c, d) Reproduced with permission from [157]. Copyright (2010) WILEY.

Liu and Guyot-Sionnest have studied the crystal structure of AuNRs using CTAB-capped and citrate-capped seeds.[156] Their results show that the single-crystalline CTAB-capped seed leads to single-crystalline nanorods with {110} facets on the side and {100} on the flat end (in the presence of silver, Figure 1. 11a), while the multiply twinned crystalline citrate-capped seed grows into multiple twinned structures with {100} and {110} side facets and {111} end facet (in the absence of silver, Figure 1. 11b). The deposition of gold atoms to the seed surface does not create a stacking default and therefore preserves the initial seed structures. Recent analysis by Liz-Marzán and co-workers suggests that the actual structure of AuNRs synthesized by seed-mediated growth method using CTAB-capped seed (in the presence of silver ions) is likely different from that in Figure 1. 11a and includes 8 higher-index {250} facets on the sides of the rods and {110} and {111} facets on the end facets (Figure 1. 11c).[157] The structure of AuNRs prepared by the electrochemical method depends on the aspect ratios and is also different from those fabricated by the seed-mediated method.[158] HRTEM and electron diffraction studies by Wang *et al.* show that short rods with an aspect ratio of 3–7 are single crystals without stacking faults, twins, or dislocations, and they have {100} and unstable {110} side facets[148] and {110} and {111} end facets with a <001> growth direction (Figure 1. 11d).[158] For longer rods with aspect ratio over 20 display one twin plane parallel to the <111> direction. The nanorods are dominated by {111} and {110} facets with a <112> growth direction.

1.2.4 The Cytotoxicity of CTAB Molecules

As mentioned before (**Section** 1.1.5.1), there is a wide array of biological applications where AuNRs are employed and, as a consequence, the well-known toxicity of CTAB (and consequently of AuNRs) should be a serious concern not only for the community interested in these applications but also for the scientists whose expertise could contribute to the identification of its causes.[159-162] Therefore, much research has been dedicated to understanding the source of CTAB-AuNR toxicity, but it still remains a controversy within the scientific community.

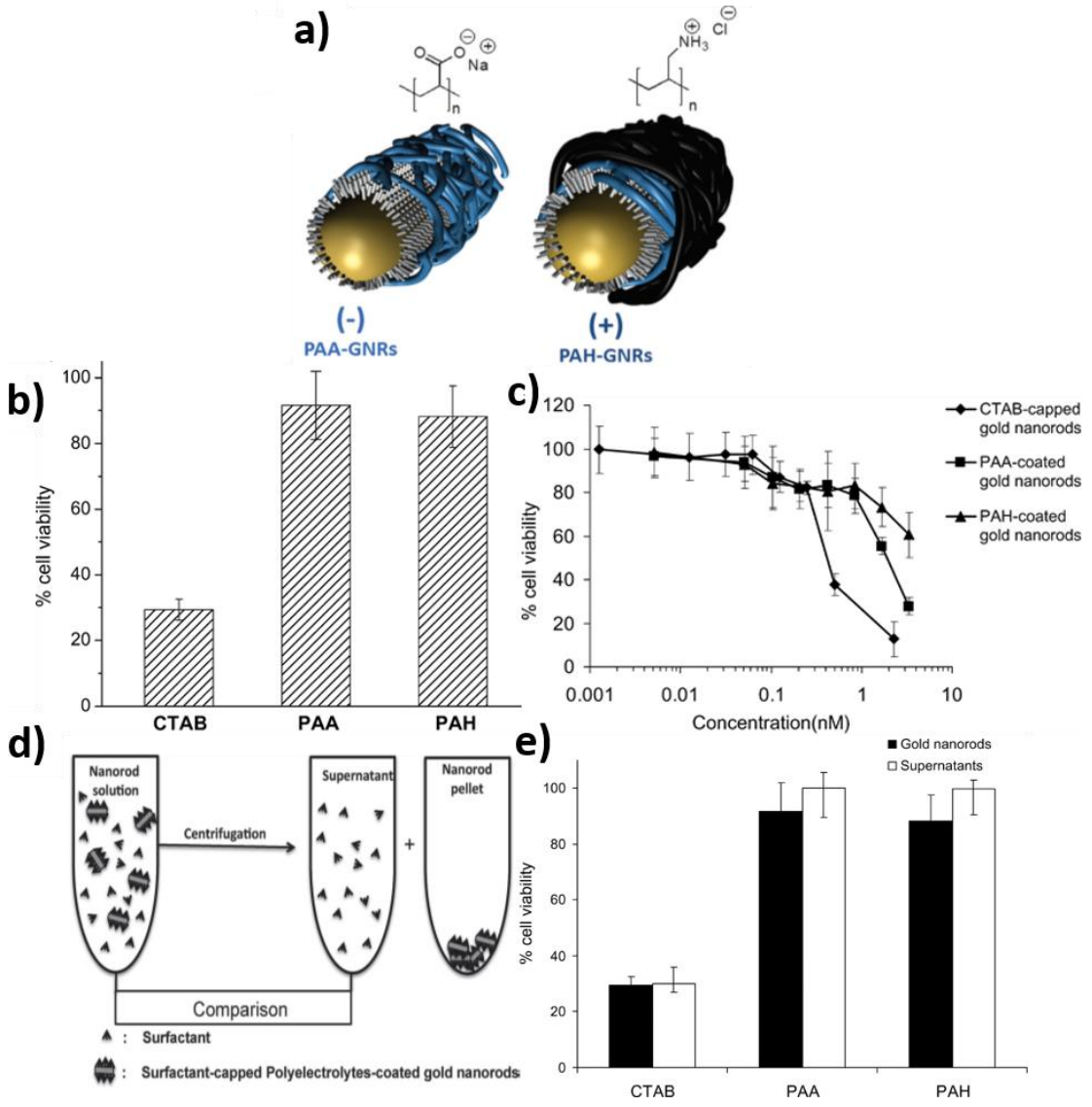

Figure 1. 12. a) Cartoon demonstrating the coating of CTAB-AuNRs with either anionic (PAA) or cationic (PAH) polyelectrolytes. The chemical structures of PAA and PAH are shown. b) The v~~V~~iability of HT-29 cells exposed to 0.4 nM AuNRs with different surface coatings for 4 days. c) The d~~D~~ose-dependent viability of HT-29 cells exposed to increasing concentrations of CTAB-, PAA-, and PAH-coated AuNRs. d) Schematic illustration of the "supernatant control" experiment. AuNRs were separated from free surfactant by centrifugation. e) The v~~V~~iability of HT-29 cells exposed to 0.4 nM of CTAB-, PAA-, and PAH-coated AuNRs (filled bars) and their supernatants (open bars) for 4 days. a, d) Reproduced with permission from [162]. Copyright (2012) WILEY. b, c, e) Reproduced with permission from [159]. Copyright (2009) WILEY

Does it originate from the surface charge of AuNRs? It has been reported that the cytotoxicity of CTAB-AuNRs significantly reduces after coating with polyelectrolytes (both anionic and cationic) or ligands such as PEG and alkanethiols, in which cases only a negligible loss of cell viability has been reported (Figure 1. 12b, c).[163-166] Therefore, it seems that there is no correlation between the overall surface charge and the cytotoxicity of AuNRs.

Does it originate from free CTAB molecules in suspension or from AuNR-bound CTAB? In order to investigate the origin of the cytotoxicity, CTAB-capped AuNRs were centrifuged, and the toxicity of the supernatant was compared to that of the precipitates resuspended in water and to the original CTAB-AuNRs (Figure 1. 12d,e).[159] The cytotoxicity of the supernatant was found to be comparable to that of the free CTAB alone and of the original CTAB-AuNRs suspension, thereby revealing that free CTAB is a dominating factor contributing to overall toxicity (Figure 1. 12d). Similar experiments were also performed on PAA-AuNRs and PAH-AuNRs, for which the CTAB concentration in the supernatant was found to be below the detection limits of the mass spectrometer, and showed little cytotoxicity (Figure 1. 12e). Therefore, it seems that the cytotoxicity arises from free CTAB molecules in the suspension not from the surface charge of the AuNRs nor from the AuNRs themselves~~,~~ and that the polyelectrolyte encapsulation might reduce the exposure of the cells to the desorbed CTAB. However, Sonnichsen's group reported that AuNRs might act as a CTAB carrier, releasing surface-bound CTAB upon cellular internalization, thereby causing more toxicity than the free CTAB ~~in solution~~ that directly interacts with only the cell exterior having a limited ability to cross the cell membrane.[167]

It should be noted that it is not an easy and fair task to draw generalized conclusions on AuNR cytotoxicity based solely on the literature. These studies have used a wide range of AuNR concentrations, aspect ratios, incubation times, and most importantly different cell lines and cell models (in vitro and in vivo), which mainly dictate the level of cytotoxicity. Therefore, it is necessary to propose standardized toxicological parameters to systematically analyz~~s~~e the interactions between AuNRs and biological materials, allowing us to draw accurate conclusions.

1.3 Thesis Structure and Chapter Outline

This thesis consists of seven chapters, and the outline of each chapter is summarized below:

1. Chapter 1 (Introduction) contains a brief introduction to AuNRs including the properties of AuNRs, the surrounding environment of AuNRs. The thesis structure and chapter outline are provided at the end of this chapter.

2. Chapter 2 (Literature Review) systematically introduces the background of synthesis, surface modification, and photocatalysis of AuNRs. The advantages and disadvantages of each method, the progress, and the challenge, and the motivation of this thesis are also provided.

3. Chapter 3 provides detailed experimental procedures and thorough mechanism discussion for the seedless synthesis of AuNRs. In this chapter, a facile, highly reproducible seedless synthesis technique, based on synergistic template modification and growth kinetics regulation, is described. By this method, monodispersed AuNRs with high yield (~ 100%) and highly adjustable longitudinal SPR are reproducibly synthesized. The parameters that influence the AuNRs growth were thoroughly investigated in terms of growth kinetics and soft-template regulation, offering a better understanding of the template-based mechanism. A useful scheme was proposed as a reference in predicting and customizing the dimensions of AuNRs. This work has been published as a journal article in ***Chemistry-A European Journal*** (*Chemistry – A European Journal* **2017,** *23*, 3291-3299), named *"Seedless Synthesis of Monodispersed Gold Nanorods with Remarkably High Yield: Synergistic Effect of Template Modification and Growth Kinetics Regulation"*.[168] The content in this chapter was reproduced with permission from [168]. Copyright (2012) WILEY.

4. Chapter 4 demonstrates detailed experimental procedures and thorough mechanism discussion for the surface modification of AuNRs. In this chapter, a simple, reliable, robust functionalization procedure is introduced to produce colloidally stable and biocompatible (i.e., CTAB free) AuNRs. This one-step surface functionalization method

allows for the complete removal of the surface-bound CTAB and the most active surface silver from the AuNRs. The produced AuNRs showed far lower toxicity than other methods to PEGylate AuNRs, with no apparent toxicity when their concentration is lower than 5 μg/mL. Even at a high concentration of 80 μg/mL, their cell viability is still four times higher than that of the tip-modified AuNRs. This work has been published as a journal article in ***Langmuir*** (*Langmuir* **2015,** *31*, 4973−4980), named *"Biocompatible Gold Nanorods: One-Step Surface Functionalization, Highly Colloidal Stability, and Low Cytotoxicity"*.[169] The content in this chapter was reproduced with permission from [169]. Copyright (2015) American Chemical Society.

5. Chapter 5 demonstrates detailed experimental procedures and thorough mechanism discussion for the synthesis of AuNRs@anatase TiO_2 core-shell nanostructures for efficient H_2 production. In this chapter, we report the facile synthesis of AuNRs@anatase TiO_2 core-shell nanostructures by uniformly coating TiO_2 on AuNRs through elaborate-controlled hydrolysis of titania precursor followed by hydrothermal treatment (~75℃, ~1.4 atm). Using this method, the amorphous TiO_2 can be effectively crystalized into anatase phase and the intactness of AuNRs can be well preserved. Comparing to other photocatalysts, the as-synthesized AuNRs@anatase TiO_2 core-shell nanoparticles show significantly enhanced H_2 generation ability under UV-Vis-NIR light irradiation.

6. Chapter 6 consists of a summary and suggestions for future work.

7. Chapter 7 consists of all of the references cited in this thesis.

Chapter 2 Literature Review

2.1 Synthesis of AuNRs

Shape-controlled synthesis of AuNRs in high monodispersity has received widespread interest due to their outstanding anisotropic properties are attractive in optical, electronic, biological and catalytic applications. Although the history of the modern synthesis of AuNSs dates back more than a century (1857 by Faraday),[4] the successful and reliable synthesis of AuNRs was achieved only during the past decade. In this section, great progress that has been made for obtaining AuNRs with high yield, quality, and uniformity will be briefly reviewed.

2.1.1 Electrochemical Synthesis

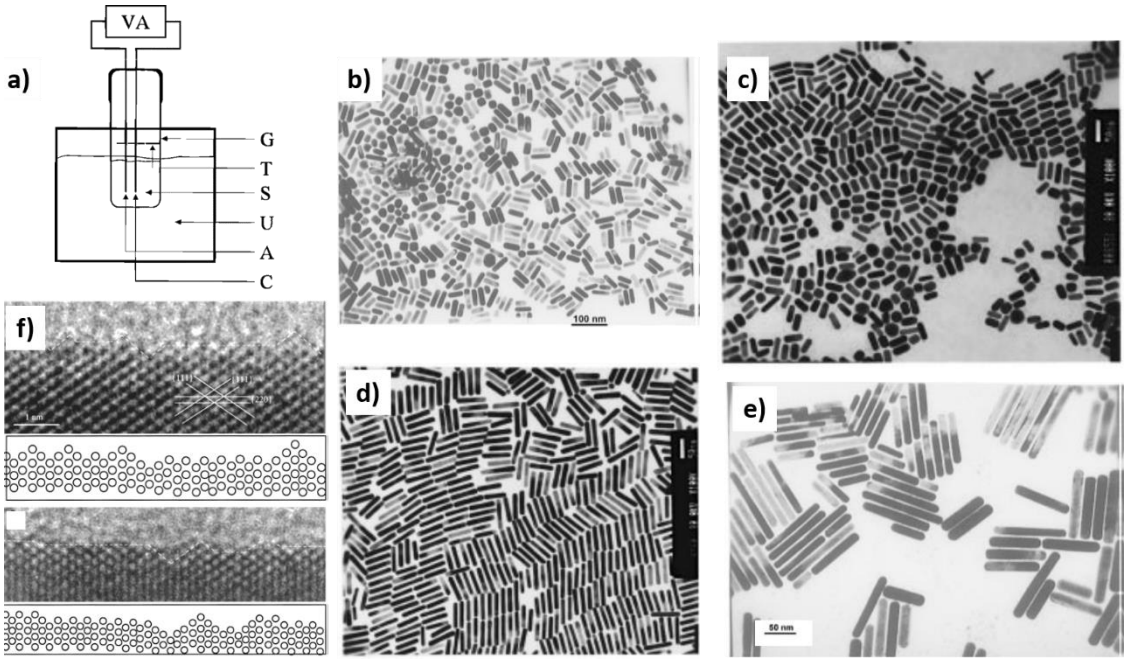

Figure 2. 1. a) Schematic diagram of the set-up for electrochemical synthesis of AuNRs containing: VA, power supply; G, glassware electrochemical cell; T, Teflon spacer and the electrode holder; S, electrolytic solution; U, ultrasonic cleaner; A, anode (Au); C, cathode (Pt). b-e) TEM images of AuNRs synthesized by electrochemical method with different mean aspect ratios: b) 2.6; c) 2.7; d) 6.1; e) 7.6. f) HRTEM images recorded

from a [110]-oriented AuNR and the corresponding positions of the projected atom rows. a, c, d) Reproduced with permission from [170]. Copyright (1999) American Chemical Society. b, e) Reproduced with permission from [23]. Copyright (1997) American Chemical Society. f) Reproduced with permission from [148]. Copyright (2000) American Chemical Society.

In the 1990s, Wang and co-workers initially reported the synthesis of AuNRs by an electrochemical method, in which an Au plate anode and a Pt plate cathode were immersed in an electrolyte containing cationic CTAB and cationic tetradodecylammonium bromide (TOAB) as a co-surfactant.[23, 170] During the electrolysis, Au ions in the form of $AuBr_4^-$ were generated from an Au anode, which then complexes with the CTAB micelle and migrates to the Pt cathode where Au ions are reduced to Au atoms (Figure 2. 1. a). The aspect ratio is controlled by the presence of Ag^+ ions produced from the redox reaction between the Au ion and Ag plate (Figure 2. 1b-e). This method produces AuNRs that are single crystals without stacking faults, twins, or dislocations, as shown by HRTEM and diffraction studies (Figure 1. 11d and Figure 2. 1f). Small amounts of acetone and cyclohexane additives were also added before the electrolysis and the entire setup was sonicated throughout the reaction. Acetone was used for loosening the micellar frame-work and cyclohexane was necessary to enhance the formation of elongated rod-like CTAB micelles.[170] Ultrasonication is required to dissipate the AuNRs away from the cathode during the electrolysis.

2.1.2 Seed-Mediated Methods

2.1.2.1 Methods Using Citrate-Capped Seeds

Among the various AuNRs synthesis protocols, the seed-mediated growth method is the most popular method for the synthesis of colloidal AuNRs due to their simplicity of the procedure, high quality and yield of nanorods, ease of particle size-controlling, and flexibility for structural modifications. The current concept of seed-mediated chemical growth is originated in 2001 by Murphy *et al.*[27], in which chloroauric acid ($HAuCl_4$) instead of Au electrode is applied as the source of Au and the electrochemical reduction

was replaced with chemical reduction using a weak reducing agent (ascorbic acid, AA) and silver nitrate. The AuNRs was prepared by the addition of (about 3 nm) citrate-capped seed particles to a bulk $HAuCl_2$ growth solution reduced from $HAuCl_4$ by AA in the presence of CTAB and silver ions. The AA used in this synthesis (high CTAB concentration and low pH~2.5) can only reduce Au ions to the metallic state in the presence of seeds NPs that catalyzse the reduction reaction.[155] As a result, AuNRs with various aspect ratios were produced by adding different volumes of seed solution to the growth solution (Figure 2. 2).[171] However, the shape-yield of nanorods was still relatively low and a large numberamount of spherical impurities was present.

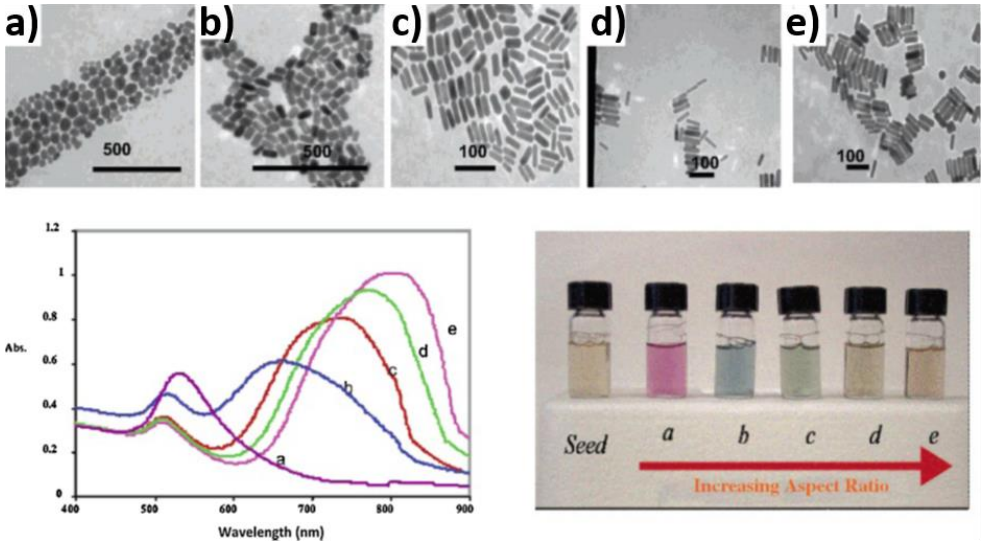

Figure 2. 2. TEM images (top), absorbance spectra (bottom-left) and photographs (bottom-right) of aqueous solutions of AuNRs with various aspect ratios ranging from: a) 1.35 ± 0.32; b) 1.95 ± 0.34; c) 3.06 ± 0.28; d) 3.50 ± 0.29; e) 4.42 ± 0.24. Reproduced with permission from [171]–. Copyright (2005) American Chemical Society.

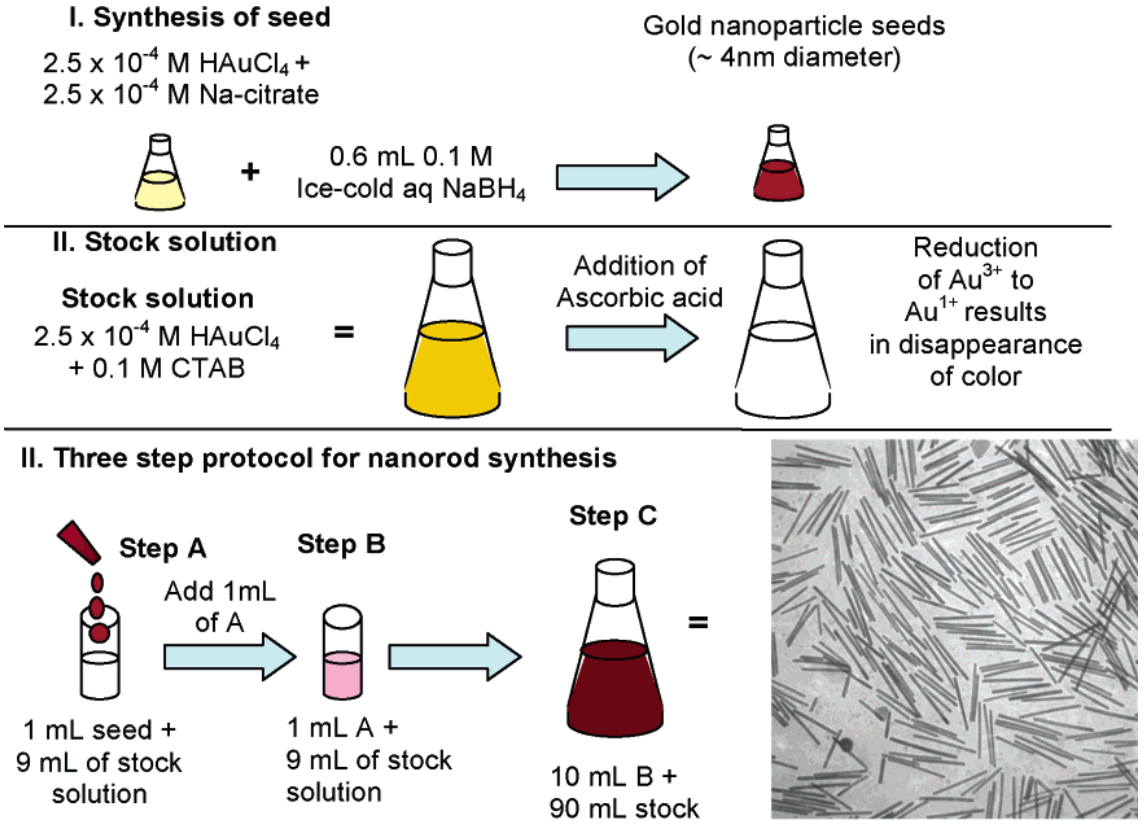

Figure 2. 3. Three-step seed-mediated growth approach for making Au and Ag nanorods with a controlled aspect ratio. Reproduced with permission from [171]. Copyright (2005) American Chemical Society.

In subsequent work, Murphy group modified the above method and proposed a three-step procedure in the absence of $AgNO_3$ allowing for longer AuNRs with aspect ratios up to 25 to be prepared.[26, 110, 171-172] In the typical procedure, first-stage AuNRs (about 4 nm citrate-capped seed NPs) are used as seeds for second growth, which are sequentially used as seeds for third growth (Figure 2. 3). The result is the synthesis of multiple twined AuNRs (Figure 1. 11b) with 20~22 nm diameter and higher aspect ratio. Currently, it is not possible to further decrease the rod diameter below 20 nm, although the length can be pushed to above 1 μm while maintaining nearly the same diameter by altering the reaction conditions.[173] This method is the basis of all available methods to grow crystalline AuNRs with high aspect ratios, but, unfortunately, this method accompanies large fraction of impurities (>95%) including AuNSs as well as nanoplatelets produced,[172] which requires time-consuming separation steps.

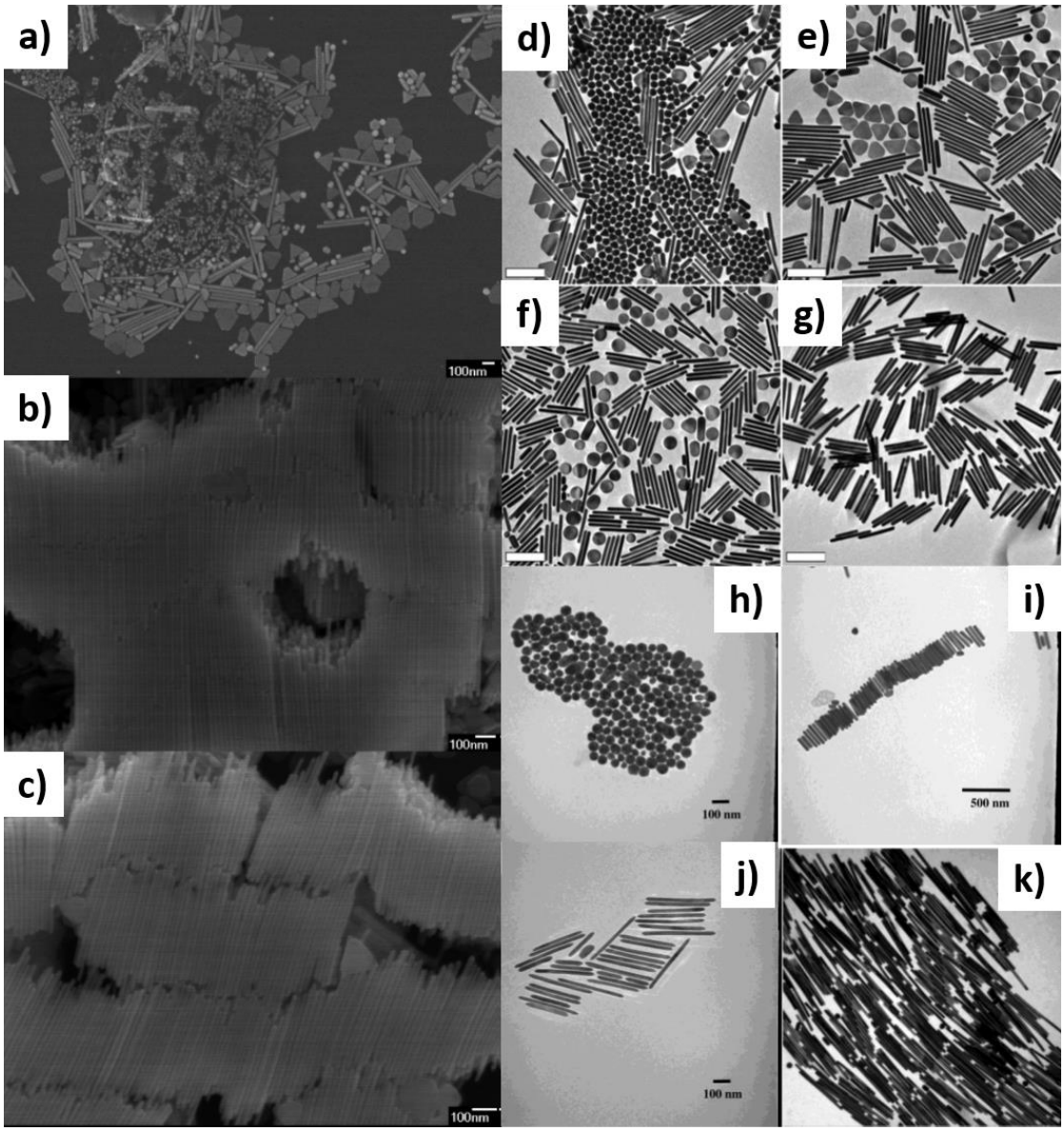

Figure 2. 4. a-c) SEM image of AuNPs prepared by a three-step seed-mediated method with the addition of a) 0 μL, b) 200 μL and c) 400 μL HNO_3 during the growth process. d-f) TEM images of AuNPs prepared by a three-step seed-mediated method: d) as-synthesized mixture; e) mixture of faceted platelets and rods after the removal of small spherical particles; f) mixture of nanodisks and rods that was obtained by treating the mixture shown in panel e with Au(III)-CTAB complex; g) nanorods precipitated from the solution of the mixture shown in panel f. h-k) TEM micrographs of AuNPs prepared by a three-step seed-mediated method in the presence of h) C_{10}TAB, i) C_{12}TAB, j) C_{14}TAB, and k) C_{16}TAB, after purification to remove the spheres. a-c) Reproduced with

permission from [174]. Copyright (2005) American Chemical Society. d-g) Reproduced with permission from [175]. Copyright (2008) American Chemical Society. h-k) Reproduced with permission from [176]. Copyright (2003) American Chemical Society.

Many efforts have been made to the optimization of the original three-step procedure to improve the yield of rod-shape NPs. Murphy group first reported that increasing the pH of the growth solution using NaOH significantly increased the percentage of AuNRs in the products.[172] Interestingly, a later report by Wu *et al.* demonstrated that addition of HNO_3 to the final growth solution also led to an increase in the quality of the rods, although this was attributed to the presence of nitrate ion rather than a change in pH (Figure 2. 4a-c).[174] In 2008, Zubarev group developed a separation procedure that allows for the isolation of nearly all nanorods that were present in the initial solution and brings about > 99% of rod-shape NPs in the purified products (Figure 2. 4d-g).[175] In this method, the NPs in the solution are first treated with Au(III)-CTAB solution, which leads to oxidation along the entire circumference of platelets and the tips of rods, transforming platelets into smaller nanodisks and giving them higher solubility. While the resulting nanorods, having a shorter length and the same diameter due to the oxidation, slowly precipitate at the bottom and can be collected and separated by centrifugation. Further insight into the three-step procedure was gained by investigating the effects of the size of the seed NPs and the capping-agent on the nanorods synthesis.[110] The effect of varying the surfactant chain length and structure was also studied by Murphy group.[176] The AuNRs with higher aspect ratios were produced when increasing the alkyl chain length in the alkyl-trimethylammonium bromide from decyl to hexadecyl (Figure 2. 4h-k). It's worth mentioning that reducing the chain length to ten carbon atoms led to complete disappearance of high aspect ratio rods (Figure 2. 4k). In 2009, Kitahata *et al.* reported that high-aspect-ratio AuNRs (~50) were synthesized with a yield of 90% using a gelled mixture of CTAB and octadecyltrimethylammonium bromide (OTAB) as surfactants, whereas no high-aspect-ratio AuNRs were obtained when the solution did not gel.[173] Optimized gelation conditions, i.e. higher OTAB concentration and lower temperature, were explored for the synthesis of rods with the highest aspect ratios of 30–50, which indicates that there

is a close relationship between the gelation of a surfactant solution and the elongation of AuNRs.[173]

2.1.2.2 Methods Using CTAB-Capped Seeds

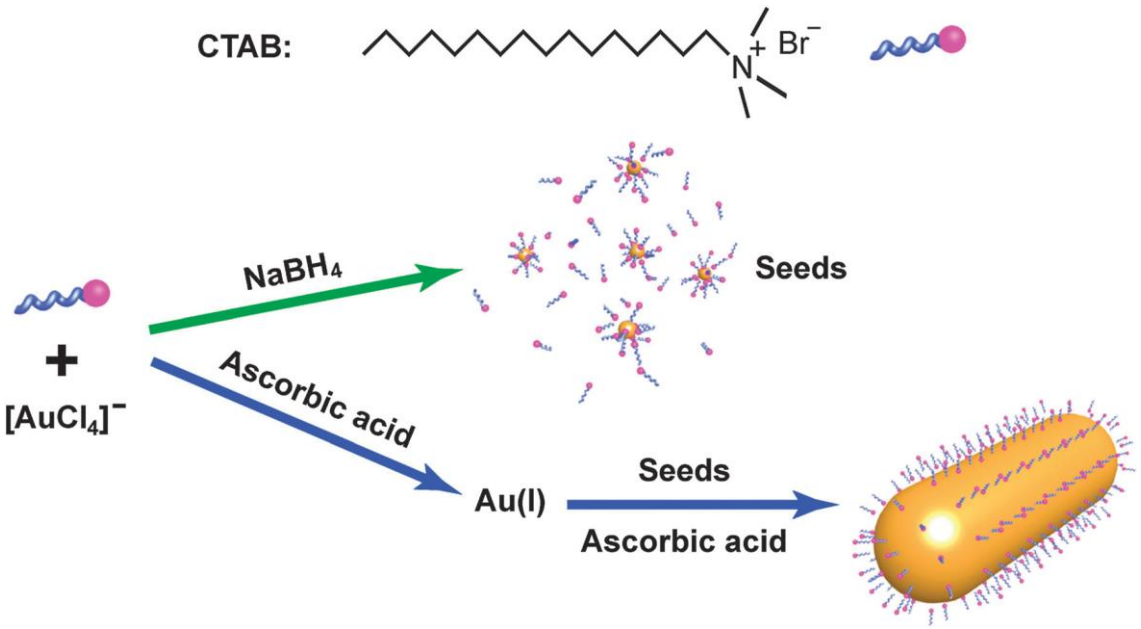

Figure 2. 5. Schematic illustration of the seed-mediated method for the synthesis of AuNRs using CTAB-capped seeds. Reproduced with permission from [21]. Copyright (2012) Royal Society of Chemistry.

In 2003, significant improvement of the seed-mediated method was achieved by El-Sayed *et al.* who were able to minimize the formation of spherical particles and produce rod-like morphology in high yield.[28] In this method, two major modifications were made: 1) replacing sodium citrate with a stronger CTAB stabilizer in the seed formation process; 2) utilizing silver ions to control the aspect ratio of AuNRs. In a typical growth, CTAB-capped seeds of ~1.5 nm in size are first prepared by reducing $HAuCl_4$ with ice-cold $NaBH_4$; a certain amount of the seed solution is then added into the Au(I) growth solution reduced from $HAuCl_4$ by AA in the presence of CTAB and $AgNO_3$ (Figure 2. 5~~Figure 2. 5. Schematic illustration of the seed-mediated method for the synthesis of AuNRs using CTAB-capped seeds. Reproduced with permission from [21]. Copyright (2012) Royal Society of Chemistry.).~~ The added seeds thereafter catalyzse the further

reduction of Au(I) complex ions to form AuNRs. Using this method, a yield as high as 99% for the AuNRs (with aspect ratios from 1.5~4.5) was obtained, which avoids repetitive centrifugations for impurities separation. Due to the high quality and yield of AuNRs produced, this method has been further optimized to produce AuNRs with higher monodispersity and improved tunability of the aspect ratios (or LSPR).

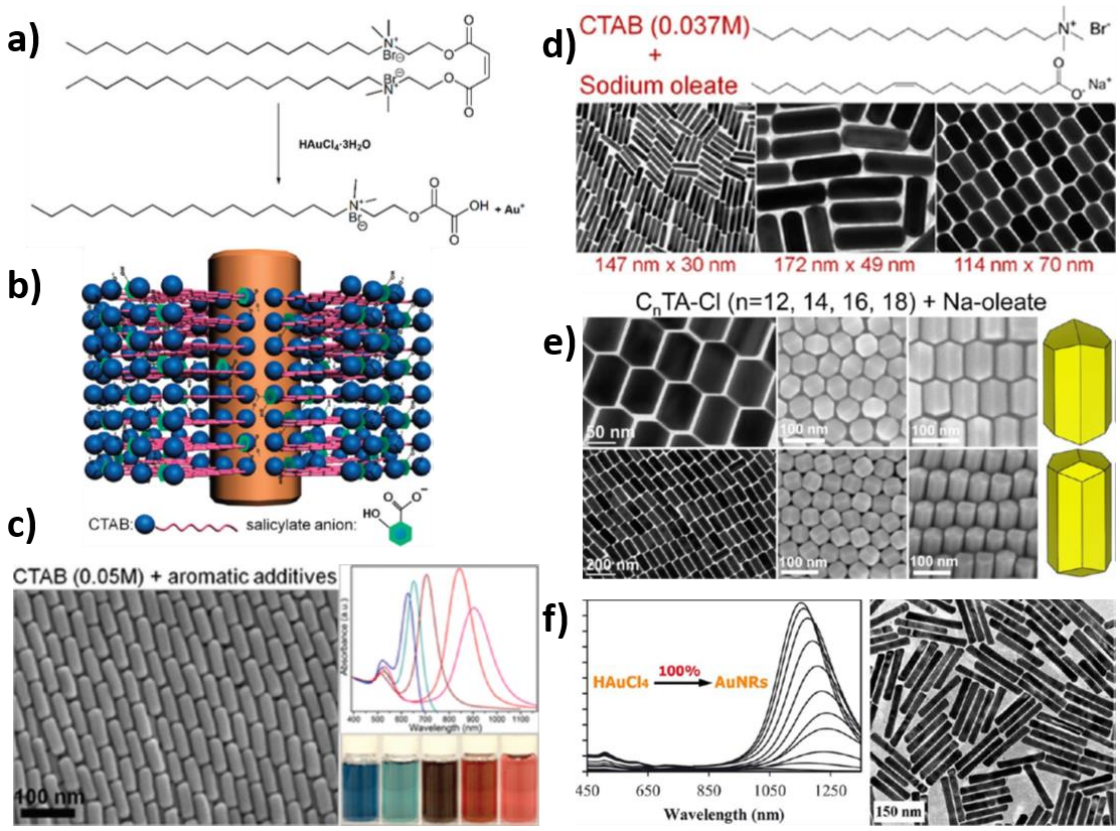

Figure 2. 6. a) Schematic illustration of the pre-reduction of Au^{3+} by gemini surfactant (P16-8-16). b) A cartoon illustrating the proposed mechanism to explain the role of aromatic additives (sodium salicylate is shown as an example) in mediating the binding between CTAB bilayers and certain facets of growing AuNRs. Note that surfactant molecules are not drawn at the nanorod tip region for clarity purposes. c) SEM, UV-Vis, and optical images of AuNRs synthesized using CTAB (0.05 M) and aromatic additives. d) TEM images of AuNRs synthesized using CTAB (0.0375 M) and NaOL. e) TEM and SEM images of AuNRs synthesized using CTAC and NaOL, and structural models showing AuNR's 3D morphology. f) UV-Vis spectra and TEM images of AuNRs synthesized by applying HQ as reducing agent. a) Reproduced with permission

from [177]. Copyright (2015) Royal Society of Chemistry. b, c) Reproduced with permission from [144]. Copyright (2012) American Chemical Society. d) Reproduced with permission from [112]. Copyright (2013) American Chemical Society. e) Reproduced with permission from [30]. Copyright (2013) American Chemical Society. f) Reproduced with permission from [178]. Copyright (2013) American Chemical Society.

Higher aspect ratios up to 10 or 20 were obtained upon addition of a co-surfactant (BDAC[28] or Pluronic F-127[111]) to the growth solution together with adjusting the $AgNO_3$ concentration. The use of the dual-surfactant system, however, significantly increases the level of impurities, as evidenced by the weak absorbance peak ratio (<4:1) compared to that (10:1) for the single-surfactant method. Further, even higher aspect ratios of up to 70 have been obtained by fourth additions of growth medium with increased volumes accompanied by shape changes from fusiform into 1D rods.[179] Zhang group developed a method to large-scale, low-cost synthesis of monodispersed AuNRs with aspect ratios ranging from ~2.4 to ~6.3 using a gemini surfactant in growth solution (P16-8-16).[177] In 2010, Prasad group reported the synthesis of high-quality AuNRs with tunable aspect ratios (2.5~8) by deliberately adjusting the pH of growth solution and concentration of $AgNO_3$ (Figure 2. 6a).[180] Later in 2012, Murray and co-workers demonstrated tuning of LSPR (627~1246 nm) through the addition of aromatic salicylate additives as well as HCl, which was explained through an effect on the micellar structure adjustment of CTAB during rod growth (Figure 2. 6b, c).[144] Interestingly, the concentration of the CTAB in growth solution was reduced from the value of 0.1 M, which was applied in the original approach, to 0.05 M. As CTAB has been proven to be highly cytotoxic, the reduction of CTAB concentration is highly desirable towards the synthesis of biocompatible AuNRs by facilitating their surface modification with other ligands (e.g. thiolated-PEG).[169] In 2013, they succeeded in further lowering the concentration of CTAB to 0.037 M using a binary surfactant mixture composed of CTAB and sodium oleate (NaOL) (Figure 2. 6d).[112] The CTAB−NaOL binary surfactant mixture overcomes the difficulty of growing uniform thick AuNRs often associated with the single-component CTAB system and greatly expands the dimensions of AuNRs that are accessible through a one-pot seeded growth

process. In the same year, the same group reported the synthesis of monodisperse AuNRs with broadly tunable dimensions and LSPR using a bromide-free surfactant mixture composed of alkyltrimethylammonium chloride (CTAC) and NaOL (Figure 2. 6e).[30] It is also found that by using the CTAC-NaOL mixture, uniform AuNRs can still be obtained even with an iodide concentration approaching 100 μM in the growth solution, which is drastically different from the traditional method where submicromolar levels of iodide can already suppress AuNR formation. In contrast to conventional wisdom, their results provide conclusive evidence that neither bromide as the surfactant counterion nor a high concentration of bromide ions in the growth solution is essential for AuNR formation.[30]

This seed-mediated method is very sensitive to the AA concentration and high-quality AuNRs are available only when AA concentration falls within a very narrow window.[141] This brings about a fact that only ~ 15% of Au ions present in the solution isare reduced into AuNRs, therefore, many efforts have been made to improve that yield. Zhu *et al.* reported the synthesis of monodispersed AuNRs using dopamine as reducing agent, in which ~80% of Au ions were reduced to AuNRs.[181] Tracy *et al.* reported a secondary (seeded) growth procedure, wherein continuous addition of AA to a stirring solution of AuNRs, deposits the unreacted Au precursor onto the AuNRs.[182] In this method, the tunability of aspect ratios was achieved by controlling the rate of AA addition and adjusting the mixture of surfactants present during secondary growth, which demonstrates unprecedented ability to tailor the optical properties of AuNRs during secondary growth. Recently, Zubarev group used Hydroquinone (HQ), a much weaker reducing agent compared to AA, to produce AuNRs with extremely high yield of ionic-to-metallic gold conversion (~100%) (Figure 2. 6f).[178] In addition, their synthetic technique is not sensitive to the concentration of HQ and the tunability of the LSRPs was demonstrated in a wide-range from 770 to 1230 nm.

2.1.3 Seedless Methods

Another strategy is to perform a one-pot synthesis of nanorods by adding $NaBH_4$ directly to the growth solution instead of forming a separate seed solution to obviate the

drawbacks associated with the seed-mediated methods, such as unsatisfactory reproducibility resulting from the time-dependent stability of the seeds together with many variations involved in multi-step procedure,[183-184] and strict requirements on experimental parameters (especially AA and $HAuCl_4$ concentration).[178] Although these methods are generally termed "seedless", the addition of $NaBH_4$ still forms seed NPs in situ.

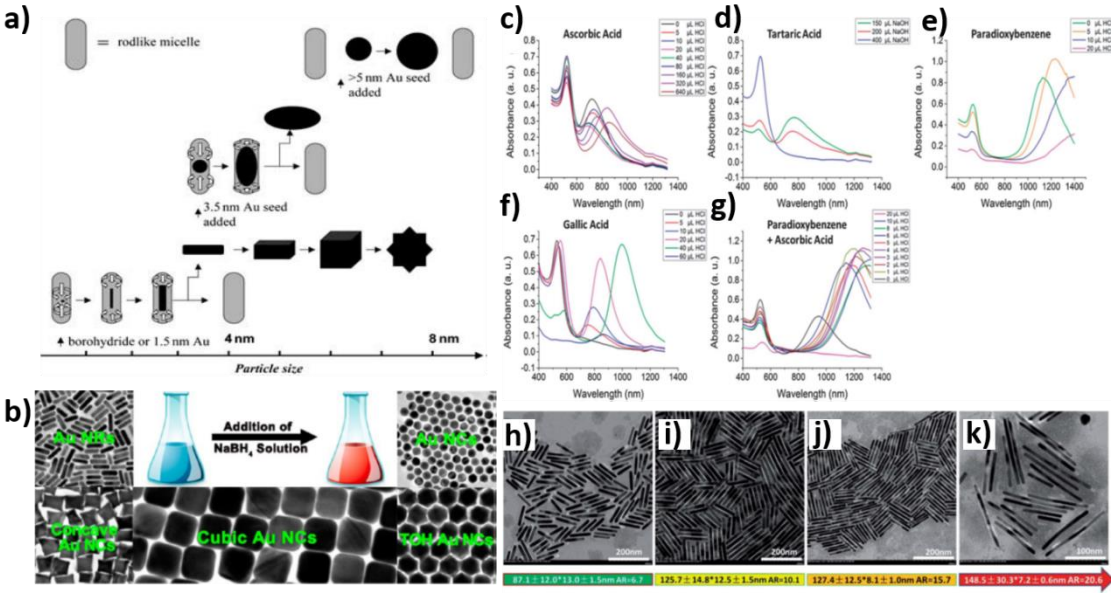

Figure 2. 7 a) Proposed micelle template mechanism showing the origin of various shapes at different stages of symmetry breaking. b) Seedless synthesis of AuNPs with various shapes. c-g) UV-Vis-NIR spectra of AuNRs synthesized by a seedless method using different reducing agents: c) 0.8 mM ascorbic acid; d) 2.5 mM tartaric acid; e) 2.5 mM paradioxybenzene (HQ); f) 2.5 mM gallic acid, g) 2.5 mM paradioxybenzene and 0.1 mM ascorbic acid. h-k) TEM images of AuNRs synthesized by the seedless method using paradioxybenzene as reducing agent with different amount of HCl solution (1.19 M) added: h) 0 µL; i) 5 µL; j) 10 µL; k) 20 µL. a) Reproduced with permission from [185]. Copyright (2005) WILEY. b) Reproduced with permission from [184]. Copyright (2014) American Chemical Society. c-k) Reproduced with permission from [183]. Copyright (2013) Royal Society of Chemistry.

In situ seed formation, or "seedless" growth was initially reported by Jana *et al.* in 2001.[185] They were able to control ~~of~~ the size and shape of AuNRs via adjusting the

nucleation rate through varying the molar-ratio of strong ($NaBH_4$) and weak (AA) reducing agents.[185] However, the limitation of this method was the formation of a significant amount of impurities. They proposed a micelle template mechanism to explain the origin of various shapes of nanoparticles, in which the final shape of the nanoparticle strongly depends on the size of the embryo that undergoes symmetry breaking (Figure 2. 7a). The proposed mechanism also explains the importance of a delicate balance in the nucleation and growth rates in producing anisotropic nanoparticle as the final product. For example, if the nucleation rate is too high, the NP stops growth before symmetry breaking, and the resulting particles are small (<5 nm) and spherical. If the growth rate is too slow, either the NP does not grow along the guiding of the template or AuNRs produced by the template mechanism further grow two or three dimensions and eventually lose their anisotropy. Therefore, they concluded that the intermediate and optimum nucleation-growth rate is essential for an effective template mechanism.

In 2012, El-Sayed group regulated the nucleation-growth process by lowering the reducibility of both $NaBH_4$ and AA through decreasing the pH (< 2) of the growth solution, thus slowing down the growth of AuNRs and improving the monodispersity.[186] In 2014, Tao group reported the seedless synthesis of high-quality AuNPs with various shapes including quasi-spherical, rod-like, cubic, concave cubic, and trisoctahedral by adjusting the composition of growth solutions that mainly composed of $HAuCl_4$, ascorbic acid, and surfactants (Figure 2. 7b).[184] They also found that upon $NaBH_4$ addition, the stirring time of the reaction mixture before aging is crucial for the quality and yield of AuNPs, which should be properly prolonged to produce high-quality NPs. After the stirring time was optimized in the range of 25~30 s, the sizes and structural features of as-prepared AuNPs can be easily regulated by the composition of the reaction mixtures and the concentrations of various reactants, mainly $NaBH_4$. In 2014, Liang group reported the seedless synthesis of high aspect ratios AuNRs by using different reducing agent together with the adjustment of pH (Figure 2. 7c-g).[183] As the reducers they used were more active when the pH value was high, a small amount of HCl or NaOH was added to adjust the growth kinetics to the proper points. Taking the gallic acid as an example (Figure 2. 7f), when the amount of added

HCl increases from 0 μL to 40 μL, the intensity ratio of longitudinal to transverse LSPR increases, indicating a relative mild growth kinetics favo~~u~~rs the formation of anisotropic AuNRs. Figure 2. 7h-k shows that as the pH was reduced, the produced AuNRs became longer (from 87.1 nm to 148.5 nm) and thinner (from 13.0 nm to 7.2 nm) and the aspect ratio increased from 6.7 to 20.6. Their work indicates that no matter whether the seedless method or the seed-mediated method was employed, appropriate growth kinetics is~~are~~ always the prerequisite for the synthesis of uniform AuNRs.

2.1.4 Photochemical Methods

One other common synthetic method is the photochemical reduction, the earliest method used to form colloidal AuNRs.[187] In this method, $HAuCl_4$ is bound to rod-like cationic micelle surfactants to form ion pairs and then excited by UV light to reduce metal ions to form metals via electron transfer from metal ions to ligands.[188-191] The surfactant micelle stabilizes a specific crystal face, as in the seed-growth methods, thereby leading to the formation of rod-like structures.[188-191] The addition of NaCl electrolyte increases the yield and aspect ratio of the AuNRs through the modification of the micellar size and particle crystallization process.[189] Similar to the role in seed-mediated methods, the presence of Ag^+ ions greatly improves the yield of rod-shape NPs and uniformity as well as efficiently adjusts the aspect ratio of AuNRs (Figure 2. 8a-d).[188] It was found possible to produce longer AuNRs with narrower size distributions by applying a 300 nm UV light source from a 245 nm one, and this also accelerates the growth of AuNRs.[190] In addition, the necessary reaction time can be reduced to less than 30 minutes by combining the chemical and photochemical techniques (Figure 2. 8e).[192-193] Figure 2. 8f-i shows that the only few minutes of photoreaction is required for the formation of uniform AuNRs (Figure 2. 8g). The cylindrical particles with bulged ends (Figure 2. 8h) may be one of the transient states of reshaping from the cylindrical particles to the round-corner particles (Figure 2. 8i), which might be obtained by the realignment of gold atoms induced by UV-irradiation. The involved mechanism was also investigated: Au(III~~I~~) is first reduced to the Au(I) by AA, and the nucleation is subsequently induced by UV irradiation of acetone additive while further growth occurs in the dark (Figure 2. 8j).[192-193] Interestingly, the

AA concentration can be adjusted between 0.75 to 6.2 times the $HAuCl_4$ concentration,[191] which is not possible in the standard seed-mediated synthesis.

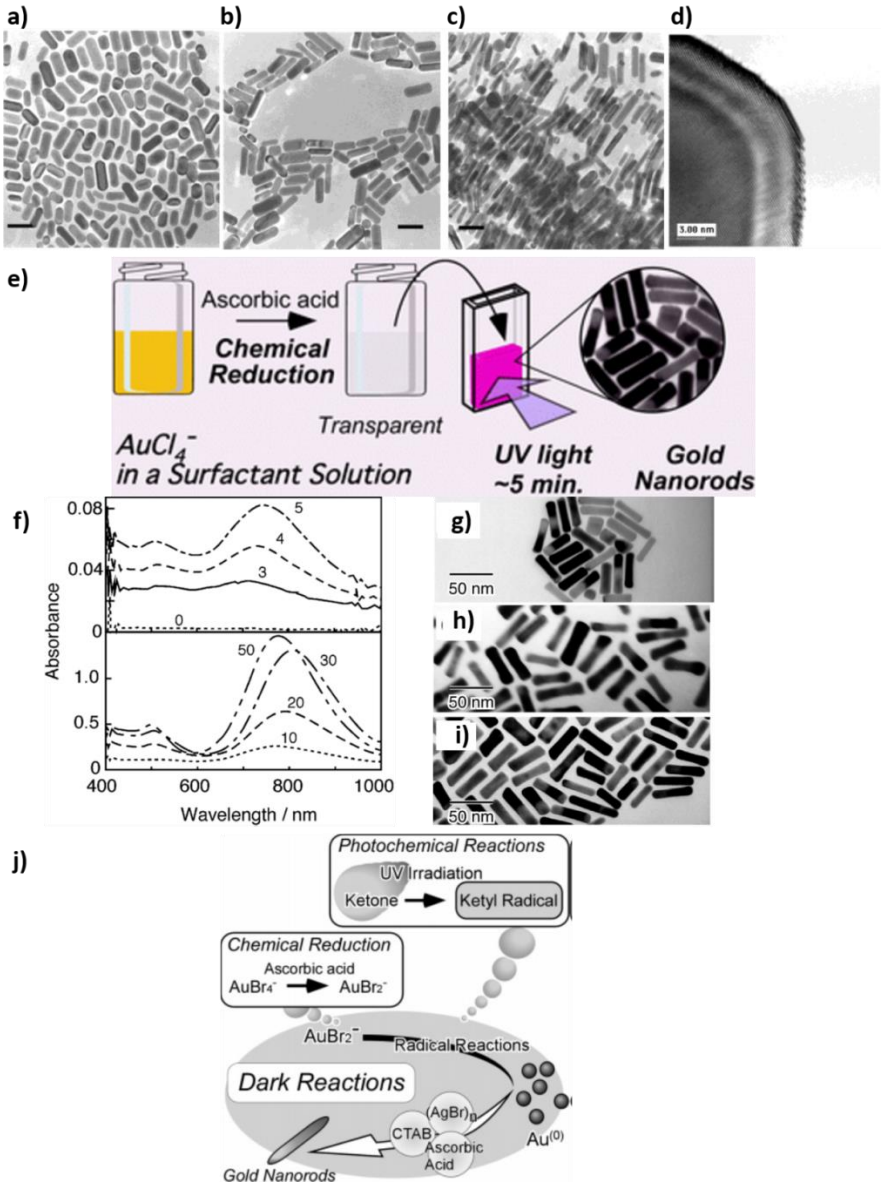

Figure 2. 8. a-d) TEM and HRTEM images of AuNRs synthesized by a photochemical method with: a) 15.8 µL; b) 23.7 µL; (c) 31.5 µL of $AgNO_3$ solution. The bar indicates 50 nm. e) Schematic illustration of the synthesis of AuNRs by the combination of chemical reduction and photoirradiation processes. f) Effects of UV-irradiation times on the absorption spectral changes of the reaction solution after the addition of AA with 200 mL of the silver nitrate solution. Numbers beside the curves show the irradiation times. g-i) TEM images of AuNRs obtained from the UV-irradiation of the reaction

solution (in Panel f) with different irradiation times: g) 5; h) 30; i) 50 min. a-d) Reproduced with permission from [188]. Copyright (2002) American Chemical Society. e-i) Reproduced with permission from [192]. Copyright (2003) Royal Society of Chemistry. j) Reproduced with permission from [193]. Copyright (2007) American Chemical Society.

2.1.5 Templated Methods

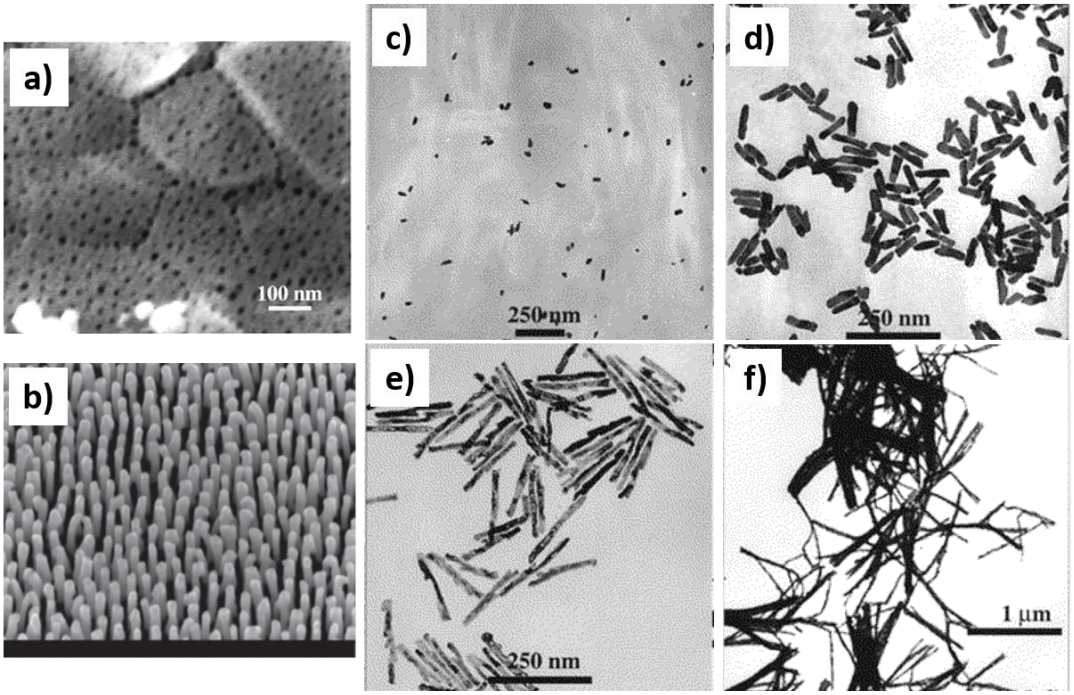

Figure 2. 9. a) FEG-SEM image of the alumin~~i~~a membrane template. b) SEM image of free-standing array of AuNRs after the dissolution of alumina template. c-f) TEM images of released AuNRs synthesized by template method. a~~,~~ c-f) Reproduced with permission from [194]. Copyright (2000) American Chemical Society. b) Reproduced with permission from [195]. Copyright (2011) Nature Publishing Group.

In order to obtain elongated AuNRs, it is also possible to utilize "harder" templates out of various materials that possess rod-shaped openings (Figure 2. 9a). Template methods involve the use of nanoporous track-etched polycarbonate or an anodized alumina membrane as the template where Au atoms are electrochemically deposited from an Au ion precursor in an electrochemical cell.[24-25, 194, 196-199] The subsequent chemical

etching helps to release the nanorods from the template and disperse them into the solvent for subsequent applications (Figure 2. 9b-f). The width of the nanorods is equivalent to the diameter of the membrane template, make it fairly controllable. The length can be controlled by adjusting the amount of the Au deposited and thus the aspect ratio can be tuned accordingly. However, the length control is more difficult to achieve due to the variation in the plating current efficiency.[200] Therefore, the resulted polydispersity in the sample together with the polycrystalline causes broadening of the longitudinal LSPR. Another disadvantage of this method lies in the limited amount of material that can be synthesized at one time as well as the scalability of the technique, because the rod growth is limited to a two-dimensional area of a membrane rather than taking place in a three-dimensional volume as in the wet-chemical synthesis.[201] The apparent advantage of this method is the ease of surface modification due to the completely bare surface, which makes them particularly attractive for some applications compared to wet-chemically synthesized rods that have relatively strongly bound CTAB.[201]

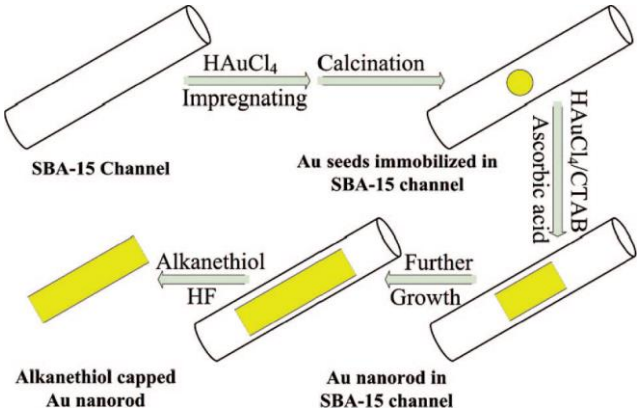

Figure 2. 10. The synthesis scheme of in situ growth of AuNRs in the channels of mesoporous silica (SBA-15). Reproduced with permission from [202]. Copyright (2008) American Chemical Society.

Recently, mesoporous silica has been utilized as templates for synthesizing anisotropic metal NPs.[202-204] For example, an amine-modified SBA-15 is impregnated with Au seeds via calcination and rods are further grown under conditions modified from the wet-chemical growth of rods including CTAB, $AgNO_3$, etc. (Figure 2. 10).[202]

The synthesized AuNRs have a diameter about 6~7 nm and tunable aspect ratios from 3 to 30 with single crystalline structure. Further, the silica template can be etched by HF to free the rods. Recently, Yin group reported a promising synthetic strategy that used silica nanotubes as the template for Au (or Ag, Pt, and Pd) rod growth.[204] The controlled growth of the metals occurs exclusively on the seeds (reduced by $NaBH_4$) inside the silica nanotubes, which act as hard templates to confine the one-dimensional growth of the metal nanorods and define their aspect ratios. The silica templates, produced by coating uniform nickel-hydrazine rod-like nanocrystals with a layer of silica and subsequent remove of the nickel-hydrazine templates,[205] can be synthesized in gram scale, which makes it possible to produce AuNRs in large scale. The wide applicability of this method to the synthesis of noble metal nanorods of various compositions, which were previously difficult to fabricate with high quality and in large quantity, opens up great opportunities for discovering new properties and designing novel materials for diverse future applications.[204]

2.1.6 Other Methods

Several other techniques have been developed including ultrasonication,[206] bioreduction,[207] photo beam irradiation,[208] γ–irradiation,[209-210] microwave reduction,[211] and solvothermal reduction etc.[212] In addition, electron beam lithography (EBL), a lithographic technique commonly used in the generation of metallic nanostructures, has also been reported for the fabrication of AuNRs.[213-214] Xia and co-workers have reported the synthesis of AuNRs in an organic environment.[215] Their method involves the room-temperature aging of a mixture of the AuCl(oleylamine) complex with amorphous Fe nanoparticles in chloroform. After ageing, single crystalline AuNRs with a uniform diameter of 2 nm and an average aspect ratio of 30 were obtained. The rods grow along the <111> direction, which might be guided by oleylamine. The above methods constitute good supplements to the fabrication of AuNRs although with less popularity.

2.2 Surface Modification of AuNRs

As is the case for most NPs, the synthesis of AuNRs is often not, by itself, enough to make them useful for most applications. The nanorod surface must first be functionalized with the proper organic or inorganic material to grant stability under the necessary conditions as well as to provide added functionality. In general, the functionalization of AuNRs can be significantly more challenging than the functionalization of AuNSs, even through the well-known gold-thiol chemistry, due to the unique surfactant capping of as-synthesized nanorods. Different from AuNSs that can be directly thiol-functionalized during the synthesis or coated only with a weakly-bound anion, AuNRs are usually synthesized in the presence CTAB, which binds more strongly to the nanorod surface. As the side facet of AuNRs is~~are~~ densely capped by the CTAB capping molecules through strong Au–N bonds,[114] replacement of this surfactant layer with other ligands such as thiolated chemicals is significantly challenging.[22] So far, numerous strategies have been proposed to tune the surface chemistry of AuNRs and, in general, they can be classified into two main categories: surface coating and ligand exchange.

2.2.1 Surface Coating

A popular method to the covalent functionalization of nanorods was developed by Murphy co-workers, which utilizes layer-by-layer (LBL) deposition of polyelectrolytes directly onto the CTAB bilayer surrounding rods.[216-217] In this technique, alternate layers of anionic and cationic polyelectrolytes are deposited onto AuNRs layer by layer via consecutive electrostatic adsorption to manipulate surface properties. First, a negatively-charged polymer such as polyacrylic acid (PAA) or poly(sodium-4-styrenesulfonate) (PSS) is mixed with positively-charged CTAB-AuNRs, leading to its deposition on the rods and switching the net charge on the rod to negative. This can be followed by a layer of cationic polymers such as poly(diallyldimethylammonium chloride) or poly(allylamine hydrochloride) and the cycle can be repeated multiple times, similar to standard LBL deposition techniques.[218-220] Finally, the coated AuNRs

can be purified by centrifugation or dialysis and are soluble under high salt conditions, in biological media, and even in polar organic solvents.[216, 221-222]

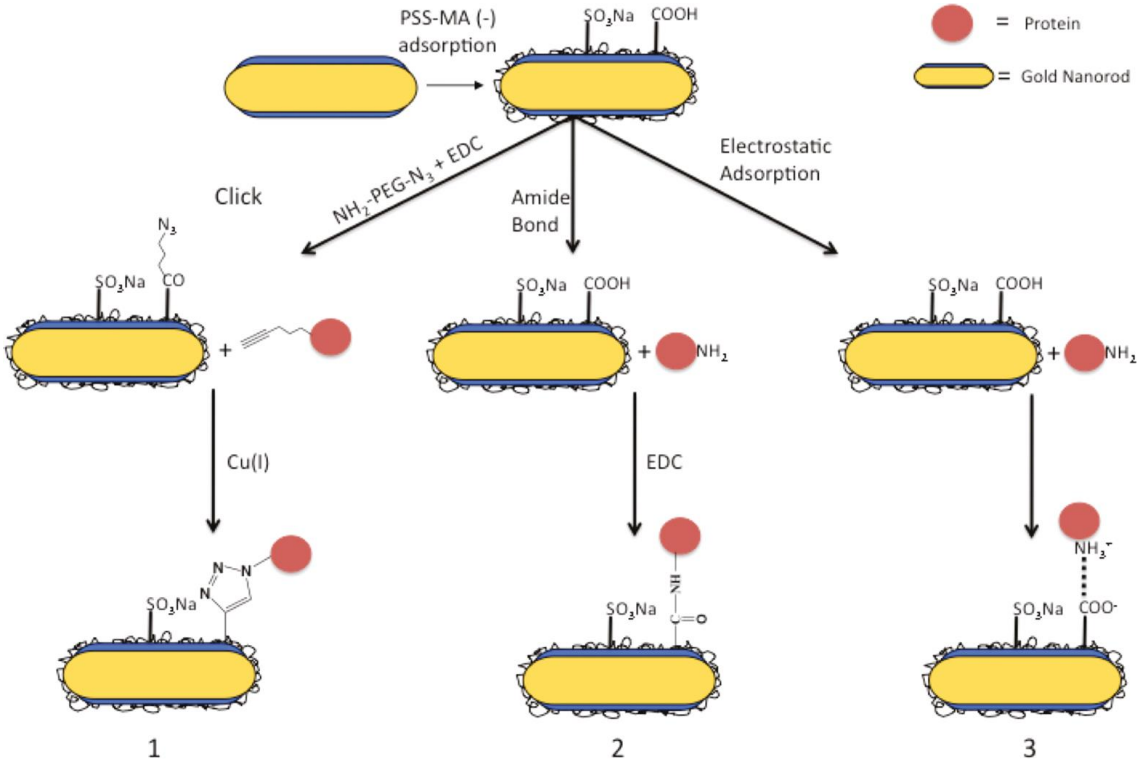

Figure 2. 11. Surface-coating of CTAB-AuNRs with a PSS-maleic acid (MA) copolymer renders the nanorods with a net negative charge at pH 7; the sulfonates maintain charge through subsequent processes, while the carboxylic acid groups may react. Pathway 1: An amine-PEG-azide molecule is conjugated to the carboxylates on the nanorods, using a water-soluble carbodiimide (EDC) to make amide bonds. The terminal amine groups on the protein are modified with a pentynoic acid to yield accessible alkynes on the protein. Finally, the nanorods and protein are clicked together with a Cu(I) catalyst. Pathway 2: The terminal amines on the protein are reacted with the terminal carboxylic acid groups on the nanorods to form amide linkages using EDC chemistry. Pathway 3: At pH 7, nanorods bear a net negative charge from the terminal acid groups, and the protein bears a net positive charge from the terminal amine groups; simple mixing results in electrostatic adsorption. Reproduced with permission from [223]. Copyright (2010) American Chemical Society.

After LBL coating, AuNRs bear charged groups that face the external environment. Functional groups introduced by this technique can include amine and carboxylic acid and further reactions can be carried out to include new functionality, for example, an azide group for "click" chemistry (Figure 2. 11, Pathway 1) or carboxyl group for EDC/NHS coupling reaction (Figure 2. 11, Pathway 2).[223-225] For example, PAA or PSS-Maleic acid (MA) coating renders carboxyl functional groups on the surface of AuNRs and protein or amine-terminated small molecules can be thereafter covalently conjugated to the AuNRs via EDC/NHS coupling reaction.[225] In addition, electrostatic adsorption of proteins directly onto CTAB-AuNRs or LBL-modified rods has also been demonstrated (Figure 2. 11, Pathway 3).[97, 223, 226-227] Murphy group has used fluorescence assays to compare the specific activity of the protein bound on AuNRs using method in Figure 2. 11 Path 1 and 3, and they found that 10~20% of the bound protein retained its specific activity for electrostatic adsorption and amide bond linkages; 57% of protein activity was retained in the case of the click reaction.[224] It's worth mentioning that the click chemistry produces a longer chain length between the protein and the nanorod surface than the other two methods and may improve any steric hindrance associated with the protein performing its reaction on the nanorod.[223] In conclusion, this surface coating functionalization method is ease of operation and fast, but the stability of the coating obtained through electrostatic interaction is questionable for long-term storage or for *in vivo* applications.[22]

2.2.2 Ligand Exchange

Another common strategy for surface modification is to replace the attached CTAB bilayers with thiolated ligands through ligand exchange reactions via strong Au-S covalent bonds. By taking advantage of this strong bonds, desired incoming molecules form a self-assembled monolayer on the AuNR surface, ideally displacing the CTAB bilayer completely. The advantage of this method is its potential to completely remove CTAB, which can greatly reduce the cytotoxicity of AuNRs and increase their biocompatibility. However, as this method involves the removal of the CTAB molecule, the chance of the AuNRs aggregation will also increase due to the loss of protection of CTAB. Successful approaches for ligand exchange on AuNRs can primarily be divided

into three categories: one-pot, phase transfer, and solid-phase ligand exchange. Here, we will briefly review these strategies fortoward ligand exchange on AuNRs together with their advantages and disadvantages related to CTAB removal and direct application in bio-nanotechnology.[94]

2.2.2.1 One-Pot Ligand Exchange

One-pot ligand exchange is the most straightforward approach, carried out by introducing the thiolated ligand into the aqueous AuNRs solution, and leaving the ligand exchange product in the reaction medium. However, direct addition of the thiol ligands to the nanorod surface may not lead to complete functionalization, and functionalization in this case preferentially occurs at the nanorod tips which has been attributed to a less dense CTAB bilayer at the tips compared to the sides of the rods (see **Section 1.2.1**). For example, direct exchange of CTAB with the hydrophobic mercaptoundecanoic acid (MUA) generally leads to irreversible aggregation or only partial exchange.[228] The addition of an ethanolic solution of MUA to rods has been reported.[229] For complete exchange, sonication and heating haves been used to help to take the CTAB off while preventing the nanoparticles from aggregation.[230] Another challenge of this method is the interference of the electrostatic interaction between negatively charged thiolated ligand and positively charged CTAB-AuNRs.

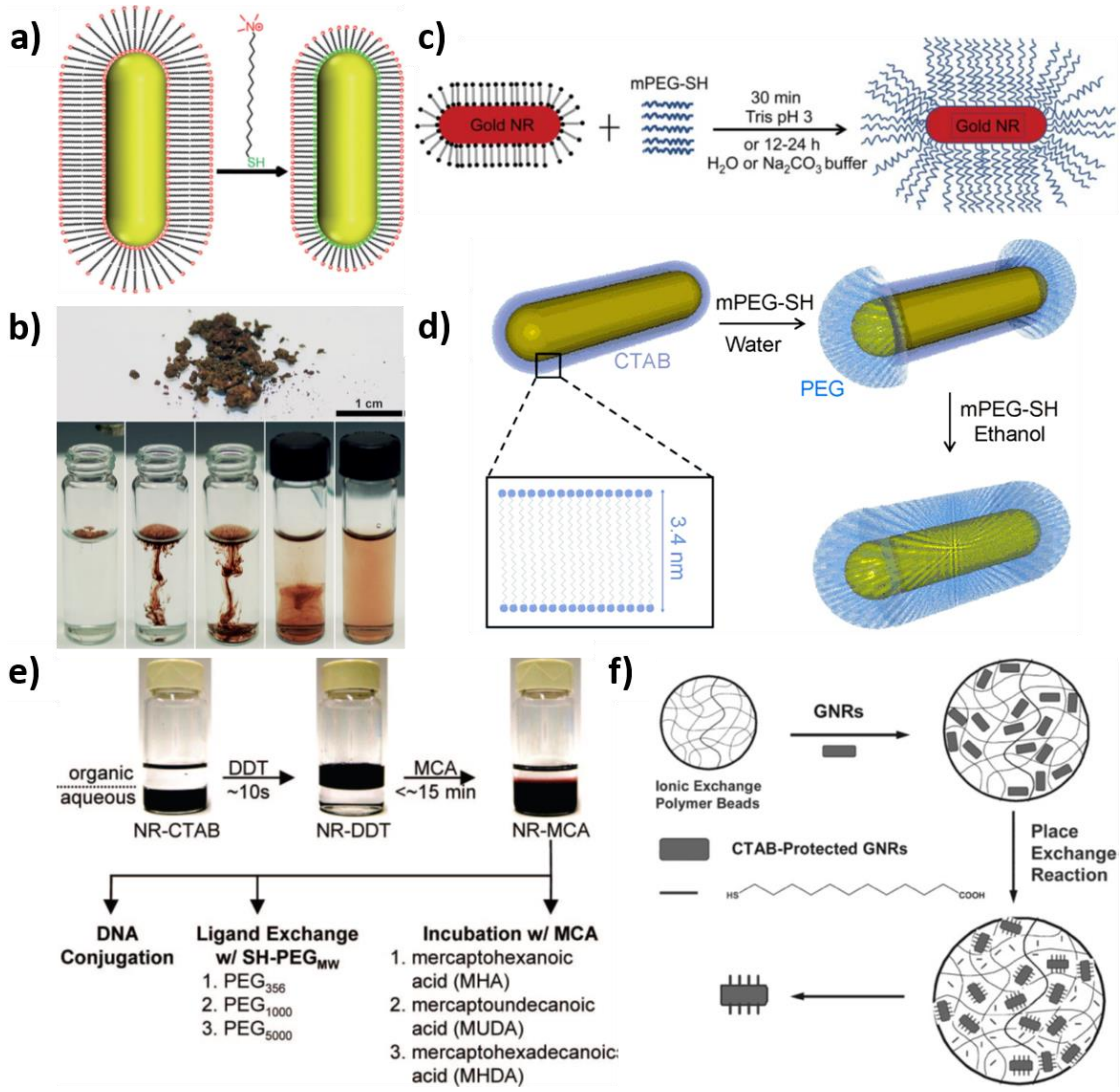

Figure 2. 12. a) Exchange of the CTAB bilayer for the MTAB thiol monolayer using one-pot ligand exchange. b) Top: Photograph of lyophilized powder of MTAB-functionalized AuNRs and Bottom: its spontaneous dissolution in pure water. The images were taken consecutively at~~within~~ intervals of five second. c) Scheme of loading thiolated PEG on AuNRs in different buffers. d) Scheme of loading thiolated PEG on AuNRs using a two-step place exchange with the assistance of ethanol. e) Schematic illustration of round-trip ligand exchange in for AuNRs modification with different ligands. f) Schematic illustration of the surface modification ~~of AuNRs~~ using thiol place exchange reaction inside ionic exchange polymer beads. a, b) Reproduced with permission from [231]. Copyright (2012) WILEY. c) Reproduced with permission from [232]. Copyright (2014) Royal Society of Chemistry. d) Reproduced with permission

from [233]. Copyright (2013) WILEY. e) Reproduced with permission from [234]. Copyright (2008) American Chemical Society. f) Reproduced with permission from [235]. Copyright (2008) Royal Society of Chemistry.

Exchange with cationic molecules is usually less problematic than exchange with anionic molecules as the charge character is more similar to the native CTAB coating. Recently, Vigderman *et al.* reported an effective one-pot ligand exchange using a thiolated CTAB analog~~ue~~, (16-mercaptohexadecyl) trimethylammonium bromide (MTAB) to produce highly stable, functionalized AuNRs (Figure 2. 12a).[231] By simply adding MTAB to a concentrated AuNR solution, and purifying solution phase surfactants after a 48 h incubation, CTAB can be completely removed from the NR surface, as indicated by ^{1}H NMR spectroscopy. The MTAB-AuNRs showed a highly increased stability to multiple rounds of purification compared to CTAB-AuNRs. In addition, the MTAB-AuNRs powder, obtained by treating the aqueous solution with lyophilization technique, rapidly dissolves as manifested by the concentration swirls and a continuous diffusion of the colo~~u~~red solute (Figure 2. 12b). MTAB-AuNRs were also found to be nontoxic, and can readily be taken up by mammalian cancer cells *in vitro* in very large amounts, thus indicating that MTAB-AuNRs can be leveraged as a platform for subsequent bio-applications.

In the surface modification, small molecules are usually not preferred because the steric effect introduced by small molecules cannot overcome the large attractive force among AuNRs.[21] Therefore, the bonding of small thiol molecules often leads to poor dispersibility and irreversible aggregation of AuNRs. Surface functionalization with large thiol-terminated polymers with high molecular weights, such as PEGs, is often used to impart a high degree of anti-fouling ability, colloidal stability, and biocompatibility.[228, 232-233, 236-238] Liao et al. developed a standard procedure for AuNR PEGylation via a one-step ligand exchange reaction (referred to as the Liao method).[237] This reaction can be significantly accelerated in the presence of tris-buffer with pH of 3 (Figure 2. 12c).[232] The main drawback of this one-step PEGylation method is that only the more weakly bound CTAB molecules at the tips are displaced with thiolated PEG, producing partially functionalized AuNRs.[230] To achieve higher PEGylation efficiency,

Kinnear et al. recently established a two-step ligand exchange method that takes advantage of ethanol to desorb the CTAB from the sides of the partially modified AuNRs followed by another PEGylation step (referred to as the Kinnear method, Figure 2. 12d).[233] The authors claimed that this method enables the complete functionalization of AuNRs with thiolated PEG. However, a small quantity of CTAB was still observed on the AuNRs as indicated by ^{1}H NMR.[233] This may still cause cytotoxicity at an elevated AuNR concentration required for high cellular uptake of AuNRs.[159, 163]

2.2.2.2 Phase Transfer

As most thiol molecules are not water-soluble, the use of organic solvents (such as ethanol and chloroform) and phase transfer can greatly facilitate the surface modification of hydrophobic ligands. In a typical phase transfer reaction, a hydrophobic ligand dispersed in an organic solvent is introduced into an aqueous CTAB-AuNR solution. As before, solvents known for increasing CTAB's CMC are employed to facilitate ligand exchange, and, upon successful grafting of the AuNR surface, the AuNRs undergo immediate precipitation from solution, where they can be subsequently dispersed in organic solvents.[94] However, despite the broad application of this method, hydrophobic AuNRs, which are able to disperse in organic solvents are not directly applicable in biological systems, and would require subsequent functionalization to render them solubility in aqueous solvents.[94] In addition, when enough hydrophobic polymer bounds to the AuNR surface, the AuNRs will precipitate, and likely terminate the ligand exchange reaction prematurely. Therefore, the efficiency of phase transfer-induced ligand exchange in CTAB removal is questioned. Gentili *et al.* performed successful phase transfer by introduced ethanolic solutions of ethyl-11-mercaptoundecanoate to AuNRs extracted from water into chloroform, evidencing that very little residual CTAB remained, falling below the detection limits of ^{1}H NMR and XPS.[229]

In 2008, Wijaya and co-workers developed an efficient procedure based on aqueous-organic-aqueous phase transfer to produce AuNRs viable for biological applications through what is more commonly known as round-trip ligand exchange.[234] In this method, highly concentrated CTAB-AuNRs (~10^{-8} M) are first transferred into a highly-

concentrated dodecanethiolacetone solution (DDT) in the presence of acetone, centrifuged to remove excess thiol, and then heated in the presence of a variety of mercaptocarboxylic acids (C_6, C_{11}, and C_{16}) until aggregation occurs, after which the rods become soluble in aqueous environment (Figure 2. 12e). The possibility of further "customization" of the surface via the further addition of a variety of thiolated compounds such as more acid, PEG, or DNA could make this technique useful for a variety of biomedical applications.

2.2.2.3 Solid-Phase Ligand Exchange

As phase transfer places challenges for the modification of AuNRs with hydrophobic ligands due to the aggregation in organic solvents. A smart way to perform ligand exchange was reported by Dai *et al.* who conducted the reaction inside an ion-exchange resin to prevent the irreversible aggregation of AuNRs (Figure 2. 12f).[235] Specifically, the anionic ion exchange resin Amberlite IRA-67 were firstly loaded with AuNRs via capillary force and then incubated in an 11-mercaptoundecanoic acids (MUDA) chloroform solution. The ligand exchange reaction took place inside the polymer beads, and the thiolated nanorods diffused out of beads into the chloroform solution after a sufficient degree of ligand exchange. The chloroform was dried and the nanorods could be dissolved in aqueous or organic solvents. X-ray photoelectron spectroscopy (XPS) was performed to characterize the surface components of AuNRs after ligand exchange, which indicates that the residual CTAB concentration was negligible.[235] Solid-phase exchange gains advantage in preventing aggregation of particles during functionalization, but the versatility of this procedure in fabricating water-soluble ligand exchange products needs to be further demonstrated.

2.3 AuNPs in Photocatalysis

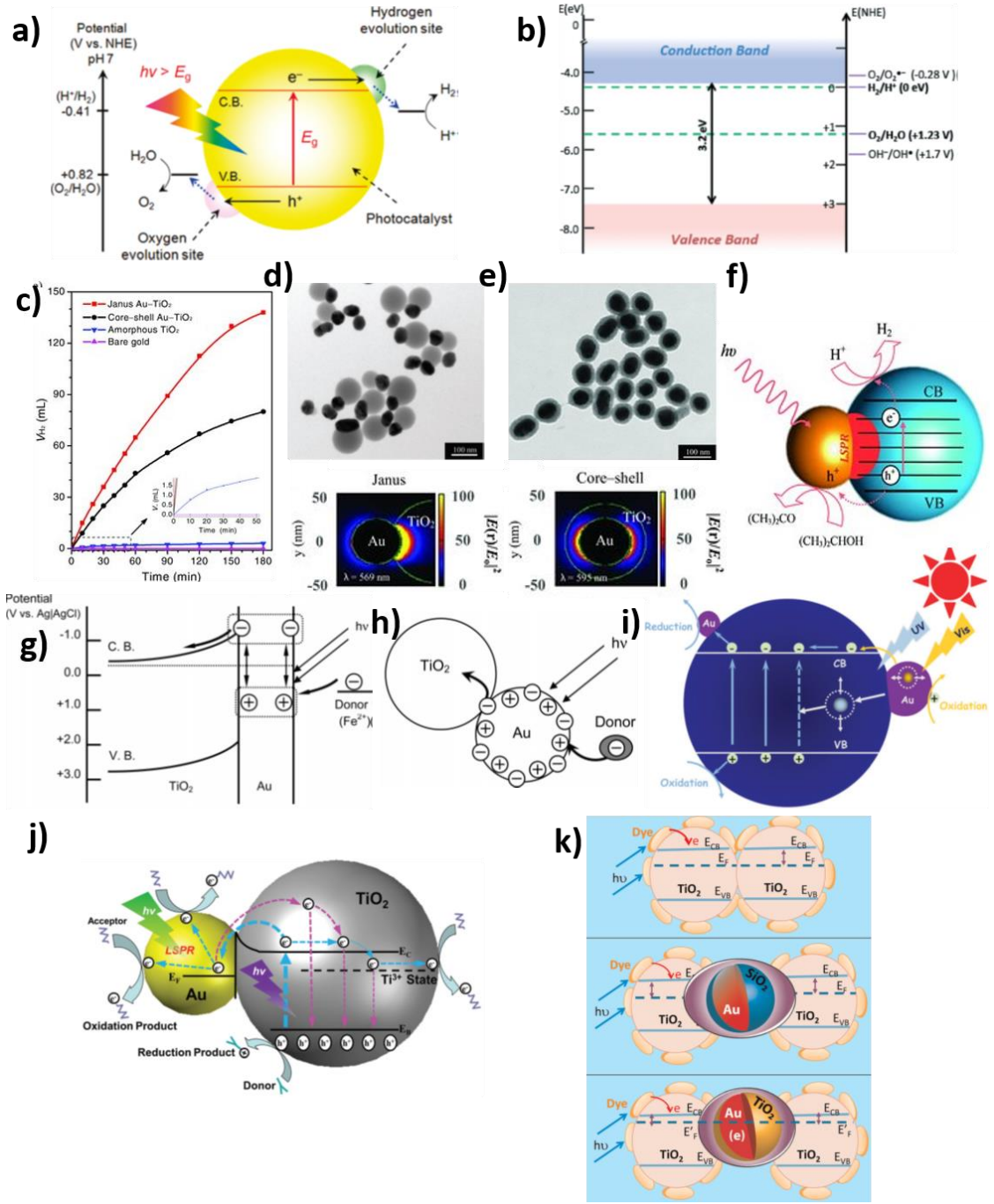

Figure 2. 13. a) Schematic energy diagrams of photocatalytic water splitting of TiO_2. b) Schematic representation of the position of CB and VB of TiO_2 and the redox potentials vs. NHE at pH 0. c) Volume of hydrogen generated (V_{H2}) under visible-light irradiation using Janus and core-shell $Au_{50\ nm}$-TiO_2 nanostructures, as well as amorphous TiO_2 and

bare AuNSs (50 nm). d) TEM images of Janus $Au_{50\ nm}$-TiO_2 nanostructures and plasmonic near-field maps (cross-section view at z = 0) simulated using DDA. e) TEM images of core-shell $Au_{50\ nm}$-TiO_2 nanostructures and plasmonic near-field maps (cross-section view at z = 0) simulated using DDA. f) Proposed photocatalytic process for efficient H_2 generation using the Janus Au-TiO2 nanostructures, based on excitation of the LSPR under visible-light irradiation. g, h) Proposed mechanism for the photoelectrochemistry. Charges are separated at a visible-light-irradiated AuNSs-TiO_2 system. i) Promotion effects of AuNSs on the photocatalytic activity of TiO_2 under UV-visible light irradiation. j) The entire mechanism of the effects of LSPR on the photocatalytic activity of Au/TiO_2 under UV-vis light irradiation. k) Electron equilibration and its influence on the apparent Fermi level (E_F): (Top) dye-TiO_2 (Middle) dye-TiO_2/Au@-SiO_2, and (Bottom) dye-TiO_2/Au@TiO_2. Note that LSPR influence is seen in both (Middle) and (Bottom), and shift in Fermi level as a result of electron accumulation in the metal core is seen in only (Bottom). a) Reproduced with permission from [239]. Copyright (2010) American Chemical Society. b) Reproduced with permission from [240]. Copyright (2015) Royal Society of Chemistry. c-f) Reproduced with permission from [241]. Copyright (2012) WILEY. g, h) Reproduced with permission from [242]. Copyright (2005) American Chemical Society. i) Reproduced with permission from [243]. Copyright (2013) Royal Society of Chemistry. j) Reproduced with permission from [244]. Copyright (2015) Royal Society of Chemistry. k) Reproduced with permission from [245]. Copyright (2012) American Chemical Society.

Semiconductor NPs have been widely explored and applied in solar cells,[246-248] water splitting,[239-240] artificial photosynthesis,[249-251] and degradation of environmental pollutants.[252-253] As the most promising and extensively studied semiconductor catalyst, TiO_2 have been attracting tremendous attention ever since its extraordinary photocatalytic activity was discovered by Fujishima and Honda.[254] TiO_2 is only sensitive to UV-light, which accounts for ~4% of the total solar light. Under UV-light irradiation, the absorbed photons excite the negatively-charged electrons of TiO_2 from valence band (VB) electrons to the conduction band (CB), leaving behind a positively-charged hole in the VB as shown in the following equation:

$$TiO_2 + hv \rightarrow TiO_2(e^-) + TiO_2(h^+)$$ (Equation 2. 1)

The light utilization efficiency can be drastically reduced due to the unwanted dissipation of energy in form of electron-hole recombination.[255] The excited electrons without recombination participate in the reduction reaction with reactant adsorbed on the TiO_2 surface, while the holes remaining in the VB participate in the oxidation of adsorbed species (Figure 2. 13a). The reduction and oxidation reactions are the basis of photocatalytic H_2 production and photodegradation of organic pollutants, respectively (Figure 2. 13b). For water splitting, the CB level should be more negative than the redox potential of H^+/H_2, while the VB level should be more positive than the redox potential of O_2/H_2O.[256] The holes are able to oxidize H_2O to form O_2 gas (Equation 2.2), while the electrons reduce the H^+ ions to produce H_2 (Equation 2.3) respectively. In the photodegradation of organic compounds, the photoexcited electrons react with dissolved oxygen molecules and produce oxygen peroxide radicals (Equation 2.4), while the holes (h^+) react with OH^- derived from H_2O to form hydroxyl radicals $OH^\cdot$ (Equation 2.5 and 2.6). $O_2^{\cdot -}$ and $OH^\cdot$ are powerful oxidizing agents capable of degrading most pollutants.[257-258] The organic compounds can be photodegraded by the $O_2^{\cdot -}$ and $OH^\cdot$ radicals to CO_2, H_2O, or other mineralization (Equation 2.7).[240]

$$4h^+ + 2H_2O \rightarrow O_2 + 4H^+$$ (Equation 2. 2)

$$2e^- + 2H^+ \rightarrow H_2$$ (Equation 2. 3)

$$e^- + O_2 \rightarrow O_2^{\cdot -}$$ (Equation 2. 4)

$$h^+ + OH^- \rightarrow OH^\cdot$$ (Equation 2. 5)

$$h^+ + H_2O \rightarrow OH^\cdot + H^+$$ (Equation 2. 6)

$$O_2^{\cdot -} \text{ or } OH^\cdot + \text{organic pollutants} \rightarrow \text{degradation products}$$ (Equation 2. 7)

It was found that the H_2 production rate can be significantly boosted upon the addition of alcohol, particularly methanol. The added alcohol acts as a sacrificial agent to suppress the $O_2^{\cdot -}$ induced side reaction by alcohol reforming process. The alcohol is consumed by two different processes: 1) alcohol reformation where holes combine with

the alcohol to give H_2 and CO_2 and 2) O_2 scavenging leading to the formation of H_2O and CO_2.[259-260]

$$CH_3OH + 3/2\,O_2 \rightarrow CO_2 + 2H_2O \qquad \text{(Equation 2. 8)}$$

The amount of O_2 and CO_2 evolved are constant and non-negligible, which indicates that all O_2 produced after water splitting is not scavenged by alcohol. In addition, the presence of O_2 in the exhaust gas suggests that water splitting and holes consumption by water instead of alcohol that ultimately brings about the formation of O_2.[260]

$$H_2O + 2h^+ \rightarrow 2H^+ + O_2 \qquad \text{(Equation 2. 9)}$$

Consequently, the overall H_2 production in the presence of alcohol (take methanol for example) can be represented by the following surface reaction:

$$CH_3OH + H_2O \rightarrow CO_2 + 3H_2 \qquad \text{(Equation 2. 10)}$$

In spite of the advantages of TiO_2 in terms of abundance, chemical and thermal stability, and non-toxicity, pure TiO_2 is still far from being a perfect photocatalyst.[261] This is mainly because the photo-response is limited to UV light region resulting from its large band gap (3.2 eV) and the relative low photocatalytic efficiency owing to fast recombination of photo-generated electron-hole pairs. Many strategies, including doping TiO_2 with metal (e.g. Ag,[262] Au,[68-69] Pt,[263] etc.) or non-metal elements (e.g. N,[264] C,[265] etc.), sensitizing TiO_2 with small band gap quantum dots (e.g. CdS,[249] PbS,[266] etc.) or dyes,[267-269] have been proposed to improve the photocatalytic performance of TiO_2. Among these methods, the integration of AuNPs with TiO_2 has been proved as a promising and viable one.

2.3.1 Photocatalysis in AuNSs/TiO_2 under Visible Light Irradiation

To date, most studies focused on the fabrication of Au/TiO_2 nanocomposites using AuNSs with narrow LSPR band and limited light-harvesting ability.[241, 243-245, 270-274] By coupling semiconductor nanostructures with AuNPs one can observe an enhancement in

their photocatalytic or photovoltaic behaviour. A variety of explanations have been put forward to explain the observed improvement in photo-conversion efficiency including: 1) increased absorption due to surface plasmons and light-trapping effects; 2) improved charge separation as a result of localized electromagnetic field; 3) promoting electron transfer to adsorbed species, and 4) electron storage effects that can drive the Fermi level to more negative potentials.[245, 275]

AuNSs/TiO_2 nanocomposites show photocatalytic activity in both UV-Vis as well as visible light irradiation. Han group developed an electric near-field effect mechanism by comparing the photocatalysis activity of Janus and core-shell AuNSs/TiO_2 nanocomposites (Figure 2. 13c-f).[241] Excitation of the LSPR of AuNSs occurs under visible light irradiation, resulting in the generation of plasmonic near-fields that are strongly localized near the Au-TiO_2 interface (Figure 2. 13d, e). Compared with their symmetric core-shell counterparts, the Janus photocatalysts exhibited a much higher rate of hydrogen generation due to the stronger localization of plasmonic near-fields in the vicinity of the Au-TiO_2 interface on one side of the AuNSs (Figure 2. 13c). In this region, the surface-plasmon excitations excite electron-hole pairs via optical transitions between the localized electronic states in the band gap of the amorphous TiO_2. The presence of gold, being a large electron reservoir, facilitates efficient charge separation by capturing the photo-generated holes, leaving electrons in the TiO_2. The holes will subsequently be quenched by the sacrificial reagent, while the electrons can migrate effectively to the surface of TiO_2, where they will reduce hydrogen ions in the aqueous solution, forming hydrogen gas (Figure 2. 13f).[241, 276] In 2011, Cronin *et al.* used electromagnetic simulations to demonstrate that the increased photocatalytic water splitting of anodic TiO_2 with AuNPs under visible light irradiation resulted from the local electric field enhancement near the TiO_2 surface instead of electron transfer from Au to the CB of TiO_2.[277] Christopher *et al.* explained the enhanced visible activity of Ag/TiO_2 as due to the higher concentration of charge carriers in the semiconductor by plasmon mediated radiative transfer of energy from Ag nanoparticles to TiO_2, no electron flow from Ag to TiO_2 was observed.[278]

Electron transfer from AuNSs to TiO_2 under visible light irradiation is another important phenomenon, although the formation of the Schottky barrier at the metal-semiconductor interface does not favour this electron movement.[260, 279-281] Recent evidence shows that AuNSs might act like a dye molecule in the dye-sensitized solar cell, supporting this electron transfer mechanism.[242] In 2004, Tatsuma group verified that charge separation at the plasmonexcited AuNSs incorporated in TiO_2 and found that the charge separation is accomplished by electron transfer from the excited AuNSs to TiO_2 and that from a donor to the AuNSs (Figure 2. 13g, h). In addition, the Au-TiO_2, as a class of visible-light-sensitive photocatalysts, is potentially applicable to visible-light-induced photocatalytic oxidation of ethanol and methanol and reduction of oxygen.[242] Silva *et al.* investigated the influence of excitation wavelength (UV or Visible Light) on the photocatalytic activity of Au-TiO_2 for the generation of H_2 or O_2 from Water.[270] They found that, using excitation wavelengths corresponding to Au plasmon band, AuNSs can absorb photons and inject electrons into the semiconductor conduction band.[270] Though this photoinduced electron injection into the conduction band of a semiconductor is unusual for a metal, the nanometric size of the AuNSs and the operation of quantum size effects might be responsible for the occurrence of this mechanism.

2.3.2 Photocatalysis in AuNSs/TiO_2 under UV and UV-Vis Light Irradiation

Under UV irradiation, only one side electron transfer (from TiO_2 to Au) is possible, however, in case of UV–Vis a two side (from TiO_2 to Au and Au to TiO_2) electron transfer might happen in Au-TiO_2 photocatalysts. In 2013, Li *et al.* reported the synergetic promotion effects of AuNSs on the photocatalytic activity of TiO_2 under UV-Vis light irradiation (Figure 2. 13i).[243] Figure 2. 13i shows that electrons in large AuNSs are excited by the LSPR (with visible light) and subsequently transfer to the CB of adjacent TiO_2. Additionally, large AuNSs can also enhance the local electric field of adjacent TiO_2 to promote the separation of electron–hole pairs under UV light irradiation. Small AuNSs on TiO_2 can act as efficient co-catalysts and trap the photo-excited electrons from the conduction band of TiO_2. Under UV-visible light irradiation,

triple synergetic promotion effect on the separation of photo-generated electron–hole pairs over TiO_2 by Au deposition with both large and small particles can be achieved.[243] Later in 2015, Hu *et al.* found that when employing UV-Vis mixed light irradiation, both pros and cons exist simultaneously for the role of LSPR in the photocatalytic reaction of Au/TiO_2. Under UV-Vis light irradiation, the LSPR injected hot electrons (from the AuNSs to TiO_2 under green light irradiation) may surmount the Schottky barrier formed between the AuNSs and TiO_2, and flow back into the TiO_2.[244] As a result, these electrons may compensate for and even surpass those transferred from TiO_2 to the AuNSs, thus accelerating the recombination of UV excited electron–hole pairs in TiO_2, which is the negative effect of LSPR (Figure 2. 13j).[244] On the other hand, the Au trapped electrons driven by LSPR in response to the visible light have more opportunities to reach the surfaces of the AuNSs; thus, it becomes easier for the acceptors to capture them, which is the positive effect of LSPR on the photocatalytic performance of Au/TiO_2 (Figure 2. 13j). Regarding the question of which mechanism, and to what extent the above two competitors would dominate the overall photocatalytic reaction, it depends on the intensity ratio of visible to UV light applied to the Au/TiO_2 structure.

As discussed above, the Fermi level of AuNPs (E_F = +0.45V versus NHE at pH 7 for bulk Au) is more positive than the bottom of the CB of TiO_2 (E_{CB} = −0.5V versus NHE at pH 7), which favours the electron transfer from photoexcited TiO_2 to Au. However, the reduction potential of water is −0.41V (NHE at pH 7), and the transferred electrons cannot reduce water until the Fermi level of Au decreases to negative potentials.[282] There are several reports in the literature regarding metal NP storing electrons in its Fermi level and shifting the Fermi level to more negative potentials when they come into contact with a photoexcited semiconductor NP (e.g. TiO_2).[279, 283-288] This kind of electron transfer from semiconductor to metal will not stop until Fermi level equilibration takes place.[282] Choi *et al.* showed that under UV irradiation, Au@TiO_2 core-shell nanoparticles exhibit a blue shift in the surface plasmon resonance band maxima due to the transfer of electrons from TiO_2 to Au core and the Fermi level shift to negative potentials (Figure 2. 13k).[245] Au cannot undergo this kind of the Fermi level shift without taking electrons from a semiconductor.[245]

2.3.3 Photocatalysis in AuNRs/TiO_2

While the huge potential of AuNRs, with broad and intense absorption band ranging from visible to NIR range, has not been fully exploited in the photocatalytic applications. Among the limited reports, AuNRs/TiO_2 nanocomposites have been fabricated in the form of yolk-shell,[80] core-shell,[67, 78, 289] dumbbell-shaped,[68] and so on.[69, 290-292] In most cases, the TiO_2 component is amorphous which is inactive under UV light, thus, limiting the photocatalytic performance of these AuNRs/TiO_2 nanocomposites within Vis and/or NIR range. As anatase is generally considered the most efficient TiO_2 polymorph in photocatalytic reactions,[293] high-temperature calcination (above 450 °C) is usually required for the crystallization.[294] A significant challenge arises when treating anisotropic AuNRs involved nanocomposites for high-temperature calcination as they will transform into the most thermodynamically stable spherical shape at temperatures much lower than the melting point of bulk gold, thus losing their extraordinary optical properties (see **Section 1.1.5.3**).[102] It seems that a compromise has to be made between the crystallization of TiO_2 and the stability of AuNRs. The fabrication of intimate integrated AuNRs/TiO_2 nanocomposites that can fully utilize UV-Vis-NIR light is still highly desired.

2.4 Summary of Literature Review

2.4.1 Summary of AuNRs Synthesis

To date, the seed-mediated method, initiated by Murphy group [26-27] and subsequently modified by El-Sayed group,[28] has been the most successful and widely used method for the synthesis of AuNRs. In this method, colloidal AuNRs were prepared by adding the Au seeds into an Au^{+} growth solution reduced from Au^{3+} by ascorbic acid (AA) in the presence of soft-template (cetyltrimethylammonium bromide (CTAB)). Many modifications to~~on~~ this two-step recipe have been carried out to produce AuNRs with higher monodispersity and improved tunability of the LSPR; they can be classified into two general categories: 1). Regulation of growth kinetics, including adjusting pH,[172, 174, 180] temperature,[295] and using an alternative reducing agent (e.g., hydroquinone (HQ),[178] and dopamine,[181] etc); 2). Modification of the CTAB template using Hofmeister salts,[296] aromatic additives,[144] gemini [177] or binary surfactant [111-112], etc. However, there are several drawbacks associated with the existing seed-mediated methods, such as unsatisfactory reproducibility resulting from the time-dependent stability of the seeds together with many variations involved in multi-step procedure,[183-184] strict requirements on experimental parameters (especially AA and $HAuCl_4$ concentration),[178] and limited LSPR tunability, which make the current seed-mediated methods less desirable. Recently, extensive interest has been shown on a much simpler seedless synthesis technique, where the seeds are generated *in situ* instead of preparing a separate seed solution, to address the ~~s~~ above limitations.[183-186, 297] Jana group initially proposed the non-seeding synthesis scheme to produce AuNRs in a gram-scale.[185] Rough control of the size and shape was achieved by varying the molar ratio of strong ($NaBH_4$) and weak (AA) reducing agents.[185] The main limitation of this method is the formation of a significant amount of spherical impurities. El-Sayed group optimized the synthesis scheme by lowering the reducibility of both $NaBH_4$ and AA through decreasing the pH (< 2) of the growth solution, thus slowing down the growth of AuNRs and improving the monodispersity.[186] However, the monodispersity of AuNRs synthesized from the existing seedless methods is still far comparable with those produced through optimized seed-mediated methods.

2.4.2 Summary of AuNRs Surface Modification

So far, considerable effort has been devoted to the development of surface functionalization strategies aiming at replacing CTAB with more biocompatible surface ligands, such as thiol-terminated polyethylene glycol (HS-PEG),[232-233, 236-238] alkanethiols,[47, 228, 235, 298-299] thiolated CTAB analogues,[231] thiolated glycans[34] and phospholipids.[117, 300] Among these ligands, thiolated PEGs are the most widely used molecules as they provide AuNRs with a high degree of anti-fouling ability, colloidal stability, and biocompatibility in biological media.[228, 232-233, 236-238] Liao et al. developed a standard procedure for AuNR PEGylation via a one-step ligand exchange reaction (referred to as the Liao method).[237] This reaction can be significantly accelerated in the presence of tris-buffer with pH of 3.[232] The main drawback of this one-step PEGylation method is that only the more weakly bound CTAB molecules at the tips are displaced with thiolated PEG, producing partially functionalized AuNRs.[230] To achieve higher PEGylation efficiency, Kinnear et al. recently established a two-step ligand exchange method that takes advantage of ethanol to desorb the CTAB from the sides of the partially modified AuNRs followed by another PEGylation step (referred to as the Kinnear method).[233] The authors claimed that this method enables the complete functionalization of AuNRs with thiolated PEG. However, a small quantity of CTAB was still observed on the AuNRs.[233] This may still cause cytotoxicity at an elevated AuNR concentration required for high cellular uptake of AuNRs.[159, 163]

Despite the above-mentioned advances, there are still several challenges for the surface modification of AuNRs with thiolated PEG. Firstly, the existing methods usually suffer from a low PEGylation efficiency,[232, 237] which can limit the effectiveness of the PEG layer as surface coverage has been shown to be important for the effectiveness of PEG layers.[301] Moreover, they are also quite complicated[233] or experience a serious loss of AuNRs due to the irreversible nanorod aggregation during the purification process.[237]

2.4.3 Summary of AuNPs in Photocatalysis

To date, most studies focused on the fabrication of Au/TiO_2 nanocomposites using gold nanospheres (AuNPs) with narrow SPR band and limited light-harvesting ability.[241, 243-

[245, 270-274] While the huge potential of gold nanorods (AuNRs), with intense absorption band ranging from Vis to NIR range, has not been fully exploited in the photocatalytic applications. Among the limited reports, AuNRs/TiO_2 nanocomposites have been fabricated in the form of yolk-shell,[80] core-shell,[67, 78, 289] dumbbell-shaped nanostructures,[68] and so on.[69, 290-292] In most cases, the amorphous TiO_2 component that is inactive under UV light is applied, thus, limiting the photocatalytic performance of these AuNRs/TiO_2 nanocomposites within Vis and/or NIR range. As anatase is generally considered the most efficient TiO_2 polymorph in photocatalytic reactions,[293] high-temperature calcination (above 450 ℃) is usually required for the crystallization.[294] A significant challenge arises when treating anisotropic AuNRs involved nanocomposites with high-temperature calcination, as they will transform into the most thermodynamically stable spherical shape at temperatures much lower than the melting point of bulk gold, thus losing their extraordinary optical properties.[102] It seems that a compromise has to be made between the crystallization of TiO_2 and the stability of AuNRs. The fabrication of intimate integrated AuNRs/anatase TiO_2 nanocomposites that can fully utilize UV-Vis-NIR light is still strongly desired.

Chapter 3 Seedless Synthesis of AuNRs

As discussed in **Section 2.1**, conventional seed-mediated synthesis is not only limited by the operational complexity and over-sensitivity towards subtle changes of experimental conditions but also suffers from low yield (~15%). Many modifications toon this two-step recipe have been carried out to produce AuNRs with higher monodispersity and improved tunability of the LSPR; they can be classified into two general categories: 1). Regulation of growth kinetics, including adjusting pH,[172, 174, 180] temperature,[295] and using an alternative reducing agent (e.g., hydroquinone (HQ),[178] and dopamine,[181] etc); 2). Modification of the CTAB template using Hofmeister salts,[296] aromatic additives,[144] gemini [177] or binary surfactant [111-112], etc. However, there are several drawbacks associated with the existing seed-mediated methods, such as unsatisfactory reproducibility resulting from the time-dependent stability of the seeds together with many variations involved in multi-step procedure,[183-184] strict requirements on experimental parameters (especially AA and $HAuCl_4$ concentration),[178] and limited LSPR tunability, which make the current seed-mediated methods less desirable.

Recently, extensive interest has been shown on a much simpler seedless synthesis technique, where the seeds are generated *in situ* instead of preparing a separate seed solution, to address the above limitations.[183-186, 297] Jana group initially proposed the non-seeding synthesis scheme to produce AuNRs in a gram-scale.[185] Rough control of the size and shape was achieved by varying the molar ratio of strong ($NaBH_4$) and weak (AA) reducing agents.[185] The main limitation of this method is the formation of a significant amount of spherical impurities. El-Sayed group optimized the synthesis scheme by lowering the reducibility of both $NaBH_4$ and AA through decreasing the pH (< 2) of the growth solution, thus slowing down the growth of AuNRs and improving the monodispersity.[186] However, the monodispersity of AuNRs synthesized from the existing seedless methods is still far comparable with those produced through optimized seed-mediated methods.

In this chapter, we describe a facile, highly reproducible seedless synthesis technique based on synergistic template modification and growth kinetics regulation. Specifically, 5-Bromosalicylic acid (5-BA) is adopted as template regulator, while the use of HQ, a much weaker reducing agent, makes the modified template more effective in inducing the anisotropic growth. The important parameters in the seedless synthesis protocol were also studied in detail, e.g., Au/CTAB ratio, 5-BA/CTAB ratio, HQ concentration, Ag concentration, $NaBH_4$ concentration, and pH value. This work has been published as a journal article in ***Chemistry-A European Journal*** (*Chemistry – A European Journal* **2017,** *23*, 3291-3299), named *"Seedless Synthesis of Monodispersed Gold Nanorods with Remarkably High Yield: Synergistic Effect of Template Modification and Growth Kinetics Regulation"*.[168] The content in this chapter was reproduced with permission from [168]. Copyright (2017) WILEY.

3.1 Experimental Section

3.1.1 Chemicals and Materials

The following chemicals were purchased from Sigma-Aldrich and used as received without further purification: gold (III) chloride trihydrate ($HAuCl_4 \cdot 3H_2O$, ≥99.9%), hexadecyltrimethylammonium bromide (CTAB≥99%), sodium borohydride (≥99%), silver nitrate (≥99%), ascorbic acid (AA≥99.5%), hydroquinone (HQ≥99%), 5-Bromosalicylic acid (5-BA, 90%), hydrochloric acid (32 wt. %). Ultra-pure water (18.2 MΩ•cm) was used for all experiments.

3.1.2 Seedless Synthesis Method

In a typical synthesis procedure, 5 mL CTAB together with certain amounts of 5-BA were first dissolved in warm water (~60 °C) and then cooled to 30 °C. After the addition of a different volume of $AgNO_3$ (4 mM), the mixture was kept undisturbed at 30 °C for 15 min. Then 5 mL $HAuCl_4$ and HCl (32 wt. %) were added to the previous solution and genteelly stirred for 30 min. To this solution, 0.1 M HQ was added, and the orange-yellow color gradually fading to colorless. After that, freshly-prepared $NaBH_4$ (0.25

mM) was added to initiate the reaction. Subsequently, the reactant mixture was stirred for 30 s and left undisturbed at 30 °C for 24 h for AuNR growth. The AuNRs were then purified by two centrifugation cycles (16200 rcf, 30 min) to remove excess CTAB and unreacted products. After purification, the AuNRs were redispersed in ultrapure water. For detailed synthesis, please see the Supporting Information.

For the synthesis of TiO_2 nanorods, $TiCl_3$ solution (200 μL, 12 wt. %) and water (6 mL) were first added into a 10 mL 5-BA/CTAB solution (5-BA/CTAB=0.2, CTAB=50 mM) under ice-bath treatment. $NaHCO_3$ solution (0.93 M, 1.2 mL) was then dropped, followed by gentle stirring for 30 min. Then the products underwent two rounds of centrifugation (5000 rcf, 20 min), and finally dispersed in ultrapure water. The amorphous NPs solution placed in a 20 mL vial was transferred into a 40 mL Teflon-line stainless autoclave, and thermal treated for several hours. After that, the solution was centrifuged (4000 rcf, 10 min) and dispersed in water, this process was repeated for 3 times.

For the synthesis of Ag nanorods, 0.25 mL $AgNO_3$ was added into into a 10 mL 5-BA/CTAB solution (5-BA/CTAB=0.2, CTAB=50 mM). After vigorous stirring for 30 min, a certain amount of HQ (0.1 M) was added ~~in~~to the above solution. Subsequently, NaOH (1 M) was added to adjust the pH of the solution. After the incubation of 30 min, the products underwent two rounds of centrifugation (5000 rcf, 20 min), and finally dispersed in ultrapure water.

In the seed-mediated method, 0.3 mL $NaBH_4$ (10 mM) was added into a solution containing 5 mL $AgNO_3$ (0.5 mM) and 5 mL CTAB solution (0.2 M). The above solution was used as seed solution after incubation at dark for 2 h.

3.1.3 Characterization

UV−vis absorption spectra of the as-prepared AuNRs were recorded by a Shimadzu UV mini 1240 UV−vis spectrophotometer with a 1 cm quartz cell at room temperature. Morphologies and structure of the AuNRs were characterized with SEM (FEI Nova NanoSEM 450 FESEM) and TEM (FEI Tecnai G2 F20 and FEI Tecnai G2 T20).

Inductively Coupled Plasma Optical Emission Spectrometer (ICP-OES) analysis was performed on a SPECTRO ARCOS End-On-Plasma (SPECTRO Analytical Instruments GmbH). The samples were presented to the ICP-OES via a Tyledyne CETAC ASX-520 Autosampler (also from SPECTRO Analytical Instruments GmbH). Specifically, the as-synthesized AuNRs were purified by three rounds of centrifugation to remove excessive CTAB and unreacted Au ions. After the samples were digested with Aqua Regia (HNO_3 : HCl=1 : 3) and stabilized with Mercury, an ICP-OES was used to determine the Au concentration.

3.2 Results and Discussion

3.2.1 Mechanism of Proposed Method

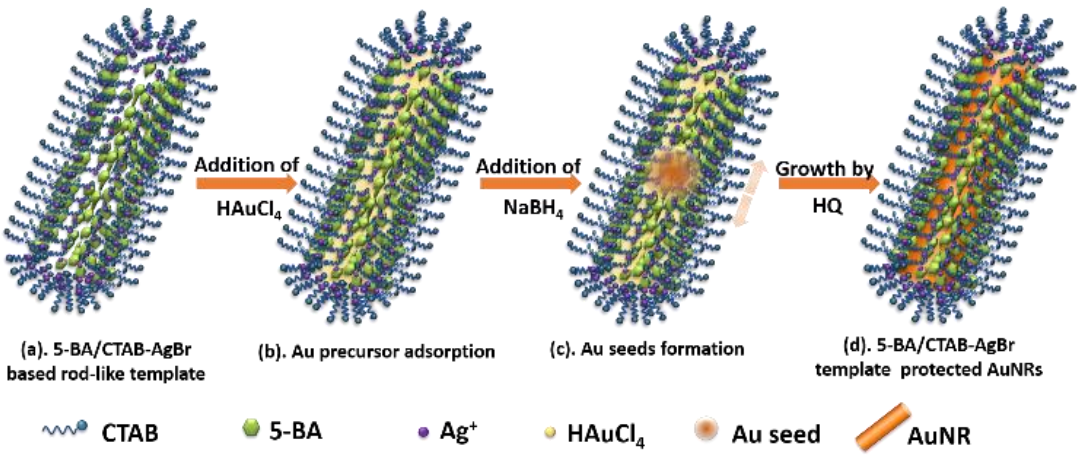

Figure 3. 1. Schematic illustration of the proposed seedless synthesis technique. Note that the chemical components are not shown to scale.

It has been shown that when the concentration is above the second critical micelle concentration (~ 20 mM), CTAB micelles present rod-shaped morphology in the solution.[302] While Ag^+ ions serve as an essential part of the soft-template in inducing the formation of the anisotropic nanostructures by forming CTAB-AgBr complex (Figure 3. 1a).[138, 185, 303] After the addition of $HAuCl_4$, Au ions are adsorbed on the CTAB Stern layer via the formation of ion pairs between cationic CTA^+ and the anionic metal halide complex (Figure 3. 1b).[185, 304] Upon introduction of $NaBH_4$, Au seeds are

generated *in situ* immediately (Figure 3. 1c). The generated Au seeds with CTAB-AgBr complex preferentially adsorbed on specific facets slowly elongate along specific crystal orientation until all Au precursor has been consumed by using a weak reducing agent, i.e., HQ (Figure 3. 1d).[143, 305] In this work, 5-BA additives could intercalate into the CTAB bilayer (Figure 3. 1a), thus significantly influence the packing density of CTAB and adjust the stiffness of the soft-template.[144] The growth kinetics is well controlled by using HQ. Finally, monodispersed AuNRs with high yield are obtained by this elaborately-controlled seedless synthesis process.

3.2.2 High Reproducibility

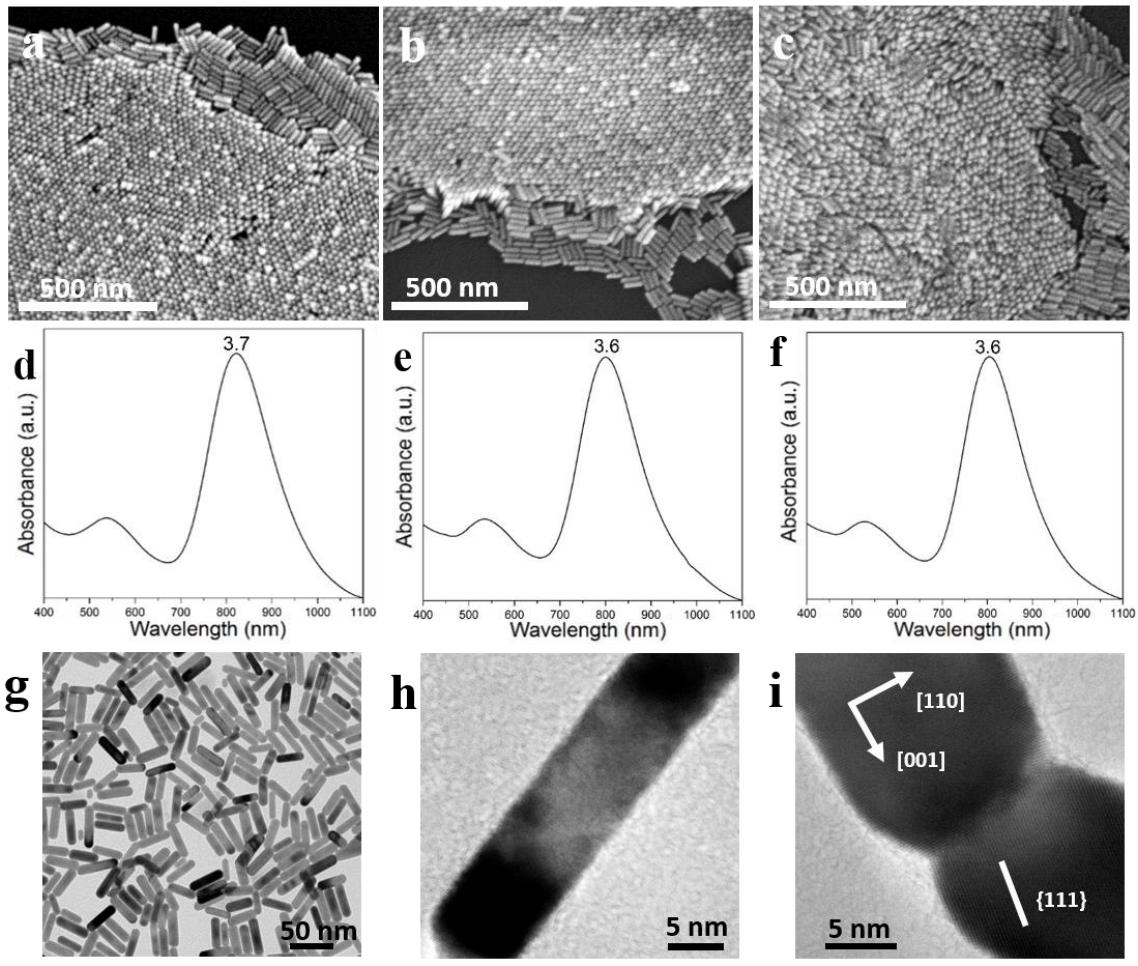

Figure 3. 2. (a-f) SEM images and the corresponding UV-Vis-NIR spectra of three different batches of AuNRs synthesized under the same conditions. (g) TEM image and

(h, i) HRTEM images of the same batch of AuNRs shown in panel (a). The average length and width (in nanometers) of the AuNRs and detailed synthetic conditions are listed in Table 3. 1. Aspect ratios of AuNRs are also provided in panel (d-f).

Number	Average length[b] (nm)	Average width (nm)	LSPR peak position (nm)
a	60 ± 4	15 ± 2	822
b	64 ± 5	18 ± 2	800
c	58 ± 4	13 ± 2	804

Table 3. 1. Synthetic conditions of AuNRs specified in Figure 3. 2. The amount of CTAB (0.1 M), 5-Bromosalicylic acid, $AgNO_3$ (4 mM), $HAuCl_4$ (1 mM), HCl (32 wt. %), hydroquinone (0.1 M) and $NaBH_4$ (0.25 mM) used for AuNR synthesis are 5 mL, 0.0219 g, 300 µL, 5 mL, 8 µL, 300 µL, and 20 µL, respectively. [b]The average length and width (in nanometers) of the AuNRs determined by measuring the dimensions of 200 AuNRs from their SEM images throughout the whole experiment.

Classic seed-mediated methods require strict control over experimental parameters, together with another tough issue, i.e., poor reproducibility resulted from the time-dependent stability of the seeds as well as many variations involved multi-step procedure.[144, 183-184] By applying our proposed seedless method that nucleation is initiated *in situ* to avoid the separate preparation of seed solution and subsequent seeds growth is elaborately regulated by the modified template and mild reducing agent (HQ), the reproducibility is significantly improved. Figure 3. 2 shows that the AuNRs were reproducibly synthesized by using our proposed method, as evidenced by delicate differences in LSPR and dimensions among three different batches of AuNRs. HRTEM images show that these AuNRs are all perfectly face-centered cubic (fcc) single-crystalline with no obvious structural faults and grow along the [001] direction (Figure 3. 2h, i).

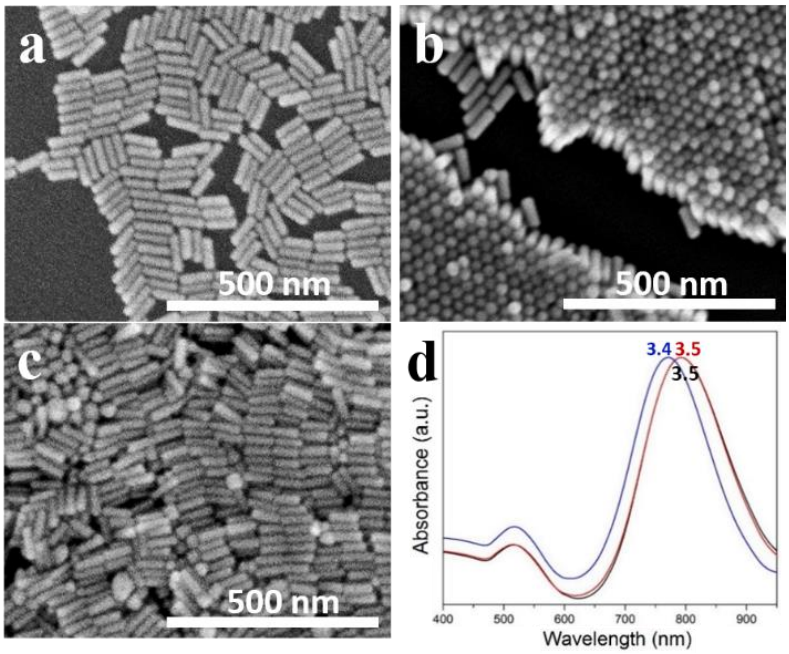

Figure 3. 3. (a−c) SEM images of AuNRs synthesized using a concentration of $NaBH_4$ from 0.2, 0.4 to 0.8 µM from a to c. The average length and width of the AuNRs and detailed synthesis conditions are listed in Table 3. 2. (d) Normalized absorbance spectra of AuNRs shown in a (black curve), b (red curve), and c (blue curve). Aspect ratios of AuNRs are also provided in panel (d).

Number	Concentration of $NaBH_4$ (µM)	Amount of added $NaBH_4$ (0.25 mM) (µL)	Average length (nm)	Average width (nm)	LSPR peak position (nm)
a	0.2	40	48 ± 6	14 ± 2	794
b	0.4	80	45 ± 6	14 ± 2	794
c	0.8	160	37 ± 4	13 ± 1	771

Table 3. 2. Synthetic conditions of AuNRs specified in Figure 3. 3. The amount of CTAB (0.1 M), 5-Bromosalicylic acid, $AgNO_3$ (4 mM), $HAuCl_4$ (1 mM), HCl (32 wt. %), and hydroquinone (0.1 M) used for AuNR synthesis are 5 mL, 0.0219 g, 250 µL, 5 mL, 8 µL, and 300 µL, respectively.

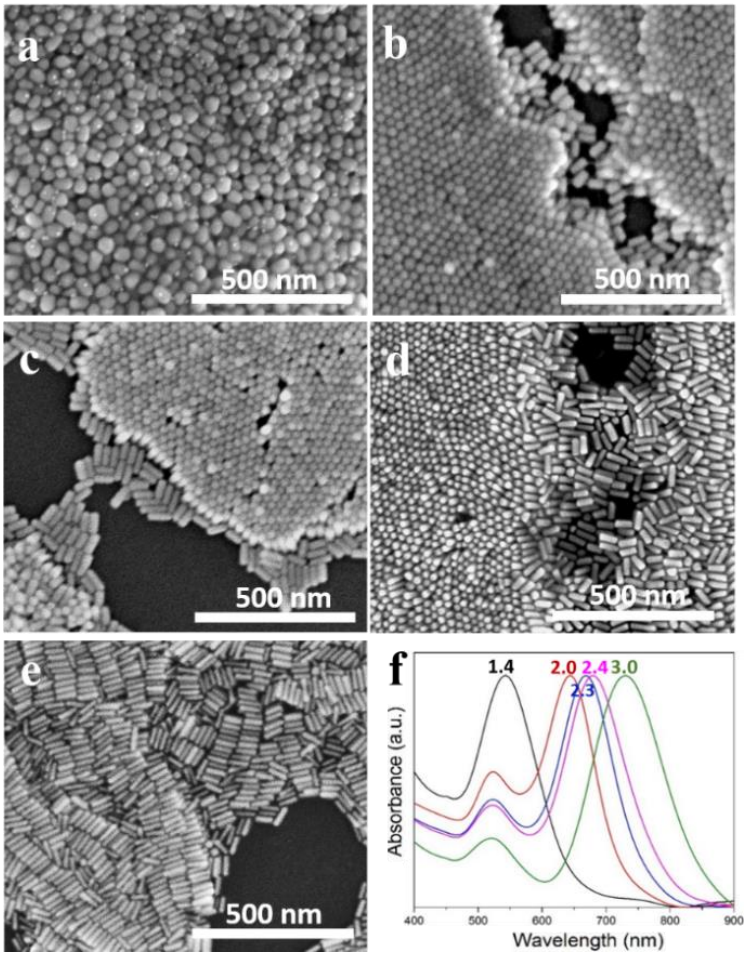

Figure 3. 4. (a−e) SEM images of AuNRs synthesized using increased concentration of hydroquinone from 0.5, 1, 2, 3 to 5 mM. The average length and width of the AuNRs and detailed synthesis conditions are listed in Table 3. 3. (f) Normalized absorbance spectra of AuNRs shown in a (black curve), b (red curve), c (blue curve), d (pink curve), and e (green curve). Aspect ratios of AuNRs are also provided in panel (f).

Number	Concentration of hydroquinone (mM)	Amount of added hydroquinone (0.1 M) (μL)	Average length (nm)	Average width (nm)	LSPR peak position (nm)
a	0.5	50	46 ± 10	32 ± 6	NA
b	1	100	50 ± 5	24 ± 3	644
c	2	200	55 ± 6	23 ± 3	668
d	3	300	63 ± 7	25 ± 3	679
e	5	500	63 ± 7	21 ± 2	730

Table 3. 3. Synthetic conditions of AuNRs specified in Figure 3. 4. The amount of CTAB (0.1 M), 5-Bromosalicylic acid, $AgNO_3$ (4 mM), $HAuCl_4$ (1 mM), HCl (32

wt. %) and $NaBH_4$ (0.25 mM) used for AuNR synthesis are 5 mL, 0.0219 g, 250 µL, 5 mL, 8 µL, and 20 µL, respectively.

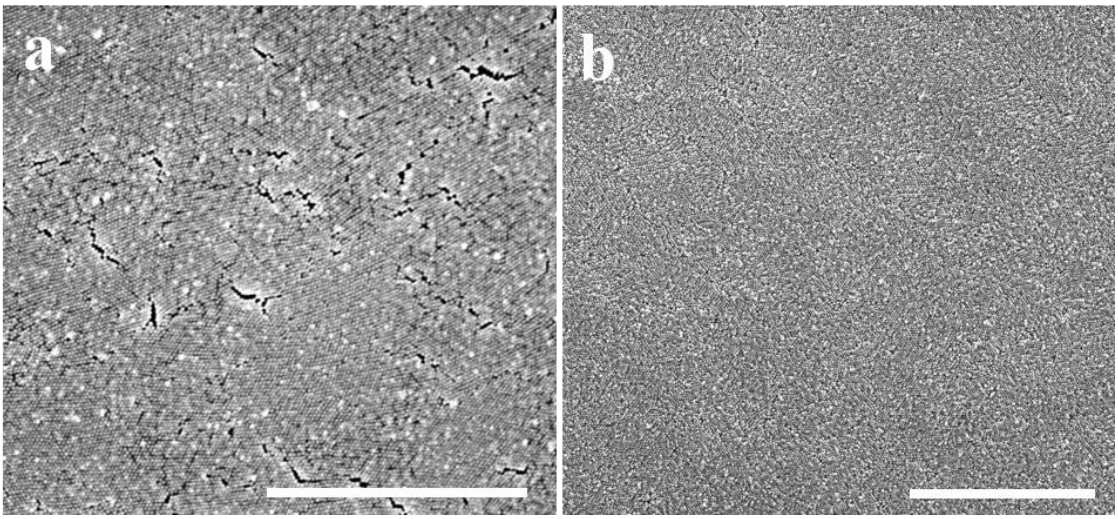

Figure 3. 5. Large-area SEM image of AuNRs synthesized using (a) 2 mM and (b) 5 mM hydroquinone. Detailed synthetic conditions are listed in Table 3. 3. All scale bars represent 2 µm.

Note: HQ undergoes a two-electron, two-proton oxidation process to form benzoquinone.

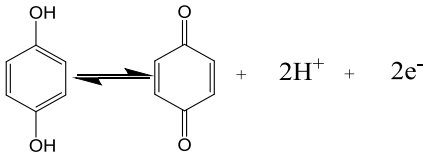

(Equation 3. 1)

The influence of pH on the reduction ability of HQ is important because H^+ are involved in the above process.[306] And it is expected that HQ reacts with AuCl4- ions in the following manner:[306]

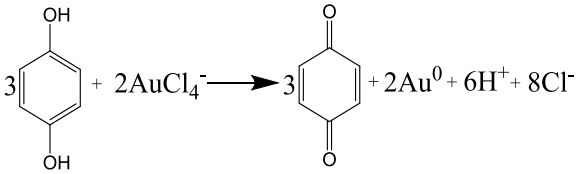

(Equation 3. 2)

For this one-step method, the nucleation process affects the monodispersity and reproducibility. As shown in Figure 3. 3 and Table 3. 2, increasing the concentration of $NaBH_4$ leads to a decrease in the aspect ratio of the AuNRs. At the same time, the LSPR wavelength blue shifts from 794 nm to 771 nm, and the level of shape impurities increases which evidenced from the higher intensity of transverse surface plasmon resonance (TSPR). As expected, when the concentration of $NaBH_4$ is too high, the number of nuclei increases significantly, resulting in smaller AuNRs and more impurities.

3.2.3 Effect of Reducing Agents

Since HQ molecules possess weak reducing ability and offer mild growth kinetics, [178, 306-308] they were used to grow Au seeds into AuNRs. Figure 3. 4 shows the effect of HQ concentration on AuNRs synthesis while keeping all other synthesis parameters identical. As the HQ concentration increases, the overall dimensions (Table 3. 3) and the aspect ratio of the AuNRs increase monotonically, resulting in the redshift of the LSPR band (Figure 3. 4f). When using a low HQ concentration of 0.5 mM (Figure 3. 4a), the spherical or quasi-spherical Au nanoparticles (AuNPs) become the dominant products. This is probably due to the incomplete growth.[178] High-quality AuNRs with high monodispersity are consistently obtained when HQ concentration varies between 1 mM and 5 mM (Figure 3. 4b-e). The large-area ordered AuNRs assemblies (Figure 3. 5) further confirms the high degree of size uniformity and shape purity of synthesized AuNRs. It is interesting to note that altering the HQ concentration becomes an extra strategy for tuning the AuNRs dimensions and optical properties, while this is almost impossible in the classic AA-based synthesis methods. The latter methods are very sensitive to the AA concentration and high-quality AuNRs are available only when AA concentration falls within a very narrow window.[141] To better understand the special role of HQ, AuNRs were also synthesized using our method but using AA instead of HQ as reducing agent. As shown in Figure 3. 6, AuNRs were obtained only at specific AA concentration (0.275 mM, Figure 3. 6), otherwise, the rods changed to dog-bone shape (Figure 3. 7). The formation of dog-bone shape impurities is due to ultra-fast formation and supply of growth units to the Au seeds in the presence of excessive AA,

thereby the seed particles grow regardless of guidance of the template. The above results verify the irreplaceable role of HQ in offering mild growth kinetics for successful synthesis of monodispersed AuNRs.

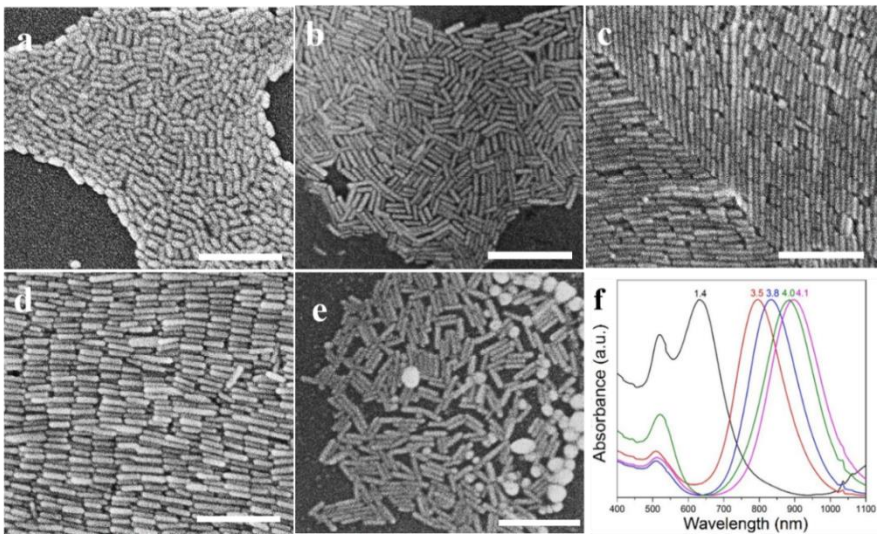

Figure 3. 6. (a−e) SEM images of AuNRs synthesized using 0.275 mM AA under increased concentration of $AgNO_3$ from 0.04, 0.1, 0.12, 0.16 to 0.24 mM from a to e. The average length and width (in nanometers) of the AuNRs and detailed synthetic conditions are listed in Table 3. 3Table 3. 4. Synthetic conditions of AuNRs specified in Figure 3. 6. The amount of CTAB (0.1 mM), 5-Bromosalicylic acid, $HAuCl_4$ (1 mM), HCl (32 wt. %), ascorbic acid (0.0788 M) and $NaBH_4$ (0.25 mM) used for AuNR synthesis are 5 mL, 0.0219 g, 5 mL, 8 µL, 35 µL, and 20 µL, respectively.. All scale bars represent 200 nm. (f) The n~~N~~ormalized absorbance spectrum of AuNRs shown in a (black curve), b (red curve), c (blue curve), d (pink curve), and e (green curve). Aspect ratios of AuNRs are also provided in panel (f).

Number	Concentration of $AgNO_3$ (mM)	Amount of added $AgNO_3$ (4 mM) (µL)	Average length (nm)	Average width (nm)	LSPR peak position (nm)
a	0.04	100	17 ± 5	13 ± 2	632
b	0.1	200	39 ± 5	11 ± 1	795
c	0.12	300	48 ± 5	13 ± 1	834
d	0.16	400	53 ± 5	14 ± 1	896
e	0.24	600	48 ± 8	12 ± 2	883

Table 3. 4. Synthetic conditions of AuNRs specified in Figure 3. 6. The amount of CTAB (0.1 mM), 5-Bromosalicylic acid, $HAuCl_4$ (1 mM), HCl (32 wt. %), ascorbic

acid (0.0788 M) and $NaBH_4$ (0.25 mM) used for AuNR synthesis are 5 mL, 0.0219 g, 5 mL, 8 µL, 35 µL, and 20 µL, respectively.

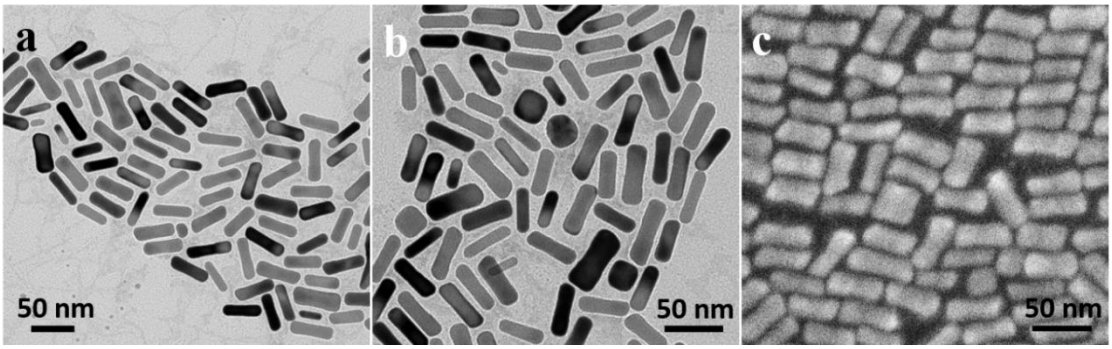

Figure 3. 7. (a−b) TEM images of AuNRs synthesized using different concentration of AA: (a) 0.55 mM, (b) 0.707 mM. (c) SEM images of AuNRs synthesized using 0.707 mM ascorbic acid. ~~The average length and width (in nanometers) of the AuNRs and detailed synthetic conditions are listed in Table 3. 5~~

Number	Ascorbic acid (mM)
a	0.55
b	0.707

~~Table 3. 5. Synthetic conditions of AuNRs specified in Figure 3. 7.~~ The amount of CTAB (0.1 mM), 5-Bromosalicylic acid, $AgNO_3$ (4 mM), $HAuCl_4$ (1 mM), HCl (32 wt. %), and $NaBH_4$ (0.25 mM) used for AuNR synthesis are 5 mL, 0.0219 g, 5 mL, 200 µL, 5 mL, 8 µL, and 20 µL, respectively.

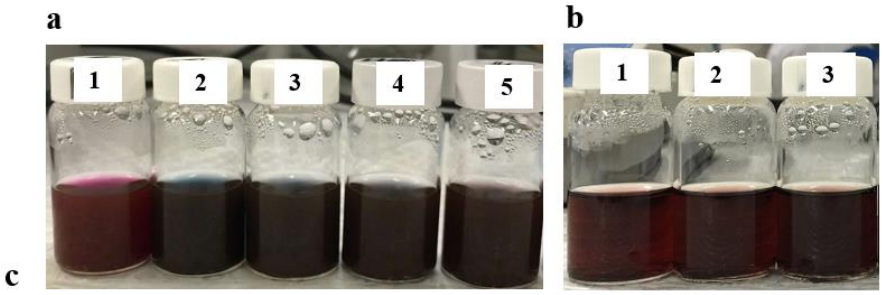

c

Sample number	Type of reducing agent	Concentration of reducing agent (mM)	Percentage of Au precursor reduction (%)	Figure number
a1	HQ	0.50	52.3 ± 3.8	29 a
a2	HQ	1	83.0 ± 5.3	29 b
a3	HQ	2	95.5 ± 2.6	29 c
a4	HQ	3	97.1 ± 2.8	29 d
a5	HQ	5	95.7 ± 2.2	29 e
b1	AA	0.275	36.1 ± 2.4	31 b
b2	AA	0.55	60.3 ± 3.6	32 a
b3	AA	0.707	59.0 ± 3.5	32 b

Figure 3. 8. Optical images of AuNRs synthesized using different reducing agents: (a) HQ and (b) AA. The concentration of HQ increased from 0.50, 1, 2, 3 to 5 mM from left to right in panel (a), and the amount of AA increased from 0.275, 0.55 to 0.707 mM from left to right in panel (b). Detailed synthetic conditions of AuNRs in (a) and (b) are listed in Table 3. 3 and~~,~~ Table 3. 4~~, Table 3. 5,~~ respectively. The concentration of added reducing agent and percentage of Au precursor reduction are listed in panel (c).

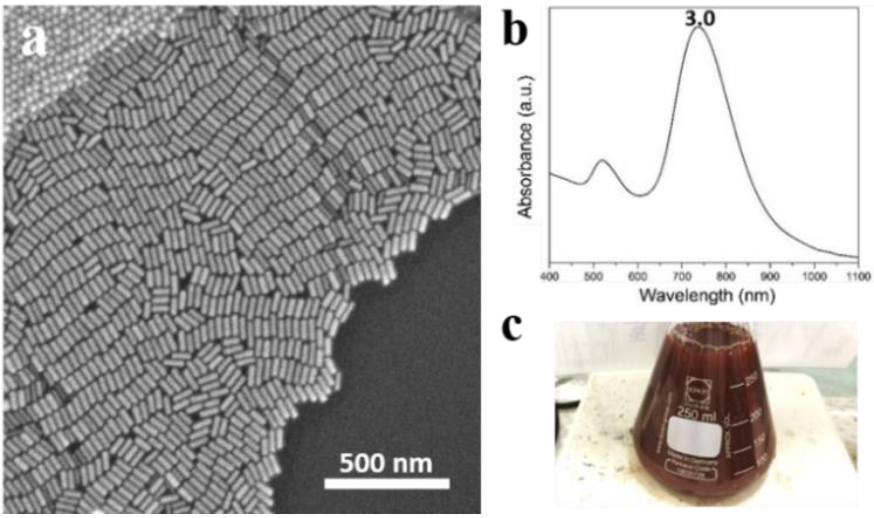

Figure 3. 9. (a–c) SEM image, the corresponding UV-Vis-NIR spectrum, and optical image of AuNRs obtained by a 25-time scale-up synthesis under the conditions specified below:~~in Table 3. 6.~~

Average length (nm)	Average width (nm)	LSPR peak position (nm)
76 ± 7	25 ± 2	736

~~Table 3. 6. Synthetic conditions of AuNRs specified in Figure 3. 9. T~~ the amount of CTAB (0.1 M), 5-Bromosalicylic acid, $AgNO_3$ (4 mM), $HAuCl_4$ (1 mM), HCl (32 wt. %), hydroquinone (0.1 M) and $NaBH_4$ (0.25 mM) used for AuNR synthesis are 125 mL, 0.5475 g, 7.5 mL, 125 mL, 0.2 mL, 7.5 mL, and 0.5 mL, respectively.

Another significant improvement induced by HQ is that nearly 100 % Au precursor is reduced to metallic Au, which is much advantageous than classic seed-mediated methods.[141] Low yield is rather wasteful considering the cost of starting materials and impedes the process to be an efficient synthesis protocol towards commercialization. Inductively coupled plasma optical emission spectrometry (ICP-OES) analysis was used to determine the actual yield of Au precursor reduction. From ~~Figure 3. 8. Optical images of AuNRs synthesized using different reducing agents: (a) HQ and (b) AA. The concentration of HQ increased from 0.50, 1, 2, 3 to 5 mM from left to right in panel (a), and the amount of AA increased from 0.275, 0.55 to 0.707 mM from left to right in panel (b). Detailed synthetic conditions of AuNRs in (a) and (b) are listed in Table 3. 3, Table 3. 4, Table 3. 5, respectively. The concentration of added reducing agent and percentage of Au precursor reduction are listed in panel (c).~~ Figure 3. 8, ~~,~~ the yield is larger than 95 % when the HQ concentration is larger than 2 mM. In contrast, when using AA as reducing agent, the yield only reaches to 36.1 % at 0.275 mM, and a further increase in the AA concentration leads to the formation of a large amount of dog-bone shape AuNPs (Figure 3. 7). The high yield is also reflected in the much denser color of AuNRs solution synthesized using HQ as reducing agent compared to AA, as shown in ~~Figure 3. 8. Optical images of AuNRs synthesized using different reducing agents: (a) HQ and (b) AA. The concentration of HQ increased from 0.50, 1, 2, 3 to 5 mM from left to right in panel (a), and the amount of AA increased from 0.275, 0.55 to 0.707 mM from left to right in panel (b). Detailed synthetic conditions of AuNRs in (a) and (b) are listed in Table 3. 3, Table 3. 4, Table 3. 5, respectively. The concentration of added reducing agent and percentage of Au precursor reduction are listed in panel (c).~~

Figure 3. 8. HQ is a significantly weaker reducing agent than AA and is able to present in large excess without affecting the template-induced anisotropic growth, thus affording a slower and controlled growth of AuNRs until all Au precursor has been consumed.[178] In addition, Figure 3. 9 shows that it is viable to scale-up synthesize AuNRs using our seedless method. The facile synthesis, high reproducibility, high yield, and ease of scale-up make our seedless method particularly promising for the future industrial mass production of monodispersed AuNRs for diverse applications in catalysis, sensing, and biomedicine.

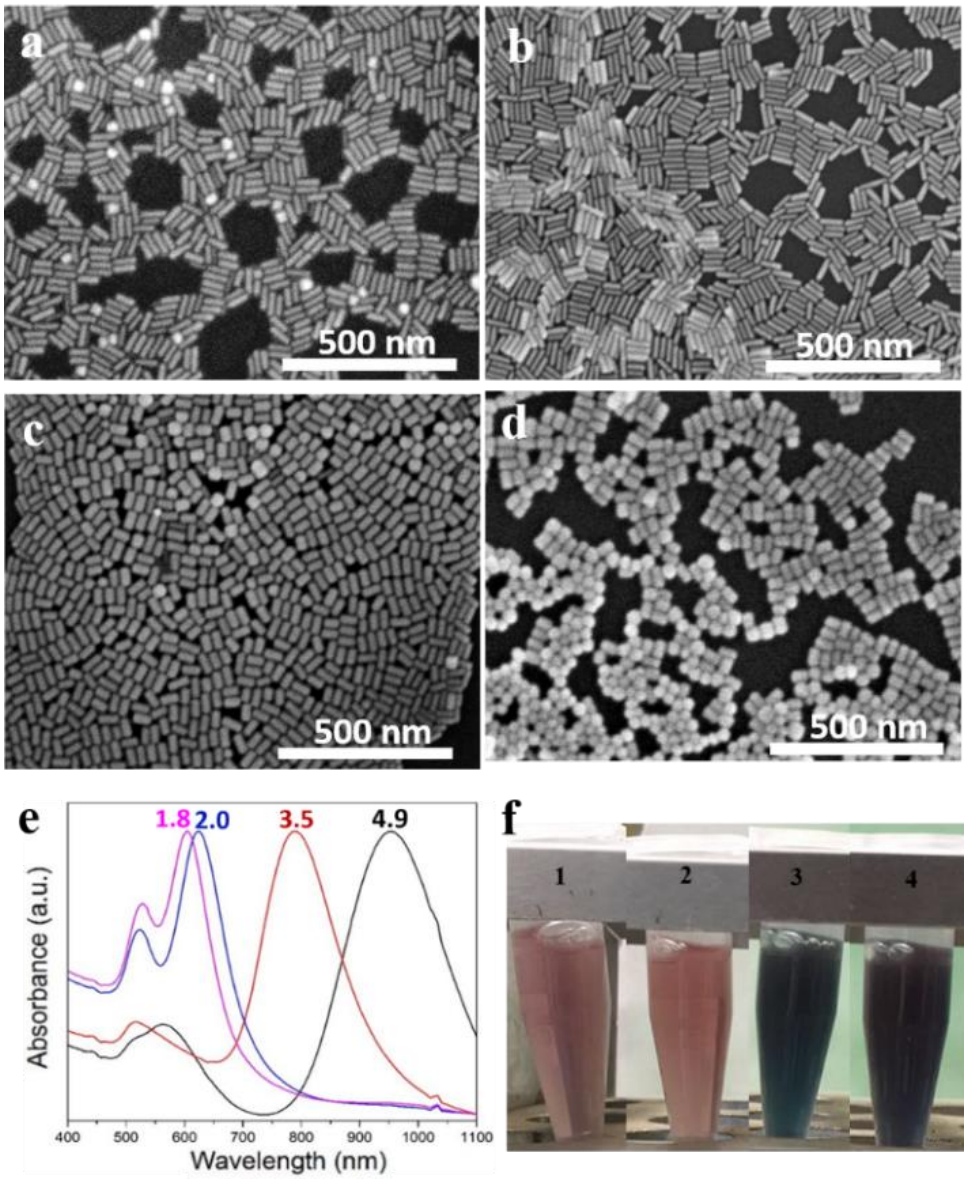

Figure 3. 10. (a−d) SEM images of AuNRs synthesized using increased $HAuCl_4$ concentrations: (a) 0.25 mM, (b) 0.375 mM, (c) 0.75 mM, (d) 0.875 mM. The CTAB concentration is fixed at 50 mM. The corresponding Au/CTAB ratio is 0.005, 0.0075, 0.015, and 0.0175, respectively. The average length and width of the AuNRs and detailed synthesis conditions are listed in Table 3. 5. (e) Normalized absorbance spectra of AuNRs shown in panel a (black curve), panel b (red curve), panel c (blue curve), panel d (pink curve). Aspect ratios of AuNRs are also provided in panel (e). (f) Optical images of AuNRs shown in panel (a-d) from left to right.

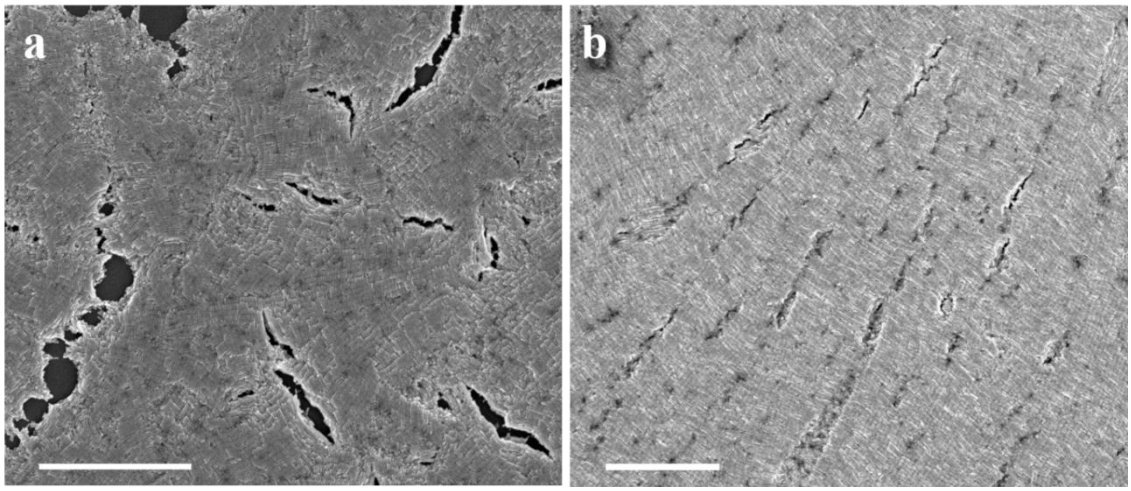

Figure 3. 11. Large-area SEM image of AuNRs synthesized using different Au/CTAB ratio: (a) 0.005, (b) 0.0075. Detailed synthetic conditions are listed in Table 3. 5. All scale bars represent 2 µm.

Number	Concentration of $HAuCl_4$ (mM)	Au/CTAB ratio	Average length (nm)	Average width (nm)	LSPR peak position (nm)
a	0.25	0.005	75 ± 8	15 ± 2	952
b	0.375	0.0075	67 ± 8	18 ± 2	790
c	0.75	0.015	51 ± 5	24 ± 3	624
d	0.875	0.0175	49 ± 5	29 ± 5	604

Table 3. 5. Synthetic conditions of AuNRs specified in Figure 3. 10 and Figure 3. 11. The amount of CTAB (0.1 M), 5-Bromosalicylic acid, $AgNO_3$ (4 mM), $HAuCl_4$ (1 mM), HCl (32 wt. %), hydroquinone (0.1 M) and $NaBH_4$ (0.25 mM) used for AuNR synthesis are 5 mL, 0.0219 g, 300 µL, 5 mL, 8 µL, 300 µL, and 20 µL, respectively.

3.2.4 Effect of Au Concentrations

In order to have a better understanding of AuNRs formation in our seedless method, the effect of Au ions concentration on growth kinetics was investigated by varying it from 0.25 mM to 0.875 mM, as shown in Figure 3. 10 and Figure 3. 11. The amount of HQ was scaled along with the Au concentration to eliminate the effect of the Au-to-HQ ratio on the reaction. When the Au ions concentration is relatively low (0.25 mM, Figure 3. 10a), AuNRs with high aspect ratio of 4.9 were obtained together with small amount of spherical impurities. When it increases to 0.375 mM (Figure 3. 10b), monodispersed AuNRs were synthesized and the corresponding aspect ratio decreases to 3.5. Further increase of the Au ions concentration leads to the decrease of the aspect ratio (Figure 3. 10c, d), and a significant amount of impurities appear at the highest concentration explored (0.875 mM, Figure 3. 10d). The effect of Au ions can be better understood in the form of Au/CTAB ratio. As bromide ions may drastically modify the geometries of the resulting Au nanoparticles by selectively adsorbing on and blocking some growing facets of the Au seeds, Au ions influence their availability by forming metal halide complex.[143, 305] At low Au/CTAB ratio (0.005, Figure 3. 10a), the relative excess bromide ions in the medium block most of the crystal {111} and {100} facets of the initially formed seed particles that are usually available for nanorod growth.[143] In this way, the anisotropic growth of those Au seeds is hindered to some extent, resulting in the presence of spherical impurities (Figure 3. 10a). When this ratio increases (0.0075, Figure 3. 10b), the growing facets of the Au seeds are no longer blocked, thus anisotropic growth is favored and monodispersed AuNRs are obtained. A higher Au/CTAB ratio results in a lower proportion of rod-shaped products (0.0175, Figure 3. 10d), which indicates that there is not enough bromide ions to block the specific facets and gives rise to the formation of irregular impurities and much wider AuNRs. This is also verified by the presence of a significant amount of cubic-like byproducts at high Au/CTAB ratios (0.015 and 0.0175, Figure 3. 10c, d), which is an obvious sign of the relatively free growth of {111} facets.[303] As shown in Figure 3. 10, with increasing of the Au ions concentration, a decrease in the aspect ratio and blue shift of the LSPR band are observed. This is explained by the fact that with the increasing of Au ions, the density of bromide ions which dynamically distributed around AuNRs gradually

decreases, therefore the AuNRs tend to grow relatively isotropic. These results demonstrate that Au/CTAB ratio kinetically influences the nanoparticle growth by adjusting the availability of bromide ions. It's worth mentioning that the concentration of Au ions in our method can be applied in a relatively wide range (from 0.25 mM to 0.75 mM), which is much advantageous compared to classic seed-mediated methods that Au ions have to be present at large excess and slight decrease in the Au ions concentration leads to a significant decrease in the percentage of rod shape.[141]

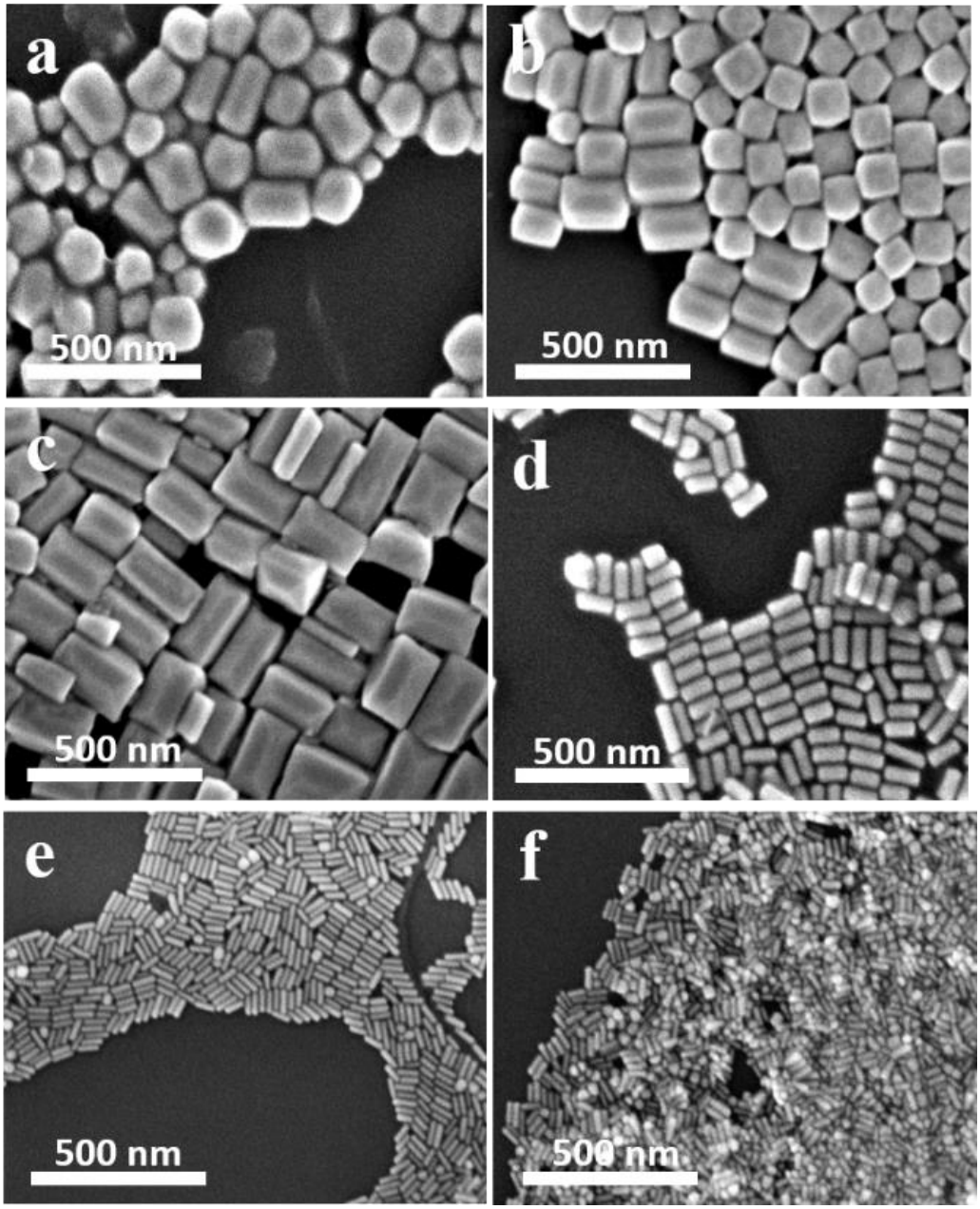

Figure 3. 12. (a−f) SEM images of AuNRs synthesized using increased 5-BA concentration: (a) 0 mM, (b) 5 mM, (c) 7.5 mM, (d) 10 mM, (e) 12.5 mM, (f) 15 mM. The CTAB concentration is fixed at 50 mM. The corresponding 5-BA/CTAB ratio is 0, 0.1, 0.15, 0.2, 0.25, and 0.3, respectively. The average length and width of the AuNRs and detailed synthesis conditions are listed in Table 3. 6.

Number	Amount of 5-BA (g)	5-BA/CTAB ratio	Average length (nm)	Average width (nm)	Aspect ratio
a	0	0	NA	NA	NA
b	0.0108	0.1	158 ± 23	103 ± 18	1.6
c	0.0163	0.15	190 ±35	113 ± 21	1.7
d	0.0217	0.2	92 ± 8	42 ± 5	2.2
e	0.0271	0.25	56 ± 5	16 ± 2	3.5
f	0.0326	0.3	52 ± 7	17 ± 3	3.2

Table 3. 6. Synthetic conditions of AuNRs specified in Figure 3. 12. The amount of CTAB (0.1 M), $AgNO_3$ (4 mM), $HAuCl_4$ (1 mM), HCl (32 wt. %), hydroquinone (0.1 M) and $NaBH_4$ (0.25 mM) used for AuNR synthesis are 5 mL, 300 µL, 5 mL, 8 µL, 300 µL, and 20 µL, respectively.

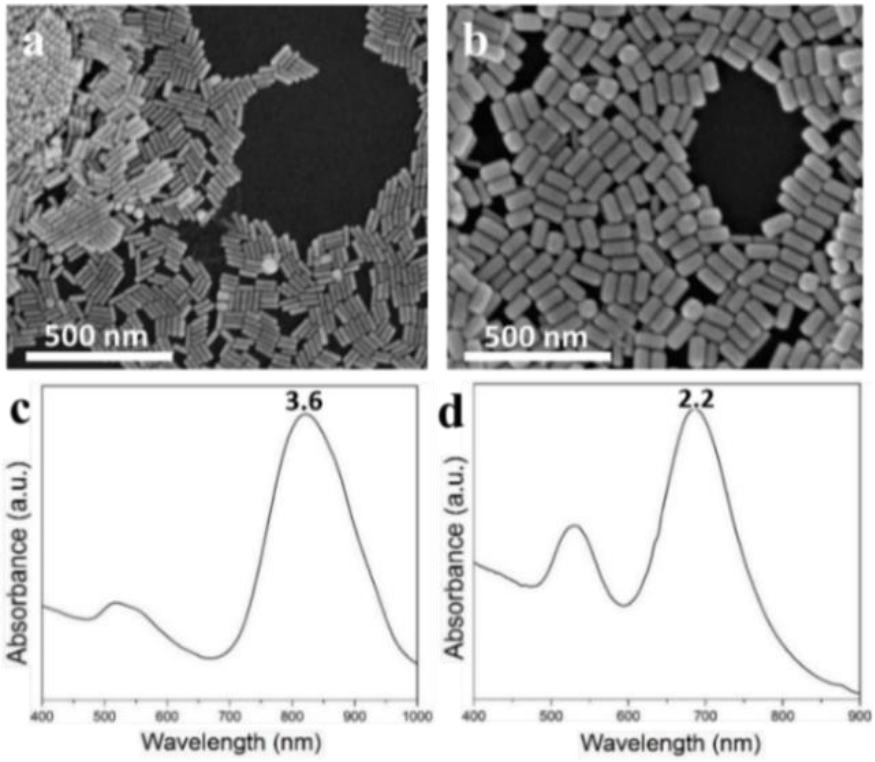

Figure 3. 13. (a, c) SEM image and the corresponding UV-Vis-NIR spectrum of AuNRs synthesized using 0.0375 M CTAB, (b, d) SEM image and the corresponding UV-Vis-NIR spectrum of AuNRs synthesized using 0.0625 M CTAB. The 5-BA concentration is fixed at 10 mM. The corresponding 5-BA/CTAB ratio is 0.27, and 0.16, respectively. The average length and width of the AuNRs and detailed synthesis conditions are listed in Table 3. 7. Aspect ratios of AuNRs are also provided in panel (c) and (d).

Number	Concentration of CTAB (M)	5-BA/CTAB ratio	Average length (nm)	Average width (nm)	LSPR peak position (nm)
a	0.0375	0.27	65 ± 6	18 ± 2	822
b	0.0625	0.16	107 ± 8	53 ± 4	686

Table 3. 7. Synthetic conditions of AuNRs specified in Figure 3. 13. The amount of CTAB (0.1 M), 5-Bromosalicyclic acid, $AgNO_3$ (4 mM), $HAuCl_4$ (1 mM), HCl (32 wt. %), hydroquinone (0.1 M) and $NaBH_4$ (0.25 mM) used for AuNR synthesis are 5 mL, 0.0219g, 300 µL, 5 mL, 8 µL, 300 µL, and 20 µL, respectively.

3.2.5 Effect of 5-BA and CTAB concentrations

As the "structure-directing" and stabilizing agent, CTAB together with 5-BA and Ag^+ ions offer elongated templates so that the growth of Au seeds is directed along with these templates, resulting in symmetry breaking.[143, 305] The hydrophobic benzene ring and salicylate anion of 5-BA could effectively change the micellar packing parameter

$$p = v/Al \qquad \text{(Equation 3. 3)}$$

where v is the effective volume of the hydrophobic chain, A is the effective area of the polar head group, and l is the length of the hydrocarbon chain of CTAB micelles.[137] The inserted phenyl moiety of 5-BA increases the v, while the anion association ($-COO^-$ of 5-BA) decreases A by reducing the electrostatic repulsion between the quaternary ammonium groups, thus the packing parameter (p) increases and promotes the spherical to rod-like transition of CTAB micelle.[144] Based on the fact that 5-BA molecules intercalate into the CTAB bilayer and influence the packing density, it is more reasonable to investigate how 5-BA/CTAB ratio influences the AuNRs formation

instead of 5-BA concentration. When no 5-BA is applied, the main products are irregular nanoparticles (Figure 3. 12a). As the 5-BA/CTAB ratio increases from 0.1 to 0.25, AuNRs are produced (Figure 3. 12b-e). This indicates that 5-BA is an indispensable template regulator for successful synthesis of AuNRs at such low CTAB concentration (50 mM). However, the CTAB template is seriously deteriorated at too high 5-BA/CTAB ratio (0.3, Figure 3. 12f), as evidenced by the presence of a significant amount of spherical impurities. Figure 3. 12 and Table 3. 6 show that as 5-BA/CTAB ratio increases, the overall dimensions decrease, and the aspect ratio increases. This can be explained by the fact that higher 5-BA/CTAB ratio facilitates the anisotropic growth of AuNRs. It is reasonable to predict that an opposite trend will be obtained when decreasing 5-BA/CTAB ratio by increasing the CTAB concentration at constant 5-BA concentration. Figure 3. 13 and Table 3. 7 show that AuNRs synthesized using 0.0375 M CTAB (5-BA/CTAB = 0.27) are smaller in size while larger in aspect ratio compared with those synthesized using 0.0625 M CTAB (5-BA/CTAB = 0.16) provided other reaction conditions are identical. This successfully verified our prediction.

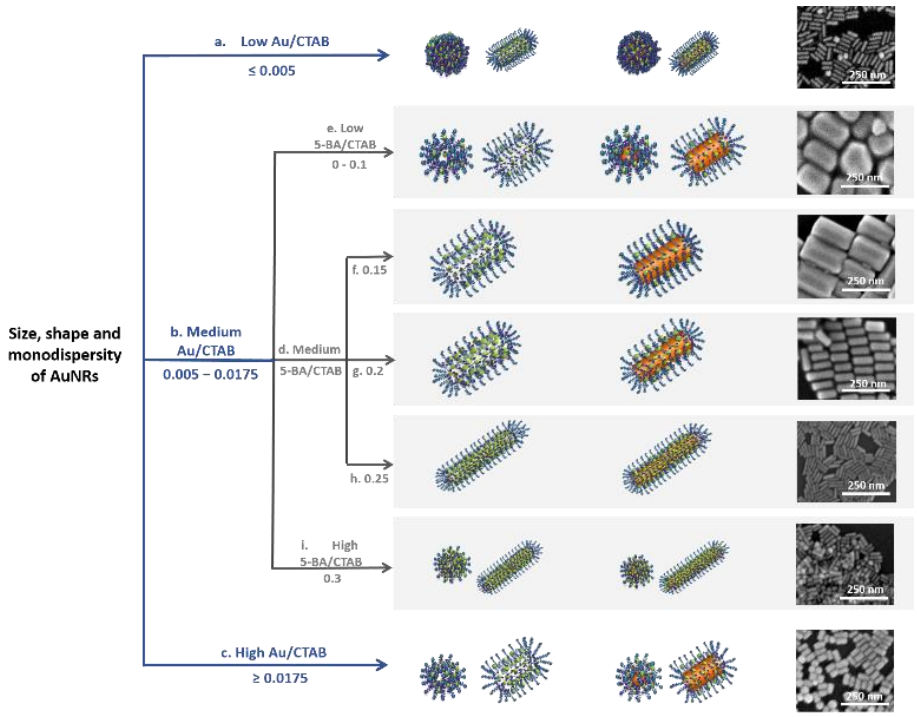

Figure 3. 14. Schematically illustrate the effect of Au/CTAB and 5-BA/CTAB ratio on the dimensions and morphology of synthesized AuNRs. Note that the chemical components are not shown to scale.

In this work, we found that Au/CTAB ratio together with 5-BA/CTAB ratio effectively influences the dimensions and morphology of final products. After analyzing the effect of Au/CTAB and 5-BA/CTAB ratio on the AuNRs synthesis, Figure 3. 14 is proposed as a reference in predicting and customizing the dimensions of AuNRs. At extreme conditions, excessive bromide ions suppress the anisotropic growth (Au/CTAB ≤ 0.005, Figure 3. 14a), and insufficient bromide ions are not enough to induce the anisotropic growth (Au/CTAB ≥ 0.0175, Figure 3. 14c), thus thinner and wider AuNRs together with impurities are produced, respectively (Figure 3. 10a, d). At intermediate Au/CTAB ratios (0.005 ~ 0.0175, Figure 3. 14b), anisotropic growth is favored and monodispersed AuNRs are obtained. In this case, the dimension of AuNRs can be further regulated by adjusting 5-BA/CTAB ratio (Figure 3. 14e-i). Generally, smaller AuNRs with higher aspect ratio are produced due to the formation of a stiffer anisotropic CTAB template at higher 5-BA/CTAB ratios (Figure 3. 14f-h and Figure 3. 12b-e). At low 5-BA/CTAB ratio (0 ~ 0.1, Figure 3. 14e), the proportion of nanorods is low (Figure 3. 12a, b). However, when 5-BA/CTAB ratio is too high (≥ 0.3, Figure 3. 14i), a significant amount of spherical impurities appears (Figure 3. 12f). The dimensions of AuNRs are adjusted in a wide range (length: 52 ~ 158 nm, and width: 16 ~ 113 nm) simply by changing the 5-BA/CTAB ratio. Furthermore, as 5-BA molecules influence the packing density of CTAB, the concentration of CTAB required for producing high-quality AuNRs can be reduced to approximately 1/3 of that in the widely-used protocols. This is of great significance not only in reducing the materials costs for AuNRs synthesis but also in offering better control over the nanorod dimensions. Moreover, as CTAB has been proven to be highly cytotoxic, the reduction of CTAB concentration is also desirable towards the synthesis of biocompatible AuNRs by facilitating their surface modification with other ligands (e.g. thiolated-PEG).[169]

3.2.6 Effect of Ag Concentrations

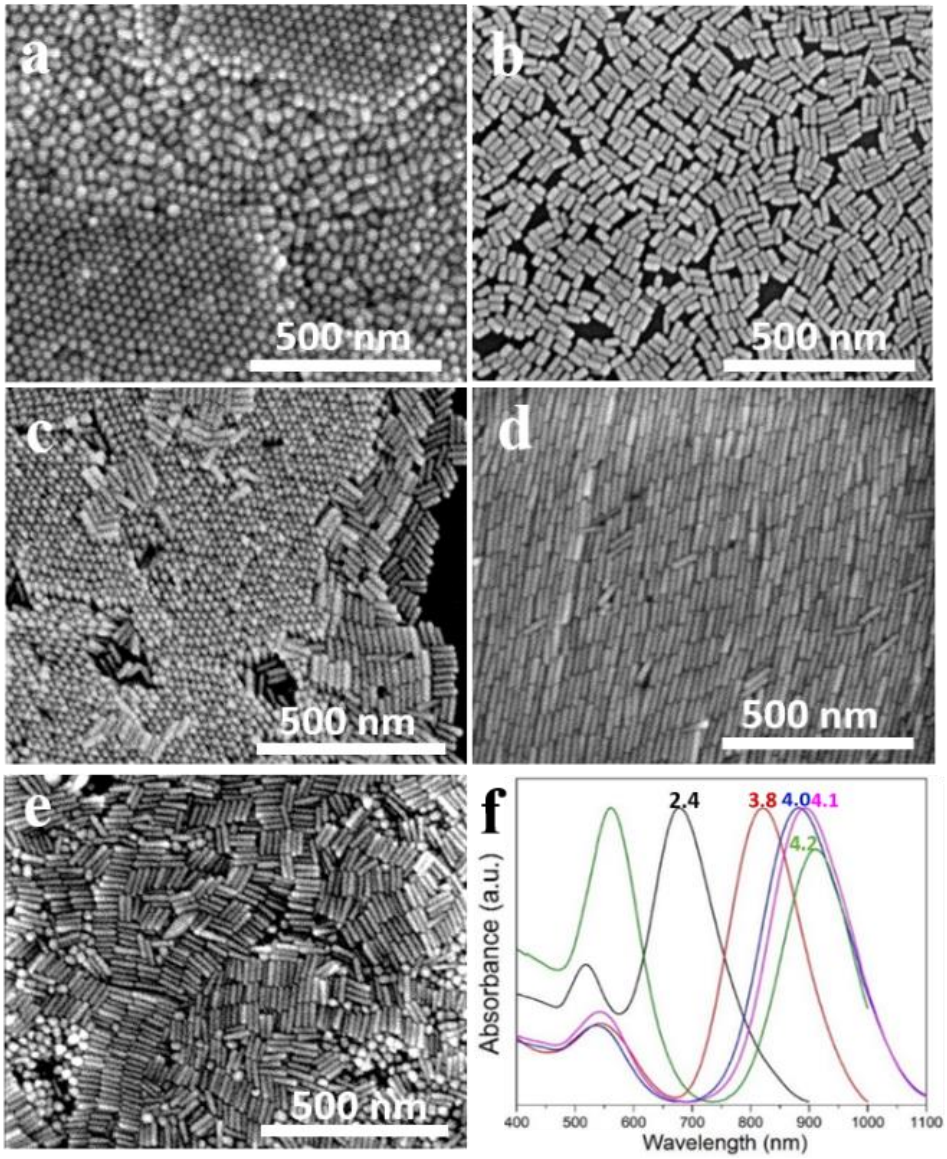

Figure 3. 15. (a−e) SEM images of AuNRs synthesized using increased concentration of AgNO3 from 0.04, 0.08, 0.12, 0.16 to 0.24 mM. The average length and width of the AuNRs and detailed synthesis conditions are listed in Table 3. 8. (f) Normalized absorbance spectrum of AuNRs shown in a (black curve), b (red curve), c (blue curve), d (pink curve), and e (green curve). Aspect ratios of AuNRs are also provided in panel (f).

Number	Concentration of $AgNO_3$ (mM)	Amount of $AgNO_3$ (4 mM) (µL)	Average length (nm)	Average width (nm)	LSPR peak position (nm)
a	0.04	100	38 ± 4	21 ± 3	595
b	0.08	200	45 ± 5	15 ± 2	679
c	0.12	300	60 ± 5	15 ± 2	819
d	0.16	400	52 ± 5	12 ± 1	881
e	0.24	600	65 ± 6	14 ± 1	910

Table 3. 8. Synthetic conditions of AuNRs specified in Figure 3. 15. The amount of CTAB (0.1 M), 5-Bromosalicyclic acid, $HAuCl_4$ (1 mM), HCl (32 wt. %), hydroquinone (0.1 M) and $NaBH_4$ (0.25 mM) used for AuNR synthesis are 5 mL, 0.0219g, 5 mL, 8 µL, 300 µL, and 20 µL, respectively.

It has been shown that the Ag^+ ions serve as an essential part of the elongated template, which is important in symmetry breaking of the embryonic nanocrystals and the subsequent formation of single-crystal AuNRs.[138, 303] Figure 3. 15 shows the SEM images and extinction spectra of AuNRs synthesized at increased concentrations of $AgNO_3$ using the proposed seedless method. The aspect ratio can be continuously adjusted from 1.8 to 4.2 by increasing $AgNO_3$ concentration from 0.04 mM to 0.24 mM (Figure 3. 15a-e). However, at too high $AgNO_3$ (0.24 mM, Figure 3. 15e) concentrations, a significant amount of spherical and quasi-spherical impurities was produced. This indicates that an appropriate $AgNO_3$ concentration is essential for the synthesis of high-quality nanorods, and the nanorod synthesis is deteriorated at extreme Ag^+ concentrations.

3.2.7 Effect of pH

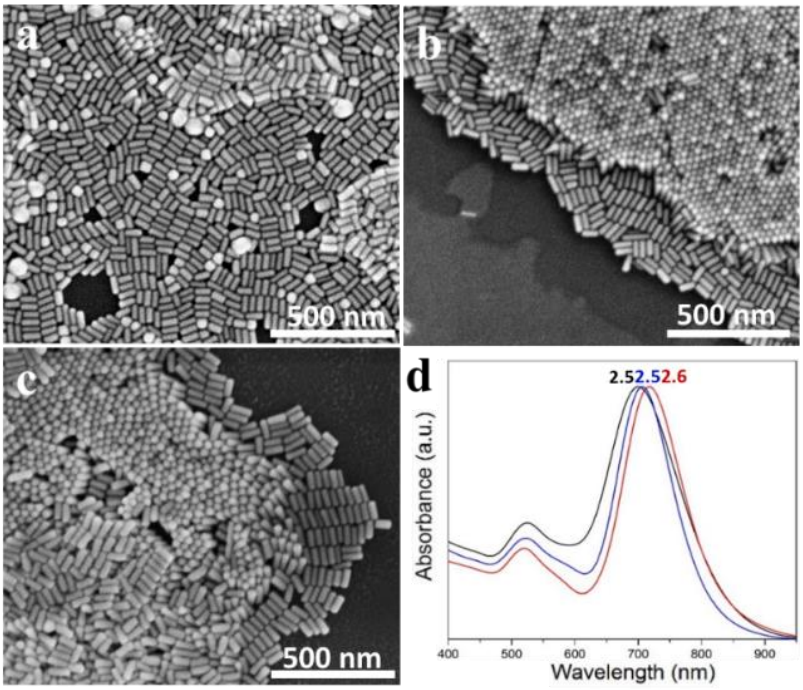

Figure 3. 16. (a−c) SEM images of AuNRs synthesized using an increased amount of HCl (32 wt. %) from 0, 30 to 50 µL. The corresponding pH of the solution is 2.31, 1.7, and 1.56, respectively. The average length and width of the AuNRs and detailed synthesis conditions are listed in Table 3. 9. (d) Normalized absorbance spectrum of AuNRs shown in a (black curve), b (red curve), and c (blue curve). Aspect ratios of AuNRs are also provided in panel (d).

Number	Amount of HCl (32 wt. %) (µL)	pH	Average length (nm)	Average width (nm)	LSPR peak position (nm)
a	0	2.31	66 ± 8	25 ± 3	701
b	30	1.7	69 ± 8	23 ± 2	718
c	50	1.56	75 ± 8	28 ± 3	707

Table 3. 9. Synthetic conditions of AuNRs specified in Figure 3. 16. The amount of CTAB (0.1 M), 5-Bromosalicyclic acid, $AgNO_3$ (4 mM), $HAuCl_4$ (1 mM), hydroquinone (0.1 M) and $NaBH_4$ (0.25 mM) used for AuNR synthesis are 5 mL, 0.0219g, 5 mL, 250 µL, 300 µL, and 20 µL, respectively.

The pH of the solution influences both the nucleation process and growth kinetics by regulating the reducing ability of $NaBH_4$ and HQ, thereby has a great impact on the AuNRs synthesis.[112, 183, 186] For the proposed seedless method, the size and shape uniformity of AuNRs are improved at a more acidic growth media, as evidenced by the obvious increase of the LSPR to TSPR band intensity ratio (Figure 3. 16). As the pH of the growth solution decreases, both dimensions and aspect ratio of AuNRs increase slightly, resulting in the redshift of the LSPR band (Figure 3. 16 and Table 3. 9). Theoretically, the reduction ability of $NaBH_4$ and HQ decreases when pH of the solution decreases. Thus, the nucleation process is suppressed resulting in the formation of fewer nuclei, while milder growth condition can effectively eliminate secondary nucleation and make modified-template more effective in inducing anisotropic growth. Consequently, monodispersed and uniform AuNRs are produced at more acidic solutions.

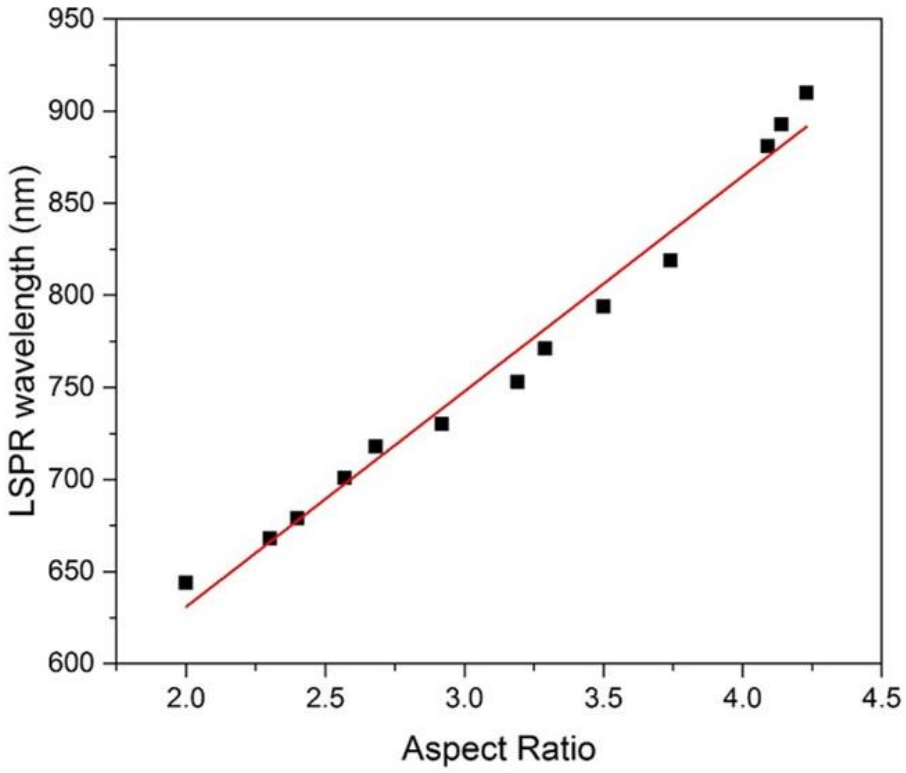

Figure 3. 17. Dependence of LSPR wavelength on the aspect ratio of AuNRs prepared using hydroquinone as reducing agent. A linear correlation can be established between

LSPR wavelength and the average aspect ratio. LSPR wavelength = 116.93 × aspect ratio + 397, and R^2 = 0.99131.

In this work, the growth behavior of AuNRs is effectively controlled by many factors including Au/CTAB ratio, 5-BA/CTAB ratio, HQ concentration, Ag concentration, $NaBH_4$ concentration, and pH value. Specifically, CTAB together with 5-BA and Ag^+ ions provide a stiff rod-like template directing the growth of nanorods. The elaborately-controlled growth kinetics makes the modified template more effective in inducing anisotropic growth. Many parameters are controlled in order to optimize the growth kinetics, including Au/CTAB ratio, $NaBH_4$, HQ concentration, and pH value. It's worth mentioning that HQ is irreplaceable for successful synthesis of monodispersed AuNRs with high yield. The synergistic effect of template modification and growth kinetics regulation offers a better tolerance for the variations in the experimental parameters. In the traditional methods, high monomer concentrations have to be maintained so as to induce better stability of anisotropic nanoparticle embryos.[141, 185] In contrast, the concentrations of key components in our work, e.g. CTAB, $HAuCl_4$, $AgNO_3$, and HQ, can be applied in a flexible range. As the AuNRs synthesized by our methods are quite monodispersed, a linear correlation is established between the LSPR peak position and the average AuNRs aspect ratio determined by SEM studies (Figure 3. 17).

3.3 Conclusions

In summary, we demonstrate that monodispersed AuNRs with remarkably high yield are reproducibly synthesized by using the proposed seedless synthetic technique. The significance of our research and several major findings are described below:

1. We investigated the mechanism of AuNRs formation, and the soft-template theory is enriched and supported through a series of experimental results. The current work shines light on how soft-template and well-controlled growth kinetics synergistically influence the nanorods synthesis, and provides valuable instructions on synthesizing monodisperse AuNRs with different dimensions.

2. The 5-BA/CTAB ratio and Ag^+ ions concentration are studied for better understanding the important role of the template in inducing anisotropic growth and regulating the dimensions of AuNRs. It's found that 5-BA serves as template regulator and promotes the spherical to rod-like/worm-like micellar transition. While Ag^+ ions serve as an essential part of the soft-template in inducing the formation of the anisotropic nanostructures by forming CTAB-AgBr complex.

3. The Au/CTAB ratio, $NaBH_4$, HQ concentration and pH are explored thoroughly to optimize the growth kinetics. $NaBH_4$ is used to generate seeds *in situ*, and the use of HQ at lower pH affords a mild condition for AuNRs growth. Consequently, the modified-template becomes more effective and monodispersed AuNRs formation is favored.

4. A useful scheme is proposed as a reference in predicting and customizing the dimensions of AuNRs. The Au/CTAB ratio kinetically regulates the growth of AuNRs by adjusting the availability of bromide ions that can selectively adsorb on and block the growing facets of the Au seeds. At the optimized Au/CTAB ratios, the dimension of AuNRs can be further regulated by adjusting the packing density of CTAB micelle through changing the 5-BA/CTAB ratio.

The facile synthesis, broad tunability of LSRP, high reproducibility, remarkably high yield, and easey of scale-up make our seedless method particularly promising for the future industrial mass production of monodispersed AuNRs. Moreover, our work also makes an important step towards a better understanding of AuNRs growth and may have profound implications for seedless (or seed-mediated) synthesis of other anisotropic metal nanostructures.

Chapter 4 Surface Modification of AuNRs

The nanorods synthesis involves the use of CTAB and silver nitrate to control over nanorod formation and aspect ratio.[28, 138, 309] The CTAB tightly adsorbs on the gold surface to form a dense surface-confined cationic bilayer with the trimethylammonium head facing the external environment. This makes it difficult to remove CTAB without causing nanorod aggregation. On the other hand, it has been shown that, during the AuNR synthesis, silver ions are reduced and deposited on the gold surface in the form of atomic silver monolayers or sub-monolayers at a potential much less negative than bulk reduction, known as underpotential deposition.[156] Jackson et al. experimentally observed that the silver atoms were located in the outermost ~2 nm surface layer of the AuNRs, rather than in the core.[139] Under aerobic conditions, the surface silver atoms dissolve in aqueous solutions as a form of silver ions.[310] This reaction is hindered to a large extent when AuNRs are coated with long--chain organic molecules.[311]

Both CTAB and silver ions in the colloidal AuNR solution pose a threat to many biological systems, as they are known to be cytotoxic.[156, 159, 163, 236, 312-315] It has been reported that CTAB can disrupt the lipid bilayer of cell membrane forming nanoscale holes within the membrane due to the electrostatic adsorption of quaternary ammonium cations onto the membrane, thus increasing its permeability.[312] There is also an evidence that silver ions interact with cell membranes and lead to actin depolymerization in the cytoskeleton connecting tightly with the membrane, ultimately causing the cell death.[315] Therefore, the ability to completely remove CTAB, prevent silver ion leaching and maintain AuNR colloidal stability will be key requirements towards their in vivo diagnostic and therapeutic applications.

So far, considerable effort has been devoted to the development of surface functionalization strategies aiming at replacing CTAB with more biocompatible surface ligands, such as thiol-terminated polyethylene glycol (HS-PEG),[232-233, 236-238] alkanethiols,[47, 228, 235, 298-299] thiolated CTAB analogues,[231] thiolated glycans[34] and phospholipids.[117, 300] Among these ligands, thiolated PEGs are the most widely used molecules as they provide AuNRs with a high degree of anti-fouling ability, colloidal

stability, and biocompatibility in biological media.[228, 232-233, 236-238] Liao et al. developed a standard procedure for AuNR PEGylation via a one-step ligand exchange reaction (referred to as the Liao method).[237] This reaction can be significantly accelerated in the presence of tris-buffer with pH of 3.[232] The main drawback of this one-step PEGylation method is that only the more weakly bound CTAB molecules at the tips are displaced with thiolated PEG, producing partially functionalized AuNRs.[230] To achieve higher PEGylation efficiency, Kinnear et al. recently established a two-step ligand exchange method that takes advantage of ethanol to desorb the CTAB from the sides of the partially modified AuNRs followed by another PEGylation step (referred to as the Kinnear method).[233] The authors claimed that this method enables the complete functionalization of AuNRs with thiolated PEG. However, a small quantity of CTAB was still observed on the AuNRs.[233] This may still cause cytotoxicity at an elevated AuNR concentration required for high cellular uptake of AuNRs.[159, 163]

Despite the above-mentioned advances, there are still several challenges for the surface modification of AuNRs with thiolated PEG. Firstly, the existing methods usually suffer from a low PEGylation efficiency,[232, 237] which can limit the effectiveness of the PEG layer as surface coverage has been shown to be important for the effectiveness of PEG layers.[301] Moreover, they are also quite complicated[233] or experience a serious loss of AuNRs due to the irreversible nanorod aggregation during the purification process.[237] Therefore, a major goal of the field is to design a simple, reliable, robust functionalization procedure to produce colloidally stable and biocompatible (i.e. CTAB free) AuNRs. ~~This work has been published as a journal article in ***Langmuir*** (*Langmuir* **2015,** *31*, 4973−4980), named *"Biocompatible Gold Nanorods: One-Step Surface Functionalization, Highly Colloidal Stability, and Low Cytotoxicity".*[169] The content in this chapter was reproduced with permission from [169]. Copyright (2015) American Chemical Society.~~

4.1 Experimental Section

4.1.1 Chemicals and Materials

All chemicals and reagents were purchased from Sigma-Aldrich and used as received, unless otherwise stated. Milli-Q water (18.2 MΩ) was used for all experiments.

4.1.2 Synthesis of CTAB-Capped AuNRs

Gold nanorods (AuNRs) with an average aspect ratio of 3.2 were synthesized by the seed-mediated method described by El-Sayed et al.[28] In a typical procedure, a seed solution was prepared by adding an ice-cold $NaBH_4$ solution (0.6 mL, 0.01 M) into a mixture of CTAB solution (5 mL, 0.20 M) and $HAuCl_4$ (5 mL, 0.5 mM). The mixture was then vigorously stirred for 2 min, followed by an incubation at 30 °C for 2 h. A growth solution (~60 mL) was made by successively adding 1.5 mL of $AgNO_3$ (4 mM), 30 mL of 1 mM of $HAuCl_4$, and 0.42 mL of 78.8 mM ascorbic acid into 30 mL of 0.2 M CTAB solution. The color of the growth solution changed from yellow–brown to colorless immediately. Subsequently, the seed solution (72 μL) was added to the growth solution and incubated at 30 °C overnight. The AuNRs were then purified by three centrifugation cycles (14800 rpm, 30 min, Sigma 1-14 Microfuge) to remove excess CTAB and unreacted products. After the final step of purification, the AuNRs were redispersed in ultrapure water (18.2 mΩ).

4.1.2 Preparation of PEGylated AuNRs

In a typical procedure, AuNR PEGylation was conducted by successive addition of 5 μL of 2 vol% Tween 20 (Sigma-Aldrich) aqueous solution, 5 μL of 0.1 M bis(p-sulfonateophenyl)phenylphosphine dihydrate dipotassium salt (BSPP: Sigma-Aldrich), 12.6 μL of 1.6 mM thiol-terminal polyethylene glycol (SH-PEG, MW ≈ 2000 g/mol, Sigma-Aldrich; [SH-PEG]/[AuNR] = 1.24×10^5), 50 μL of 2 M NaCl and 30 μL of water into 100 μL of concentrated AuNR solution (10 times concentrated as the original AuNR solution). The mixture was placed in a ThermoMixer C (Eppendorf) and incubated at room temperature for 24 h (900 rpm). The PEGylated AuNRs were

purified by three centrifugation cycles (14800 rpm, 30 min) and redispersed in 100 µL ultrapure water.

For comparison, AuNRs were also PEGylated by methods developed by Liao *et al.* (Liao method)[237] and Kinnear *et al.* (Kinnear method).[233]

Liao method: 12.6 µL of 1.6 mM SH-PEG and 90 µL of water were added into 100 µL of a concentrated AuNR solution (10 times concentrated as the original AuNR solution), followed by an incubation for 24 h (900 rpm). The PEGylated AuNRs were purified by three centrifugation cycles (14800 rpm, 30 min) and redispersed in 100µL ultrapure water.

Kinnear method: 12.6 µL of 1.6 mM SH-PEG and 90 µL were added into 100 µL concentrated AuNRs solution (10 times concentrated as the original AuNR solution), followed by an incubation for 24 h (900 rpm). The PEGylated AuNRs were washed with water for 3 times by centrifugation (14800 rpm, 30 min) and redispersed in 1 mL of ethanol (90 vol% ethanol in water). After that, 12.6 µL of an ethanolic solution of SH-PEG (1.6 mM in 90 vol% ethanol in water) was added, followed by an incubation for 24 h (900 rpm). The PEGylated AuNRs were washed with water for 2 times by centrifugation (14800 rpm, 30 min) and redispersed in 100µL ultrapure water.

4.1.3 Fabrication of Positively Charged Silicon Substrate

In a typical procedure, silicon substrates were cleaned with Piranha solution for 30 min, washed with water three times and then dried under a stream of argon. The substrates were subsequently exposed to a mixture of 4 µL of (3-aminopropyl)triethoxysilane (APTES, Sigma-Aldrich), 190 µL of ethanol and 6 µL of water for 1 h, washed with ethanol three times and then dried under a stream of argon. After that, the substrates were baked at 110℃ for 10 min.

4.1.4 Electrostatic Immobilization of AuNRs onto APTES Modified Silicon Substrates

The electrostatic assembly of PEGylated AuNRs onto APTES-modified silicon substrates were performed in a petri dish where droplets of water were placed to maintain a constant humidity during the AuNR immobilization. 20 µL of completely PEGylated AuNR (10 times concentrated as the original AuNR solution) solution was placed onto a positively charged substrate (i.e. APTES modified substrate) and left to incubate for 4 h. The substrate was thereafter dipped in and out three times in water to remove non-specific adsorbed AuNRs and dried under a stream of argon.

4.1.5 Cell culture

Human cervical cancer cells line (HeLa cells) were cultured in Dulbecco's modified Eagle's medium (DMEM, Life Technologies, 11885-084) supplemented with 10 vol% fetal bovine serum, 50 U/mL penicillin, and 50 mg/mL streptomycin.

4.1.6 3-(4,5-dimethylthiazol-2-yl)-2,5-diphenyltetrazolium Bromide Assay

Cell toxicity was measured using the standard MTT assay. The cytotoxicity of PEGylated AuNRs wasere analyzed by using a HeLa cells line. The cells were seeded in 96-well flat bottom plates at a concentration of 3000 cells per well and were incubated for 24 h at 37 ºC (constant temperature and humidity, 5% CO_2). Then, the PEGylated AuNRs with concentrations ranging from 1.25 to 80 µg/mL were added into the plate wells. The cells were further incubated for 24 h at 37 ºC. Cell viability was determined by the addition of MTT (30 µL, 5 mg/mL in sterile phosphate buffered saline). The plates were further incubated for 4 h at 37 ºC, allowing viable cells to convert the pale yellow MTT to an insoluble purple formazan. Then the medium was carefully removed and 100 µL dimethyl sulfoxide (DMSO) was added to dissolve the insoluble formazan reduced from MTT by living cells. The absorbance of the colored medium was measured at 550 nm by using a scanning multiwell spectrophotometer (FLUOstar

Omega, BMG LABTECH). The viability of HeLa cells was also recorded by the morphological criteria using an optical microscope. After treatment with PEGylated AuNRs for 4 h, the cell morphology was observed by bright-field microscopy (Leica DM IL LED inverted phase contrast microscope). The magnification was set at × 200 for all samples.

4.1.7 Calculation of PEGylation Efficiency

Types of AuNRs	Completely PEGylated AuNRs 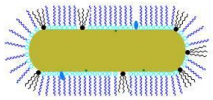	Partially PEGylated AuNRs 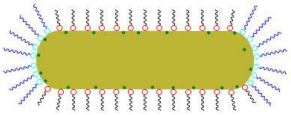			CTAB-capped AuNRs 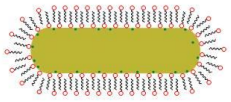
PEGylation conditions	Tween 20, BSPP, SH-PEG, NaCl	Tween 20, BSPP, SH-PEG	Tween 20, SH-PEG, NaCl	SH-PEG (Liao method)	
Surface bound CTAB	C= [CTAB (N at %)]	C= [CTAB (N at %)]			C_0= [CTAB (N at %)]/2
	0	1.08%	1.77%	1.6%	6.6%/2=3.3%
PEGylation efficiency (η)	$\eta = (C_0 - C)/C_0 \times 100\%$				
	100%	67%	46%	52%	0%

The PEGylation efficiency (η) defined as

$$(C_0\text{-}C)/C_0 \times 100\% \qquad \text{(Equation 4. 1)}$$

where C_0 is the amount of CTAB bound to the original AuNRs, C is the amount of CTAB remaining on the AuNRs after PEGylation. The amount of CTAB bound to the surface of AuNRs before and after PEGylation is determined by the *N* atomic percentage obtained from the XPS survey spectra.

4.1.8 Calculation of Mass Concentration of AuNRs

$$\text{Mass concentration} = C \times N_A \times V \times \rho \qquad \text{(Equation 4. 2)}$$

C ---------- Molar concentration, determined by UV-VIS spectroscopy based on the experimental extinction coefficients.

N_A ---------- Avogadro constant, 6.022×10^{23}.

V ---------- Average volume per AuNR, based on the dimensions obtained from SEM (51.5 ± 5 nm in length, 16.0 ± 2.2 nm in width). An average volume of each AuNR is calculated by assuming the AuNR to a cylinder with two half spheres on its ends.

ρ ---------- Density of gold, 19.32×10^3 mg/mL.

4.1.9 "Coffee-ring" effect

Previous research~~es~~ indicates that even though the CTAB has~~ve~~ been replaced from the AuNRs surface, there is a possibility for CTAB to be entangled by the polymeric brush chains of PEG, which is not desirable for AuNRs complete PEGylation.[232-233, 238] In our research, we took advantage of "coffee-ring", a common phenomenon~~a~~ happens in a typical Raman sample preparation process, that can concentrate AuNRs along the perimeter of the ring and produce uniformly distributed hotspots and strong electromagnetic field coupling there (Figure 4. 1).[184, 316-317] Due to strong electromagnetic field enhancement effect, the entrapped CTAB (if any) can still yield SERS signals even if there are less Au-Br bonds between the nanorod gold core and CTAB.[238, 318] As a consequence, all of our Raman spectra were obtained from the "ring region" to ensure sensitive and precise SERS detection of a trace amount of CTAB on the surface of AuNRs. From Raman spectra, all AuNRs functionalized with our proposed method present no Au-Br peak, which rules out the possibility that replaced CTAB remain entrapped among the PEG chains.

4.1.10 Silver etching mechanism

The presence of silver at the surface of AuNRs was previously reported by Orendorff and Murphy who suggested that silver is mostly distributed on the surface of the particles according to the underpotential deposition theory (UPD) proposed by Liu and Guyot-Sionnest for AuNRs growth.[156, 309] Anisotropy growth of AuNRs is caused by fast silver deposition on side facets followed by strong CTAB binding which inhibits gold growth on side facets.[138]

Ag is sensitive to the presence of oxidants and under oxygenated conditions, Ag^0 at the AuNRs surface dissolves to release Ag^+ as follows:[319]

$$Ag^0 + 1/2\ O_2 + H_2O \longrightarrow Ag^+ + 2OH^- \qquad \text{(Equation 4. 3)}$$

In a dilute aqueous suspension of AuNRs at equilibrium with atmospheric oxygen, but lacking other electrolytes, dissolution of the surface layer of Ag^0 is hindered due to the adsorption and accumulation of Ag^+ at the particle surface.[320-321] NaCl and BSPP can etch Ag^0 by disrupting this equilibrium (Equation 4.3) in different way. In case of NaCl, Ag^+ can react with Cl^- by forming AgCl, which causes a shift in the dissolution of Ag^0 described in Equation 4.3 due to a redistribution in the absorbed Ag^+.[321] For BSPP, it is believed that BSPP chelated with the Ag^+, forming BSPP-Ag^+ complexes. The decrease in the Ag^+ concentration in the solution due to the formation of BSPP-Ag^+ complexes shifted the equilibrium, resulting in the dissolution of Ag^0.[319, 322-323]

4.1.11 Characterization

UV-Vis absorption spectra were obtained with a Shimadzu UV-2401PC UV-VIS spectrophotometer at room temperature. The concentration of AuNRs solution was determined by UV-VIS spectroscopy based on the experimental extinction coefficients previously reported.[309] Raman spectra were collected on a RamanMicro 300 Raman Microscope (PerkinElmer). For all Raman measurements, the samples were exposed to a near-infrared diode laser (λ_{ex} = 785 nm, P_{ex} = 80 mW) for 4 s, and the Raman signals were collected from 5 scans. During the measurements, the laser beam was positioned

through an Olympus imaging microscope objective lens (100×). For the Raman sample preparation, AuNRs was drop-cast onto a gold-coated silicon substrate (thickness of gold film: 30 nm) and then dried in air. All Raman spectra were taken from the "coffee-ring" area (see Figure 4. 1). Elemental analyses were conducted using X-ray photoelectron spectroscopy (XPS). A Kratos Axis ULTRA XPS incorporating 165 mm hemispherical electron energy was used. The incident radiation was monochromatic A1 X-rays (1486.6 eV) at 225 W (15 kV, 15 ma). Survey (wide) scans were taken at an analyzer pass energy of 160 eV and multiplex (narrow) higher resolution scans at 20 eV. Survey scans were carried out over 1200 eV binding energy with 1.0 eV steps and a dwell time of 100 ms. Binding energy wasere calibrated with C1s peak at 285.0 eV to compensate for surface charging effect. Component fitting of the high-resolution spectra was performed using Avantage software. Silicon substrates were used as supporting substrates for the XPS measurements. All XPS spectra were taken from the "coffee-ring" area, as presented in Figure 4. 1. For the Raman and XPS measurements, the PEGylated AuNRs were purified by eight centrifugation cycles after the surface functionalization with PEG (Note: The AuNR solutions were diluted by 20 times after each centrifugation cycle). The Ag/Au elemental ratios of the samples were determined by means of inductively coupled plasma mass spectrometry (ICP-MS) (Perkin Elmer, NexION 300D with Universal cell technology). A 100 µL of –concentrated AuNR solution (OD = 9) wasere diluted to 500 µL using 2 vol% HNO_3. An aliquot of 200 µL of the diluted solution was further diluted to 500 µL with 2 vol% aqua regia, then analyzed by ICP-MS for Au content. Ag content was analyzed in a similar way except treating with 2 vol% HNO_3. Scanning electron microscopy (SEM) images of the AuNRs were taken using an FEI NOVA 230 operating at 5 kV (Figure 4. 2).

4.2 Results and Discussion

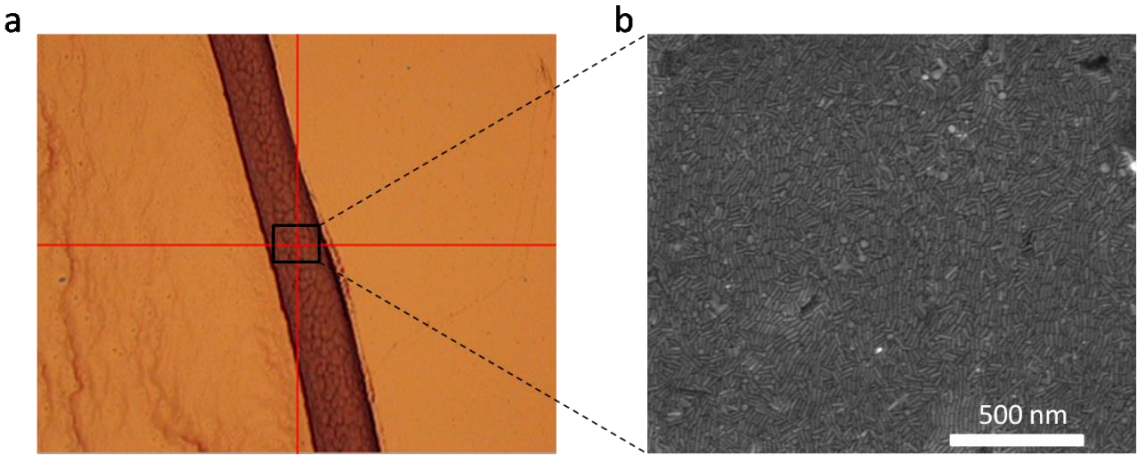

Figure 4. 1. (a) Optical (20× magnification) and (b) SEM images taken from the "coffee-ring" area. In a typical Raman sample preparation process, a droplet of AuNR solution was dropped on a clean Au substrate, forming a so-called "coffee-ring" (dark brown colored area in panel a) on the substrate. This is because the three-phase contact line is pinned, and a capillary flow due to solvent loss by evaporation, drives AuNRs to move outward from the center of the droplet to the droplet's edge. As a result, AuNRs are accumulated along the original droplet edge, forming a "coffee-ring" on the substrate.

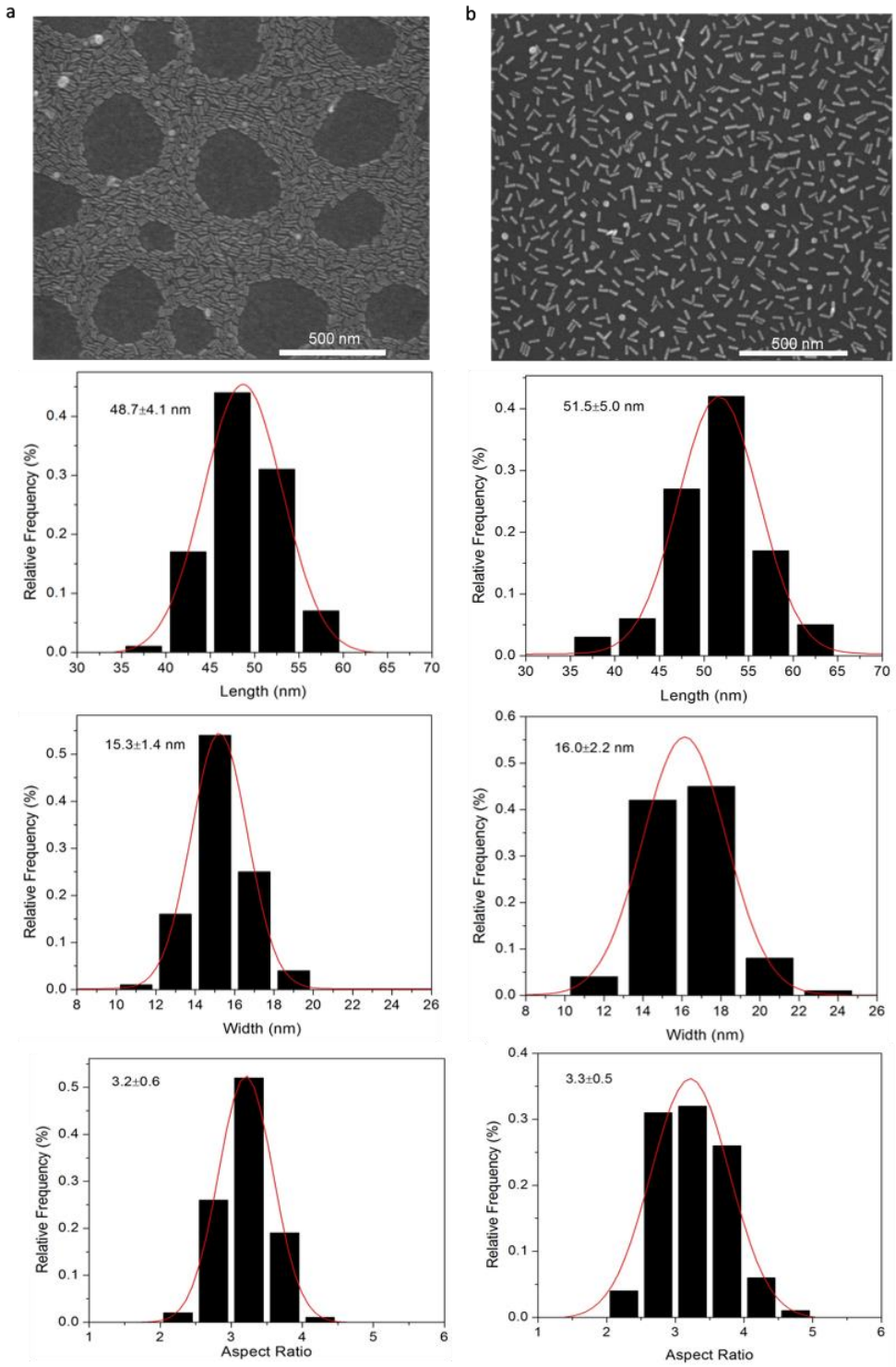

Figure 4. 2. SEM image and statistical analysis: (a) CTAB-capped AuNRs and (b) AuNRs PEGylated by our method. The SEM-based size distribution histograms (row 2-4) are determined by measuring the sizes of 100 nanorods.

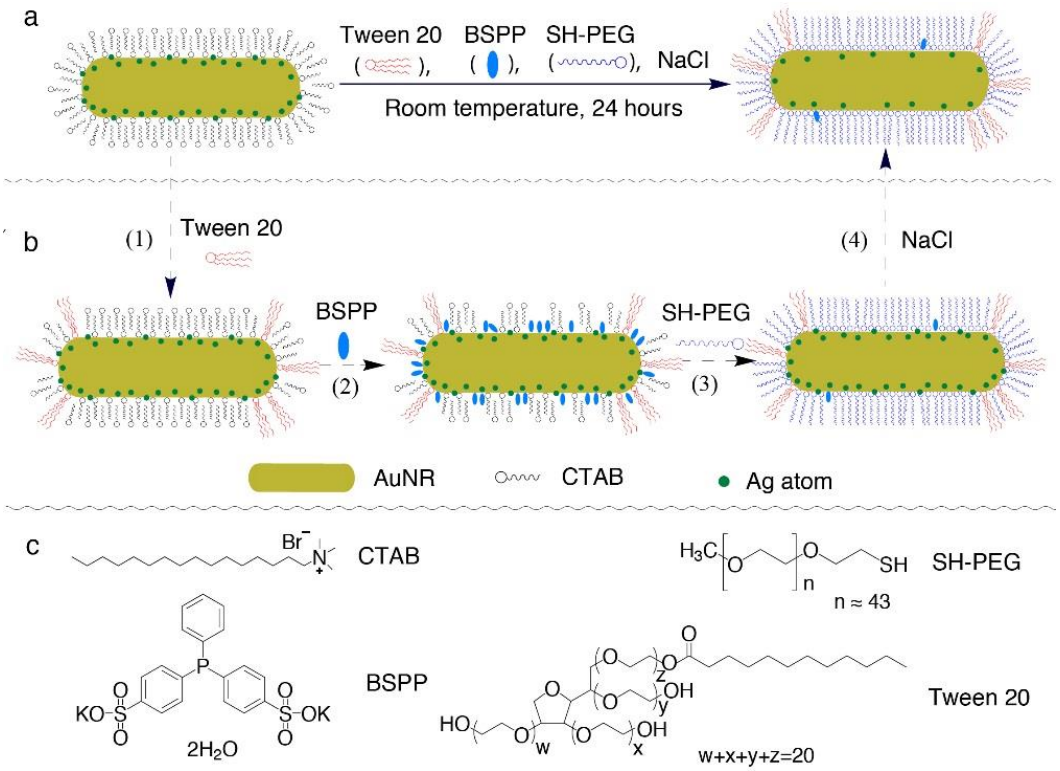

Figure 4. 3. a) A schematic representation of the one-step surface functionalization of AuNRs with thiolated PEG: the PEGylation was conducted by successively adding surfactant Tween 20, bis(p-sulfonatophenyl)phenylphosphine dihydrate dipotassium (BSPP), HS-PEG and NaCl into a CTAB-capped AuNR solution, followed by an incubation at room temperature for 24 h, b) the proposed surface modification mechanism, and c) chemical structures of surface-active compounds. The components are not shown to scale.

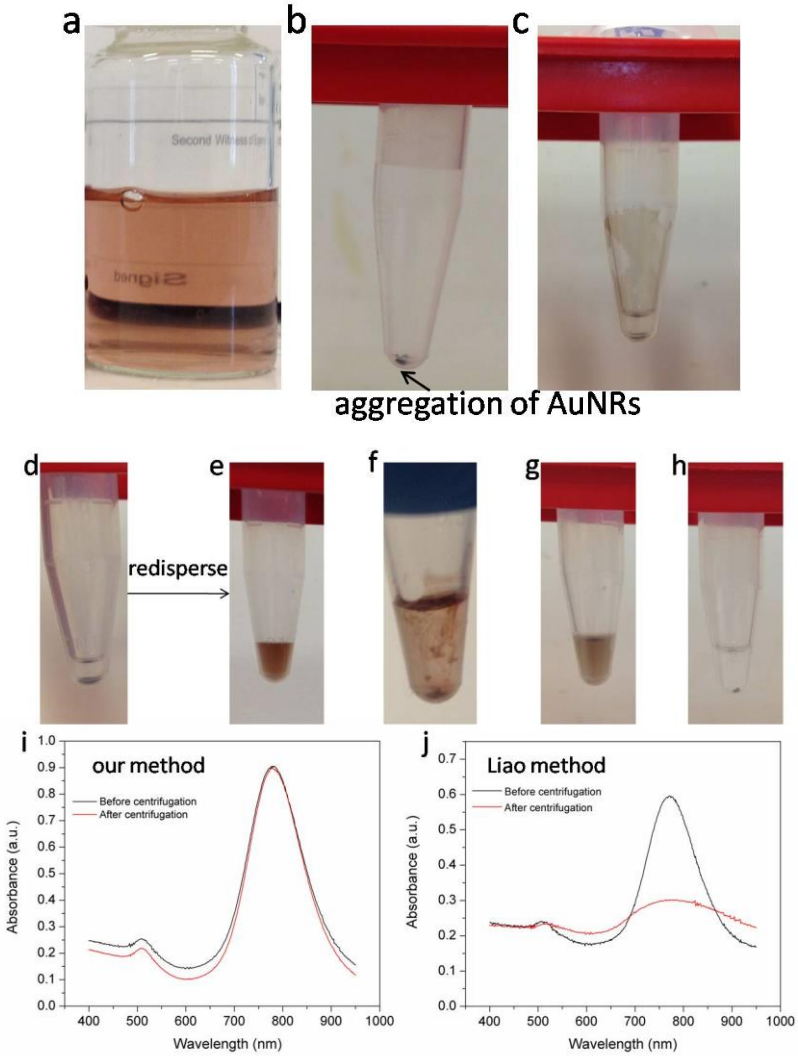

Figure 4. 4. Optical images of CTAB-capped AuNRs: (a) as-synthesized and (b) after four times centrifugation (14800 rpm, 30 min). Four rounds of centrifugation cycles decreased the free CTAB concentration to 0.1 mM (lower than the CTAB critical micelle concentration, 0.8 mM). This results in irreversible aggregation of AuNRs as evidenced in panel b. (c) An optical image of AuNRs PEGylated under the condition of BSPP, SH-PEG, NaCl (without Tween 20). In the absence of Tween 20, the AuNRs tend to stick to~~on~~ the tube wall during centrifugation, which leads to serious loss of AuNRs. (d, e, f) Optical images of PEGylated AuNRs solutions after centrifugation, (g, h) optical images of PEGylated and CTAB-capped AuNRs in a solution containing 0.5 M NaCl and 20 mM phosphate buffer (pH = 7.5). (i, j) UV-vis absorption spectra of AuNRs before (black curve) and after (red curve) centrifugation. The AuNRs were

PEGylated under the conditions of (d, e, g) Tween 20, BSPP, SH-PEG and NaCl (our method), and (f) SH-PEG (Liao method). AuNRs in panel (h) are CTAB-capped AuNRs after three centrifugation cycles. For the AuNRs PEGylated with our method (panel i), they show almost the same absorption spectrum as the original AuNR solution after three centrifugation cycles (14800 rpm, 30 min), indicating their improved colloidal stability. However, for the AuNRs PEGylated with Liao method (panel j), the absorption peak at longer wavelength becomes wider and its intensity drops significantly, which is a sign of partial aggregation of AuNRs.

The purpose of this paper is to report a facile one-step AuNR PEGylation method that allows for the complete removal of surface-confined CTAB (Figure 4. 3). Experimentally, CTAB-capped AuNRs were synthesized through the seed-mediated method developed by El-Sayed et al.[28] The as-synthesized AuNRs are 48.7 ± 4.1 nm in length and 15.3 ± 1.4 nm in width (Figure 4. 2). To effectively exchange the surface-confined CTAB with thiolated PEG, the concentration of free CTAB in the AuNR solution was lowered to a point (~1 mM) where the AuNRs are still colloidally stable and the surface ligand exchange is favourable. A further decrease of free CTAB concentration results in the irreversible aggregation of the AuNRs (Figure 4. 4b).

Once the AuNRs were formed, the AuNR PEGylation was conducted with the successive addition of Tween 20, bis(p-sulfonatophenyl)phenylphosphine (BSPP), monothiol-PEG (HS-PEG, Mw ≈ 2000 g/mol), and NaCl into the CTAB-capped AuNR solution, followed by an incubation at room temperature for 24 h (Figure 4. 3). This method takes advantage of Tween 20 to stabilize AuNRs (step 1, Figure 4. 3b), BSPP to activate the AuNR surface (step 2, Figure 4. 3b) and NaCl to etch silver on the AuNR surface (step 4, Figure 4. 3b). Tween 20, a nonionic and biocompatible surfactant, has been widely used as a stabilizer for the surface modification of gold nanoparticles (AuNPs),[324] and halogens are known to etch silver NPs.[324-325] The reason for choosing BSPP as a surface activation agent is that (1) it is relatively small compared with the PEG molecule and can more easily penetrate through the CTAB bilayer to the AuNR surface, to which it readily chemisorbs; (2) it carries two charges that electrostatically stabilize AuNRs during the surface activation; and (3) the strength of gold-phosphine

bond (13-20 kcal/mol)[326] is in-between those of gold-nitrogen (8 kcal/mol)[327] and gold-sulfur (40-50 kcal/mol) bonds, thus allowing it to displace the CTAB but itself be displaced by the HS-PEG.[328]

To gain further insight into the AuNR PEGylation mechanism, we modified AuNRs with HS-PEG following the procedure illustrated in Figure 4. 3a and compared them by leaving out some key components, such as Tween 20, BSPP and NaCl. The AuNRs PEGylated by our method show an increased colloidal stability against a concentrated saline buffer solution and multiple rounds of centrifugation compared with CTAB-capped ones. They are extremely stable in a solution containing 0.5 M NaCl and 20 mM phosphate buffer (pH, 7.5) while the CTAB-capped ones completely precipitated in the same medium within 1 h (Figure 4. 4). Without Tween 20, the PEGylated AuNRs tend to stick on the wall of centrifuge tubes during the purification process, resulting in a serious loss of AuNRs (Figure 4. 4). Subjected to three centrifugation cycles, the loss of AuNR was 0.8% for our method, while it was 60% for the Liao method (no Tween 20).

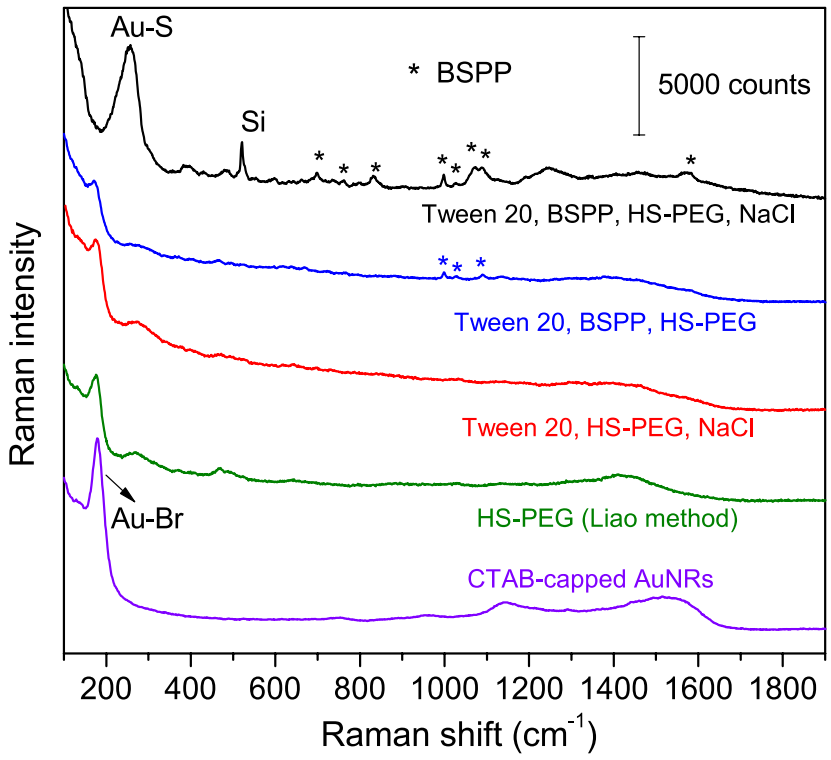

Figure 4. 5. Raman spectra of PEGylated AuNRs prepared under conditions of Tween 20, BSPP, HS-PEG, and NaCl (our method, black curve), Tween 20, BSPP and HS-

PEG (blue curve), Tween 20, HS-PEG and NaCl (red curve) and HS-PEG (the Liao method, green curve). For comparison, the Raman spectrum of CTAB-capped AuNRs (violet curve) is provided as a reference.

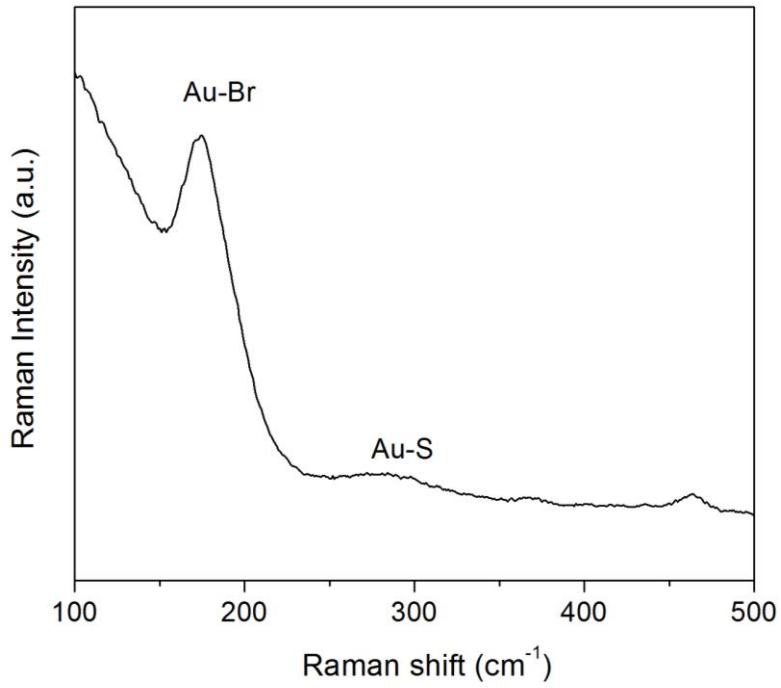

Figure 4. 6. Raman spectrum of AuNRs modified with SH-PEG using a Kinnear method. [233]

Figure 4. 5 shows the Raman spectra of the AuNRs before and after surface modification. All Raman spectra were taken from the "coffee-ring" area, where AuNRs are closely packed, to ensure sensitive and precise surface-plasmon enhanced Raman detection of the surface--bound molecules (Figure 4. 1). As shown in Figure 4. 5, there is only one Raman peak in the range of 100-400 cm^{-1} for the AuNRs prior to (i.e., CTAB-capped AuNRs, violet curve) and after the PEGylation by our method (black spectrum). The Raman peak at 182 cm^{-1} is assigned to the Au-Br bond, while the one at 250 cm^{-1} is ascribed to the Au-S bond.[232, 237] It has been suggested that CTAB adsorbed on the AuNR surface via an Au-Br-N bridge.[114] Upon the PEGylation, the Au-Br peak completely vanishes, suggesting that CTAB has been completely displaced by the PEG molecules. However, both of Au-Br and Au-S peaks are observed for the AuNRs PEGylated by the Liao method (green curve) and our method in the absence of

NaCl (blue curve) or BSPP (red curve). It is worthwhile to mention that Liao et al. observed only Au-S peak rather than Au-Br and Au-S peaks in their Raman experiments.[27] This is because their spectrum was taken from isolated AuNRs[27] rather than from coupled AuNRs as we did here. For isolated AuNRs, the Raman hot spots locate at the tips of the AuNRs and only the molecules at the tips can be excited, while for coupled AuNRs (coffee ring area), as shown in Figure 4. 1, the Raman hot spots locate at the gaps between two adjacent AuNRs and the molecules at both tips and sides of the nanorods can be excited. The observation of only Au-S peak from isolated AuNRs PEGyalted by the Liao method and both Au-Br and Au-S peaks from the coupled ones further confirms that the Liao method produces only tip-modified AuNRs. A similar observation to the Liao method is made for the PEGylated AuNRs prepared using the Kinnear method (Figure 4. 6). In Kinnear's work, the presence of CTAB and HS-PEG on the AuNR surface were revealed by nuclear magnetic resonance spectroscopy.[233] When BSPP is used for the AuNR PEGylation, several new Raman peaks at e.g., 998, 1026 and 1089 cm^{-1} are observed (black and blue curves). These peaks stem from the vibration bands of the phenyl ring of BSPP adsorbed on the AuNR surface,[329] suggesting that BSPP molecules penetrate through the CTAB bilayer and partially replace them (step 2, Figure 4. 3b). The Raman signals of BSPP become stronger for the AuNRs PEGylated in the presence of NaCl (black curve) compared with in the absence of NaCl (blue curve), showing that NaCl facilitates the adsorption of BSPP onto the AuNRs and the removal of the CTAB.

Figure 4. 7 shows high-resolution N1s, Br3d, C1s and Ag3d XPS spectra of the PEGylated AuNRs. In Figure 4. 7 a and b, both N1s (402.6 eV) and Br3d (68.6 and 69.6 eV) peaks are absent for the AuNRs PEGylated by our method (black curve) but if no NaCl (blue curve) or BSPP (red curve) is used, or in the case of the Liao method (green curve) they are observed. This reveals that our method is capable of completely removing CTAB molecules from the AuNRs. The PEGylation efficiency (defined as $\eta = (C_0\text{-}C)/C_0 \times 100\%$, where C_0 is the amount of CTAB bound to the original AuNRs and C is the amount of CTAB remaining on the AuNRs after PEGylation as determined using the nitrogen contents obtained from the XPS measurements derived from the CTAB) is calculated to be 52% (the Liao method)[237], 46% (without BSPP), 67%

(without NaCl) and 100% (our method) (see Supporting Information for calculation details). The higher PEGylation efficiency for AuNRs modified in the presence of BSPP further confirms that BSPP serves as a surface activation agent for the AuNR PEGylation, which is in good agreement with the Raman results shown in Figure 4. 5.

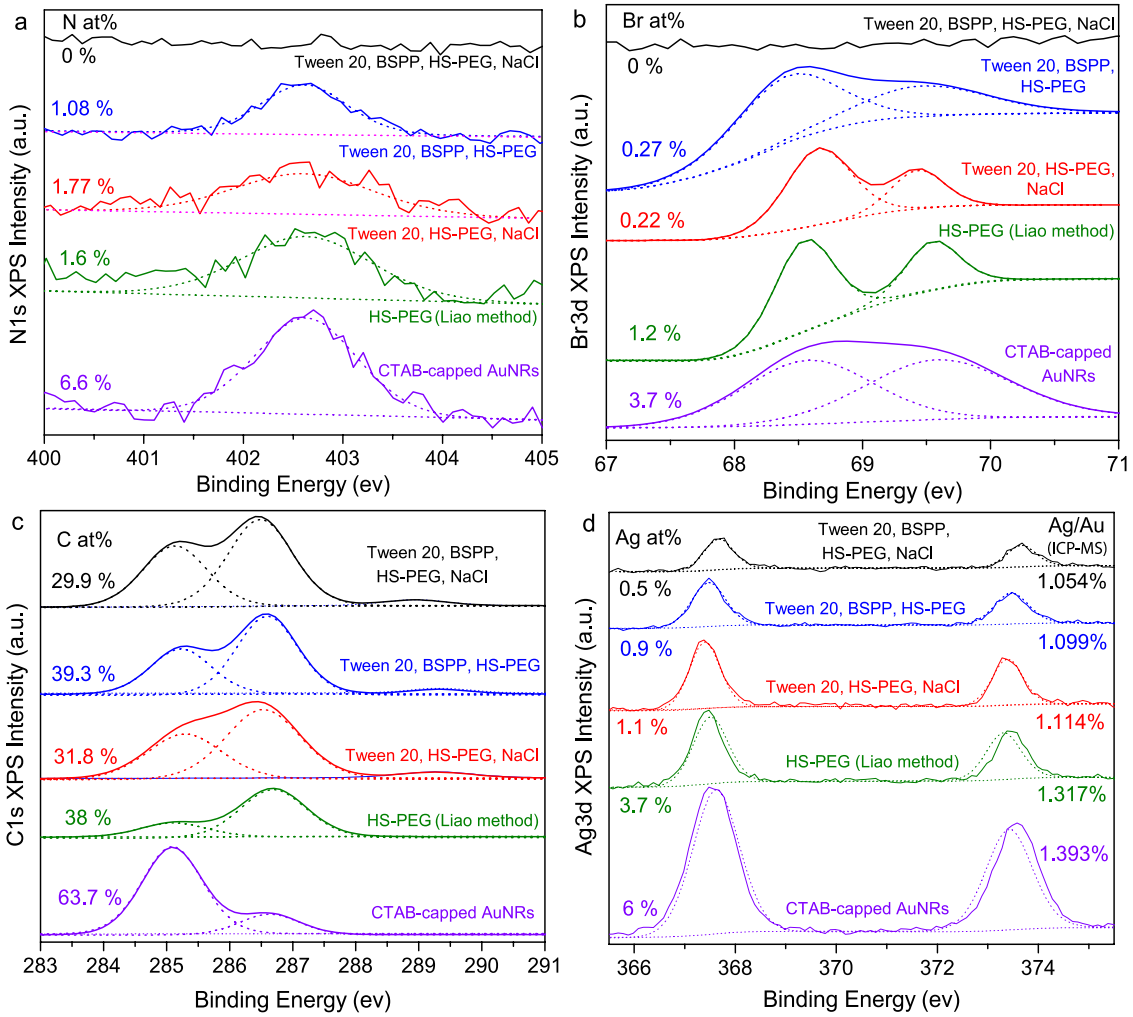

Figure 4. 7. High-resolution a) N1s, b) Br3d, c) C1s, and d) Ag3d XPS spectra of PEGylated AuNRs synthesized under conditions of Tween 20, BSPP, HS-PEG and NaCl (our method; black curve), Tween 20, BSPP and HS-PEG (blue curve), Tween 20, HS-PEG and NaCl (red curve), and HS-PEG (Liao method; green curve). For comparison, N1s, Br3d, C1s, and Ag3d spectra of CTAB-capped AuNRs (violet curves) are provided as references. The atomic percentage of N, Br, C, and Ag obtained from XPS survey spectra (Figure 4. 9) are listed in the corresponding panels. The Ag/Au ratio obtained from ICP-MS measurements are also listed in panel d.

High-resolution C1s spectra (Figure 4. 7c) show two peaks at 285.0 and 286.5 eV that are assigned to C-C and C-O bonds for all samples. The C-O peak observed in the CTAB-capped AuNRs (violet curve) might arise from adventitious carbon contaminants while the C-C peak is derived mainly from the alkyl chain of CTAB. A new C1s peak at 288.5 eV is observed from the AuNRs PEGylated in the presence of Tween 20 (black, blue and red curves). This peak is ascribed to the ester group in the surfactant Tween 20, providing evidence that Tween 20 adsorbs onto the AuNRs. This also suggests that the C-C component for the AuNRs PEGylated by our method (black curve) predominantly comes from the long alkyl chain of Tween 20 rather than CTAB, as no CTAB signal (N1s) is observed in Figure 4. 7a. Compared with CTAB-capped AuNRs, the increase of C-O/C-C ratio following HS-PEG loading is indicative of the presence of $(-CH_2-CH_2-O-)_n$ repeating unit of PEG molecules[330] on the AuNRs. The AuNRs PEGylated by our method have relatively low percentage of C compared to that of AuNRs PEGylated by Liao method, which might result~~ing~~ from the presence of Tween 20 in our method (Figure Figure 4. 8).

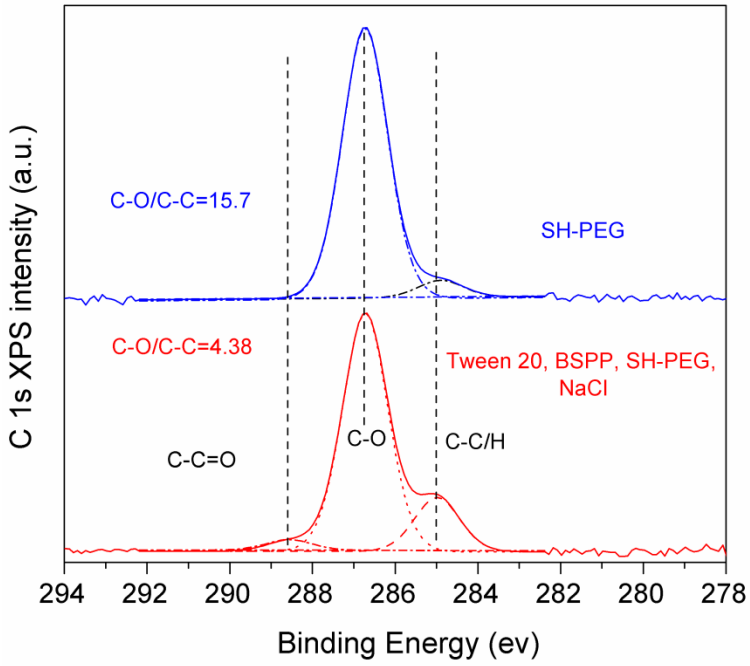

Figure 4. 8. High-resolution C1s XPS spectra of a cleaned Au substrate incubated with PEG2000-SH for 24 h (blue curve); Tween 20, mPEG2000-SH, BSPP, NaCl for 24 h (red curve).

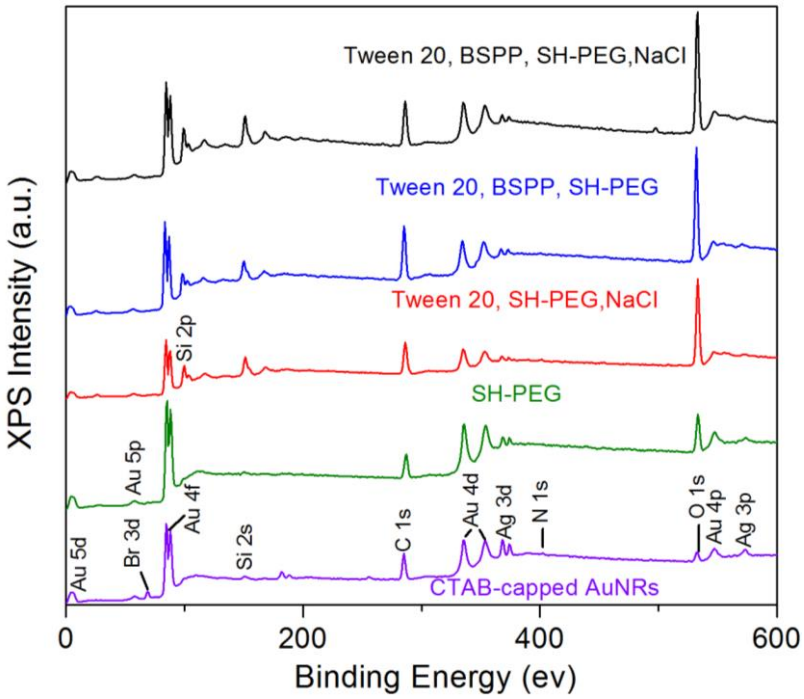

Figure 4. 9. Survey scan of PEGylated AuNRs synthesized under conditions of Tween 20, BSPP, SH-PEG and NaCl (our method, black curve), Tween 20, BSPP and SH-PEG (blue curve), Tween 20, SH-PEG and NaCl (red curve), and SH-PEG (i.e., Liao method, green curve). For comparison, a survey scan of CTAB- capped AuNRs is provided as a reference (violet curve).

Samples	% XPS elemental composition						
	P	C	O	N	Br	Ag	Au
1	0.27	29.9	67.5	0	0	0.5	0.68
2	0.14	39.3	55.7	1.08	0.27	0.9	2.38
3	-	31.8	62.1	1.77	0.22	1.1	2.7
4	-	38	42.4	1.6	1.1	3.7	12.01
5	-	63.7	8.4	6.6	3.7	6	8.06

Table 4. 1. Elemental percentages of AuNRs PEGylated under conditions of (1) Tween 20, BSPP, HS-PEG, and NaCl, (2) Tween 20, BSPP and HS-PEG, (3) Tween 20, HS-PEG and NaCl, and (4) HS-PEG (i.e., the Liao method. For comparison, the elemental percentages of (5) CTAB-capped AuNRs are provided as a reference.

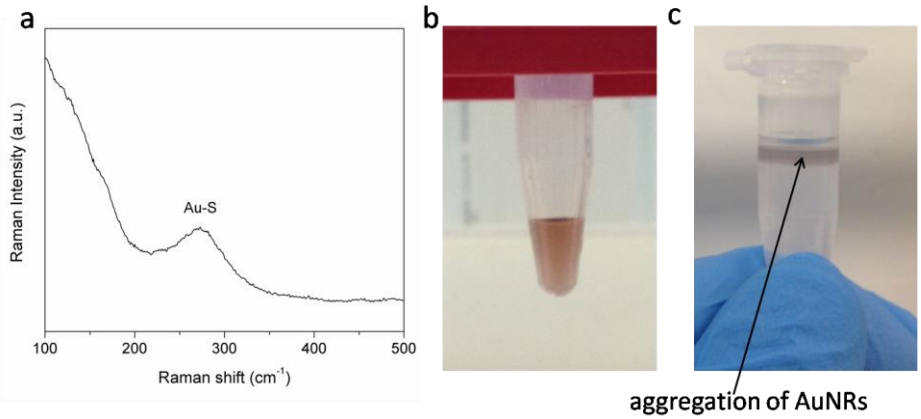

Figure 4. 10 (a) Raman spectra of AuNRs modified by SH-PEG-COOH (SH-$C_{11}H_{22}$-$(OCH_2CH_2)_6$-OCH_2COOH: Prochimia) using our method. (b) Optical images of AuNRs after the surface modification with SH-PEG-COOH using (b) our method and (c) Liao method

As shown in Figure 4. 7d, two Ag3d peaks (367.6 and 373.6 eV) are observed for all samples. The Ag content decreases significantly from CTAB-capped AuNRs (violet curve), to AuNRs prepared by the Liao method (green curve) and again to AuNRs PEGylated by our method (black curve). It has been reported that BSPP and NaCl can etch silver forming BSPP-Ag^+ complex[319, 322-323] and AgCl,[319, 321] respectively. The silver etching reaction with BSPP is competitive with the AuNR surface activation reaction illustrated in scheme 1b (step 2). The use of NaCl for silver etching promotes the AuNR surface activation, which explains the higher PEGylation efficiency in the presence of both BSPP and NaCl. Inductively coupled plasma mass spectrometry (ICP-MS) measurements show that ~25% of silver was removed from the AuNRs by our method. Further exposure of these AuNRs to an air-equilibrated water for two weeks, the Ag/Au ratio of the AuNRs (1.059%) remains almost unchanged, revealing that the most active silver atoms on the AuNR surface were removed during the PEGylation process. It is worth noting that the surface functionalization method developed here can also be extended to other surface ligands, such as thiol-PEG-carboxyl (Figure 4. 10). The direct exposure of positively charged CTAB-capped AuNRs to these negatively charged surface ligands involves a change of surface charge from positive to negative. This results in the irreversible aggregation of AuNRs (Figure 4. 10).

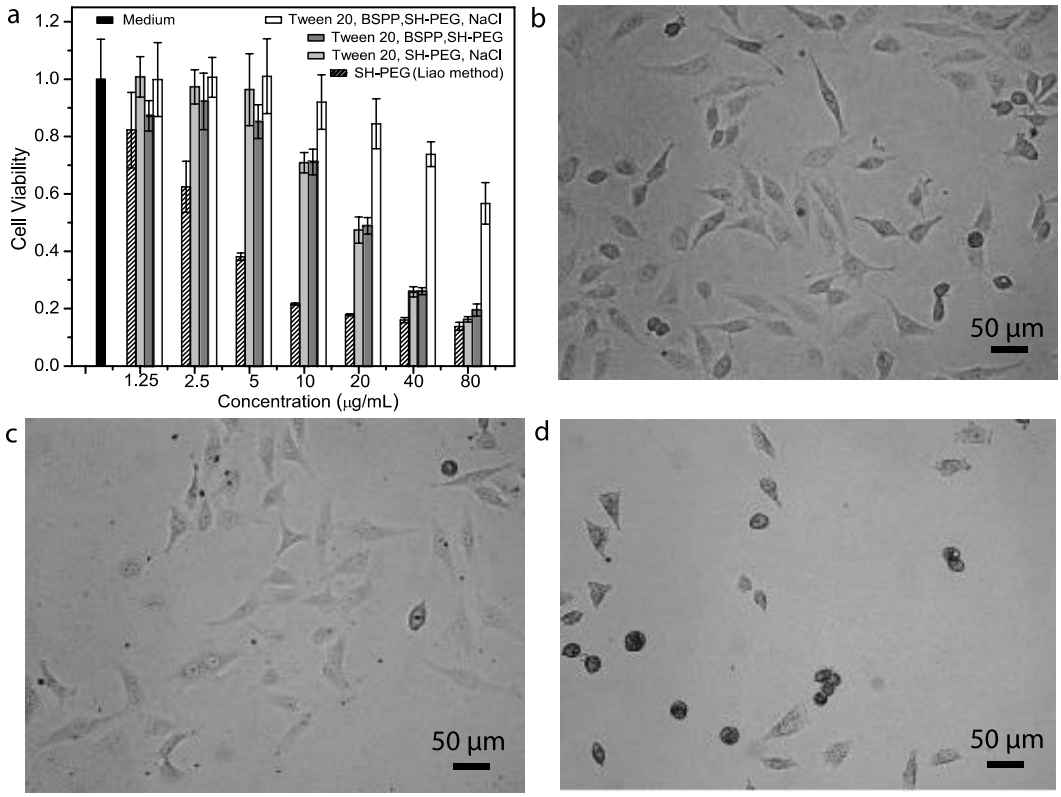

Figure 4. 11. Cell viability: a) Dose-dependent cell viability of HeLa cells determined by the MTT assay after exposure to AuNRs for 24 h and optical images of HeLa cells treated with b) DMEM (control), c) 80 μg/mL of AuNRs PEGylated by our method and d) 80 μg/mL of AuNRs PEGylated by Liao method (incubation time: 4 hours).

As AuNRs have emerged as a new type of nanostructure for diagnostic and therapeutic applications,[38, 171] it is important to understand their potential risks to human health. Hence the in vitro cytotoxicity of the PEGylated AuNRs on HeLa cells (human cervical carcinoma cell line) using MTT-based colorimetric assay was examined. HeLa cells were chosen in our research as they are sensitive to CTAB.[312] The cytotoxicity of the CTAB-capped AuNRs is not shown here because these AuNRs completely precipitated in the cell culture medium (Dulbecco's modified Eagle's medium). Figure 4. 11a shows the cell viability of HeLa cells as a function of AuNR concentration. As presented in Figure 4. 11a, the cell viability is critically dependent on the AuNR concentration and the amount of remaining CTAB and Ag on the AuNRs. The cell viability decreases with the increase in the amount of AuNRs. However, when using the same amount of

AuNRs, the cell viability decreases with an increase in the amount of residual CTAB and Ag on the AuNRs. The AuNRs PEGylated by our method showed by far the lowest toxicity with no apparent toxicity when the AuNR concentration is below a concentration of 5 μg/mL. Even at a high AuNR concentration of 80 μg/mL, they still show a cell viability of ~57%, which is four times higher than that (~14%) of the AuNRs PEGylated by the Liao method. The viability of HeLa cells was also recorded by the morphological criteria using optical microscope (Figure 4. 11b-d). The majority of the cells treated with AuNRs PEGylated by our method (Figure 4. 11c) show a typical spindle-like shape the same as those shown in the control experiment (Figure 4. 11b), which is indicative of the cells being alive and healthy (AuNR concentration: 80 μg/mL, incubation time: 4 h). However, the cells incubated under the same conditions with AuNRs PEGylated by the Liao method (Figure 4. 11d) are round in shape, which is a sign of cell death for HeLa cells. It is believed that the complete removal of CTAB and the most active silver on the surface layer of AuNRs are responsible for the high cell viability of the AuNRs PEGylated by our method.

4.3 Conclusions

In conclusion, we have developed a novel, simple, one-step surface modification method to produce biocompatible AuNRs. This was achieved by using a nonionic surfactant – Tween 20 to stabilize the AuNRs, BSPP to activate the AuNR surface for the subsequent PEGylation and NaCl to etch silver pre-deposited on the surface of AuNRs. This method allows for the complete functionalization of AuNRs with thiolated PEG and the removal of the most active silver on the AuNR surface. The PEGylated AuNRs show a significantly enhanced colloidal stability against a high concentration buffered saline solution and multiple rounds of centrifugation compared to CTAB-capped and partially modified AuNRs. We also investigated the cytotoxicity of the PEGylated AuNRs using HeLa cells as model cells. The AuNRs PEGylated by our method exhibit a complete detoxification at an AuNR concentration lower than 5 μg/mL. At a high concentration of 80 μg/mL, their cytotoxicity is about four times lower than that of the AuNRs PEGylated by the Liao method. Finally, this work represents a simple proof-of-concept experiment for the complete PEGylation and detoxification of

CTAB-capped AuNRs. The surface modification method developed here can be easily extended to negatively-charged surface ligands, e.g. thiol-PEG-carboxyl, and other NP systems with different compositions and shapes.

Chapter 5 Applications: Effective Photocatalysts by Compositing AuNRs with Crystallized TiO_2

Semiconductor nanoparticles have been widely explored and applied in solar cells,[246-248] water splitting,[239-240] artificial photosynthesis,[249-251] and degradation of environmental pollutants.[252-253] As the most promising and extensively studied semiconductor catalyst, TiO_2 has been attracting tremendous attention ever since its extraordinary photocatalytic activity was discovered by Fujishima and Honda.[254] In spite of the advantages of TiO_2 in terms of abundance, chemical and thermal stability, and non-toxicity, pure TiO_2 is still far from being a perfect photocatalyst.[261] This is mainly because the photoresponse of TiO_2 is limited to UV light region resulting from its large band gap (3.2 eV) together with the relative low photocatalytic efficiency owing to fast recombination of photogenerated electron-hole pairs. Many strategies, including doping TiO_2 with metal (e.g. Ag,[262] Au,[68-69] Pt,[263] etc.) or non-metal elements (e.g. N,[264] C,[265] etc.), sensitizing TiO_2 with small band gap quantum dots (e.g. CdS,[249] PbS,[266] etc.) or dyes,[267-269] have been proposed to improve the photocatalytic performance of TiO_2. Among these methods, the integration of AuNPs with TiO_2 has been proved as a promising and viable one. As is well-known that conduction band electrons of AuNPs interact strongly with light and undergo a collective oscillation, this leads to the so-called SPR.[32] Therefore, the extinction cross-section and the localized electromagnetic field of these nanoparticles are largely boosted, which can help to enhance the light adsorption of TiO_2 and promote the charge separation.[69, 240, 260, 282]

To date, most studies focused on the fabrication of Au/TiO_2 nanocomposites using AuNSs with narrow SPR band and limited light-harvesting ability.[241, 243-245, 270-274] While the huge potential of AuNRs, with intense absorption band ranging from Vis to NIR range, has not been fully exploited in the photocatalytic applications. Among the limited reports, AuNRs/TiO_2 nanocomposites have been fabricated in the form of yolk-shell,[80] core-shell,[67, 78, 289] dumbbell-shaped nanostructures,[68] and so on.[69, 290-292] In most cases, an amorphous TiO_2 component that is inactive under UV light is applied,

thus, limiting the photocatalytic performance of these AuNRs/TiO_2 nanocomposites within Vis and/or NIR range. As anatase is generally considered the most efficient TiO_2 polymorph in photocatalytic reactions,[293] high-temperature calcination (above 450℃) is usually required for the crystallization.[294] A significant challenge arises when treating anisotropic AuNRs involved nanocomposites with high-temperature calcination, as they will transform into the most thermodynamically stable spherical shape at temperatures much lower than the melting point of bulk gold, thus losing their extraordinary optical properties.[102] It seems that a compromise has to be made between the crystallization of TiO_2 and the stability of AuNRs. The fabrication of intimate integrated AuNRs/anatase TiO_2 nanocomposites that can fully utilize UV-Vis-NIR light is still strongly desired.

In this chapter, we report a facile method for the synthesis of AuNRs@anatase TiO_2 core-shell nanostructures by uniformly coating TiO_2 on AuNRs through elaborate-controlled hydrolysis of titanium dioxide precursor followed by hydrothermal treatment (~75 ℃, ~1.4 atm). Upon thermal treatment, the amorphous TiO_2 shell gets converted to crystalline oxides. The core-shell structure together with the relatively low-temperature treatment is~~are~~ important in preserving the intactness of the gold core. The shell thickness can be varied in the range of 3~20 nm by changing the concentration of titania precursor, and this method can be successfully extended to AuNRs with different aspect ratios and citrated-capped AuNSs. The AuNRs@TiO_2 nanostructures well-maintain the plasmonic character of the gold core~~,~~ and their absorption band can be easily tuned in a wide region by adjusting the aspect ratio of AuNRs. Compared to other configurations, such as yolk-shell and Janas, the core-shell structure is much advantageous not only in protecting the core from photocorrosion and reshaping~~,~~ but also in providing three-dimensional and close contact between the core and shell which facilitates the charge carrier transfer in the photocatalytic process. In addition, the AuNRs@anatase TiO_2 nanostructures show significantly enhanced H_2 generation ability under UV-Vis-NIR irradiation. The possible mechanism was also discussed by taking the composition of irradiation light into consideration.

5.1 Experimental Section

5.1.1 Chemicals and Materials

The following chemicals were purchased from Sigma-Aldrich and used as received without further purification: gold (III) chloride trihydrate ($HAuCl_4 \cdot 3H_2O$, ≥ 99.9%), hexadecyltrimethylammonium bromide (CTAB, ≥ 99%), sodium borohydride ($NaBH_4$, ≥ 99%), silver nitrate ($AgNO_3$, ≥ 99%), hydroquinone (HQ, ≥ 99%), 5-bromosalicylic acid (5-BA, 90 %), sodium citrate dihydrate (≥ 99%), Tween 20, ethylene glycol (EG, 99.8 %), titanium (IV) butoxide (TBT, 97%). Hydrochloric acid (HCl, 32 wt. %) and acetone were purchased from Merck KGaA. Ultra-pure water (18.2 MΩ) was used for all experiments.

5.1.2 Synthesis of AuNRs

CTAB-capped AuNRs were synthesized according to a seedless strategy recently reported.[168] Typically, 5 mL CTAB (0.1 M) together with 0.0219 g 5-BA were first dissolved in warm water (~60 ℃) and then cooled to 30 ℃. After the addition of 100 μL, 200 μL, 300 μL, and 400 μL $AgNO_3$ solution (4 mM), the mixture was kept undisturbed at 30 ℃ for 15 min. Then 5 mL $HAuCl_4$ (1 mM) and 8 μL HCl (32 wt. %) was added to the previous solution and gently stirred for 30 min. To this solution, 300 μL of 0.1 M HQ was added, and the orange-yellow colour gradually faded to colourless. After that, 20 μL freshly-prepared $NaBH_4$ solution (0.25 mM) was added to initiate the reaction. Subsequently, the reactant mixture was stirred for 30 s and left undisturbed at 30 ℃ for 24 h for AuNRs growth.

For the synthesis of citrate-capped AuNPs, a citrate reduction method was applied.[331] Generally, 1.0 mL sodium citrate solution (34 mM) was injected rapidly into 100 mL boiling $HAuCl_4$ solution (0.25 mM) with vigorous stirring. When the colour of the $HAuCl_4$ solution changed from black to red in 2 min, the reaction flask was immediately removed from the hot plate to a cold plate and kept stirring until cooled down to room temperature.

5.1.3 Synthesis of AuNRs@amorphous TiO_2 Core-Shell Nanostructures

A precursor solution was made by adding 50 μL TBT into 10 mL EG, and the TBT-EG mixture solution was sealed and underwent vigorous stirring overnight. This resultant precursor solution was marked as **solution A**.

For the synthesis of AuNRs@amorphous TiO_2 nanocomposites, the as-synthesized AuNRs were first purified by two centrifugation cycles (16200 rcf, 30 min) to remove excess CTAB and unreacted products. After the final step of purification, the AuNRs were redispersed in ultrapure water. Then 35 μL AuNRs solution was added into 10 mL acetone, and the solution was stirred for 5 min in ice-bath and marked as **solution B**. Subsequently, various volumes (2 μL to 20 μL) of **solution A** were added dropwise into **solution B** with gentle stirring (200 rpm) for 1 h in ice-bath. After that, the products were collected by concentration (centrifuge at 4000 rcf, 10 min) and redispersed in 0.8 mM CTAB solution, this process was repeated twice and finally dispersed in 10 mL 0.7 mM CTAB solution.

For the synthesis of AuNSs@amorphous TiO_2 nanocomposites, the as-synthesized citrate-capped AuNSs underwent two rounds of centrifugation (5000 rcf, 20 min), and finally dispersed in ultrapure water. The coating process is same as~~with~~ that of AuNR except the products were purified and dispersed in 10 mL 0.5 vol % Tween 20 solution instead of the CTAB solution.

5.1.4 Low-Temperature Hydrothermal Treatment for TiO_2 Crystallization

The amorphous core-shell nanoparticles solution placed in a 20 mL vial was transferred into a 40 mL Teflon-line stainless autoclave~~,~~ and thermally treated for several hours at 70 ℃ to 90 ℃. After that, the solution was centrifuged (4000 rcf, 10 min) and redispersed in methanol, this process was repeated for 3 times.

5.1.5 H_2 Production Tests

The H_2 production experiments were performed in a 250 mL quartz-made reactor equipped with a port for measurements of H_2 gas at regular time intervals. A known amount of catalyst was dispersed in a 200 mL methanol/water (1:4 by volume) solution and subsequently added into the reactor. Here, methanol was applied as the sacrificial agent. The reaction media was carefully thermostated at 25 ℃ to prevent any significant evaporation of the sacrificial agent through a fan in the chamber and the water-cooling system. The solution was purged in advance with pure N_2 for 30 min to remove the dissolved oxygen before irradiation. Then, the reactor was photoirradiated with magnetic stirring using a 300 W Xenon lamp with the light wavelength ranging from 200 nm to 2500 nm through a filter. The irradiation intensity was 0.4 $W \cdot cm^{-2}$. The H_2 content was measured at 30 min intervals for 3 h using a gas chromatograph system (GC 2060, Ramiin) with a flame ionization detector (FID).

5.1.6 Photoelectrochemical (PEC) Measurements.

The photoelectrodes were prepared by the drop-casting method. In a typical process, 2 mg of the catalyst was dispersed in 0.5 mL of ethanol by sonication, and then the suspension was dropped onto fluorine-doped tin oxide glass (FTO, 2 cm × 1.5 cm) through a layer-by-layer method. Photocurrent measurements were undertaken in a 0.2 M Na_2SO_4 solution as the electrolyte at room temperature by using an electrochemical workstation (PARSTAT 2273) with a bias of 0.3 V in a two-electrode PEC cell with Pt as the counter electrode and reference electrode and the catalyst-coated FTO glass as the working electrode. The electrolyte solution was purged with pure N_2 for 10 min prior to the measurement, and the purging process continued for the whole photocurrent measurements. The photocurrent was recorded under the irradiation of a 300 W Xe lamp. To minimize the heat effect, a water jacket was placed between the Xe lamp and the PEC cell.

5.1.7 Characterization

UV-Vis-NIR absorption spectra were recorded by a Shimadzu UV mini 1240 UV-Vis-NIR spectrophotometer with a 1 cm quartz cell at room temperature. Morphologies and structure of the nanocomposites were characterized with SEM (FEI Nova NanoSEM 450 FESEM) and TEM (FEI Tecnai G2 T20). The metal loading of gold was determined by means of inductively coupled plasma optical emission spectrometer (ICP-OES) analysis which performed on a SPECTRO ARCOS End-On-Plasma (SPECTRO Analytical Instruments GmbH). Powder X-ray diffraction (PXRD) patterns were recorded in the 2θ range of 20˚- 90˚ at room temperature using a Miniflex 600 diffractometer (Rigaku, Japan) in a transmission geometry using Cu Kα radiation (15 mA and 40 kV) at a scan rate of 2 ˚/min and a step size of 0.02˚.

5.2 Results and Discussion

5.2.1 Growth Mechanism and Optical Properties

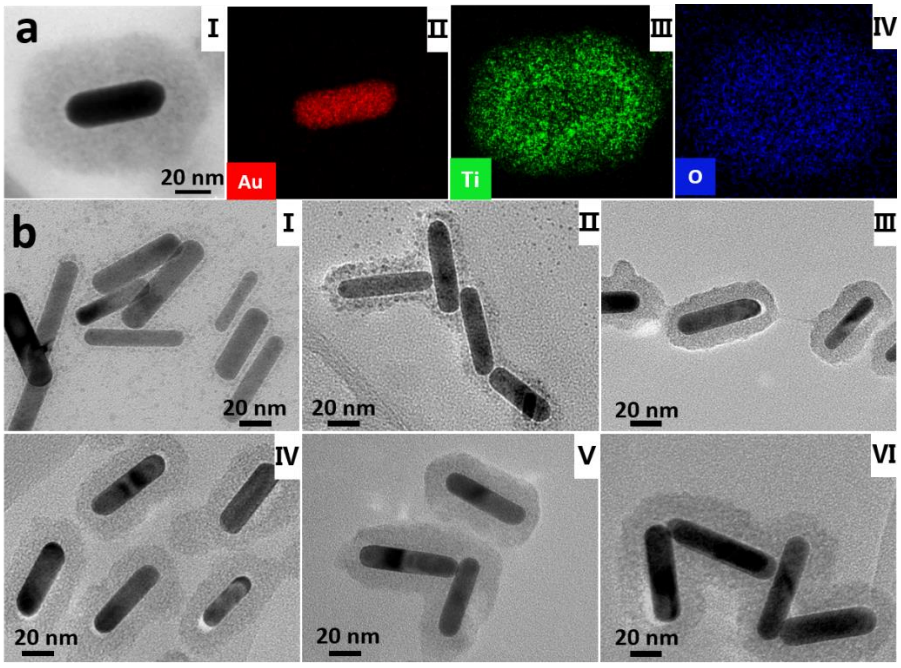

Figure 5. 1. (a) TEM image and elemental mapping of a single AuNR@TiO_2 core-shell nanoparticle. (b) TEM images of AuNRs@TiO_2 nanoparticles synthesized by adding 2

μL, 5 μL, 7 μL, 10 μL, 15 μL, and 20 μL **solution A** into 10 mL **solution B**, respectively. The thicknesses of the shell are measured to be 3 ± 1 nm, 7 ± 2 nm, 10 ± 2 nm, 13 ± 4, nm, 17 ± 4 nm, 22 ± 5 nm, respectively.

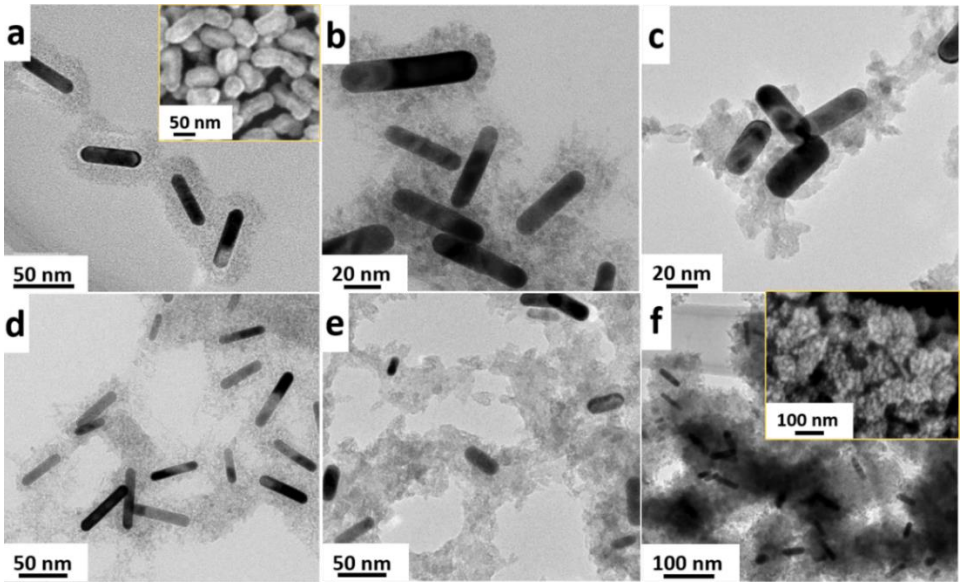

Figure 5. 2. TEM images of TiO_2@AuNRs core-shell nanoparticles prepared with different water content: (a) 0.35 v %, (b) 0.50 v %, (c) 1.00 v %, (d) 1.50 v %, (e) 2.00 v %, (f) 3.50 v %. Insets are the SEM images of the samples corresponding to (a) and (f).

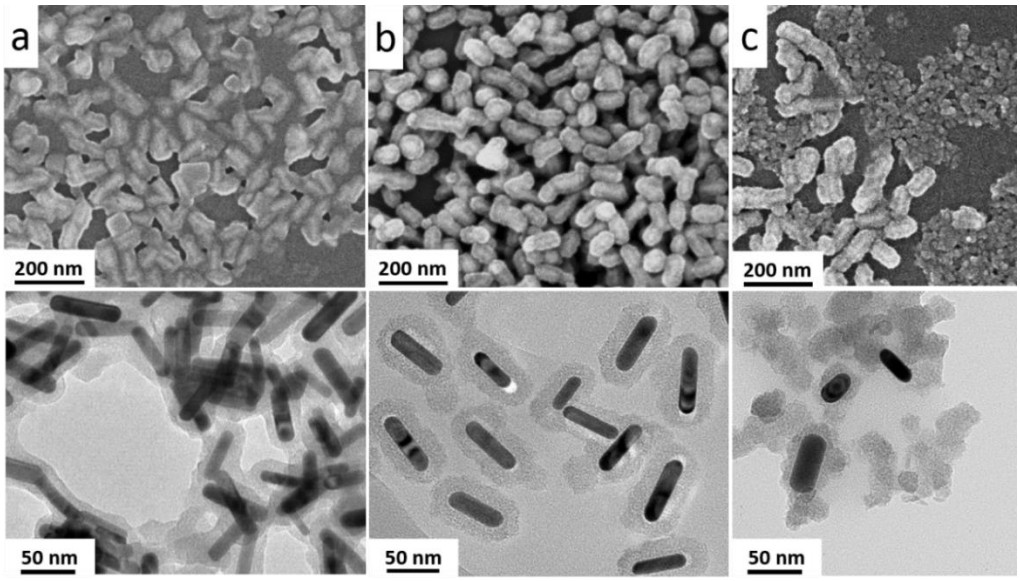

Figure 5. 3. TEM and SEM images of TiO_2@AuNRs nanoparticles dispersed in (a) pure water, (b) 0.7 mM CTAB, and (c) 1.2 mM CTAB during hydrothermal treatment.

Figure 5. 1 shows that AuNRs@TiO_2 core-shell nanostructures were successfully obtained through controlled hydrolysis of TBT-EG precursors in an aqueous solution containing CTAB-AuNRs and acetone. The formation of the core-shell structures was further confirmed by energy-dispersive x-ray (EDX) mapping. Figure 5. 1a(II, III, IV) shows that the core contains element of Au and the shell is made of Ti and O. The TiO_2 shell thickness can be readily controlled from about 3 nm to 22 nm by adjusting the amount of titanium glycolate (**solution A**) added into the acetone solution (**solution B**) (Figure 5. 1b). Uniform TiO_2 coating with a controllable thickness on metal nanoparticles has been proved to be challenging mainly due to the fast hydrolysis of titania precursors and concurrent nucleation and growth process. In our stepwise coating procedure, the hydrolysis of titania precursor was tempered by forming relatively stable TBT-EG complex, which effectively helps to separate nucleation and growth of TiO_2.[332] While acetone acts as an important media in enhancing the affinity between TiO_2 and AuNRs by means of reacting with elemental Ti in TBT-EG via covalent bond and chemically adsorbing on the metal surface through a dipole-dipole interaction.[333]

It's worth mentioning that the water content is an important factor for the formation of uniform core-shell structure. A small amount of water (~ 0.35 v %) is required for the hydrolysis of titania precursors in the formation of isolated AuNRs@TiO_2 core-shell nanostructures, as shown in Figure 5. 2a. At higher water content (0.5 v % to 3.5 v %, Figure 5. 2b-f), the AuNRs were also coated with titanium dioxide shell, however, they were cross-linked together by a titanium dioxide network and isolated core-shell structure was hardly formed. In addition, the presence of hydroxyl group on the surface of TiO_2 tends to make the as-synthesized AuNRs@TiO_2 nanoparticles adhered together by forming the hydrogen bond.[267] To preserve the TiO_2 shell morphology and prevent the fusion during the thermal treatment, the SiO_2 coating is usually applied as the protective layer which can be removed by a base etching process afterwards.[80, 334] In our work, this is achieved simply by using the dilute CTAB solution as a stabilizer during the hydrothermal treatment (Figure 5. 3). To confirm the critical role of CTAB, two control experiments were carried out. Figure 5. 3a shows that without the protection of CTAB, the synthesized nanoparticles agglomerated together. On the other hand, when excess CTAB was applied (1.2 mM, Figure 5. 3c), a large amount of quasi-

spherical TiO_2 nanoparticles were produced, which is a sign of self-nucleation. Figure 5. 3b shows that AuNRs@TiO_2 core-shell nanoparticles were synthesized under the protection of 0.7 mM CTAB. The use of proper water content and appropriate CTAB concentration are vital for the successful synthesis of core-shell nanostructure in our method.

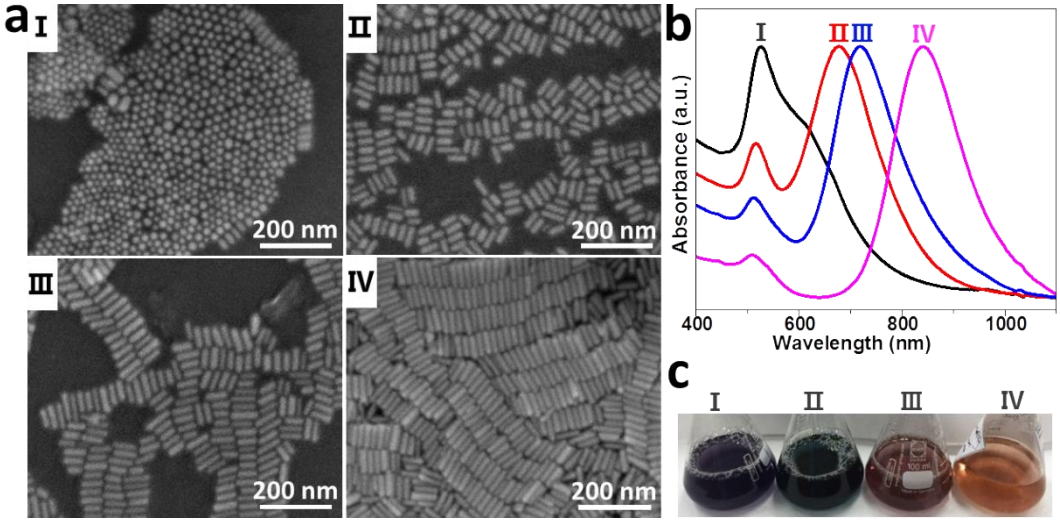

Figure 5. 4. (a) SEM images, (b) UV-Vis spectra and (c) digital photos of AuNRs synthesized using different amount of 4 mM $AgNO_3$ (100 μL, 200 μL, 300 μL, and 400 μL). The average length and width of the AuNRs are: (Ⅰ) 20.11 ± 1.95 nm, 13.57 ± 10.49 nm, (Ⅱ) 45.94 ± 5.84 nm, 17.96 ± 2.45 nm, (Ⅲ) 54.33 ± 8.13 nm, 15.79 ± 1.68 nm, (Ⅳ) 59.21 ± 4.22 nm, 15.98 ± 1.52 nm.

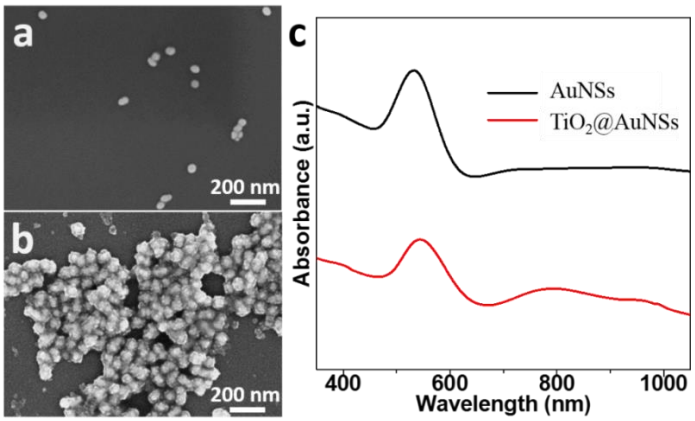

Figure 5. 5. SEM images of (a) AuNSs and (b) TiO_2@AuNSs, (c) UV-Vis-NIR spectra of AuNSs and TiO_2@AuNSs. The gold loading is determined to be 3.1 wt. %.

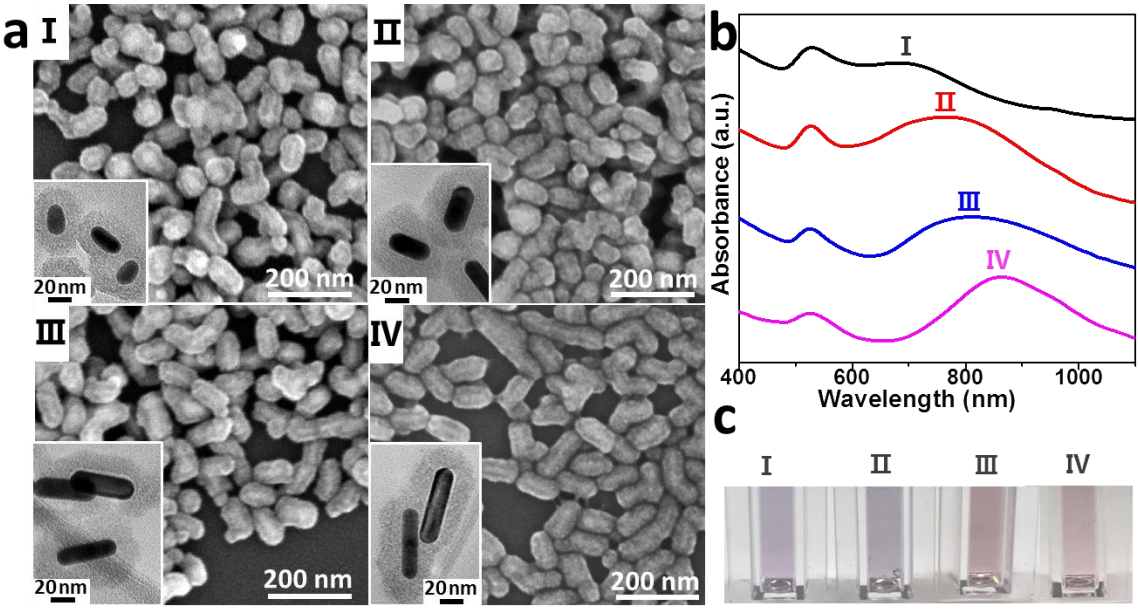

Figure 5. 6. (a) SEM images and TEM images, (b) UV-Vis spectra and (c) digital photos of AuNRs@amorphous TiO_2 nanoparticles prepared using gold cores specified in Figure 5. 4. The gold loading determined by ICP-OES are: (Ⅰ) 2.9 wt. %, (Ⅱ) 2.8 wt. % (Ⅲ) 3.4 wt. %, (Ⅳ) 3.7 wt. %.

Furthermore, the coating method can be successfully extended to AuNRs with different aspect ratios (Figure 5. 4) and citrate-capped AuNPs (Figure 5. 5). Note that, for the successful fabrication of AuNPs@TiO_2 core-shell nanostructures, the citrate-capped AuNPs also need to be dispersed in a stabilizing medium (0.5 v % Tween 20 in this case) during the hydrothermal treatment process. UV-Vis-NIR absorption spectra of AuNRs@TiO_2, and AuNSs@TiO_2 are shown in Figure 5. 6 and Figure 5. 5. Figure 5. 6 shows that two absorption peaks appear in the Vis and NIR regions for AuNRs@TiO_2, and the longitudinal SPR band can be tuned from 720 nm to 880 nm by adjusting the aspect ratio of the gold core. These observations indicate that the gold core has a crucial effect on the optical properties of the core-shell nanoparticles: the light-harvesting ability of TiO_2 is improved by loading gold nanoparticles. Tunable light-harvesting ability in a wide range is achieved when AuNRs are applied. The extraordinary light-

harvesting ability of AuNRs@TiO_2 nanoparticles makes them promising in the photocatalytic reaction under UV-Vis-NIR irradiation.

5.2.2 Hydrothermal Treatment and AuNRs Stability

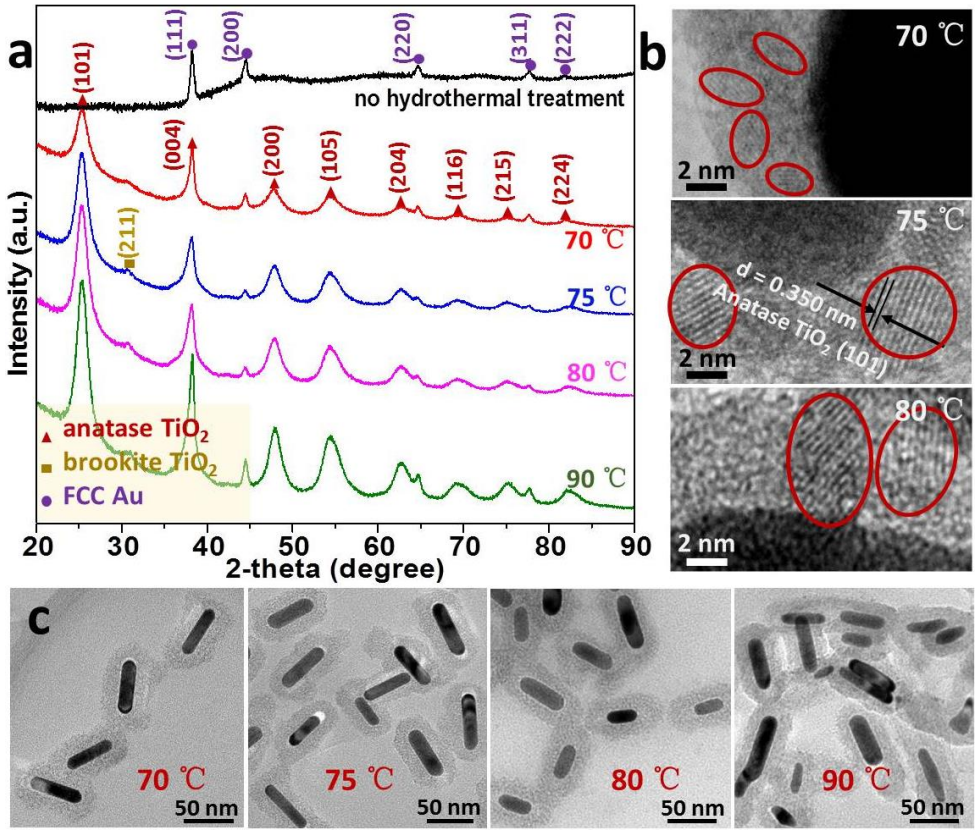

Figure 5. 7. (a) XRD patterns, (b) HRTEM images, and (c) TEM images of AuNRs@TiO_2 core-shell nanoparticles after hydrothermal treatment at different temperature for 4 h: 70 ℃, 75 ℃, 80 ℃, and 90 ℃. The dimensions of the gold core without hydrothermal treatment are 54.33 ± 8.13 nm, 15.79 ± 1.68 nm (the sample in Figure 5. 6aIII). After hydrothermal treatment, the length and width of the gold core are 53.15 ± 8.22 nm, 15.49 ± 2.13 (70 ℃), 53.62 ± 8.52 nm, 16.39 ± 3.49 nm (75 ℃), 44.43 ± 10.11 nm, 17.86 ± 5.52 nm (80 ℃), 33.41 ± 15.91, 24.43 ± 19.41 nm (90℃), respectively.

The XRD pattern tookaken on the AuNRs@TiO_2 nanoparticles without hydrothermal treatment only shows the diffraction peaks of Au, indicating that the as-synthesized

TiO_2 shell is amorphous (Figure 5. 7a). This is consistent with the common understanding that the phase transformation from amorphous to anatase TiO_2 requires calcination at 450-550 ℃.[335] In order to crystallize the TiO_2 shell into anatase phase (UV-active) and preserve the anisotropic morphology of the gold core, low-temperature hydrothermal treatment was applied. When treated at 70-90 ℃, the amorphous TiO_2 are crystallized into anatase, as revealed by the presence of peaks at 25.5˚, 38.2˚, 48.0˚, 54.3˚, 62.8˚, 69. 5˚, 75.3˚, and 82.6˚ in corresponding XRD patterns (Figure 5. 74a). With the increase of temperature from 70 ℃ to 90 ℃, the peak intensity of anatase gradually increases and the width of the diffraction peak slightly become narrower, indicating the enhancement of crystallization. Notably, the intensity of Au peaks is quite weaker than that of anatase TiO_2. This can be explained by the fact that Au cores were embedded inside the TiO_2 shells that may shield their XRD signals. HRTEM images in Figure 5. 7b show the random orientation of interplanars, confirming the presence of anatase TiO_2 in samples treated at 70 ℃ ~ 80 ℃, which is in agreement with XRD analysis. The interplanar spacing is about 0.35 nm corresponding to the (101) plane of the anatase TiO_2. The lattice spacing of the Au core cannot be resolved might also due to the encapsulation of the TiO_2 shell. It has been reported that water molecules are essential in the phase transformation from amorphous TiO_2 to anatase at low temperature.[336-337] Wang et al. proposed that water molecules might catalyze the structural rearrangement of TiO_6^{2-} octahedral units via a dissolution-precipitation process, resulting in the crystallization of anatase crystallites.[336] In our work, phase transformation is kinetically accelerated at a higher temperature (70-90 ℃).

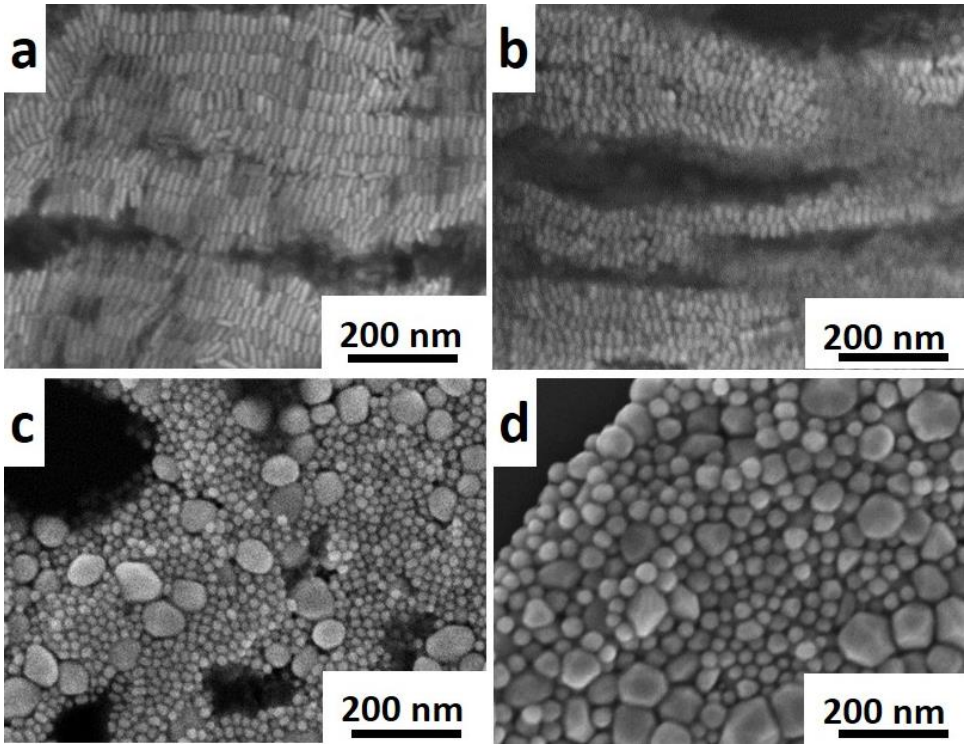

Figure 5. 8. SEM images of AuNRs after heating at different temperature for 30 min: (a) 70℃, (b) 100 ℃, (c) 140 ℃, (d) 180 ℃.

The stability of AuNRs has to be addressed when considering any potential applications. The thermodynamic tendency of lowering surface energy makes the anisotropic nanostructures potentially unstable.[101, 106, 109] It's reported that AuNRs undergo morphological and structural transitions into the most thermodynamic stable spherical shape if sufficient energy is provided, thus losing their peculiar properties.[106] Figure 5. 8 shows that bare AuNRs cannot survive after heating treatment at a temperature higher than 100 ℃ for 30 min. It's important to point out that the morphology of the anisotropic AuNRs is well-preserved after TiO_2 coating and thermal treatment at 70 ℃ and 75 ℃ (Figure 5. 7c), however, it cannot survive at higher temperatures treatment, evidenced from the presence of irregular-shaped and significantly-shortened nanoparticles at 80 ℃and 90 ℃. The shape deformation might be attributed to Ostwald ripening, which can also be significantly slowed down by reducing the concentration of CTAB or providing a stiffer coating.[109] In our work, the use of diluted CTAB (0.7 mM) solution is of great significance not only in facilitating the uniform TiO_2 coating

on AuNRs, but also in suppressing the reshaping process by slowing down the formation of soluble gold species.[109] Further experiments were carried out under 75 ℃ so as to achieve both high crystallinity of TiO_2 and preserve the anisotropic morphology of AuNRs.

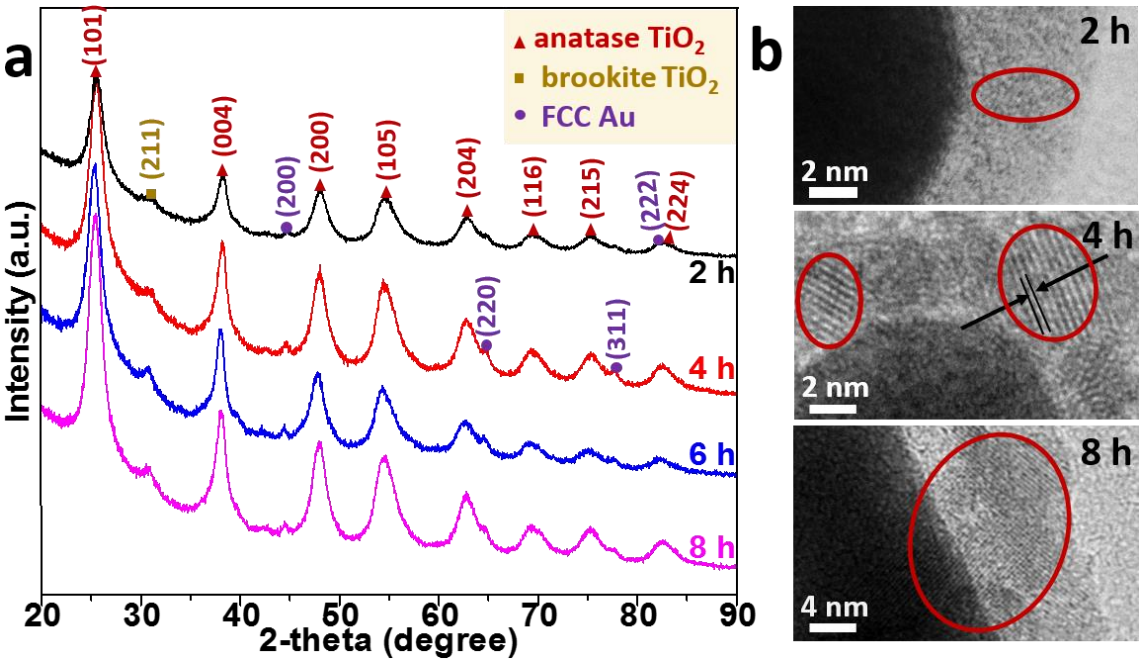

Figure 5. 9. (a) XRD patterns and (b) HRTEM images of AuNRs@TiO_2 core-shell nanoparticles after thermal treatment at 75 ℃ for different time.

Figure 5. 9a shows the XRD patterns of the AuNRs@TiO_2 nanoparticles obtained by hydrothermal treatment at 75 ℃ with different durations. It demonstrates that the crystallization starts within 2 h of treatment. For longer incubation time, the crystallinity of TiO_2 is enhanced and the crystallization process saturates after 4 h of treatment. This aspect is well evidenced by the evolution of the average crystallite size, estimated through the Scherrer formula, as a function of the hydrothermal treatment time (Figure 5. 9b). The average crystallite size is approximately 4 nm after 4 h of treatment and does not evolve significantly for longer incubation time. Based on the above results, it can be concluded that AuNRs@TiO_2 nanoparticles can be effectively crystalized into anatase phase by hydrothermal treatment at 75 ℃, and the intactness of AuNRs is well-preserved. This is of great significance for the fabrication of the AuNRs@anatase TiO_2

core-shell nanocomposites with wide-range light harvesting ability in photocatalytic applications.

5.2.3 H_2 Production

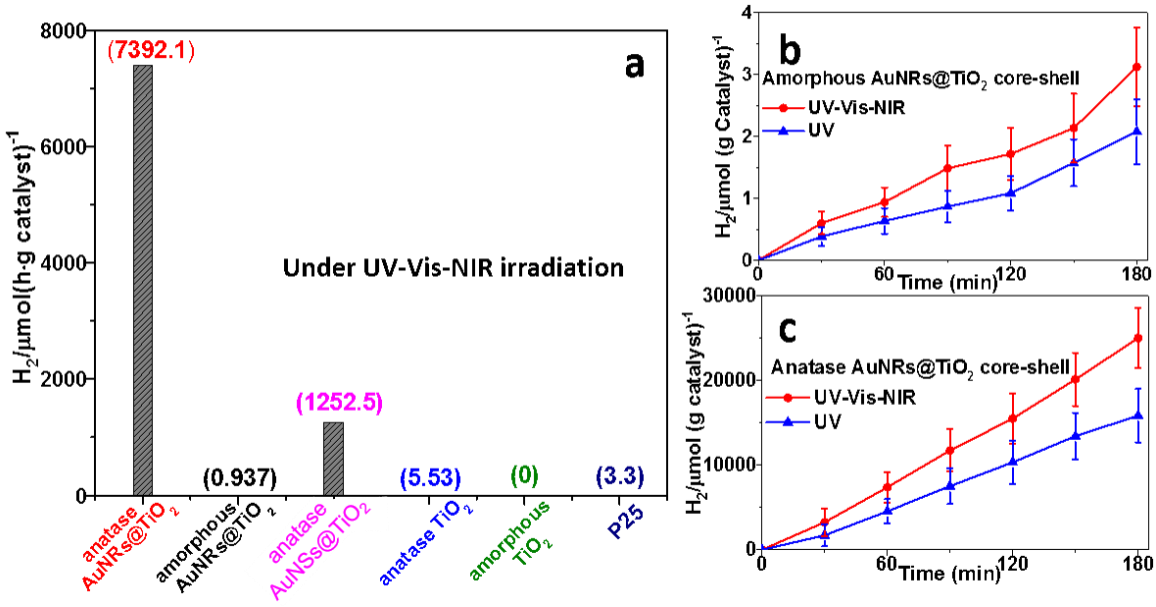

Figure 5. 10. (a) Photocatalytic H_2 production of different photocatalysts under UV-Vis-NIR light irradiation. Photocatalytic H_2 production of (b) AuNRs@amorphous TiO_2 and (c) AuNRs@anatase TiO_2 under UV-Vis-NIR and UV light irradiation. UV-Vis-NIR: 200~2000 nm; UV light: 200~420 nm.

Recently, TiO_2 and AuNRs nanocomposites have been extensively investigated in the field of photocatalysis.[68-69, 80, 290, 338] However, most studies used the amorphous TiO_2, because it is challenging to crystalize TiO_2 into UV-active anatase phase while keeping the anisotropic morphology of AuNRs unchanged. In our work, the successful fabrication of AuNRs@anatase TiO_2 core-shell nanostructures makes it possible to investigate the photocatalytic activity under the UV-Vis-NIR light. Figure 5. 10a shows the H_2 evolution rates of different photocatalysts under UV-Vis-NIR light irradiation. Hydrothermal treated AuNPs@TiO_2 core-shell nanostructures exhibit a higher H_2 yield of 1252.5 $\mu mol \cdot h^{-1} \cdot g^{-1}$ compared with that of anatase TiO_2 (5.53 $\mu mol \cdot h^{-1} \cdot g^{-1}$), confirming the effectiveness of introducing gold into the TiO_2 system to promote the photocatalytic performance. The H_2 yield of the photocatalysts boosts from 1252.5

μmol·h^{-1}·g^{-1} to 7392.1 μmol·h^{-1}·g^{-1} when changing the AuNPs core to AuNRs, indicating that AuNRs significantly enhance their light-harvesting ability in contrast to AuNPs. The photocatalytic performance of AuNRs@amorphous TiO_2 (0.937 mol·h^{-1}·g^{-1}) can be drastically improved after crystallizing the TiO_2 component (7392.1 mol·h^{-1}·g^{-1}), emphasizing the significance of our work in utilizing the crystalized TiO_2 in photocatalysis. Furthermore, the H_2 yield of the AuNRs@TiO_2 core-shell nanostructures under different light irradiation was compared in Figure 5. 10b, c. Figure 5. 10b, c show that the H_2 yield increases after extending the irradiation light wavelength from UV (200-420 nm) light to UV-Vis-NIR (200~2000 nm) to cover the longitudinal SPR of AuNRs. These observations again underline the significance of our work in designing crystalized TiO_2 encapsulated AuNRs nanocomposites for efficient photocatalysis by fully utilizing UV-Vis-NIR light.

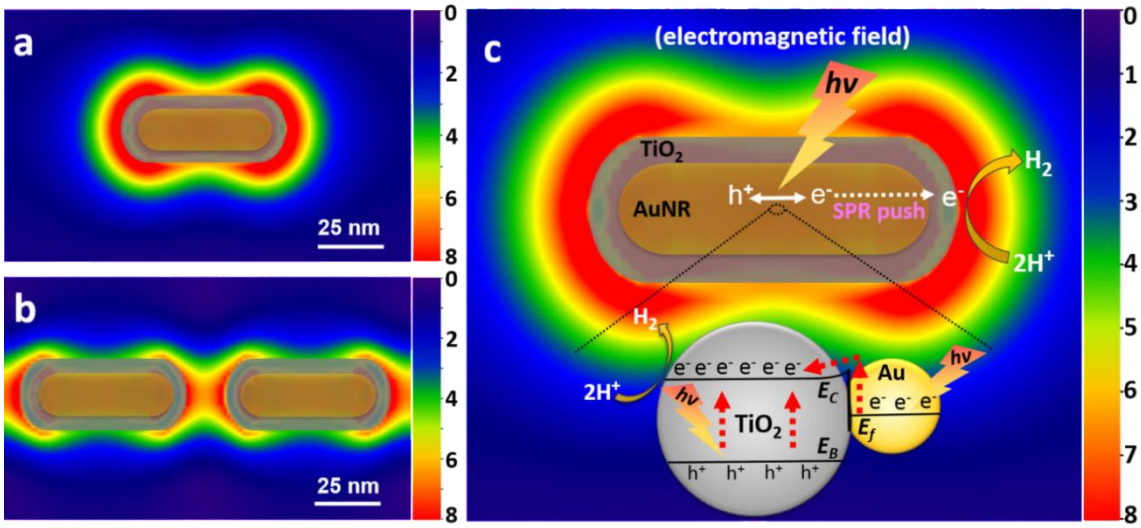

Figure 5. 11. Electromagnetic field intensity at the surface of (a) a single AuNR@TiO_2 and (b) an AuNRs@TiO_2 dimer calculated using FDTD simulation. (c) Scheme of the SPR-enhanced photocatalysis of AuNR@TiO_2.

The working mechanism of a photocatalyst composed of AuNRs and TiO_2 can be understood in terms of the composition of irradiation light. Under UV irradiation, TiO_2 absorbs photons with energy equal or greater than its band gap, and valence band electrons are excited to the conduction band, thus the electron-holes pairs are generated. The photoinduced electrons subsequently transfer to AuNRs, and this electron transfer

is energetically favored considering that the conduction band of anatase TiO_2 is higher in energy than the Fermi energy of gold.[277, 339] In addition, the recombination of electron-holes is suppressed due to the existence of Schottky barrier in the gold and TiO_2 interface.[244, 260, 274, 339] As the encapsulated AuNRs do not interact with the reactants, the accumulated electrons, instead of participating in the photocatalytic reaction directly, form an electrostatic field around AuNRs repelling the electrons towards the surface of TiO_2. In this manner, the electron-holes separation is improved and the photocatalytic activity of TiO_2 is enhanced.

Under UV-Vis-NIR light irradiation, the UV light absorbed by TiO_2 together with the Vis-NIR light absorbed by AuNRs contribute to the overall photocatalysis. Due to the SPR, a localized electromagnetic field is excited around AuNRs and spreads away from the Au/TiO_2 interface to the TiO_2.[22, 32-33] Figure 5. 11 shows the cross-sectional plot of the electromagnetic field distribution of a single AuNR@TiO_2 (Figure 5. 11a) and an AuNR@TiO_2 dimer (Figure 5. 11b) calculated using FDTD simulation. The field intensity in the vicinity of AuNR@TiO_2 boosts compared to the incident electric field intensity. In this situation, AuNRs contribute to the overall photocatalysis by forming SPR-induced electromagnetic field, which is different from the electrostatic field in case of pure UV light irradiation. This strong electromagnetic field can effectively separate the electron-hole pairs generated from TiO_2 (Figure 5. 11c), promoting the photocatalytic performance of TiO_2. Compared to AuNPs, AuNRs absorb light a wider range of light and have a much stronger electromagnetic field,[21] thus facilitating the separation of electron-hole pairs more efficiently (Figure 5. 10a), which verifies our prediction.

It is worth mentioning that charge transfer mechanism, in which the SPR-induced "hot" electrons in the metal nanoparticles surpass the Schottky barrier and are injected into the conduction band of TiO_2, has been proposed to explain the Vis-NIR light induced photocatalytic activity.[68-69, 243-245] Different from these systems with the bare interface (e.g. Janus and yolk-shell nanostructures), the gold core in our case does not interact with the reactants due to the configuration of the core-shell structure, therefore, this charge transfer process is largely limited. The H_2 yield of AuNRs@TiO_2 under Vis-NIR

light irradiation has also been explored (data not shown) and no obvious H_2 was generated within 3 hours. Similarly, Stucky group also reported that AuNRs@TiO_2 core-shell nanostructures exhibited no photocatalytic activity under Vis-NIR light irradiation, supporting our prediction.[68]

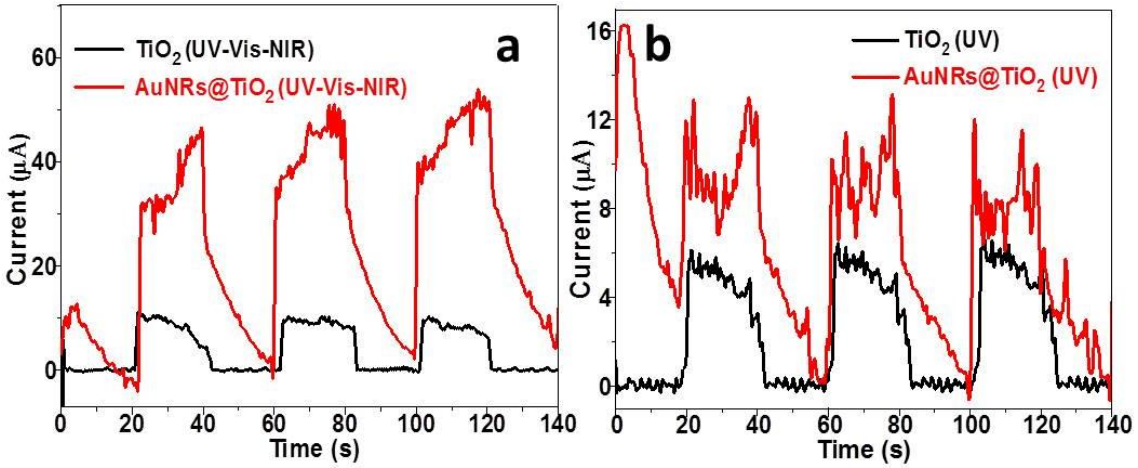

Figure 5. 12. Photocurrent response (in chopping mode, light on-off repeatedly) of the anatase TiO_2 and AuNRs@anatase TiO_2 photocatalysts under UV-Vis-NIR and UV light irradiation (Xe Lamp 300 W).

The improved charge separation on the AuNRs@TiO_2 photocatalysts was confirmed by the photocurrent responses in a two-electrode electrochemical cell. The photogenerated electrons can transfer through the material to produce photocurrent upon light irradiation, therefore, the photocurrent represents the photocatalytic activity of the catalysts. As shown in Figure 5. 12, a fast and uniform photocurrent response was observed for both TiO_2 and AuNRs@TiO_2 photocatalysts on each switch on/off cycle under irradiation. Figure 5. 12 shows that the photocurrent of the AuNRs@TiO_2 coated electrode is higher than that of the bare TiO_2 coated electrode under UV-Vis-NIR or UV light illumination, which agrees with the fact that AuNRs@TiO_2 nanoparticles possess higher H_2 yield compared to TiO_2 (Figure 5. 10a). The photocurrent of TiO_2 under UV-Vis-NIR irradiation is similar to that under UV irradiation, confirming that TiO_2 cannot utilize Vis-NIR light. In addition, the photocurrent of AuNRs@TiO_2 significantly increases when extending the light range from UV to UV-Vis-NIR (Figure 5. 12). This not only emphasizes the importance of AuNRs in harvesting Vis-NIR light for

improved photocatalytic activity, but also indicates that the SPR-induced electromagnetic field (under UV-Vis-NIR light) is more efficient in promoting the electron-holes separation compared to the electrostatic field (under UV light).

For the TiO_2 and AuNRs@TiO_2 photocatalysts coated electrodes, the photocurrent rapidly increases once the light is switched on. Subsequently, the photocurrent gradually decreases in the case of TiO_2 photocatalysts, indicating the recombination of the electron-hole pairs occurs. However, for the AuNRs@TiO_2 photocatalysts under UV-Vis-NIR light irradiation (Figure 5. 12a), the charge carriers can be efficiently separated by the SPR-induced electromagnetic field, resulting in the obvious increase of the photocurrent. While under UV light illumination (Figure 5. 12b), the behaviour of charge carriers in the AuNRs@TiO_2 system is much complicated, making the photocurrent fluctuant. It is obvious that when the light is off, the photocurrent of TiO_2 vanishes immediately, while the photocurrent of AuNRs@TiO_2 gradually decreases to zero. Similarly, Hirakawa and Kamat found that Ag in the Ag@TiO_2 nanocomposites exhibits reversible charge and discharge phenomena by capturing and releasing the electrons from the TiO_2 layer.[262, 287] When the Ag@TiO_2 composites were irradiated with UV light, electrons gradually transferred to the Ag core and the SPR of Ag core slightly blue-shifted. After removing the light source, the electrons were gradually released by Ag cores and the SPR slowly red-shifted to its initial position.

5.2.4 Three-Dimensional Contact

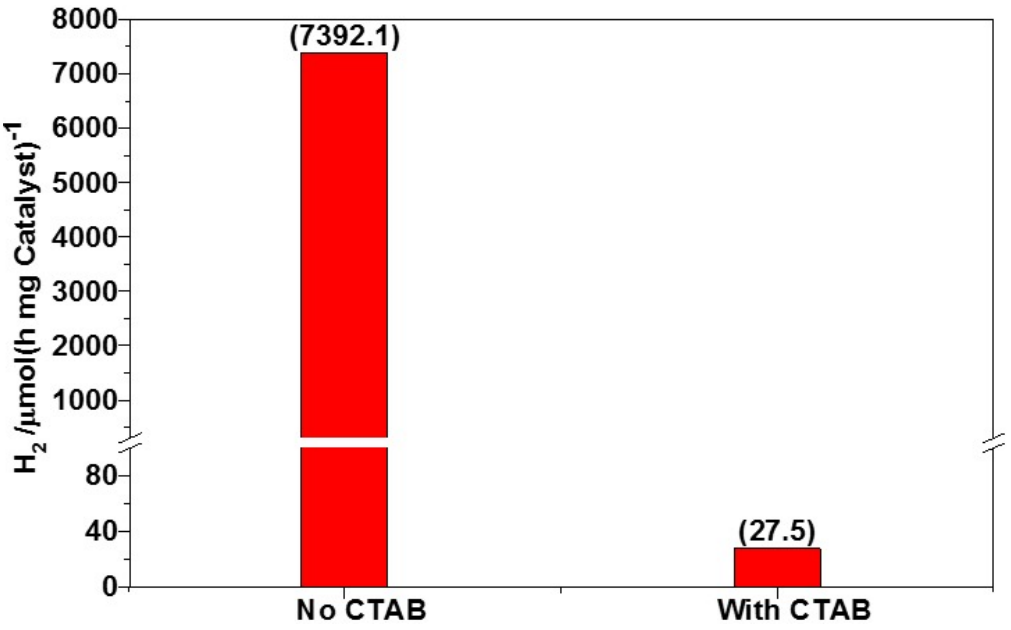

Figure 5. 13. Photocatalytic H_2 production under UV-Vis-NIR light over different catalyst.

As discussed above, the photocatalysis process involved UV-induced charge generation and transfer and electron-hole pairs separation resulting from the SPR-induced electromagnetic fielled. Thus, the tight contact between core and shell is strongly desired for efficient photocatalysis. The core-shell nanostructures areis much advantageous in providing three-dimensional contact between the core and the shell compared to other configurations, such as yolk-shell,[80, 271] Janus,[241] etc. The tight contact maximizes the core-shell interaction in terms of charge transfery and localized SPR effect.

In our work, an appropriate amount of CTAB is important in facilitating the formation of uniform core-shell structure and suppressing the AuNRs reshape. However, the presence of CTAB will hinder the direct charge transfer or dramatically decrease the intensity of SPR-induced electromagnetic field at the AuNR@TiO_2 surface, as this field decays exponentially with distance. Consequently, the photocatalysts were washed twice withby methanol before photocatalytic reactions, which is an effective way to

remove CTAB.[233] Figure 5. 13 shows that H_2 production yield of AuNRs@crystalized TiO_2 nanocomposite without removing CTAB is 27.5 $mol \cdot h^{-1} \cdot mg^{-1}$ under UV-Vis-NIR light irradiation, and dramatic activity increase was observed after the removal of surfactant (7392.1 $mol \cdot h^{-1} \cdot mg^{-1}$, Figure 5. 13).

5.3 Conclusions

In this work, AuNRs@anatase core-shell nanoparticles were innovatively synthesized and applied in hydrogen production through water splitting. On the premise of keeping the anisotropic structure of AuNRs, TiO_2 layer successfully transform to the anatase phase, making AuNRs@TiO_2 system perfectly combine the high SPR of AuNRs and high photocatalytic activity of anatase. For the AuNRs@anatase system under the UV-Vis-NIR light, photogenerated charge carriers from TiO_2 under UV light are promoted to separate by the electromagnetic field induced by~~from~~ the SPR of AuNRs. Comparing to other photocatalysts, AuNRs@anatase shows super high photocatalytic activity in producing hydrogen through water splitting.

Chapter 6 Summary and Future Works

In this chapter, a brief summary of chapter 3, chapter 4, and chapter 5 wasere given, and suggestions of future works based on the synthesis, surface modification, and applications were outlined.

In chapter 3, we demonstrated that monodispersed AuNRs with remarkably high yield are reproducibly synthesized by using the proposed seedless synthetic technique. 5-BA serves as template regulator and promotes the spherical to rod-like/worm-like micellar transition. While Ag^+ ions serve as an essential part of the soft-template in inducing the formation of the anisotropic nanostructures by forming CTAB-AgBr complex. $NaBH_4$ is used to generate seeds *in situ*, and the use of HQ at lower pH affords a mild condition for AuNRs growth. Consequently, the modified template becomes more effective and monodispersed AuNRs formation is favoured. The facile synthesis, broad tunability of LSRP, high reproducibility, remarkably high yield, and ease of scale-up make our seedless method particularly promising for the future industrial mass production of monodispersed AuNRs for diverse applications in catalysis, sensing, and biomedicine. Moreover, our work also makes an important step towards a better understanding of AuNRs growth, which has profound implications for seedless (or seed-mediated) synthesis of other related anisotropic metal nanostructures. Preliminary results have been obtained in the synthesis of Ag nanorods and TiO_2 nanorods using our method, the yield of Ag nanorods is quite low at the current stage and future work will focus on promoting the yield of the nanoparticles and extending this technique to other nanoparticle systems.

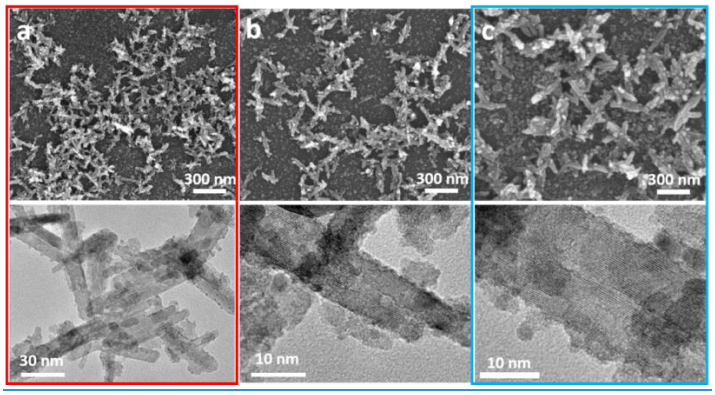

Figure 6. 1. SEM and TEM images of titanium dioxide nanorods synthesized under similar conditions of AuNRs synthesis. The hydrothermal treatment was performed at 70 ℃ for 4 h.

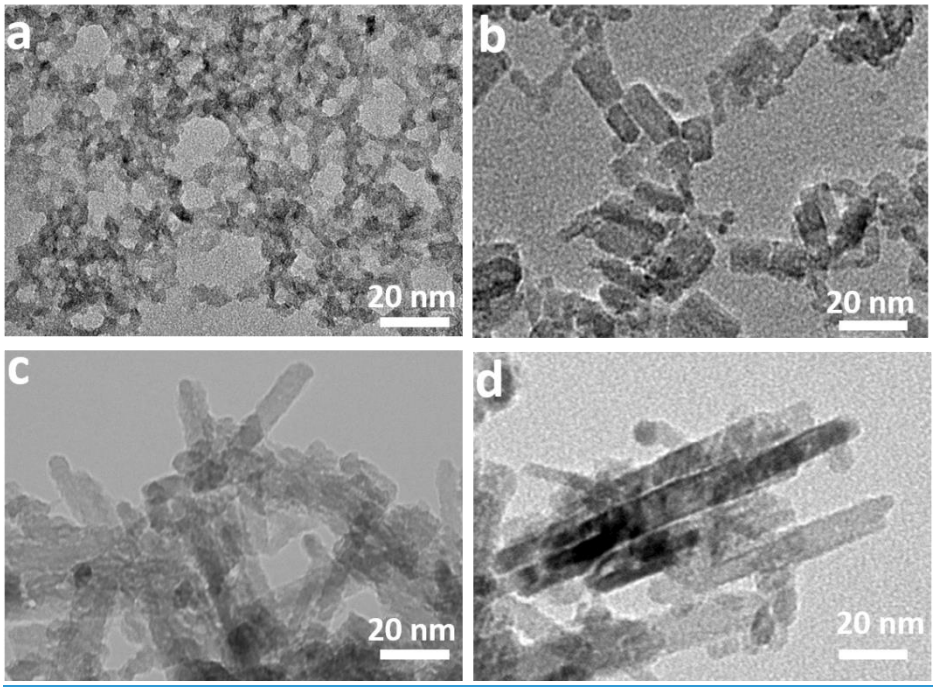

Figure 6. 2. TEM images of titanium dioxide nanorods. The hydrothermal treatment was performed at 70 ℃ for a) 2 h, b) 3h, c) 4h, d) 5h.

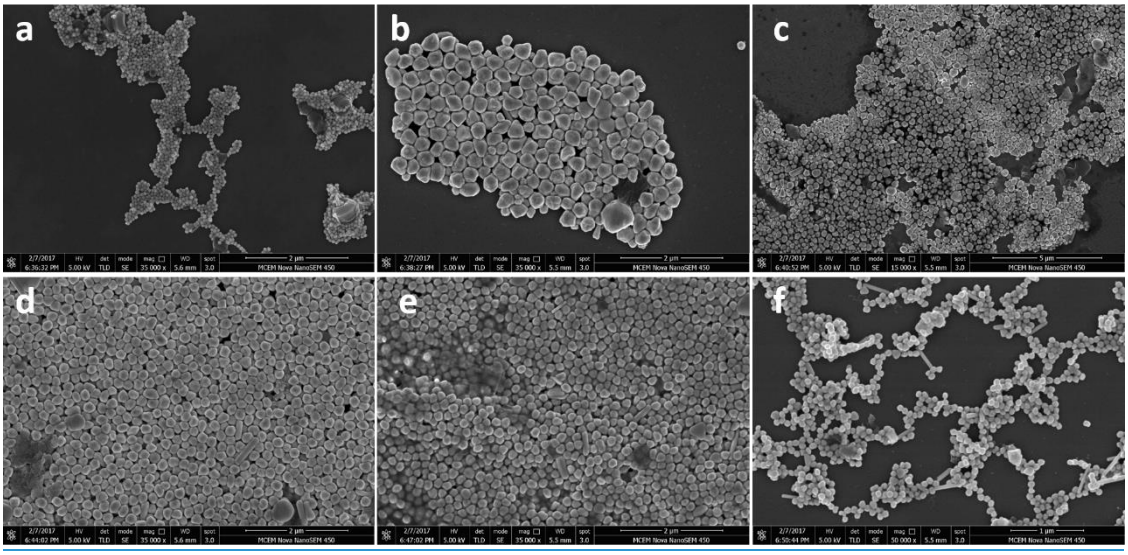

Figure 6. 3. SEM images of Ag nanorods using the proposed seedless method using an increased amount of $NaBH_4$: a) 10 µL, b) 20 µL, c) 40 µL, d) 60 µL, e) 80 µL, f) 100 µL. The added NaOH and HQ was 0.2 mL and 0.2 mL.

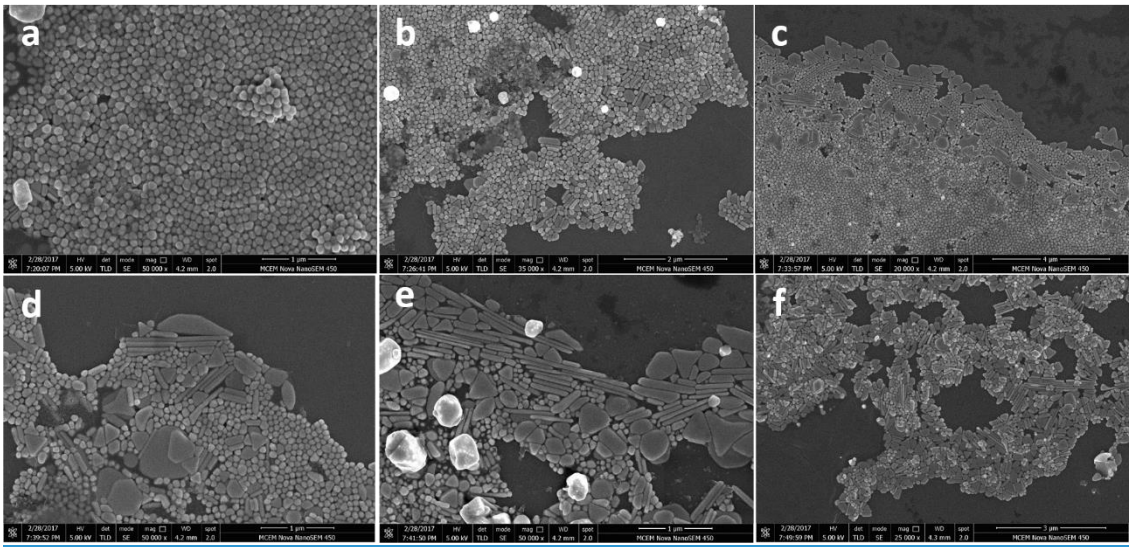

Figure 6. 4. SEM images of Ag nanorods using the proposed seedless method using an increased amount of HQ: a) 70 µL, b) 100 µL, c) 130 µL, d) 150 µL, e) 170 µL, f) 200 µL. The added NaOH and $NaBH_4$ was 0.2 mL and 0.1 mL.

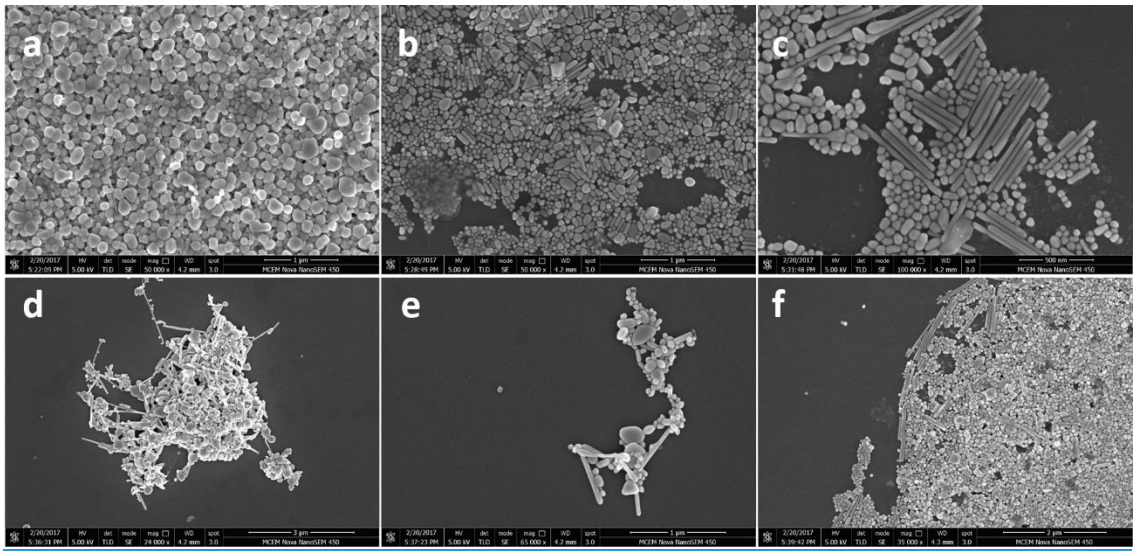

Figure 6. 5. SEM images of Ag nanorods using the proposed seedless method using an increased amount of NaOH: a) 100 µL, b) 120 µL, c) 140 µL, d) 160 µL, e) 180 µL, f) 200 µL. The added HQ and $NaBH_4$ was 0.2 mL and 0.1 mL.

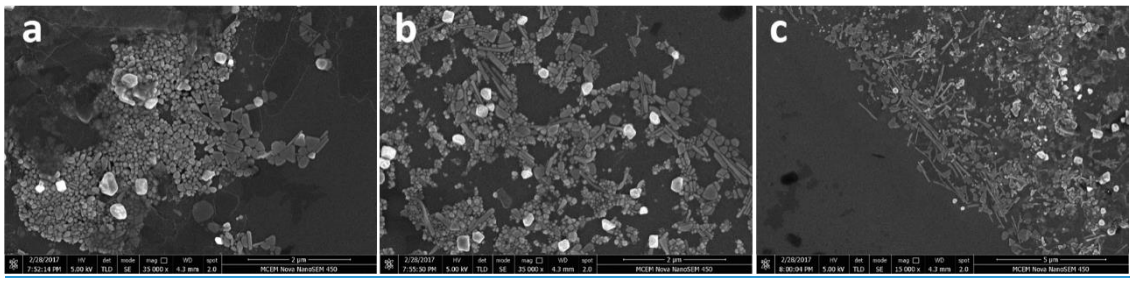

Figure 6. 6. SEM images of Ag nanorods using the proposed seedless method using an increased amount of $CuCl_2$: a) 0 µL, b) 25 µL, c) 50 µL. The added HQ, $NaBH_4$, and NaOH was 0.2 mL, 0.1 mL, and 0.1 mL.

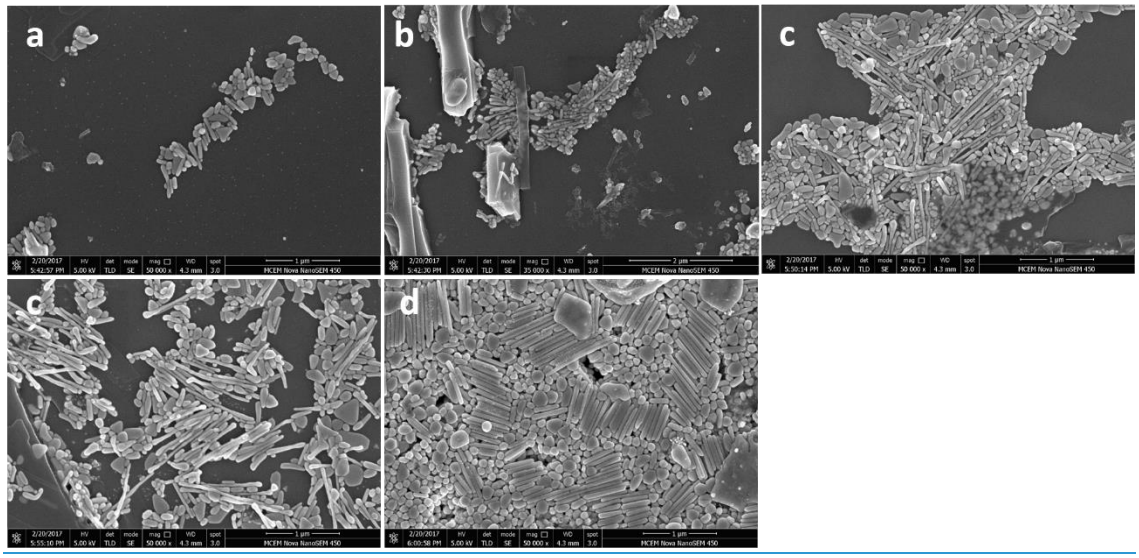

Figure 6. 7. SEM images of Ag nanorods using the seed-mediated method using an increased amount of seed solution: a) 50 µL, b) 70 µL, c) 90 µL, d) 130 µL, e) 150 µL.

The proposed method has been extended to the synthesis of anisotropic semiconductor (TiO_2, Figure 6. 1and Figure 6. 2) and Ag NPs (Figure 6. 3, Figure 6. 4, Figure 6. 5, Figure 6. 6, and Figure 6. 7). For the synthesis of TiO_2 nanorods, the thermal treatment is able to crystallize the as-synthesized NPs (Figure 6. 1 and Figure 6. 2). The synthesis of monodispersed Ag nanorods has been a challenging task, and our method seems promising in achieving that (e.g. Figure 6. 5c, Figure 6. 7d). More work is still undergoing to optimize the methods in synthesizing monodisperse TiO_2 and Ag nanorods.

In chapter 4, we developed a novel, simple, one-step surface modification method to produce biocompatible AuNRs. This method allows for the complete functionalization of AuNRs with thiolated PEG and the removal of the most active silver on the AuNR surface. The PEGylated AuNRs show a significantly enhanced colloidal stability against a high concentration buffered saline solution and multiple rounds of centrifugation compared to CTAB-capped and partially modified AuNRs. Finally, this work represents a simple proof-of-concept experiment for the complete PEGylation and detoxification of CTAB-capped AuNRs. The surface modification method developed here can be easily extended to negatively-charged surface ligands, e.g. thiol-PEG-carboxyl, and other NP systems with different compositions and shapes.

Future work will focus on the applications of carboxyl-AuNRs and DNA-AuNRs in terms of bacteria/ions detection and self-assembly. In addition, the CTAB bilayer molecules are unevenly distributed on the surface of AuNRs due to the variation of surface curvature between the longitudinal and the transverse surfaces, as well as the tips.[120] The inhomogeneity in the packing density of the adsorbed CTAB bilayer, where the highly curved tip exhibits a lower density of CTAB than the longitudinal facets, making the functionalization of the tips energetically more favourable than that of the sides.[121] The selective functionalization can be taken advantage of to assemble the AuNRs either tip-to-tip or side-by-side, and has been widely exploited in the device community.[119, 122-131] In the future, thiolated ligands (for example, DNA or PEG or carboxyl) can be selectively functionalized on the whole surface, end-facets, and side-facets. Therefore, these selective-functionalized AuNRs can be used as multifunctional building blocks in self-assembly and sensitive Raman detection. The fact that CTAB bilayer molecules are unevenly distributed on the surface of AuNRs can also be utilized in the selective adsorption of precursors (e.g. $AgNO_3$, $TiCl_3$) to fabricate nanocomposites for the applications in catalysis and sensing.

After the modification by using our one-step method, AuNRs bear functional groups that face the external environment. Carboxyl functionalization introduced by our method can be carried out to include new functionality, for example, carboxyl group for

EDC/NHS coupling reaction. Therefore, protein or amine-terminated small molecules can be thereafter covalently conjugated to the AuNRs via EDC/NHS coupling reaction.[225] Further applications in bacteria, ions sensing can be achieved in this way.

As introduced in Chapter 1, the absorbed light can be converted into heat by the plasmonic NPs via a series of photophysical processes, which can lead to temperature rises in the surrounding environment.[60, 81-84] Consequently, the surrounding medium can be heated, melted, vaporized, or deteriorated depending on the temperature reached by the NPs. In all cases, a stress wave due to the medium thermal expansion propagates in the surroundings of the heated NPs. In PTT application, AuNRs can be located selectively at the targeted region and act as photoabsorbers, which can be achieved by surface modification of AuNPs with specific ligands, to reduce nonspecific injury to adjacent healthy tissue. Similarly, an alternative drug/gene release strategy is to incorporate AuNRs into composite materials loaded with drug/gene, where AuNRs act as the light absorber and the composites are drug carriers. Under laser illumination, the photothermal conversion of the nanorods heats up the surrounding composites, leading to their structural changes and thereafter the release of the embedded drugs/genes.[21]

In chapter 5, we successfully synthesized AuNRs@anatase core-shell nanostructures and studied their photocatalytic performance. On the premise of keeping the anisotropic structure of AuNRs, TiO_2 layer successfully transform to the anatase phase, making AuNRs@TiO2 system perfectly combine the high SPR of AuNRs and high photocatalytic activity of anatase. For the AuNRs@anatase system under the UV-Vis-NIR light, photogenerated charge carriers from TiO_2 under UV light are promoted to separate by the electromagnetic field induced byfrom the SPR of AuNRs. Future work will be carried out to synthesize AuNRs@TiO_2 with higher crystallinity and AuNRs/TiO_2 nanocomposites with different configurations, and investigate their photocatalytic performance. The synthesis of AuNRs@Ag@TiO_2 core-shell nanostructures has been initiated. The introduction of Ag shell is of great significance in terms of proving an extra protection to the AuNRs cores and affording the nanocomposites enhanced light harvesting ability.

In addition, the fact that CTAB bilayer molecules are unevenly distributed on the surface of AuNRs can be utilized in the synthesis of anatase TiO_2/AuNRs dumbbell nanostructure with efficient photocatalytic ability. According to the reference [68], the anisotropic growth of TiO_2 on AuNRs into dumbbell nanostructures can be achieved by the addition of dilute $TiCl_3$ into AuNRs solution low CTAB concentration. Subsequent addition of tetraethyl orthosilicate (TEOS) occupies the side facets of AuNRs. After the hydrolysis, therefore, AuNRs/TiO_2/SiO_2 nanocomposites can be obtained with TiO_2 at the end facets and SiO_2 at the side facets. After hydrothermal treatment, anatase TiO_2 can be obtained. Due to the protection of TiO_2 and SiO_2, the intactness of AuNRs can be preserved. In the later process, the SiO_2 can be removed by treating with NaOH solution. Finally, anatase TiO_2/AuNRs dumbbell nanostructure with UV-Vis-NIR light harvesting ability can be synthesized.

References

[1] K. Critchley, B. P. Khanal, M. Ł. Górzny, L. Vigderman, S. D. Evans, E. R. Zubarev and N. A. Kotov, *Adv. Mater* **2010,** *22*, 2338-2342.
[2] M.-C. Daniel and D. Astruc, *Chem.Rev* **2004,** *104*, 293-346.
[3] L. B. Hunt, *Gold Bulletin* **1976,** *9*, 134-139.
[4] M. Faraday, *Philosophical Transactions of the Royal Society of London* **1857,** *147*, 145-181.
[5] P. Mulvaney, *Langmuir* **1996,** *12*, 788-800.
[6] Y.-C. Yeh, B. Creran and V. M. Rotello, *Nanoscale* **2012,** *4*, 1871-1880.
[7] M. J. Banholzer, J. E. Millstone, L. Qin and C. A. Mirkin, *Chem. Soc. Rev* **2008,** *37*, 885-897.
[8] S. Kim, J. Jin, Y.-J. Kim, I.-Y. Park, Y. Kim and S.-W. Kim, *Nature* **2008,** *453*, 757-760.
[9] V. Giannini, A. I. Fernández-Domínguez, S. C. Heck and S. A. Maier, *Chem.Rev* **2011,** *111*, 3888-3912.
[10] S. Savasta, R. Saija, A. Ridolfo, O. Di Stefano, P. Denti and F. Borghese, *ACS Nano* **2010,** *4*, 6369-6376.
[11] Y.-W. Hao, H.-Y. Wang, Y. Jiang, Q.-D. Chen, K. Ueno, W.-Q. Wang, H. Misawa and H.-B. Sun, *Angew. Chem. Int. Ed* **2011,** *50*, 7824-7828.
[12] Z. Qin and J. C. Bischof, *Chem. Soc. Rev* **2012,** *41*, 1191-1217.
[13] L. Brus, *Acc. Chem. Res* **2008,** *41*, 1742-1749.
[14] Y. Nishijima, K. Ueno, Y. Kotake, K. Murakoshi, H. Inoue and H. Misawa, *J. Phys. Chem. Lett* **2012,** *3*, 1248-1252.
[15] S. Lal, S. E. Clare and N. J. Halas, *Acc. Chem. Res* **2008,** *41*, 1842-1851.
[16] C. Burda, X. Chen, R. Narayanan and M. A. El-Sayed, *Chem.Rev* **2005,** *105*, 1025-1102.
[17] Y. Yin and A. P. Alivisatos, *Nature* **2005,** *437*, 664-670.
[18] S. Schlücker, *Angew. Chem. Int. Ed* **2014,** *53*, 4756-4795.
[19] B. M. Quinn, P. Liljeroth, V. Ruiz, T. Laaksonen and K. Kontturi, *J. Am. Chem. Soc* **2003,** *125*, 6644-6645.
[20] N. Dimitratos, J. A. Lopez-Sanchez and G. J. Hutchings, *Chem. Sci* **2012,** *3*, 20-44.
[21] H. Chen, L. Shao, Q. Li and J. Wang, *Chem. Soc. Rev* **2013,** *42*, 2679-2724.
[22] X. Huang, S. Neretina and M. A. El-Sayed, *Adv. Mater* **2009,** *21*, 4880-4910.
[23] Yu, S.-S. Chang, C.-L. Lee and C. R. C. Wang, *J. Phys. Chem. B* **1997,** *101*, 6661-6664.
[24] C. A. Foss, G. L. Hornyak, J. A. Stockert and C. R. Martin, *J. Phys. Chem* **1992,** *96*, 7497-7499.
[25] C. A. Foss, G. L. Hornyak, J. A. Stockert and C. R. Martin, *J. Phys. Chem* **1994,** *98*, 2963-2971.
[26] N. R. Jana, L. Gearheart and C. J. Murphy, *J. Phys. Chem. B* **2001,** *105*, 4065-4067.
[27] N. R. Jana, L. Gearheart and C. J. Murphy, *Adv. Mater* **2001,** *13*, 1389-1393.
[28] B. Nikoobakht and M. A. El-Sayed, *Chem. Mater* **2003,** *15*, 1957-1962.
[29] V. Sebastian, S.-K. Lee, C. Zhou, M. F. Kraus, J. G. Fujimoto and K. F. Jensen, *Chem. Commun* **2012,** *48*, 6654-6656.
[30] X. Ye, Y. Gao, J. Chen, D. C. Reifsnyder, C. Zheng and C. B. Murray, *Nano Lett* **2013,** *13*, 2163-2171.

[31] S. Gómez-Graña, F. Hubert, F. Testard, A. Guerrero-Martínez, I. Grillo, L. M. Liz-Marzán and O. Spalla, *Langmuir* **2012,** *28*, 1453-1459.
[32] K. A. Willets and R. P. V. Duyne, *Annu. Rev. Phys. Chem* **2007,** *58*, 267-297.
[33] J. N. Anker, W. P. Hall, O. Lyandres, N. C. Shah, J. Zhao and R. P. Van Duyne, *Nat Mater* **2008,** *7*, 442-453.
[34] R. Gans, *Annalen der Physik* **1915,** *352*, 270-284.
[35] S. Link, M. B. Mohamed and M. A. El-Sayed, *J. Phys. Chem. B* **1999,** *103*, 3073-3077.
[36] S. Link and M. A. El-Sayed, *J. Phys. Chem. B* **2005,** *109*, 10531-10532.
[37] A. Brioude, X. C. Jiang and M. P. Pileni, *J. Phys. Chem. B* **2005,** *109*, 13138-13142.
[38] P. K. Jain, K. S. Lee, I. H. El-Sayed and M. A. El-Sayed, *J. Phys. Chem. B* **2006,** *110*, 7238-7248.
[39] S. Eustis and M. A. El-Sayed, *Chem. Soc. Rev* **2006,** *35*, 209-217.
[40] S. Link and M. A. El-Sayed, *J. Phys. Chem. B* **1999,** *103*, 4212-4217.
[41] X. Huang and M. A. El-Sayed, *J. Adv. Res* **2010,** *1*, 13-28.
[42] *Quarterly Journal of the Royal Meteorological Society* **1958,** *84*, 198-199.
[43] L. Qiu, T. A. Larson, D. K. Smith, E. Vitkin, S. Zhang, M. D. Modell, I. Itzkan, E. B. Hanlon, B. A. Korgel, K. V. Sokolov and L. T. Perelman, *IEEE Journal of Selected Topics in Quantum Electronics* **2007,** *13*, 1730-1738.
[44] P. Zijlstra, P. M. R. Paulo and M. Orrit, *Nat Nanotechnol* **2012,** *7*, 379-382.
[45] H. R. Sim, A. W. Wark and H. J. Lee, *Analyst* **2010,** *135*, 2528-2532.
[46] C. Wang and J. Irudayaraj, *Small* **2008,** *4*, 2204-2208.
[47] Z. Sun, W. Ni, Z. Yang, X. Kou, L. Li and J. Wang, *Small* **2008,** *4*, 1287-1292.
[48] L. S. Jung, C. T. Campbell, T. M. Chinowsky, M. N. Mar and S. S. Yee, *Langmuir* **1998,** *14*, 5636-5648.
[49] A. J. Haes and R. P. Van Duyne, *J. Am. Chem. Soc* **2002,** *124*, 10596-10604.
[50] H. Chen, X. Kou, Z. Yang, W. Ni and J. Wang, *Langmuir* **2008,** *24*, 5233-5237.
[51] P. K. Jain, W. Huang and M. A. El-Sayed, *Nano Lett* **2007,** *7*, 2080-2088.
[52] F. J. García-Vidal and J. B. Pendry, *Phys. Rev. Lett* **1996,** *77*, 1163-1166.
[53] A. Otto, *Journal of Raman Spectroscopy* **2005,** *36*, 497-509.
[54] J. M. McLellan, A. Siekkinen, J. Chen and Y. Xia, *Chem. Phys. Lett.* **2006,** *427*, 122-126.
[55] E. Hao, G. C. Schatz and J. T. Hupp, *J. Fluoresc* **2004,** *14*, 331-341.
[56] E. Hao and G. C. Schatz, *J. Chem. Phys* **2004,** *120*, 357-366.
[57] Y. Yokota, K. Ueno and H. Misawa, *Chem. Commun* **2011,** *47*, 3505-3507.
[58] Y. Yokota, K. Ueno and H. Misawa, *Small* **2011,** *7*, 252-258.
[59] A. Mooradian, *Phys. Rev. Lett* **1969,** *22*, 185-187.
[60] S. L. and and M. A. El-Sayed, *Annu. Rev. Phys. Chem* **2003,** *54*, 331-366.
[61] E. Dulkeith, T. Niedereichholz, T. A. Klar, J. Feldmann, G. von Plessen, D. I. Gittins, K. S. Mayya and F. Caruso, *Phys. Rev. B* **2004,** *70*, 205424.
[62] M. B. Mohamed, V. Volkov, S. Link and M. A. El-Sayed, *Chem. Phys. Lett.* **2000,** *317*, 517-523.
[63] H. Wang, T. B. Huff, D. A. Zweifel, W. He, P. S. Low, A. Wei and J.-X. Cheng, *Proceedings of the National Academy of Sciences of the United States of America* **2005,** *102*, 15752-15756.
[64] J. P. Wilcoxon, J. E. Martin, F. Parsapour, B. Wiedenman and D. F. Kelley, *J. Chem. Phys* **1998,** *108*, 9137-9143.
[65] K. Imura, T. Nagahara and H. Okamoto, *J. Phys. Chem. B* **2005,** *109*, 13214-13220.

[66] D. Sivun, C. Vidal, B. Munkhbat, N. Arnold, T. A. Klar and C. Hrelescu, *Nano Lett* **2016,** *16*, 7203-7209.
[67] R. Liu and A. Sen, *J. Am. Chem. Soc* **2012,** *134*, 17505-17512.
[68] B. Wu, D. Liu, S. Mubeen, T. T. Chuong, M. Moskovits and G. D. Stucky, *J. Am. Chem. Soc* **2016,** *138*, 1114-1117.
[69] S. Mubeen, J. Lee, N. Singh, S. Kramer, G. D. Stucky and M. Moskovits, *Nat Nano* **2013,** *8*, 247-251.
[70] B. Li, T. Gu, T. Ming, J. Wang, P. Wang, J. Wang and J. C. Yu, *ACS Nano* **2014,** *8*, 8152-8162.
[71] A. Vincenzo, P. Roberto, F. Marco, M. M. Onofrio and I. Maria Antonia, *J. Phys. Condens. Matter* **2017,** *29*, 203002.
[72] M. L. Brongersma, N. J. Halas and P. Nordlander, *Nat Nano* **2015,** *10*, 25-34.
[73] J. Qiu and W. D. Wei, *J. Phys. Chem. C* **2014,** *118*, 20735-20749.
[74] Y. Ben-Shahar, F. Scotognella, I. Kriegel, L. Moretti, G. Cerullo, E. Rabani and U. Banin, **2016,** *7*, 10413.
[75] Y. Ben-Shahar, F. Scotognella, N. Waiskopf, I. Kriegel, S. Dal Conte, G. Cerullo and U. Banin, *Small* **2015,** *11*, 462-471.
[76] A. Sousa-Castillo, M. Comesaña-Hermo, B. Rodríguez-González, M. Pérez-Lorenzo, Z. Wang, X.-T. Kong, A. O. Govorov and M. A. Correa-Duarte, *J. Phys. Chem. C* **2016,** *120*, 11690-11699.
[77] Y. Zhang, C. Yam and G. C. Schatz, *J. Phys. Chem. Lett* **2016,** *7*, 1852-1858.
[78] C. Fang, H. Jia, S. Chang, Q. Ruan, P. Wang, T. Chen and J. Wang, *Energy. Environ. Sci* **2014,** *7*, 3431-3438.
[79] J.-H. Wang, M. Chen, Z.-J. Luo, L. Ma, Y.-F. Zhang, K. Chen, L. Zhou and Q.-Q. Wang, *J. Phys. Chem. C* **2016,** *120*, 14805-14812.
[80] A. Li, P. Zhang, X. Chang, W. Cai, T. Wang and J. Gong, *Small* **2015,** *11*, 1892-1899.
[81] S. Link and M. A. El-Sayed, *Int. Rev. Phys. Chem* **2000,** *19*, 409-453.
[82] M. A. El-Sayed, *Acc. Chem. Res* **2001,** *34*, 257-264.
[83] S. Link and M. A. El-Sayed, *J. Phys. Chem. B* **1999,** *103*, 8410-8426.
[84] S. Link, C. Burda, Z. L. Wang and M. A. El-Sayed, *J. Chem. Phys* **1999,** *111*, 1255-1264.
[85] N. S. Abadeer and C. J. Murphy, *J. Phys. Chem. C* **2016,** *120*, 4691-4716.
[86] A. O. Govorov and H. H. Richardson, *Nano Today* **2007,** *2*, 30-38.
[87] M. Hu, J. Chen, Z.-Y. Li, L. Au, G. V. Hartland, X. Li, M. Marquez and Y. Xia, *Chem. Soc. Rev* **2006,** *35*, 1084-1094.
[88] H. Chen, L. Shao, T. Ming, Z. Sun, C. Zhao, B. Yang and J. Wang, *Small* **2010,** *6*, 2272-2280.
[89] G. Baffou, C. Girard and R. Quidant, *Phys. Rev. Lett* **2010,** *104*, 136805.
[90] Q. Jia, J. Ge, W. Liu, S. Liu, G. Niu, L. Guo, H. Zhang and P. Wang, *Nanoscale* **2016,** *8*, 13067-13077.
[91] D. Wang, Z. Xu, H. Yu, X. Chen, B. Feng, Z. Cui, B. Lin, Q. Yin, Z. Zhang, C. Chen, J. Wang, W. Zhang and Y. Li, *Biomaterials* **2014,** *35*, 8374-8384.
[92] Z. Zhang, J. Wang, X. Nie, T. Wen, Y. Ji, X. Wu, Y. Zhao and C. Chen, *J. Am. Chem. Soc* **2014,** *136*, 7317-7326.
[93] D. B. Pacardo, B. Neupane, S. M. Rikard, Y. Lu, R. Mo, S. R. Mishra, J. B. Tracy, G. Wang, F. S. Ligler and Z. Gu, *Nanoscale* **2015,** *7*, 12096-12103.
[94] A. S. D. S. Indrasekara, R. C. Wadams and L. Fabris, *Part. Part. Syst. Charact* **2014,** *31*, 819-838.
[95] L. Tong, Q. Wei, A. Wei and J.-X. Cheng, *Photochem. Photobiol* **2009,** *85*, 21-32.

[96] E. S. Day, J. G. Morton and J. L. West, *J. Biomech. Eng* **2009,** *131*, 074001-074001-5.
[97] X. Huang, I. H. El-Sayed, W. Qian and M. A. El-Sayed, *J. Am. Chem. Soc* **2006,** *128*, 2115-2120.
[98] G. von Maltzahn, J.-H. Park, A. Agrawal, N. K. Bandaru, S. K. Das, M. J. Sailor and S. N. Bhatia, *Cancer Research* **2009,** *69*, 3892-3900.
[99] C. Mohrdieck, *ChemPhysChem* **2006,** *7*, 1149-1149.
[100] M. Borzenkov, A. Määttänen, P. Ihalainen, M. Collini, E. Cabrini, G. Dacarro, P. Pallavicini and G. Chirico, *ACS Appl. Mater. Interfaces* **2016,** *8*, 9909-9916.
[101] S. Link, Z. L. Wang and M. A. El-Sayed, *J. Phys. Chem. B* **2000,** *104*, 7867-7870.
[102] H. Petrova, J. Perez Juste, I. Pastoriza-Santos, G. V. Hartland, L. M. Liz-Marzan and P. Mulvaney, *Phys. Chem. Chem. Phys* **2006,** *8*, 814-821.
[103] S. Link, C. Burda, M. B. Mohamed, B. Nikoobakht and M. A. El-Sayed, *J. Phys. Chem. A* **1999,** *103*, 1165-1170.
[104] S. Link, C. Burda, B. Nikoobakht and M. A. El-Sayed, *J. Phys. Chem. B* **2000,** *104*, 6152-6163.
[105] S. Link and M. A. El-Sayed, *J. Chem. Phys* **2001,** *114*, 2362-2368.
[106] G. Opletal, G. Grochola, Y. H. Chui, I. K. Snook and S. P. Russo, *J. Phys. Chem. C* **2011,** *115*, 4375-4380.
[107] M. B. Mohamed, K. Z. Ismail, S. Link and M. A. El-Sayed, *J. Phys. Chem. B* **1998,** *102*, 9370-9374.
[108] Y. Horiguchi, K. Honda, Y. Kato, N. Nakashima and Y. Niidome, *Langmuir* **2008,** *24*, 12026-12031.
[109] R. Zou, Q. Zhang, Q. Zhao, F. Peng, H. Wang, H. Yu and J. Yang, *Colloids Surf A Physicochem Eng Asp* **2010,** *372*, 177-181.
[110] A. Gole and C. J. Murphy, *Chem. Mater* **2004,** *16*, 3633-3640.
[111] M. Iqbal, Y.-I. Chung and G. Tae, *J. Mater. Chem.* **2007,** *17*, 335-342.
[112] X. Ye, C. Zheng, J. Chen, Y. Gao and C. B. Murray, *Nano Lett* **2013,** *13*, 765-771.
[113] M. Samim, C. Prashant, A. Dinda, A. Maitra and I. Arora, *Int. J. Nanomedicine* **2011,** *6*, 1825.
[114] B. Nikoobakht and M. A. El-Sayed, *Langmuir* **2001,** *17*, 6368-6374.
[115] C. R.-K. Betty, R. B. Lissett, M. P. Courtney, S. D. Emily, J. E. A. Lindsey, Z. Meng, L. Seunghyun, M. M. Kathryn, Z. Tomasz, A. Liana, P. N. D. Colin, A. D. Rebekah, L. W. Jennifer and H. H. Jason, *Nanotechnology* **2009,** *20*, 434005.
[116] A. P. Leonov, J. Zheng, J. D. Clogston, S. T. Stern, A. K. Patri and A. Wei, *ACS Nano* **2008,** *2*, 2481-2488.
[117] C. J. Orendorff, T. M. Alam, D. Y. Sasaki, B. C. Bunker and J. A. Voigt, *ACS Nano* **2009,** *3*, 971-983.
[118] S. F. Tan, U. Anand and U. Mirsaidov, *ACS Nano* **2017,** *11*, 1633-1640.
[119] L. Xu, H. Kuang, C. Xu, W. Ma, L. Wang and N. A. Kotov, *J. Am. Chem. Soc* **2012,** *134*, 1699-1709.
[120] R. C. Wadams, L. Fabris, R. A. Vaia and K. Park, *Chem. Mater* **2013,** *25*, 4772-4780.
[121] K. K. Caswell, J. N. Wilson, U. H. F. Bunz and C. J. Murphy, *J. Am. Chem. Soc* **2003,** *125*, 13914-13915.
[122] D. Nepal, K. Park and R. A. Vaia, *Small* **2012,** *8*, 1013-1020.
[123] K. Liu, Z. Nie, N. Zhao, W. Li, M. Rubinstein and E. Kumacheva, *Science* **2010,** *329*, 197-200.

[124] W. Ma, H. Kuang, L. Xu, L. Ding, C. Xu, L. Wang and N. A. Kotov, **2013,** *4*, 2689.
[125] J. A. Fan, C. Wu, K. Bao, J. Bao, R. Bardhan, N. J. Halas, V. N. Manoharan, P. Nordlander, G. Shvets and F. Capasso, *Science* **2010,** *328*, 1135-1138.
[126] S. J. Tan, M. J. Campolongo, D. Luo and W. Cheng, *Nat Nano* **2011,** *6*, 268-276.
[127] J. Sharma, R. Chhabra, A. Cheng, J. Brownell, Y. Liu and H. Yan, *Science* **2009,** *323*, 112-116.
[128] M. M. Maye, D. Nykypanchuk, M. Cuisinier, D. van der Lelie and O. Gang, *Nat Mater* **2009,** *8*, 388-391.
[129] L. Zhong, X. Zhou, S. Bao, Y. Shi, Y. Wang, S. Hong, Y. Huang, X. Wang, Z. Xie and Q. Zhang, *J. Mater. Chem.* **2011,** *21*, 14448-14455.
[130] J. Kumar and K. G. Thomas, *J. Phys. Chem. Lett* **2011,** *2*, 610-615.
[131] Y. Zheng, T. Thai, P. Reineck, L. Qiu, Y. Guo and U. Bach, *Adv. Funct. Mater* **2013,** *23*, 1519-1526.
[132] P. Missel, N. Mazer, M. Carey and G. Benedek. Thermodynamics of the sphere-to-rod transition in alkyl sulfate micelles. In *Solution Behavior of Surfactants*; Springer, 1982, pp 373-388.
[133] P. J. Missel, N. A. Mazer, G. B. Benedek and M. C. Carey, *J. Phys. Chem* **1983,** *87*, 1264-1277.
[134] P. Debye and E. W. Anacker, *J. Phys. Chem* **1951,** *55*, 644-655.
[135] P. Mukerjee, *J. Phys. Chem* **1972,** *76*, 565-570.
[136] R. J. M. Tausk and J. T. G. Overbeek. SIZE, SHAPE AND SIZE DISTRIBUTION OF MICELLES IN AQUEOUS SOLUTIONS OF SHORT-CHAIN LECITHIN HOMOLOGUES A2 - KERKER, MILTON. In *Collied and Interface Science*; Academic Press, 1976, pp 379-396.
[137] J. N. Israelachvili, D. J. Mitchell and B. W. Ninham, *J. Chem. Soc., Faraday Trans. 2* **1976,** *72*, 1525-1568.
[138] N. Almora-Barrios, G. Novell-Leruth, P. Whiting, L. M. Liz-Marzán and N. López, *Nano Lett.* **2014,** *14*, 871-875.
[139] S. R. Jackson, J. R. McBride, S. J. Rosenthal and D. W. Wright, *J. Am. Chem. Soc* **2014,** *136*, 5261-5263.
[140] J. Pérez-Juste, L. M. Liz-Marzán, S. Carnie, D. Y. C. Chan and P. Mulvaney, *Adv. Funct. Mater* **2004,** *14*, 571-579.
[141] C. J. Orendorff and C. J. Murphy, *J. Phys. Chem. B* **2006,** *110*, 3990-3994.
[142] T. K. Sau and C. J. Murphy, *Langmuir* **2004,** *20*, 6414-6420.
[143] N. Garg, C. Scholl, A. Mohanty and R. Jin, *Langmuir* **2010,** *26*, 10271-10276.
[144] X. Ye, L. Jin, H. Caglayan, J. Chen, G. Xing, C. Zheng, V. Doan-Nguyen, Y. Kang, N. Engheta, C. R. Kagan and C. B. Murray, *ACS Nano* **2012,** *6*, 2804-2817.
[145] T. H. Ha, H.-J. Koo and B. H. Chung, *J. Phys. Chem. C* **2007,** *111*, 1123-1130.
[146] S. B. Velegol, B. D. Fleming, S. Biggs, E. J. Wanless and R. D. Tilton, *Langmuir* **2000,** *16*, 2548-2556.
[147] L. J. Magid, Z. Han, G. G. Warr, M. A. Cassidy, P. D. Butler and W. A. Hamilton, *J. Phys. Chem. B* **1997,** *101*, 7919-7927.
[148] Z. L. Wang, R. P. Gao, B. Nikoobakht and M. A. El-Sayed, *J. Phys. Chem. B* **2000,** *104*, 5417-5420.
[149] X.-H. Liu, X.-H. Luo, S.-X. Lu, J.-C. Zhang and W.-L. Cao, *J. Colloid. Interface. Sci* **2007,** *307*, 94-100.
[150] F. Hubert, F. Testard and O. Spalla, *Langmuir* **2008,** *24*, 9219-9222.

[151] F. Giannici, T. Placido, M. L. Curri, M. Striccoli, A. Agostiano and R. Comparelli, *Dalton Trans.* **2009**, 10367-10374.
[152] T. Placido, R. Comparelli, F. Giannici, P. D. Cozzoli, G. Capitani, M. Striccoli, A. Agostiano and M. L. Curri, *Chem. Mater* **2009,** *21*, 4192-4202.
[153] U. Kreibig and M. Vollmer. Theoretical considerations. In *Optical Properties of Metal Clusters*; Springer, 1995, pp 13-201.
[154] J. Li, L. Wang, L. Liu, L. Guo, X. Han and Z. Zhang, *Chem. Commun* **2010,** *46*, 5109-5111.
[155] T. Pal, De, N. R. Jana, N. Pradhan, R. Mandal, A. Pal, A. E. Beezer and J. C. Mitchell, *Langmuir* **1998,** *14*, 4724-4730.
[156] Liu and P. Guyot-Sionnest, *J. Phys. Chem. B* **2005,** *109*, 22192-22200.
[157] E. Carbó-Argibay, B. Rodríguez-González, S. Gómez-Graña, A. Guerrero-Martínez, I. Pastoriza-Santos, J. Pérez-Juste and L. M. Liz-Marzán, *Angew. Chem. Int. Ed* **2010,** *49*, 9397-9400.
[158] Z. L. Wang, M. B. Mohamed, S. Link and M. A. El-Sayed, *Surf. Sci* **1999,** *440*, L809-L814.
[159] A. M. Alkilany, P. K. Nagaria, C. R. Hexel, T. J. Shaw, C. J. Murphy and M. D. Wyatt, *Small* **2009,** *5*, 701-708.
[160] C. Grabinski, N. Schaeublin, A. Wijaya, H. D'Couto, S. H. Baxamusa, K. Hamad-Schifferli and S. M. Hussain, *ACS Nano* **2011,** *5*, 2870-2879.
[161] C. J. Murphy, A. M. Gole, J. W. Stone, P. N. Sisco, A. M. Alkilany, E. C. Goldsmith and S. C. Baxter, *Acc. Chem. Res* **2008,** *41*, 1721-1730.
[162] A. M. Alkilany, A. Shatanawi, T. Kurtz, R. B. Caldwell and R. W. Caldwell, *Small* **2012,** *8*, 1270-1278.
[163] T. S. Hauck, A. A. Ghazani and W. C. W. Chan, *Small* **2008,** *4*, 153-159.
[164] S. Wang, W. Lu, O. Tovmachenko, U. S. Rai, H. Yu and P. C. Ray, *Chem. Phys. Lett.* **2008,** *463*, 145-149.
[165] G. R. Raja, P. Wilma, H. Liesbeth, C. Patrick, J. Hans, W. B. v. L. Fijs, O. Cees, M. Srirang and G. v. L. Ton, *Nanotechnology* **2010,** *21*, 145101.
[166] S. Manohar, R. Rayavarapu, W. Petersen and T. G. van Leeuwen. In *Cell viability studies of PEG-thiol treated gold nanorods as optoacoustic contrast agents*, 2009, pp 71772D-71772D-8.
[167] C. Rosman, S. Pierrat, A. Henkel, M. Tarantola, D. Schneider, E. Sunnick, A. Janshoff and C. Sönnichsen, *Small* **2012,** *8*, 3683-3690.
[168] K. Liu, Y. Bu, Y. Zheng, X. Jiang, A. Yu and H. Wang, *Chemistry – A European Journal* **2017,** *23*, 3291-3299.
[169] K. Liu, Y. Zheng, X. Lu, T. Thai, N. A. Lee, U. Bach and J. J. Gooding, *Langmuir* **2015,** *31*, 4973-4980.
[170] S.-S. Chang, C.-W. Shih, C.-D. Chen, W.-C. Lai and C. R. C. Wang, *Langmuir* **1999,** *15*, 701-709.
[171] C. J. Murphy, T. K. Sau, A. M. Gole, C. J. Orendorff, J. Gao, L. Gou, S. E. Hunyadi and T. Li, *J. Phys. Chem. B* **2005,** *109*, 13857-13870.
[172] B. D. Busbee, S. O. Obare and C. J. Murphy, *Adv. Mater* **2003,** *15*, 414-416.
[173] Y. Takenaka and H. Kitahata, *Chem. Phys. Lett.* **2009,** *467*, 327-330.
[174] H.-Y. Wu, H.-C. Chu, T.-J. Kuo, C.-L. Kuo and M. H. Huang, *Chem. Mater* **2005,** *17*, 6447-6451.
[175] B. P. Khanal and E. R. Zubarev, *J. Am. Chem. Soc* **2008,** *130*, 12634-12635.
[176] J. Gao, C. M. Bender and C. J. Murphy, *Langmuir* **2003,** *19*, 9065-9070.
[177] Y. Xu, Y. Zhao, L. Chen, X. Wang, J. Sun, H. Wu, F. Bao, J. Fan and Q. Zhang, *Nanoscale* **2015,** *7*, 6790-6797.
[178] L. Vigderman and E. R. Zubarev, *Chem. Mater* **2013,** *25*, 1450-1457.

[179] H. M. Chen, H.-C. Peng, R.-S. Liu, K. Asakura, C.-L. Lee, J.-F. Lee and S.-F. Hu, *J. Phys. Chem. B* **2005,** *109*, 19553-19555.
[180] Z. Jing, Y. Ken-Tye, R. Indrajit, H. Rui, D. Hong, Z. Lingling, T. S. Mark, S. H. Guang, C. Yiping and N. P. Paras, *Nanotechnology* **2010,** *21*, 285106.
[181] G. Su, C. Yang and J.-J. Zhu, *Langmuir* **2015,** *31*, 817-823.
[182] K. A. Kozek, K. M. Kozek, W.-C. Wu, S. R. Mishra and J. B. Tracy, *Chem. Mater* **2013,** *25*, 4537-4544.
[183] X. Xu, Y. Zhao, X. Xue, S. Huo, F. Chen, G. Zou and X.-J. Liang, *J. Mater. Chem. A* **2014,** *2*, 3528-3535.
[184] J. Zhang, C. Xi, C. Feng, H. Xia, D. Wang and X. Tao, *Langmuir* **2014,** *30*, 2480-2489.
[185] N. R. Jana, *Small* **2005,** *1*, 875-882.
[186] M. R. K. Ali, B. Snyder and M. A. El-Sayed, *Langmuir* **2012,** *28*, 9807-9815.
[187] K. Esumi, K. Matsuhisa and K. Torigoe, *Langmuir* **1995,** *11*, 3285-3287.
[188] F. Kim, J. H. Song and P. D. Yang, *J. Am. Chem. Soc* **2002,** *124*, 14316-14317.
[189] E. Leontidis, K. Kleitou, T. Kyprianidou-Leodidou, V. Bekiari and P. Lianos, *Langmuir* **2002,** *18*, 3659-3668.
[190] O. R. Miranda and T. S. Ahmadi, *J. Phys. Chem. B* **2005,** *109*, 15724-15734.
[191] O. R. Miranda, N. R. Dollahon and T. S. Ahmadi, *Cryst. Growth Des.* **2006,** *6*, 2747-2753.
[192] Y. Niidome, K. Nishioka, H. Kawasaki and S. Yamada, *Chem. Commun* **2003**, 2376-2377.
[193] K. Nishioka, Y. Niidome and S. Yamada, *Langmuir* **2007,** *23*, 10353-10356.
[194] B. M. I. van der Zande, M. R. Böhmer, L. G. J. Fokkink and C. Schönenberger, *Langmuir* **2000,** *16*, 451-458.
[195] G. A. Wurtz, PollardR, HendrenW, G. P. Wiederrecht, D. J. Gosztola, V. A. Podolskiy and A. V. Zayats, *Nat Nano* **2011,** *6*, 107-111.
[196] W. Dickson, P. R. Evans, G. A. Wurtz, W. Hendren, R. Atkinson, R. J. Pollard and A. V. Zayats, *J. Microsc.* **2008,** *229*, 415-420.
[197] C. R. Martin, *Chem. Mater* **1996,** *8*, 1739-1746.
[198] V. M. Cepak and C. R. Martin, *J. Phys. Chem. B* **1998,** *102*, 9985-9990.
[199] M. J. Tierney and C. R. Martin, *J. Phys. Chem* **1989,** *93*, 2878-2880.
[200] J. C. Hulteen and C. R. Martin, *J. Mater. Chem.* **1997,** *7*, 1075-1087.
[201] L. Vigderman, B. P. Khanal and E. R. Zubarev, *Adv. Mater* **2012,** *24*, 4811-4841.
[202] Z. Li, C. Kübel, V. I. Pârvulescu and R. Richards, *ACS Nano* **2008,** *2*, 1205-1212.
[203] Y. Xie, S. Quinlivan and T. Asefa, *J. Phys. Chem. C* **2008,** *112*, 9996-10003.
[204] C. Gao, Q. Zhang, Z. Lu and Y. Yin, *J. Am. Chem. Soc* **2011,** *133*, 19706-19709.
[205] C. Gao, Z. Lu and Y. Yin, *Langmuir* **2011,** *27*, 12201-12208.
[206] K. Okitsu, K. Sharyo and R. Nishimura, *Langmuir* **2009,** *25*, 7786-7790.
[207] G. Canizal, J. A. Ascencio, J. Gardea-Torresday and M. J. Yacamán, *J. Nanopart. Res* **2001,** *3*, 475-481.
[208] Y.-J. Kim, G. Cho and J. H. Song, *Nuclear Instruments and Methods in Physics Research Section B: Beam Interactions with Materials and Atoms* **2006,** *246*, 351-354.
[209] W. Abidi, P. R. Selvakannan, Y. Guillet, I. Lampre, P. Beaunier, B. Pansu, B. Palpant and H. Remita, *J. Phys. Chem. C* **2010,** *114*, 14794-14803.
[210] J. Biswal, S. P. Ramnani, R. Tewari, G. K. Dey and S. Sabharwal, *Radiat. Phys. Chem.* **2010,** *79*, 441-445.

[211] Z. Ying-Jie and H. Xian-Luo, *Chem Lett* **2003,** *32*, 1140-1141.
[212] C. Jieming, M. Xianjia, Z. Mingbo, L. Jinsong and J. Hongmei, *Chem Lett* **2005,** *34*, 730-731.
[213] B. Alexandra, *J. Opt. A: Pure Appl. Opt.* **2009,** *11*, 114001.
[214] L. Billot, M. Lamy de la Chapelle, A. S. Grimault, A. Vial, D. Barchiesi, J. L. Bijeon, P. M. Adam and P. Royer, *Chem. Phys. Lett.* **2006,** *422*, 303-307.
[215] Z. Li, J. Tao, X. Lu, Y. Zhu and Y. Xia, *Nano Lett* **2008,** *8*, 3052-3055.
[216] A. Gole and C. J. Murphy, *Chem. Mater* **2005,** *17*, 1325-1330.
[217] C. G. Wilson, P. N. Sisco, F. A. Gadala-Maria, C. J. Murphy and E. C. Goldsmith, *Biomaterials* **2009,** *30*, 5639-5648.
[218] W. Chen and T. J. McCarthy, *Macromolecules* **1997,** *30*, 78-86.
[219] H.-C. Huang, S. Barua, D. B. Kay and K. Rege, *ACS Nano* **2009,** *3*, 2941-2952.
[220] M. C. LeMieux, Y. H. Lin, P. D. Cuong, H. S. Ahn, E. R. Zubarev and V. V. Tsukruk, *Adv. Funct. Mater* **2005,** *15*, 1529-1540.
[221] A. M. Alkilany, P. K. Nagaria, M. D. Wyatt and C. J. Murphy, *Langmuir* **2010,** *26*, 9328-9333.
[222] A. M. Alkilany, L. B. Thompson and C. J. Murphy, *ACS Appl. Mater. Interfaces* **2010,** *2*, 3417-3421.
[223] C. J. Murphy, L. B. Thompson, A. M. Alkilany, P. N. Sisco, S. P. Boulos, S. T. Sivapalan, J. A. Yang, D. J. Chernak and J. Huang, *J. Phys. Chem. Lett* **2010,** *1*, 2867-2875.
[224] A. Gole and C. J. Murphy, *Langmuir* **2008,** *24*, 266-272.
[225] A. Gole and C. J. Murphy, *Langmuir* **2005,** *21*, 10756-10762.
[226] Y. Zhu, C. Qu, H. Kuang, L. Xu, L. Liu, Y. Hua, L. Wang and C. Xu, *Biosens. Bioelectron* **2011,** *26*, 4387-4392.
[227] C.-A. Peng and C.-H. Wang, *Cancers* **2011,** *3*, 227.
[228] B. Thierry, J. Ng, T. Krieg and H. J. Griesser, *Chem. Commun* **2009**, 1724-1726.
[229] D. Gentili, G. Ori and M. Comes Franchini, *Chem. Commun* **2009**, 5874-5876.
[230] C. Yu, H. Nakshatri and J. Irudayaraj, *Nano Lett* **2007,** *7*, 2300-2306.
[231] L. Vigderman, P. Manna and E. R. Zubarev, *Angew. Chem. Int. Ed* **2012,** *51*, 636-641.
[232] Z. Zhang and M. Lin, *RSC Adv* **2014,** *4*, 17760-17767.
[233] C. Kinnear, H. Dietsch, M. J. D. Clift, C. Endes, B. Rothen-Rutishauser and A. Petri-Fink, *Angew. Chem. Int. Ed* **2013,** *52*, 1934-1938.
[234] A. Wijaya and K. Hamad-Schifferli, *Langmuir* **2008,** *24*, 9966-9969.
[235] Q. Dai, J. Coutts, J. Zou and Q. Huo, *Chem. Commun* **2008**, 2858-2860.
[236] T. Niidome, M. Yamagata, Y. Okamoto, Y. Akiyama, H. Takahashi, T. Kawano, Y. Katayama and Y. Niidome, *J. Controlled Release* **2006,** *114*, 343-347.
[237] H. Liao and J. H. Hafner, *Chem. Mater.* **2005,** *17*, 4636-4641.
[238] C. B. Sanda and A. Simion, *Nanotechnology* **2010,** *21*, 235601.
[239] K. Maeda and K. Domen, *J. Phys. Chem. Lett* **2010,** *1*, 2655-2661.
[240] M. Gao, L. Zhu, W. L. Ong, J. Wang and G. W. Ho, *Catal. Sci. Tech.* **2015,** *5*, 4703-4726.
[241] Z. W. Seh, S. Liu, M. Low, S.-Y. Zhang, Z. Liu, A. Mlayah and M.-Y. Han, *Adv. Mater* **2012,** *24*, 2310-2314.
[242] Y. Tian and T. Tatsuma, *J. Am. Chem. Soc* **2005,** *127*, 7632-7637.
[243] J. Yan, G. Wu, N. Guan and L. Li, *Chem. Commun* **2013,** *49*, 11767-11769.
[244] Z. Lin, X. Wang, J. Liu, Z. Tian, L. Dai, B. He, C. Han, Y. Wu, Z. Zeng and Z. Hu, *Nanoscale* **2015,** *7*, 4114-4123.
[245] H. Choi, W. T. Chen and P. V. Kamat, *ACS Nano* **2012,** *6*, 4418-4427.

[246] G. K. Mor, K. Shankar, M. Paulose, O. K. Varghese and C. A. Grimes, *Nano Lett* **2006,** *6*, 215-218.
[247] P. V. Kamat, K. Tvrdy, D. R. Baker and J. G. Radich, *Chem.Rev* **2010,** *110*, 6664-6688.
[248] I. Mora-Seró and J. Bisquert, *J. Phys. Chem. Lett* **2010,** *1*, 3046-3052.
[249] J. Ryu, S. H. Lee, D. H. Nam and C. B. Park, *Adv. Mater* **2011,** *23*, 1883-1888.
[250] H. Park, H.-H. Ou, A. J. Colussi and M. R. Hoffmann, *J. Phys. Chem. A* **2015,** *119*, 4658-4666.
[251] C. Liu, N. P. Dasgupta and P. Yang, *Chem. Mater* **2014,** *26*, 415-422.
[252] X. Chen, L. Liu, P. Y. Yu and S. S. Mao, *Science* **2011,** *331*, 746-750.
[253] J. M. Macak, M. Zlamal, J. Krysa and P. Schmuki, *Small* **2007,** *3*, 300-304.
[254] A. Fujishima and K. Honda, *Nature* **1972,** *238*, 37-38.
[255] J. Li and N. Wu, *Catal. Sci. Tech.* **2015,** *5*, 1360-1384.
[256] J.-J. Chen, J. C. S. Wu, P. C. Wu and D. P. Tsai, *J. Phys. Chem. C* **2011,** *115*, 210-216.
[257] Y. Amao and I. Okura. Photocatalysis-science and Technology. Kodansha-Springer, 2002.
[258] A. J. Bard, R. Parsons and J. Jordan. *Standard potentials in aqueous solution*; CRC press1985; Vol. 6.
[259] O. Rosseler, M. V. Shankar, M. K.-L. Du, L. Schmidlin, N. Keller and V. Keller, *J. Catal.* **2010,** *269*, 179-190.
[260] B. Gupta, A. A. Melvin, T. Matthews, S. Dash and A. K. Tyagi, *Renew. Sust. Energ. Rev.* **2016,** *58*, 1366-1375.
[261] X. Chen and S. S. Mao, *Chem.Rev* **2007,** *107*, 2891-2959.
[262] T. Hirakawa and P. V. Kamat, *J. Am. Chem. Soc* **2005,** *127*, 3928-3934.
[263] J. Yu, L. Qi and M. Jaroniec, *J. Phys. Chem. C* **2010,** *114*, 13118-13125.
[264] R. Asahi, T. Morikawa, T. Ohwaki, K. Aoki and Y. Taga, *Science* **2001,** *293*, 269-271.
[265] S. Sakthivel and H. Kisch, *Angew. Chem. Int. Ed* **2003,** *42*, 4908-4911.
[266] P. Hoyer and R. Könenkamp, *Appl. Phys. Lett.* **1995,** *66*, 349-351.
[267] B. O'Regan and M. Gratzel, *Nature* **1991,** *353*, 737-740.
[268] U. Bach, D. Lupo, P. Comte, J. E. Moser, F. Weissortel, J. Salbeck, H. Spreitzer and M. Gratzel, *Nature* **1998,** *395*, 583-585.
[269] K. Zhu, N. R. Neale, A. Miedaner and A. J. Frank, *Nano Lett* **2007,** *7*, 69-74.
[270] C. Gomes Silva, R. Juárez, T. Marino, R. Molinari and H. García, *J. Am. Chem. Soc* **2011,** *133*, 595-602.
[271] Y. J. Lee, J. B. Joo, Y. Yin and F. Zaera, *ACS Energy Lett.* **2016,** *1*, 52-56.
[272] D. D. Lekeufack, A. Brioude, A. Mouti, J. G. Alauzun, P. Stadelmann, A. W. Coleman and P. Miele, *Chem. Commun* **2010,** *46*, 4544-4546.
[273] Z. W. Seh, S. Liu, S.-Y. Zhang, K. W. Shah and M.-Y. Han, *Chem. Commun* **2011,** *47*, 6689-6691.
[274] J. B. Priebe, J. Radnik, A. J. J. Lennox, M.-M. Pohl, M. Karnahl, D. Hollmann, K. Grabow, U. Bentrup, H. Junge, M. Beller and A. Brückner, *ACS Catal.* **2015,** *5*, 2137-2148.
[275] K. Rajeshwar, C. R. Chenthamarakshan, Y. Ming and W. Sun, *J. Electroanal. Chem* **2002,** *538*, 173-182.
[276] X. Chen, S. Shen, L. Guo and S. S. Mao, *Chem.Rev* **2010,** *110*, 6503-6570.
[277] Z. Liu, W. Hou, P. Pavaskar, M. Aykol and S. B. Cronin, *Nano Lett* **2011,** *11*, 1111-1116.
[278] P. Christopher, D. B. Ingram and S. Linic, *J. Phys. Chem. C* **2010,** *114*, 9173-9177.

[279] M. Jakob, H. Levanon and P. V. Kamat, *Nano Lett* **2003,** *3*, 353-358.
[280] E. W. McFarland and J. Tang, *Nature* **2003,** *421*, 616-618.
[281] D. M. Schaadt, B. Feng and E. T. Yu, *Appl. Phys. Lett.* **2005,** *86*, 063106.
[282] D. Jose, C. M. Sorensen, S. S. Rayalu, K. M. Shrestha and K. J. Klabunde, *Int. J. Photoenergy* **2013,** *2013*, 10.
[283] V. Subramanian, E. E. Wolf and P. V. Kamat, *J. Am. Chem. Soc* **2004,** *126*, 4943-4950.
[284] P. V. Kamat, *J. Phys. Chem. Lett* **2012,** *3*, 663-672.
[285] A. Takai and P. V. Kamat, *ACS Nano* **2011,** *5*, 7369-7376.
[286] V. Subramanian, E. E. Wolf and P. V. Kamat, *J. Phys. Chem. B* **2003,** *107*, 7479-7485.
[287] T. Hirakawa and P. V. Kamat, *Langmuir* **2004,** *20*, 5645-5647.
[288] A. Wood, M. Giersig and P. Mulvaney, *J. Phys. Chem. B* **2001,** *105*, 8810-8815.
[289] N. Zhou, L. Polavarapu, N. Gao, Y. Pan, P. Yuan, Q. Wang and Q.-H. Xu, *Nanoscale* **2013,** *5*, 4236-4241.
[290] L. Liu, S. Ouyang and J. Ye, *Angew. Chem. Int. Ed* **2013,** *52*, 6689-6693.
[291] Y. Takahashi, N. Miyahara and S. Yamada, *Anal Sci.* **2013,** *29*, 101-105.
[292] A. Antonello, E. Della Gaspera, J. Baldauf, G. Mattei and A. Martucci, *J. Mater. Chem.* **2011,** *21*, 13074-13078.
[293] G. L. Chiarello, A. Di Paola, L. Palmisano and E. Selli, *Photoch. Photobiol. Sci.* **2011,** *10*, 355-360.
[294] O. K. Varghese, D. Gong, M. Paulose, C. A. Grimes and E. C. Dickey, *J. Mat. Res* **2003,** *18*, 156-165.
[295] V. Sharma, K. Park and M. Srinivasarao, *Mater. Sci. Eng. R-Rep.* **2009,** *65*, 1-38.
[296] R. M. Pallares, X. Su, S. H. Lim and N. T. K. Thanh, *J. Mater. Chem. C* **2016,** *4*, 53-61.
[297] A. Liopo, S. Wang, P. J. Derry, A. A. Oraevsky and E. R. Zubarev, *RSC Adv* **2015,** *5*, 91587-91593.
[298] J. M. El Khoury, X. Zhou, L. Qu, L. Dai, A. Urbas and Q. Li, *Chem. Commun.* **2009**, 2109-2111.
[299] B. P. Khanal and E. R. Zubarev, *Angew. Chem. Int. Ed.* **2007,** *46*, 2195-2198.
[300] H. Takahashi, Y. Niidome, T. Niidome, K. Kaneko, H. Kawasaki and S. Yamada, *Langmuir* **2005,** *22*, 2-5.
[301] P. Harder, M. Grunze, R. Dahint, G. M. Whitesides and P. E. Laibinis, *J. Phys. Chem. B* **1998,** *102*, 426-436.
[302] Y. Shi, H. Q. Luo and N. B. Li, *Spectrochim. Acta Mol. Biomol. Spectrosc.* **2011,** *78*, 1403-1407.
[303] M. J. Walsh, S. J. Barrow, W. Tong, A. M. Funston and J. Etheridge, *ACS Nano* **2015,** *9*, 715-724.
[304] C. J. Murphy and N. R. Jana, *Adv. Mater* **2002,** *14*, 80-82.
[305] S. Si, C. Leduc, M.-H. Delville and B. Lounis, *ChemPhysChem* **2012,** *13*, 193-202.
[306] Sirajuddin, A. Mechler, A. A. J. Torriero, A. Nafady, C.-Y. Lee, A. M. Bond, A. P. O'Mullane and S. K. Bhargava, *Colloids Surf A Physicochem Eng Asp* **2010,** *370*, 35-41.
[307] S. D. Perrault and W. C. W. Chan, *J. Am. Chem. Soc* **2009,** *131*, 17042-17043.
[308] C. Morasso, S. Picciolini, D. Schiumarini, D. Mehn, I. Ojea-Jiménez, G. Zanchetta, R. Vanna, M. Bedoni, D. Prosperi and F. Gramatica, *J. Nanopart. Res* **2015,** *17*, 1-7.
[309] C. J. M. Orendorff, Catherine J., *J. Phys. Chem. B* **2006,** *110*, 3990-3994.

[310] Z.-m. Xiu, Q.-b. Zhang, H. L. Puppala, V. L. Colvin and P. J. J. Alvarez, *Nano Lett.* **2012,** *12*, 4271-4275.
[311] R. Ma, C. Levard, S. M. Marinakos, Y. Cheng, J. Liu, F. M. Michel, G. E. Brown and G. V. Lowry, *Environ. Sci. Technol.* **2011,** *46*, 752-759.
[312] L. Wang, Y. Liu, W. Li, X. Jiang, Y. Ji, X. Wu, L. Xu, Y. Qiu, K. Zhao, T. Wei, Y. Li, Y. Zhao and C. Chen, *Nano Lett.* **2010,** *11*, 772-780.
[313] J. S. Bozich, S. E. Lohse, M. D. Torelli, C. J. Murphy, R. J. Hamers and R. D. Klaper, *Environmental Science: Nano* **2014,** *1*, 260-270.
[314] L. Wang, X. Jiang, Y. Ji, R. Bai, Y. Zhao, X. Wu and C. Chen, *Nanoscale* **2013,** *5*, 8384-8391.
[315] X. Cheng, W. Zhang, Y. Ji, J. Meng, H. Guo, J. Liu, X. Wu and H. Xu, *RSC Advances* **2013,** *3*, 2296-2305.
[316] A. Waqqar, G. Christian, E. S. Kooij and M. v. R. Jan, *Nanotechnology* **2014,** *25*, 035301.
[317] H. Hu and R. G. Larson, *The Journal of Physical Chemistry B* **2006,** *110*, 7090-7094.
[318] M. Matsuoka, S. Isotani, R. D. Mansano, W. Sucasaire, R. A. C. Pinto, J. C. R. Mittani, K. Ogata and N. Kuratani, *World Journal of Nano Science and Engineering* **2012**, 92-102.
[319] C. Xue, G. S. Métraux, J. E. Millstone and C. A. Mirkin, *J. Am. Chem. Soc.* **2008,** *130*, 8337-8344.
[320] S. Kapoor, *Langmuir* **1998,** *14*, 1021-1025.
[321] A. M. Ahern and R. L. Garrell, *Analytical Chemistry* **1987,** *59*, 2813-2816.
[322] G. P. Lee, A. I. Minett, P. C. Innis and G. G. Wallace, *J. Mater. Chem.* **2009,** *19*, 8294-8298.
[323] J. Yang, J. Y. Lee, H.-P. Too and S. Valiyaveettil, *J. Phys. Chem. B* **2005,** *110*, 125-129.
[324] P. Anstaett, Y. Zheng, T. Thai, A. M. Funston, U. Bach and G. Gasser, *Angew. Chem. Int. Ed.* **2013,** *52*, 4217-4220.
[325] Cao, R. Jin and C. A. Mirkin, *J. Am. Chem. Soc.* **2001,** *123*, 7961-7962.
[326] M. J. FORD, C. MASENS and M. B. CORTIE, *Surf. Rev. Lett.* **2006,** *13*, 297-307.
[327] T. Gschneidtner and K. Moth-Poulsen. Self-Assembly at Interfaces. In *Handbook of Single Molecule Electronics*; Pan Stanford Publishing Pte Ltd, 2009, p 23.
[328] H. Hinterwirth, S. Kappel, T. Waitz, T. Prohaska, W. Lindner and M. Lämmerhofer, *ACS Nano* **2013,** *7*, 1129-1136.
[329] C. S. Ah, W.-J. Kim, W. S. Yun and S.-W. Joo, *Curr. Appl. Phys* **2013,** *13*, 1889-1893.
[330] P. P. Joshi, S. J. Yoon, W. G. Hardin, S. Emelianov and K. V. Sokolov, *Bioconjugate Chem.* **2013,** *24*, 878-888.
[331] Y. Bu and S. Lee, *J. Nanosci. Nanotechnol.* **2013,** *13*, 4178-4182.
[332] X. Jiang, T. Herricks and Y. Xia, *Adv. Mater* **2003,** *15*, 1205-1209.
[333] X. Yang, H. Fu, A. Yu and X. Jiang, *J. Colloid. Interface. Sci* **2012,** *387*, 74-83.
[334] J. Goebl, J. B. Joo, M. Dahl and Y. Yin, *Catalysis Today* **2014,** *225*, 90-95.
[335] J. B. Joo, Q. Zhang, I. Lee, M. Dahl, F. Zaera and Y. Yin, *Adv. Funct. Mater* **2012,** *22*, 166-174.
[336] D. Wang, L. Liu, F. Zhang, K. Tao, E. Pippel and K. Domen, *Nano Lett* **2011,** *11*, 3649-3655.
[337] S. Li, G. Ye and G. Chen, *J. Phys. Chem. C* **2009,** *113*, 4031-4037.

[338] S. F. Kou, W. Ye, X. Guo, X. F. Xu, H. Y. Sun and J. Yang, *RSC Adv* **2016,** *6*, 39144-39149.
[339] A. Gallo , T. Montini, M. Marelli, A. Minguzzi, V. Gombac, R. Psaro, P. Fornasiero and V. Dal Santo, *ChemSusChem* **2012,** *5*, 1800-1811.